Synthetic model microswimmers near walls

Ketzetzi, S.

Cover Page

Universiteit Leiden

The handle http://hdl.handle.net/1887/3185906 holds various files of this Leiden University dissertation.

Author: Ketzetzi, S.
Title: Synthetic model microswimmers near walls
Issue date: 2021-06-29

SYNTHETIC MODEL MICROSWIMMERS NEAR WALLS

Proefschrift

ter verkrijging van
de graad van doctor aan de Universiteit Leiden,
op gezag van rector magnificus prof. dr. ir. H. Bijl,
volgens besluit van het college voor promoties
te verdedigen op dinsdag 29 juni 2021
klokke 11.15 uur

door

Stefania Ketzetzi

geboren te Thessaloniki (Griekenland)
in 1989

Promotores
　Dr. D. J. Kraft
　Prof. dr. M. L. van Hecke

Promotiecommissie
　Prof. dr. D. A. Wilson (Radboud Universiteit)
　Prof. dr. M. A. G. J. Orrit
　Prof. dr. E. R. Eliel
　Dr. J. de Graaf (Universiteit Utrecht)
　Dr. A. Morin

''A friend of mine (Albert R. Hibbs) suggests a very interesting possibility for relatively small machines. He says that, although it is a very wild idea, it would be interesting in surgery if you could swallow the surgeon. You put the mechanical surgeon inside the blood vessel and it goes into the heart and "looks" around. It finds out which valve is the faulty one and takes a little knife and slices it out."

Richard Feynman, *Plenty of Room at the Bottom*, Pasadena, 1959

To my brother.

Contents

1

Introduction

Preface and Abstract

Initially aimed at mimicking and understanding biological swimmer behaviors, *synthetic microswimmers* have flourished on their own right, holding these days an important place within the newly found interdisciplinary field of *active soft matter*. A widely employed model system which at the same time has great potential for applications is that of *catalytically self-propelled* microswimmers. In this thesis, we examine the near-wall behavior of these model swimmers, which surprisingly remained to date largely unexplored, despite its high significance from both fundamental studies as well as applications perspectives.

In this chapter, we aim at providing a general introduction on microswimmers by presenting basic concepts as well as references for the interested reader. However, by no means do we mean to deliver an all-inclusive overview on microswimmers; considering the evergrowing literature, this task soon proved to be quite daunting. We focus for the most part on Pt-coated swimmers that catalytically propel themselves in hydrogen peroxide solutions, with emphasis on the seminal works that have led to their current understanding. We subsequently discuss open questions about this system and, in turn, conclude with the scope of this work.

From the moment we first open our eyes, the objects that capture our interest are the ones that move. The concept of motion for all its simplicity, and at the same time complexity, fascinates scientists and philosophers since the time of Aristotle. Motion constantly takes place all around us [1]: from animals and plants at the macroscale to bacteria and cells at the microscopic scale, all living organisms display numerous complex functions that are somehow intertwined with their motions, possibly leading to intricate patterns. We have all observed majestic patterns being formed when, e.g., looking at flocks of birds in the sky or schools of fish in the water. Intriguingly, these intricate patterns and complex behaviors that we may have seen in such systems at the group level, in actuality take place without a leader to organize them. Instead, these motions happen collectively [6].
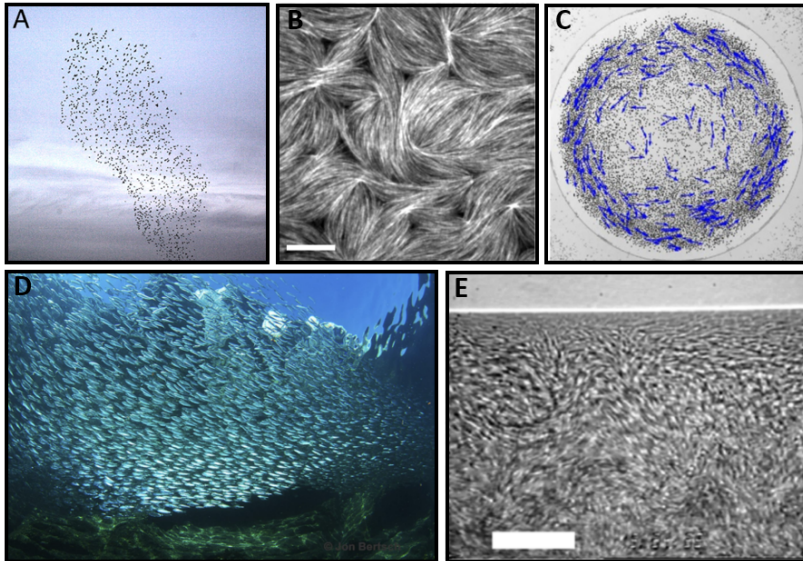
Figure 1.1: **Examples of active matter systems at the macroscopic (A, D) and microscopic (B, C, E) scale.** **A)** Flock of starlings *Sturnus vulgaris*; from Ref. [2]. **B)** Two-dimensional actomyosin network with nematic ordering, scale bar is 10 µm; from Ref. [3]. **C)** Colloidal rollers self-organized in a rotating vortex; from Ref. [4]. **D)** School of fish showing polar ordering. **E)** Bacterial turbulence in a sessile drop of *Bacillus subtilis*; scale bar is 35 µm. D, E) Reprinted from Ref. [5] with permission from the American Physical Society.

Collective motion is the main focus of the highly interdisciplinary field of *active soft matter*, which investigates out-of-equilibrium behavior and processes that include, among others, motility-induced phase separation, flocking, and collective migrations [7]. Studies are performed on the macro- and microscopic scales both on biological, *e.g.* birds, bacteria, cells and cytoskeleton components such as actin networks, as well as synthetic systems, *e.g.* self-propelled colloidal particles, droplets, and swarming robots [8]. Figure 1.1 shows prominent examples of such systems. Irrespective of their size, these systems share the feature that their constituents, commonly referred to as particles, continuously dissipate energy from their environment into directed motion, or to exert mechanical forces, at their individual level [9]. In what follows, we restrict our focus to synthetic active matter in the microscale. For an overview of active matter systems at various length scales, we point the interested reader to the 2019 "Active Matter" Collections from *Nature* [10] and *Soft Matter* [11] and "The 2020 Motile Active Matter Roadmap" [12].

Motion at the microscale

Motion of microorganisms in fluid environments is an absolutely crucial element of life. Through evolution, microorganisms have achieved robust and adaptive propulsion strategies that enable them to navigate efficiently in spatially or even time-varying environments, typically *via* different forms of taxis, i.e. motion in response to external stimuli [13]. For example, bacteria exhibit chemotaxis [14]: They move in response to chemical gradients which they utilize to find food or to avoid toxic substances. Sperm employ chemotaxis as well [15] in order to move towards the egg. But how do they propel themselves?

Due to their size, L, microorganisms in Newtonian fluids such as water, are subjected to low Reynolds (Re) number hydrodynamics, with Re being defined as:

$$Re = \frac{\rho U L}{\eta} = \frac{U L}{\nu} \tag{1.1}$$

where ρ is the fluid density, U the flow speed, η and ν the dynamic and kinematic viscosity respectively ($\nu = 10^{-2}\ cm^2/s$ for water). Thus, Re

describes the relative importance of inertial and viscous forces [16]. Using reasonable dimensions for microswimmers like bacteria, i.e. $L \approx 10\ \mu m$ and $U \approx 30\ \mu m/s$, we find $Re \approx 10^{-4}$. That is, motion is dominated by viscous forces. The dynamics of the (incompressible) fluid around the microswimmer is described by the Navier-Stokes equations:

$$\nabla \cdot \mathbf{u} = 0 \tag{1.2}$$

$$\rho\Big(\frac{\partial \mathbf{u}}{\partial t} + (\mathbf{u} \cdot \nabla)\mathbf{u}\Big) = \eta \nabla^2 \mathbf{u} - \nabla p + \mathbf{f} \tag{1.3}$$

where $\mathbf{u}$ is the flow velocity, p the pressure and $\mathbf{f}$ an external body force field. Following Refs. [17, 18], the non-linear contributions and inertial terms in Eq. 1.3 can be neglected when $Re \ll 1$, leading to the Stokes flow equation:

$$\nabla p - \eta \nabla^2 \mathbf{u} = \mathbf{f} \tag{1.4}$$

Equation 1.4, referred to as creeping flow, is linear and time-independent, i.e. it is symmetric under time transformations, which has severe implications for microscale motion in accordance with Purcell's "Scallop theorem": in a Newtonian fluid, any microswimmer that would change its body into a certain shape and, subsequently, change it back into its original shape through reversed steps like a scallop ("reciprocal motion"), would not be able to swim at the microscale [17].

Indeed, microorganisms such as bacteria and sperm swim by breaking time-reversal symmetry [19], or else by performing non-reciprocal motion, typically through the use of flexible, whip-resembling structures known as flagella (hairs) attached to their body. For example, *E. coli* swim in the direction of their long body axis by a "run and tumble" type of motion [18]. Briefly, when in the "run" phase, the flagella, rotating counterclockwise, form a bundle and the bacterium moves forward. In the "tumble" phase, however, some flagella rotate clockwise and leave the bundle, causing the bacterium to reorient. This type of motion aids them to find gradients in the fluid, e.g. in concentration of chemicals, to which they react accordingly by adjusting the duration of the "run" phases. Another strategy followed by cells such as sperm with one flagellum, involves beating the flagellum in a snake-like motion. These are but a few examples of propulsion strategies allowing biological swimmers to successfully overcome the dominant viscous drag [20];
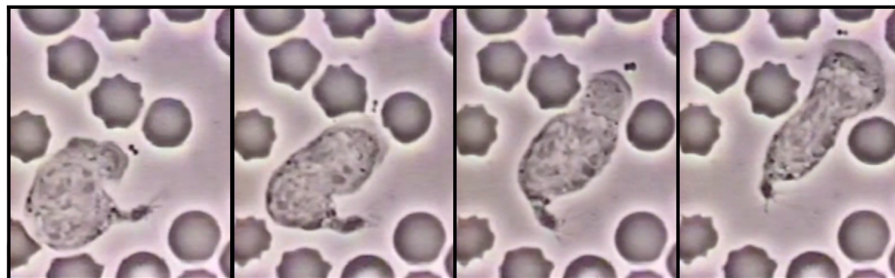
Figure 1.2: **Complex motion inside a complex environment.** These images are a set of snapshots adapted from a video taken by the late David Rogers at Vanderbilt University in the 1950's. The video, for which a blood film was adhered on a glass surface, shows a neutrophil (white blood cell) chasing a bacterium. The neutrophil constantly adjusts its shape to navigate its environment.

additional details on propulsion strategies adopted by diverse biological swimmers can be found in Ref. [18].

Biological swimmers are thus highly adaptable, resilient materials [21]: they assemble, regulate, and adjust themselves and their motility according to their environment. By further adapting to environmental conditions such as fluid flows, gravity and light, biological swimmers effectively navigate as well as perform complex tasks inside their fluid environments [13]. A great example is the neutrophil which adapts to its environment to catch the bacterium it senses in Figure 1.2. Overall, such intricate behaviors have inspired researchers to develop synthetic microswimmers, offering new opportunities for motion control at the microscale.

Synthetic active matter

In recent years, self-regulation and propulsion, omnipresent in living materials [22, 23], have inspired the development of synthetic active materials [24]. The motivation for their development is twofold. On the one hand, synthetic microswimmers may serve as *model systems* for understanding out-of-equilibrium behaviors, in turn providing insights into biological microswimmers. Figure 1.3 shows that synthetic swimmers exhibit behaviors typically found in biological systems, as is for instance the formation of ''living'' crystals, seen for both colloidal surfers in Figure 1.3A and bacteria in Figure 1.3B. The strong resemblance to their bi-

ological counterparts justifies why researchers employ synthetic systems to gain insights into processes such as dynamic self-assembly, dynamic clustering and phase separation, as shown in Figures 1.4A and B.
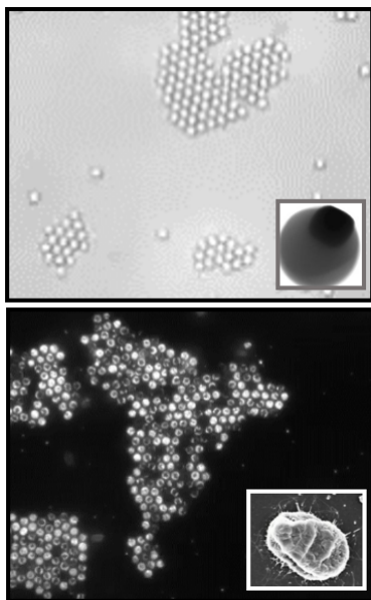

Figure 1.3: **Synthetic swimmers resembling biological microswimmer behaviors.** **A)** TPM-hematite colloidal surfers assemble into rotating crystals under blue light illumination. Adapted from Ref. [25] with permission from AAAS. **B)** *Thiovulum majus* bacteria self-organize into rotating crystals. Adapted from Ref. [26] (main panel) with permission of the American Physical Society and from Ref. [27] (inset).

On the other hand, model microswimmers are exceptional candidates for *applications* at the microscale, for example in biomedicine and microsurgery [28], where they could transport and deliver drugs at specific locations, or in environmental remediation [29], where they could locate and decompose pollution sources inside aquatic environments. Recent works in that direction are depicted in Figures 1.4C and 1.4D, showing that synthetic swimmers can indeed capture, transport, and release microcargo at different locations.

Thus, due to the far-reaching possibilities that they offer, intensive research has been dedicated to developing synthetic microswimmers which, in turn, has led to a variety of synthetic microswimmer systems becoming readily available within the past two decades. Notable synthetic systems nowadays include — but are not limited to — Pt half-coated catalytic swimmers [30] and bimetallic electrophoretic microrods [31] powered by chemical self-propulsion, Au half-coated thermophoretic swimmers powered by temperature gradients under laser irradiation [32], Au-coated swimmers in water-lutidine mixtures powered by hydrophobic-hydrophilic interactions at the swimmer surface upon critical demixing of the solvent due to light irradiation [33], mag-
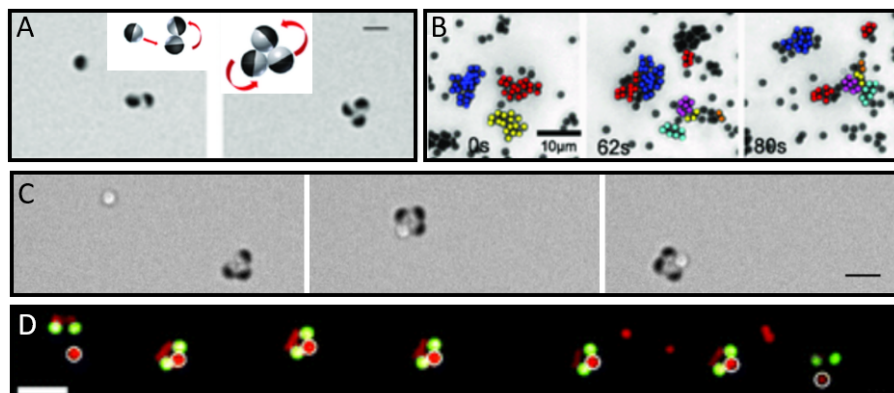
Figure 1.4: Synthetic microswimmers provide understanding of processes such as **A)** dynamic self-assembly and **B)** dynamic clustering and phase separation; scale bars are 2 μm and 10 μm, respectively. **C)** Transport of microscopic cargo by synthetic microswimmers; scale bar is 3 μm. **D)** Capture, transport, and release of cargo; scale bar is 5 μm. A, C) Adapted with permission from Ref. [43]. Copyright 2013 American Chemical Society. B) Reprinted from Ref. [44] with permission from the Americal Physical Society. D) Adapted from Ref. [45] with permission from the Royal Society of Chemistry.

netically [34] and accousto-magnetically [35] driven swimmers, swimmers powered by ultrasound [36], dielectric-Au swimmers driven by self-sustained electric fields using defocused laser beams referred to as opto-thermoelectric swimmers [37], light-activated surfers [25], colloidal rollers powered by Quincke electro-rotation [38], microscale Marangoni surfers at water-oil interfaces powered by asymmetric heating upon laser illumination [39], anisotropic Pt-coated swimmers with rough surfaces powered by periodic growth and bubble collapse [40], and swimming surfactant-stabilized liquid droplets powered by Marangoni stresses [41]. Note that propulsion in most of these systems relies at least in part on breaking the surface symmetry on the level of the swimmer, a swimming strategy first proposed by Ref. [42]. For the rest of the chapter, we restrict our discussion to catalytically self-propelled, and particularly to Pt half-coated swimmers, the model system studied in this thesis. For in-depth discussions on propulsion schemes, strengths, and weaknesses, of various synthetic systems we point the interested reader to some recent reviews on synthetic microswimmers [36, 46–51].

Catalytic particles as model microswimmers

First coming into existence in the form of bimetallic microrods in hydrogen peroxide (H_2O_2) solutions [31], catalytic microswimmers — or chemical swimmers as they are otherwise known — have nowadays become well-established model systems within the field of active matter. Two popular examples of catalytic swimmers, i.e. bimetallic microrods and dielectic-Pt Janus microspheres, are shown in Figure 1.5.

Unlike most systems mentioned in the previous section which are driven out-of-equilibrium with external light sources and fields, such particles are capable of truly autonomous motion, when suspended inside liquid environments often containing H_2O_2 [54]. The reason why this ability is highly desirable over external actuation goes back to the applications microswimmers are intended for. As discussed in Ref. [13], adjusting swimmer dynamics externally could potentially become ineffective and/or impractical. That is, synthetic swimmers should ultimately propel within environments that may be temporally and/or spatially inhomogeneous, or even varying in completely unpredictable manners. Hence, external actuations would have to be continuously as well as thoroughly adjusted to match the time and length scales at hand [13].
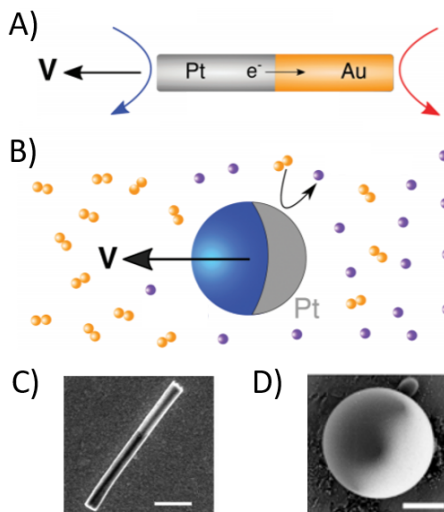
Figure 1.5: **Examples of catalytic swimmers.** **A)** Schematic representation of a bimetallic Pt-Au microrod. **B)** Schematic representation of a dielectric-Pt Janus sphere. **C)** Scanning electron microscopy (SEM) image of a Pt-Au rod. **D)** SEM image of a Pt-coated Janus sphere from our lab; the image is courtesy of Rachel Doherty. Scale bars are 1 μm. A, B) Adapted from Ref. [52] with permission from The Royal Society of Chemistry. C) Adapted with permission from Ref. [53]. Copyright 2006 American Chemical Society.

Catalytic swimmers furthermore show relatively high propulsion speeds and can thereby be more efficient in their self-propulsion in comparison to other systems, see Ref. [46] for a comparison on the propulsion efficiency of various synthetic swimmers. In addition, catalytic swimmers exhibit tunability in their properties. For example, their speeds can be tuned upon changing system parameters [30, 55–58], as we will see in detail in the following section, while their motion can also be steered inside realistic environments comprising boundaries [59–61]. Lastly, they have shown a plethora of tactic behaviors, namely chemotaxis, phototaxis, gravitaxis, and rheotaxis, in response to stimuli in their environment, see Ref. [13, 62]. Altogether, these abilities provide large versatility and prospects in regulating their trajectories and overall behavior. Therefore, these particles are expected to prove useful in applications that require "smart" swimmers [13], i.e. swimmers that move autonomously across, as well as adapt accordingly inside, different environments.

Self-phoretic motion

Unlike biological microswimmers which often achieve motion through time-asymmetric mechanical swimming, see the previous section, catalytic swimmers make use of short-ranged interactions between their surfaces and local gradients, which cause them to move through an effect known as *phoresis*. Phoresis is defined as the migration of microparticles caused by a gradient in some quantity inside a fluid medium; as Anderson has shown [63], gradients in concentration of solute molecules, electric potential, or temperature, lead to colloidal particle motion.

The motion of catalytic microswimmers uses the same principles, only in their case, it takes place due to *self-phoretic* effects instead. That is, the particles themselves generate gradients along their surfaces, and thereby instigate as well as maintain their own propulsion. In this section, following Ref. [64], we discuss general ideas behind the types of self-phoresis that are most commonly relevant for catalytic swimmers, namely, self-diffusiophoresis and self-electrophoresis [31].

To describe self-propulsion, models typically consider a particle inside a solvent that contains a dissolved solute phase [64]. The following set of equations is then used to describe the motion of the solute species i:

$$\frac{\partial c_i}{\partial t} + \nabla \cdot \mathbf{j}_i = 0 \tag{1.5}$$

$$\mathbf{j}_i = c_i \mathbf{u} - D_i(\nabla c_i + \frac{c_i}{k_B T}\nabla\psi_i) \tag{1.6}$$

with c the concentration, $\mathbf{j}$ the flux in the dilute limit, D the diffusion coefficient, k_B the Boltzmann constant, T the absolute temperature, and ψ a generalized potential that describes the interaction of the solute with the environment. The respective terms in the right-hand side of Eq. 1.6 therefore describe — from left to right — the flux of the solute because of advection i.e. transport caused by the motion of the fluid, diffusion, and migration caused by the interaction potential [64]. As discussed in section 1, fluid flow in the low-Re number regime is described by Eq. 1.2 and 1.4; here, the body force in Eq. 1.4 will depend on the interaction between the solute and the particle surface [64]. Equations 1.2 and 1.4-1.6 are generally employed to describe the motion of self-phoretic particles.

For simplification, theoretical studies often presume that phoretic effects are only manifested within an interfacial layer with thickness λ around the particle ($\lambda/\alpha \ll 1$, with α the particle radius in Figure 1.6A) [65], typically referred to as the thin-layer approximation [66]. Moreover, they consider advection to be negligible compared to diffusion, i.e. the solute simply diffuses in the interfacial layer [67]. As discussed in Ref. [64], these assumptions eliminate the effect of the fluid flow on solute transport, while the solute concentration field still drives fluid motion through the body force. Finally, within the thin-layer approximation, the phoretic effects are represented by a slip velocity — proportional to the local gradient of ψ [68] — at the particle surface; the net velocity of the particle is then equal in magnitude and opposite in direction to the surface area average of the slip velocity [68, 69].

Self-diffusiophoresis. This type of propulsion has been suggested as relevant for the motility of actin and cells [70, 71] as well as for synthetic systems, see the following section. It is generated when a particle creates a concentration gradient of a solute and in turn moves in response to the forces created by the gradient. In the simplest case of neutral solute self-diffusiophoresis, the propulsion stems from a gradient of electrically-neutral solutes interacting with the particle, see Figure 1.6A
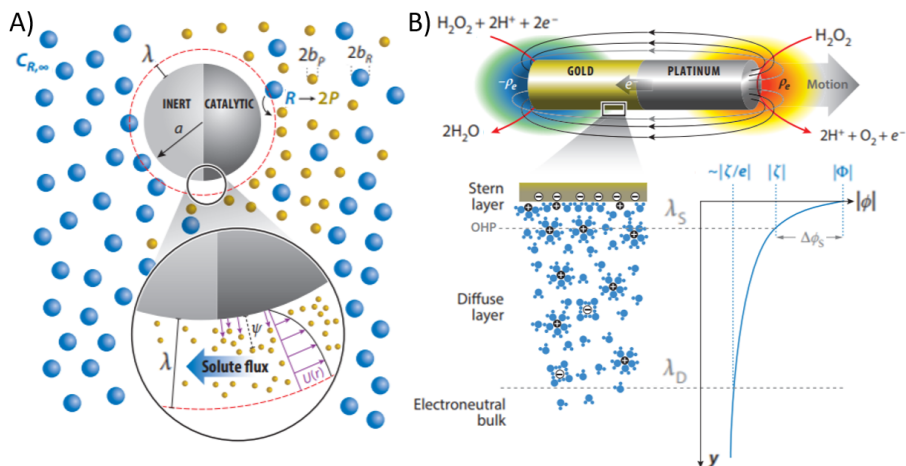
Figure 1.6: **Schematic illustrations of common self-phoretic propulsion types.**
A) Neutral self-diffusiophoresis. The particle is a Janus colloid with two distinct
hemispheres: the lighter hemisphere is the inert side, while the darker hemi-
sphere is the catalytic side that drives the reaction. The catalytic side converts one
reactant molecule (R, in blue) into two product molecules (P, in yellow). When
the interaction between particle and molecules is repulsive, a phoretic flow oc-
curs towards the catalyst, which causes the swimmer to move in the opposite
direction, i.e. away from the catalyst. **B)** Self-electrophoresis. In Pt-Au microrods
in H_2O_2, the Pt side oxidizes the H_2O_2, releasing electrons within the rod. These
conduct to the Au side where they are consumed, creating water and protons
into the fluid. The reactions generate as well as sustain an asymmetric charge
distribution and, in turn, an electric field, causing a fluid flow around the parti-
cle that ultimately moves the particle towards the Pt side. A, B) Reprinted from
Ref. [64] with permission from the Annual Reviews, Inc.

for a schematic. To model the reactions creating the gradient, models
usually view the system from a macroscopic, i.e. continuum, perspective,
and assume that the solutes are much smaller than the particle as well as
omit the interactions between the solutes themselves (dilute limit). Solute
transport is described by Eq. 1.5 and 1.6, with the interaction potential ψ
within distance λ from the particle surface defined as $\nabla\psi \equiv -\mathbf{f}_s$, with $\mathbf{f}_s$
the net force on a solute molecule [65]. Due to Eq. 1.4, the force on the
solute transfers to the fluid, causing $\mathbf{f} = -c\nabla\psi$ on the fluid. According to
Anderson [63], the neutral self-diffusiophoretic particle velocity, $U_d \propto \nabla c$.

The most commonly used potential in neutral-diffusiophoresis [72] is the excluded volume — or else hard-sphere — potential, i.e. strong repulsion at contact, while others, such as the exponential or van der Waals potentials have also been used in self-diffusiophoresis [73]. See Ref. [64] for discussions on interaction potentials as well as a review on constant flux versus reaction kinetic models in theoretical diffusiophoretic studies.

Ionic self-diffusiophoresis. This propulsion type is relevant for swimmers whose surface reactions produce both anions and cations [74]. It has been recently discussed in view of synthetic swimmers in H_2O_2 solutions, see Refs. [74–76] for in depth discussions. It is conceptually similar to neutral self-diffusiophoresis, however the fluid flow that propels the particles is in this case a result of free ionic species interacting with their surface [75]. Although ions are not present in H_2O_2 decomposition ($2H_2O_2 \rightarrow 2H_2O + O_2$), H_2O_2 may undergo ionic disocciation ($H_2O_2 \leftrightarrows HO_2^- + H^+$ [75]) which could result in an ionic gradient that ultimately produces tangential fluid flow along the particle surface. In ionic self-diffusiophoresis, ions interact with a charged particle surface through Coulomb interaction. Although the fluxes of positive and negative ions (here, H^+ and HO_2^-, respectively) are equal, i.e. there is no electrical current, the two ions may diffuse at different rates [74]. For unequal ion diffusion rates, and to maintain bulk charge neutrality [75], a (diffusion) potential is created to prevent net charge separation.

Self-electrophoresis. This type of propulsion occurs for a variety of synthetic particles whose surface consists of two metals. As mentioned earlier, the first example is that of Pt-Au rods [31] but it is also applicable to various bimetallic particles, see Ref. [53] for more examples, as well as spheres [77]. A requirement for this propulsion type is that the surface of the particle is charged. In electrolyte solutions, the charged surface attracts ions carrying opposite surface charge — named counterions — which causes a layer of immobile counterions around the particle to form, called the Stern layer (Figure 1.6B). Outside this layer, there exists a second layer, the diffuse screening layer, of both negatively and positively charged ions, depending on the position within the layer; at the end of the diffuse screening layer, negatively and positively charged ions are equally distributed, see also Figure 1.6B. Together, these two layers constitute the electric double layer (EDL) whose thickness is known as the Debye length, λ_D. When, e.g., Au-Pt particles are suspended in a H_2O_2

solution, electrochemical reactions cause ion exchange between their surface and the solution, see Figure 1.6B. In that system, H_2O_2 is oxidized at the Pt end producing protons and electrons, and, *vice versa*, reduced at the Au end [53], establishing a gradient in the concentration of charges. This asymmetry in the charge distribution results in an electric dipole around the particle which, in turn, creates an electric field that couples to the ions in the EDL [64], causing a body force in the fluid and thereby the fluid to move with respect to the particle. Hence, the particle moves in the direction of the Pt end. This process is equivalent to electrophoresis, although similar to our previous discussion on self-diffusiophoresis, the flux of charges and resulting electric field is again created by the particle itself. Specifically, ion transport is here also described by Eq. 1.5, while the flux $\mathbf{j}$ in Eq. 1.6 additionally depends on electromigration with the interaction potential given by $\psi_i = z_i e \phi$, with z_i the species and e the elementary charge. The particle-generated electric field $E = -\nabla\phi$ exerts on the fluid the body force $\mathbf{f} = \rho_e \nabla\phi$, with ρ_e the volumetric charge density, causing the fluid and, in turn, the particle to move with the self-electrophoretic speed $U_e \propto \zeta E$ where ζ is the particle zeta potential relating to its charge [78]. For details on flux-based as well as reaction-kinetic models in theoretical self-electrophoretic studies see Ref. [64].

Pt-coated Janus swimmers

We now turn to Pt-coated Janus microparticles, the focus of this thesis. Pt-coated particles a few micrometers in diameter constitute a prominent microswimmer system that has received a lot of attention since its establishment by Ref. [30] in 2007. The reason why such particles are highly interesting is that they exhibit truly autonomous motion inside H_2O_2 as well as they have great potential for adaptability. Hence, these properties make them important candidates for applications in the microscale. We point the interested reader to Ref. [54] for a discussion on the technological relevance and advantages of Pt-coated microswimmers from the perspective of applications. We note however that a challenging aspect which still remains to be tackled is their biocompatibility relating to their solvent toxicity, although there are some promising studies on bimetallic nanojets with epithelial cells [48, 79] and more recently on pH-responsive catalytic motors in varying lactic acid conditions [80].
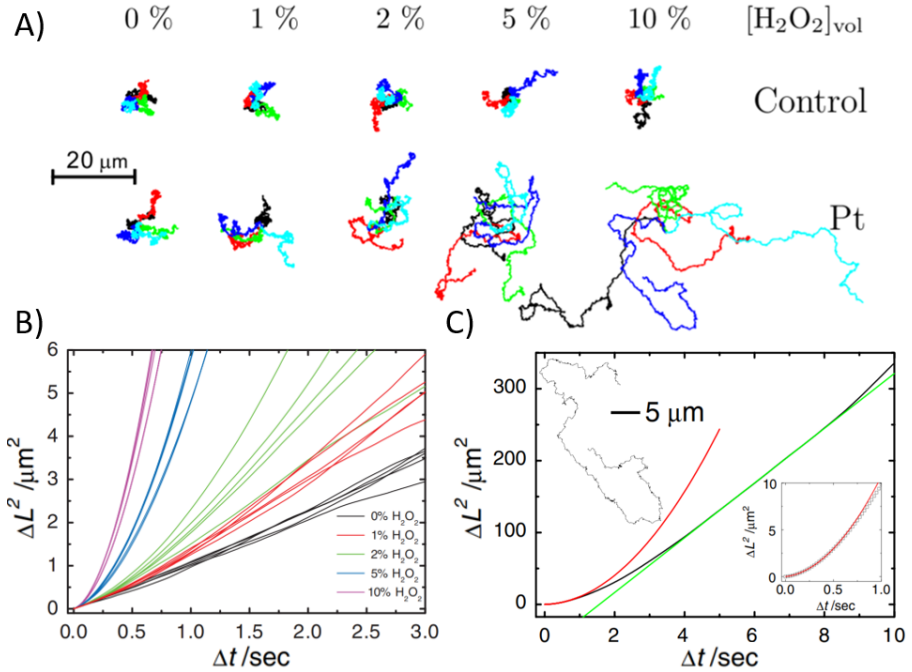
Figure 1.7: **Self-propulsion of Pt-coated swimmers in H_2O_2 solutions. A)** Unlike the uncoated (control) particle which exhibits Brownian motion for the same H_2O_2 conditions (top), Pt-coated particles perform directed motion with increasing H_2O_2 concentration (bottom). **B)** The particle mean square displacement (MSD) as a function of time changes from linear at 0% H_2O_2 (in black) to parabolic with H_2O_2 concentration. **C)** The MSD of a single particle resembles a parabola at short-time scales (in red), and a straight line (in green) at time scales much larger than the timescale for particle rotation. The inset shows a single particle trajectory (left) and the short-term MSD regime (right). All panels are reproduced from Ref. [30] with permission from the American Physical Society.

Figure 1.7 shows several key findings describing the self-propelled motion of Pt-coated particles in H_2O_2 solutions. In their pioneering experiments, Howse *et al.* verified the predictions of Ref. [42], which proposed that propulsion can be achieved by asymmetric distribution of reaction products, by demonstrating that Pt-coated particles exhibit directed motion in H_2O_2 solutions (Figure 1.7A). They found that particles cover larger distances over the same time with increasing H_2O_2 concentration,

as also reflected in the mean square particle displacements (MSDs) of Figure 1.7B. Moreover, they showed that the particle MSD can be decomposed into a short-term ballistic part and a long-term diffusive part, either of which can be fitted with appropriate expressions to provide the particle velocity. We return to the short-term behavior and corresponding MSD expression in chapter 2, where we provide an in-depth discussion on its nature and applicability. Lastly, in line with Figure 1.7B, Howse *et al.* were the first to report that particle velocity initially increases and thereafter plateaus with H_2O_2 concentration, see Figure 1.8A.

Since then, research has shown that the velocity of Pt-coated swimmers depends on several parameters, in addition to the H_2O_2 concentration, as shown in Figure 1.8. Ref [55] showed that particle velocity increases almost linearly with the thickness of the catalytic Pt layer, see red curve in Figure 1.8B named PVD after the term "physical vapor deposition" which is the standard way of coating the particles with Pt. The same work proposed an alternative way of preparing Pt-coated Janus particles in which the Pt is grown on the particle in solution. Particles prepared following their method also show Pt-thickness-dependent velocities, see the blue curve in Figure 1.8B. Moreover, swimming velocities depend upon the particle surface slip, as demonstrated by the experiments of Ref. [56], which employed otherwise similar particles with varying surface hydrophobicity, see also Figure 1.8C. This figure shows that velocity increases with H_2O_2 concentration, similar to Ref. [30] — although velocities here plateaued at a lower H_2O_2 concentration — while at the same time they reported an appreciable increase in the velocity for the hydrophobic (in black) in comparison to the hydrophilic (in red) particles. This effect was more pronounced for their larger particles of 5.2 μm, while noting that these particles always moved considerably slower than their 2 μm particles. This result was in line with the particle velocity notably decreasing with size, as found in the experiments of Ref. [58] in Figure 1.8D, wherein it was first established that swimming velocity scales inversely with swimmer size. Ref. [58] attributed this decrease to the intrinsic features of the self-diffusiophoretic propulsion mechanism.

Apart from tunable velocities, another key feature of Pt-coated swimmers is their affinity for surfaces. Pt half-coated particles depending on their mass density tend to swim upwards and/or downwards until they reach the top and/or bottom of their container, and thereafter remain there, self-

propelling parallel to their container wall. Figure 1.9A shows a video microscopy measurement of a Pt-coated swimmer that has settled above the bottom wall (substrate), moving in two dimensions with its Pt side at the back at all times [81]. This work also showed for the first time that the velocity vector corotates with the orientation of the swimmer, i.e. that the orientation of the Pt and the direction of motion are correlated. Ref. [81] additionally discussed that the direction of motion eventually becomes randomized as Brownian diffusion acts as noise, in line with the short-term and long-term behavior of the MSD from Ref. [30]. Thus, the active motion enhances the diffusion rate of the particles, with the ex-
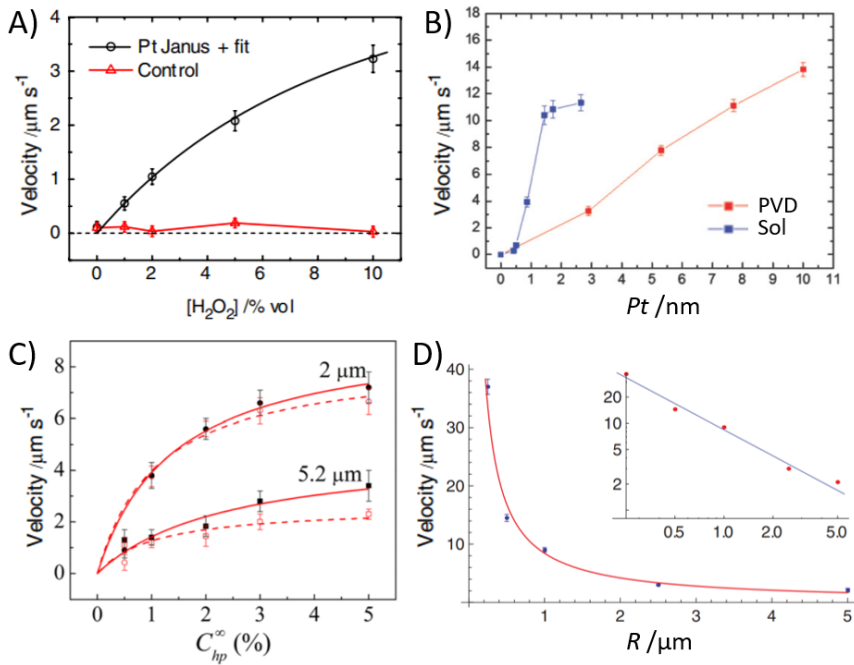
Figure 1.8: **Parameters affecting the swimming velocity of Pt-coated swimmers in H_2O_2 solutions.** These findings are compatible with self-diffusiophoresis. **A)** Velocity increases with H_2O_2 concentration [30]. **B)** Velocity increases with Pt-coating thickness; adapted from Ref. [55]. **C)** Velocity increases with the hydrophobicity of the swimmer surface, in addition to its increase with H_2O_2 concentration [56]. **D)** Velocity scales inversely with swimmer size [58]. Adapted with permission of A, D) the American Physical Society and C) AIP Publishing.
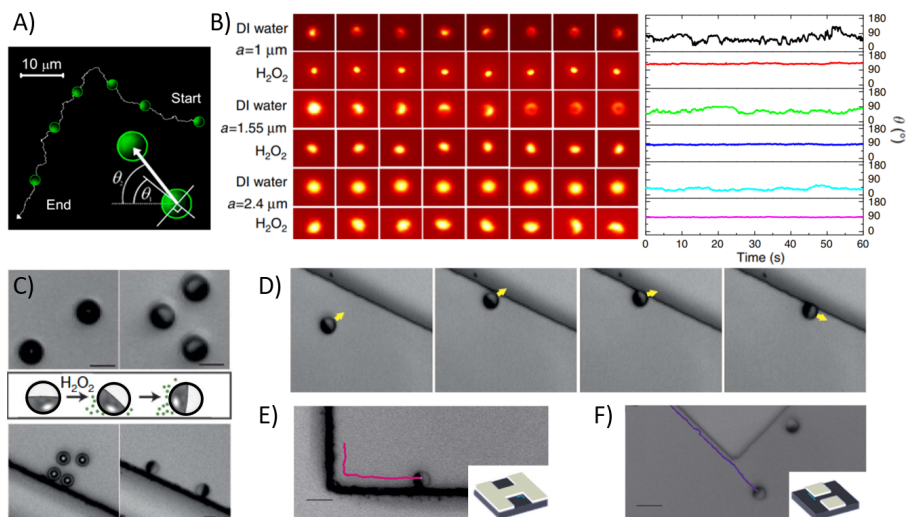
Figure 1.9: **Affinity of Pt-coated swimmers for surfaces: swimmer alignment and potential for guidance. A)** The swimmer moves away from its Pt side and over the same plane above the bottom wall of the container (substrate) [54, 81]. Reprinted with permission from Ref. [54]. Copyright 2018 American Chemical Society. **B)** The particles rotate freely in water, with rotation being slowed down with size, as shown in the fluorescent images of rows 1 (radius 1 µm), 3 (radius 1.55 µm), and 5 (radius 2.4 µm) (left), as well as in the corresponding fluctuating angles formed between the Pt-coating and substrate (right). In H_2O_2, the same particles show a steady orientation relative to the substrate, see the images in rows 2 (radius 1 µm), 4 (radius 1.55 µm), and 6 (radius 2.4 µm), and corresponding constancy in the angles (on the right), for all swimmer sizes; adapted from Ref. [59]. **C)** Bottom-heavy particles in water tend to orient themselves with the Pt cap facing down (top left), while they orient their caps vertically with respect to the wall upon addition of H_2O_2 instead (top right). In water, the particles diffuse near a secondary wall that is placed vertical to the substrate (bottom left), while in H_2O_2 they slide along the vertical wall (bottom right). **D)** In H_2O_2, when the swimmers approach a vertical wall, they reorient their axis and slide along the wall, with their cap oriented vertically to both the secondary wall and substrate. This surface affinity can be used to guide the motion of the swimmers. **E)** A swimmer can follow a 90 deg corner, while in **F)** it cannot do the same for a reflex angle of 270 deg, with the corresponding insets showing the schematics of the structures used in the experiments. C-F) Reprinted from Ref. [60].

pectation being that smaller swimmers will become diffusive faster while larger swimmers will have persistent directionalities [81].

Regarding swimmer orientation with size, Ref. [59] showed that swimmers irrespective of size have a preferred orientation with the substrate, with larger particles having a steady state orientation of 90 deg in agreement with Ref. [81], as shown in Figure 1.9B. In comparison, in the same figure, the same particles show large fluctuations in orientation above the substrate when suspended in pure water. Thus, orientational locking happens only in the active state of the particles in H_2O_2 [59]. The same behavior was at the same time also observed in the experiments of Ref. [60], see also Figure 1.9C where the particles change their orientation upon addition of H_2O_2. Their activity also keeps the particles in motion relative to secondary vertical walls, see bottom of Figure 1.9C and Figure 1.9D, where the swimmer is clearly seen to adjust its orientation with respect to the wall. Sliding at a constant orientation is observed along vertical walls, a feature additionally explored in more complicated geometries for the prospect of guiding swimmers to additionally avoid the randomization of their motion due to Brownian noise. Ref. [60] showed that although swimmers can follow 90 deg corners, they cannot follow 270 deg corners, see Figures 1.9E and 1.9F, respectively, as well as that swimmers cannot go over steps depending on their heights, see Ref. [60]. That is, a step of height larger than a few hundred nanometers will stop a swimmer from going over it. Based on these observations, employing topographical features has been proposed as a useful strategy for directing motion and increasing motion persistence in the microscale.

Another strategy that leads to modifications in their trajectories is changing the surface coverage by the catalyst. This can be achieved in a controlled way when the particles are deposited in a crystal lattice during Pt sputtering [54, 82], see also Figure 1.10A. Controlling the geometry and hence portion of the catalyst results in angular motion and/or spinning motion that may be useful for certain applications. Finally, during self-propulsion single spheres may self-assemble into dimers. Ref. [83] showed that different relative sphere orientations yield differences in the curvature of the trajectory of the assembled dimer. Although useful as a means to modify active trajectories, the configurations resulting from activity-induced self-assembly are random and thereby this process does not offer precise control. To date, employing nonspherical particles with
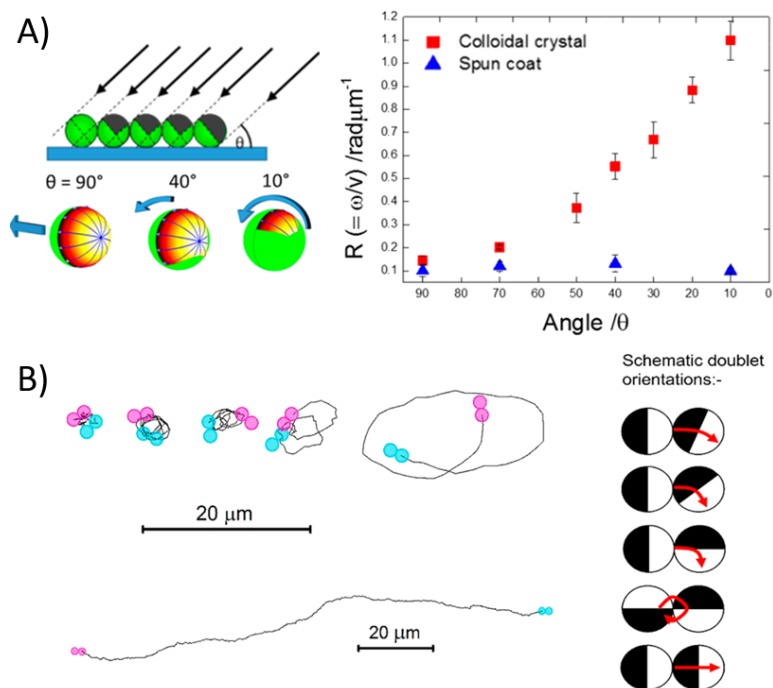
Figure 1.10: **Tuning Pt-coated swimmer trajectories. A)** Asymmetric coatings can be applied by varying the sputtering deposition angle when the particles are packed in 2-dimensional crystals [54, 82]. This simple technique can be used to tune the ratio between their translational and rotational velocity. **B)** The swimmer trajectory can be tuned from linear to highly curved by forming dimers through the active assembly of single swimmers [54, 83]. Different relative orientations of the swimmers result in trajectories with varying degrees of curvature, although precise control over the trajectory is not possible due to the random nature of the active self-assembly process. A, B) Reprinted with permission from Ref. [54]. Copyright 2018 American Chemical Society.

well-defined configurations is experimentally relatively unexplored. Although all existing experiments show that deviations from the spherical shape result in curved trajectories [84–88], controlled experiments that identify the effect of microswimmer shape are still desirable.

Open questions

Despite Pt-coated particles in H_2O_2 being a seemingly simple active system with great potential for adaptable autonomous motion, there are still several open questions and puzzling observations pertaining to it. Although the findings described earlier in this section are generally compatible with the self-diffusiophoretic mechanism originally proposed for this system [30], the behavior of these swimmers in the presence of salts and anionic surfactants is not commensurate with it. That is, the speed of Pt-coated swimmers considerably decreases upon addition of salt and certain surfactants in solution. This finding was first reported by Brown *et al.* [75] and Ebbens *et al.* [76], see also Figures 1.11A and B, respectively.

In their original experiments, Howse *et al.* proposed that Pt-coated particles propel themselves according to self-diffusiophoresis by creating gradients of molecular oxygen along their surfaces, which are the products of the H_2O_2 decomposition on the Pt end [30]. However, a few years later in 2014, Brown and Poon [75] as well as Ebbens *et al.* [76] reported ionic effects on the motion of Pt-coated swimmers. In addition, Brown and Poon [75] discussed that direction reversals have also been observed
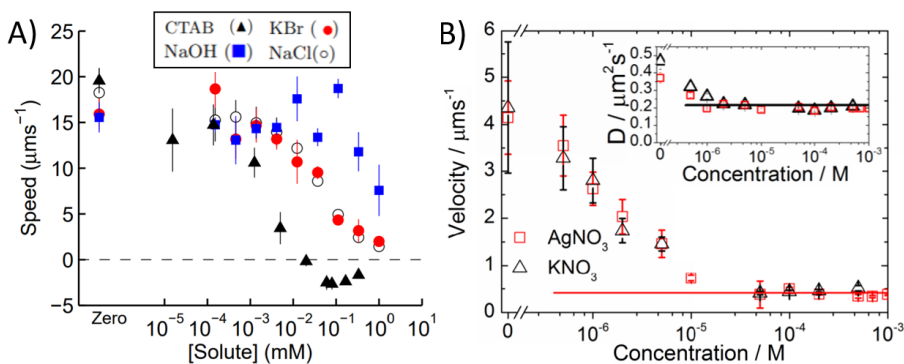
Figure 1.11: **Ionic effects on the speed of Pt-coated swimmers. A)** Swimming speed decreases when the concentration of ionic compounds such as NaOH, salts (NaCl and KBr) and surfactants (CTAB) increases from 0 and 1 mM. **B)** Similarly, swimming speed decreases when the concentration of salts (KNO_3 and $AgNO_3$) increases from 0 and 1 mM, while their diffusion coefficient remains constant between concentrations of 1 µM and 1mM. Image adapted from Ref. [76]. Adapted from A) Ref. [75] with permission from The Royal Society of Chemistry.

in catalytic systems. Both references concluded that self-diffusiophoresis cannot be the only mechanism at play. Brown *et al.* discarded the possibility that the swimmers move due to ionic self-diffusiophoresis on the basis that the observed particle velocities would require that the particles had unusually large surface zeta potentials. As a consequence, they suggested self-electrophoresis as the mechanism behind the observed behavior [75]. Although this mechanism requires two metallic ends such that there is a difference in their electron affinity, see discussion in the previous section, it was proposed that asymmetries in the Pt coating layer due to its preparation — the Pt at the pole can be thicker than the Pt at the equator of the particle surface — could cause differences in the reaction rates along the Pt end. That is, the asymmetry in the reaction rate suffices to generate a current along the particle. This was later investigated and deemed possible also from a theoretical perspective by Ibrahim *et al.* [89]. Note that all works discussed so far concerning propulsion mechanisms assume that swimming takes place in the bulk of the fluid.

Moreover, it is important to notice that discrepancies in swim speeds are often found in the literature for Pt-coated swimmers, even under similar conditions. For example, Ref. [30] measured that polystyrene particles of 1.6 μm in diameter with a 5.5 nm thick Pt layer self-propelled at ≈ 3 μm/s in 10% H_2O_2. On the other hand, polystyrene particles of 2 μm in diameter with a 5 nm thick Pt layer self-propelled on average at ≈ 18 μm/s in 10% H_2O_2. Taking into account what we have learned from Figure 1.8 on the parameters affecting swim speeds, this discrepancy is unexpected. That is, for the same H_2O_2 concentration and particle material, i.e. particle slip, we expect similar velocities. Even more so, the combination of the smaller size as well as relatively thicker Pt layer in Ref. [30] should have resulted in larger speeds in comparison to Ref. [75], opposite of what was measured. In fact, taking a closer look at the 0 mM data points of Figure 1.11A (data in the absence of salt), we notice that speed measurements by the same researchers on the exact same particles range from an average of 15 μm/s to an average of 20 μm/s. This already suggests that additional factors contribute to the experimentally measured swim speeds. Overall, the above demonstrate that the current picture of catalytic self-propulsion and speed-affecting parameters is not yet complete.

Scope of this thesis

To date, confining surfaces are known to have striking effects on the motion of microorganisms [18]. For example, surfaces can significantly modify swimming trajectories of biological swimmers: bacteria having high surface affinity tend to accumulate on walls, where they often exhibit circular motion with direction controlled by the boundary condition [90–93], in stark contrast to their run-and-tumble motion in bulk.

Seeing that Pt-coated swimmers likewise share the affinity for walls, and since their motion is typically measured near a wall, it is natural to question how, and to what extend, walls influence their motion. Surprisingly, when we were starting the work presented in this thesis, little to no research had focused at the time on the effects of the wall, in spite of walls already being considered as a means to guide active motion. That is, in interpreting as well as modeling catalytic microswimmer experiments, swimming was assumed to take place in bulk. However, understanding wall effects is important both for the use of Pt-coated swimmers as models systems as well as from the perspective of applications, since these swimmers are intended to perform tasks in complex environments where ultimately confining surfaces will be present. For the aforementioned reasons, this thesis focuses for the most part on exploring the effects that walls have on catalytic microswimmer motion.

In **chapter 2**, we consider the effect of a planar wall on the motion of Pt-coated swimmers. By performing experiments on the same particle batch above substrates made of various materials, we found that walls indeed have a strong effect on their swimming speeds. That is, walls other than glass which had typically been used in the experiments are capable of speeding up or slowing down particle motion. This effect can be attributed to an interplay between the hydrodynamic boundary condition on the wall, set by its slip, and the out-of-equilibrium chemical species generated by the swimmer, through an osmotic coupling mechanism. These findings provide a path towards resolving conflicting experimental observations regarding disparate swimmer speeds.
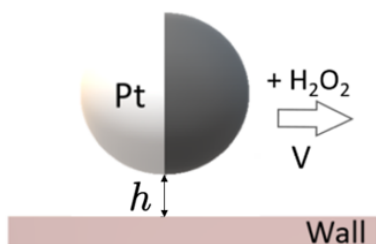
In **chapter 3**, motivated by our previous findings, we develop a method based on diffusion analysis to measure swimmer-wall separations. Using this method, we found that Pt-coated swimmers propel at ≈ 300 nm from the wall, in agreement with observations of them not being able to propel over steps of a few hundred nanometers and with the wall-dependent speed findings. Moreover, we found that swimmers assume fixed heights above the wall for a range of salt concentrations, swimmer surface charges, and swimmer sizes, which we call "ypsotaxis". Finally, our experiments in the presence of salt provide novel insights on the debated propulsion mechanism: the speed decrease may stem from long-range H_2O_2 gradients acting on the wall on the basis of an ionic diffusioosmosis mechanism along the wall, which creates a flow that counteracts swimmer motion. Nearby walls are thus dominant factors in controlling swim speeds and should be taken into account in future modeling.
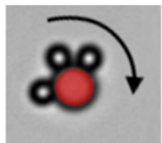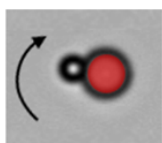
In **chapter 4**, we furthermore restrict Pt-coated swimmers to move along closed 1-dimensional paths. While single swimmers move at stable speeds independent of path curvature, multiple swimmers along the same path move at higher speeds depending on the swimmer number. At the same time, the swimmers keep at preferred distances due to an effective activity-induced potential stemming from a competition between chemical and hydrodynamic coupling. Swimmers also actively assemble into trains as well as compact chains with highly dynamic behaviors depending on path curvature. These findings open the door towards exploiting cooperation for applications inside complex environments.

In **chapter 5**, we develop a method for measuring non-coated particle-wall distances based on holographic microscopy. First, we employ it on spheres to crosscheck our diffusion-based height analysis method of chapter 3. Second, we employ it to colloidal dumbbells of different sizes to measure their height-dependent orientation with the wall, and gain insights into the largely unexplored near-wall dynamics of nonspherical microparticles. We found that dumbbell orientation with respect to the wall changes with size. At specific heights both net forces and torques on the dumbbells are simultaneously below the
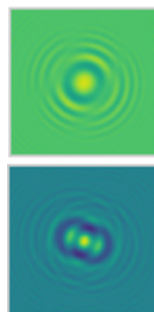
thermal force and energy, respectively, making the observed orientations possible. These results may prove useful for developing quantitative frameworks for arbitrarily shaped particle dynamics in confinement.

In **chapter 6**, motivated by the need for finely tuning catalytic swimmer trajectories for applications, as well as inspired by microorganisms whose shapes often enable them to navigate complex environments, we aimed at exploring the effect of swimmer shape on its self-propelled motion. To this end, we studied the motion of Pt-coated dumbbell-shaped swimmers with varying degree of asymmetry near walls. We find that self-propelled dumbbells move parallel to the wall, with trajectories that depend upon their shape and coating: increasing particle asymmetry leads to pronounced circular motions. We compare the radius of particle trajectories from our measurements to existing theory on asymmetric self-propelled particles near a wall, and find good agreement, confirming that the radius of circular motion depends on particle shape and coating. Our findings may prove useful for increasing swimming directionality and, in turn, motion control in complex environments.
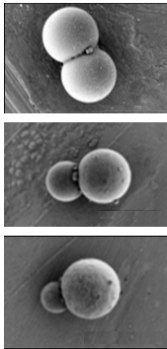
2

Wall-Dependent Propulsion Speeds

Abstract

Catalytic model microswimmers that propel due to self-generated fluid flows exhibit strong affinity for surfaces. In this chapter, we measure the speed of catalytic microswimmers near planar walls (substrates) and report a significant dependence of their speeds on the substrate material. We find that speed scales with the solution contact angle on the substrate, which relates to the associated hydrodynamic substrate slip length. We show that such speed dependence can be attributed to osmotic coupling between swimmers and substrate. Our work therefore points out that hydrodynamic slip at nearby walls, though often unconsidered, can impact self-propulsion.

The text in this chapter is based on:

Introduction

Colloidal swimmers constitute a new class of nonequilibrium model systems that also hold great promise for applications owing to their fast directed motion in liquid environments. A simple experimental realization of such microswimmers are spherical colloids half coated with Pt [54]. These colloids move autonomously in H_2O_2 solutions due to asymmetric catalytic reactions taking place on their surfaces [42] and are typically found self-propelling parallel to a substrate [59, 60, 75, 94]. This substrate affinity leads to accumulation [75] and retention [59–61] of swimmers at surfaces, such as walls and obstacles, and can be exploited as a means to guide their motion [59, 95].

Strikingly, upon approaching a surface, numerical and theoretical models predict both an increase or decrease in swimming speed depending on the considered propulsion mechanism and the physicochemical properties of the swimmer and wall [96–102]. At the same time, experimental observations also hint at non-negligible substrate effects on the speed of synthetic swimmers [103–105]. In fact, substrate effects may be at the heart of inconsistencies in catalytic microswimmer speeds under comparable experimental conditions. For example, speeds as disparate as 18 μm/s [75] and 3 μm/s [30] were found for polystyrene spheres with 5 nm Pt coating in 10% H_2O_2. This difference is even more surprising when one considers that the slower speeds were observed for the smaller species, whereas the speed of Pt-coated swimmers should scale inversely with size [58].

Recent measurements on different polymer-coated substrates revealed a propulsion speed decrease upon functionalization with either positively or negatively charged polyelectrolytes for bimetallic swimmers [103]. This is puzzling because contrary to most current predictions it indicates that the wall zeta potential does not have a dominant effect on the speed of self-electrophoretic swimmers. Furthermore, photoactivated TiO_2/SiO_2 swimmers were found to swim with 3 μm/s speed on glass, while they propelled with 4 μm/s speed on gold (Au) coated glass substrates [105]. It was proposed, based on zeta potential values for Au and glass at neutral pH conditions, that the increase in the propulsion speed stemmed from the lower zeta potential of the Au surface. However, neutral conditions are likely not met in H_2O_2 solutions. Even more so, results obtained using Au-coated substrates are hard to

interpret, because Au could in principle catalyze H_2O_2 decomposition and therefore interfere with the propulsion reaction [105]. To elucidate the origin of these intriguing observations, other surfaces ought to be examined in a quantitative manner. Understanding potential surface effects on colloid self-propulsion is essential not only for their use as model systems and the development of a quantitative framework but also for future applications that may require motion in complex environments comprising obstacles or confining walls [106].

In this chapter, we quantitatively examine the effect of various substrates, namely glass, glass coated with the organosilicon compound polydimethylsiloxane (PDMS), and plastic substrates made of a polyethylene (PE) or polystyrene (PS) derivative, on the speed of catalytic colloidal swimmers. Under otherwise fixed conditions, we observe significant differences in propulsion speeds, which cannot be fully accounted for by the substrate zeta potential. Instead, we find that speeds upon different substrates fall on a single curve as a function of the solution-substrate contact angle which relates to the substrate slip length [107]. After careful examination of the observed dependence in view of qualitative and scaling arguments, and accounting for possible couplings between swimmers and the substrate, we show that substrate-dependent speeds may result from osmotic coupling.

Results and Discussion

For all experiments, we used 2.7 μm diameter TPM colloids [108] half-coated with 4.9 nm of Pt by sputter-coating, see inset in Figure 2.1 with the brighter hemisphere indicating the coating. Colloids were prepared in one batch, hence any inhomogeneities arising from their preparation, including Pt thickness that affects H_2O_2 decomposition, should be universal. Measurements were taken in the dark typically within the hour after dispersing the colloids at dilute particle concentration in deionized water con-
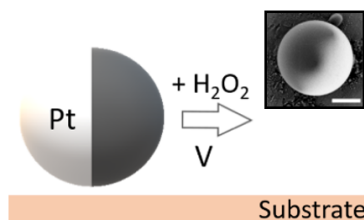

Figure 2.1: **Schematic of the experiment**. The self-propulsion of Pt-coated colloids was observed above various substrates under fixed conditions; the inset shows a SEM image of a representative colloid (scale bar is 1 μm).
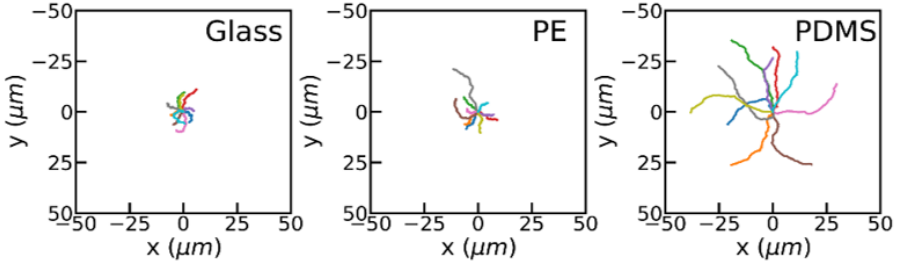
Figure 2.2: **Influence of the substrate on colloid self-propulsion.** Typical 8 s active colloid trajectories on glass, PE and PDMS.

taining 10% H_2O_2. The colloids quickly reached the lower surface and continued to self-propel parallel to it, as in Figure 2.1. Figure 2.2 shows 10 representative xy trajectories on glass, PE, and PDMS substrates acquired over a time interval of 8 s. We find that the colloids cover significantly greater distances on PDMS than on glass and PE, clearly demonstrating that the substrate affects colloid motion.

To quantify the differences in the observed behavior, we first obtain the speed V of each individual colloid from its short-term mean squared displacement following Ref. [30]. We fit the corresponding probability density function (PDF) of the speed with a log-normal distribution following Ref. [109] to obtain the speed distribution parameters on each substrate. The most frequently encountered speeds, as obtained from the fitted peak position of each PDF, are 1.05 ± 0.09, 1 ± 0.2, and 2.8 ± 0.3 μm/s, above glass, PE, and PDMS, respectively. Interestingly, though all three substrates are chemically different, the colloids show similar speeds for two of the substrates and a notably different speed for the third. At the same time, the characteristic time scale for rotation τ_R [30, 83, 110] is similar for all three substrates. Details on the determination of V and τ_R can be found in the Methods. In the absence of H_2O_2, however, the translational diffusion coefficients are similar, namely 0.099 ± 0.005, 0.098 ± 0.008, and 0.105 ± 0.005 μm^2/s, for glass, PE and PDMS, respectively. Thus, substrate-dependent differences arise only in the active state.

While speeds may be influenced by colloid properties, such as size [58], roughness [57] and slip [56, 111], these effects are negligible here since the same colloid batch was used in all experiments. Therefore, the observed

speed differences arise from differences in the substrate properties. To quantitatively unravel the origin of our observations, we consider substrate properties that may influence colloid motion. The fluid flow generated by the anisotropic catalytic reaction on the swimmer surface [112], and hence the swimmer's propulsion speed [63], has been predicted to be affected by the swimmer-wall distance [96–102], wall zeta potential [98, 105] and wall surface inhomogeneities [105]. Surprisingly, little consideration has been given until now on whether slip on the substrate impacts propulsion speeds, even though slip on the colloid has already been shown to do so [56]. Considering that hydrodynamic attraction in the active state pulls the colloids close to surfaces, to the extent that they even propel along the top of their container [75], colloid-substrate distances are expected to be small. Pt-coated swimmers of 2.5 μm radius have been found to not swim over 200 nm steps [60], and other experiments pointed out that distances may even be of the order of tens of nm [113, 114]. Since wall slip lengths ranging from several [115–118] to hundreds [119, 120] of nanometers and even micrometers [121] have been reported, boundary conditions could strongly affect the speed. Following Ref. [111], we hypothesize that deviations from the no-slip condition on the substrate enhance nearby swimmer's speeds. Surface slip relates to liquid-solid in-
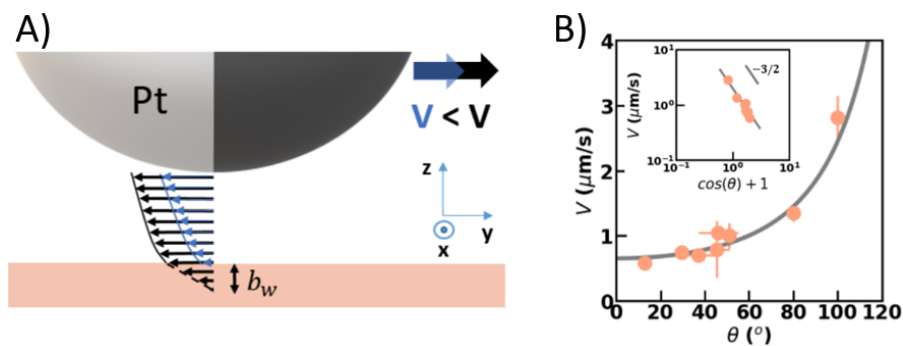
Figure 2.3: Propulsion speed V of catalytic swimmers above substrates with different contact angle θ. A) Schematic of the proposed model. At a given separation, the speed resulting from the colloid-generated fluid flow is larger on a hydrophobic substrate due to the larger slip length b_w (not to scale). Here, only the fluid flow velocity profile due to hydrodynamic slip on the wall is illustrated. B) V as a function of θ and least squares fit with $V = A(\cos\theta + 1)^{-3/2}$ that follows from our model. The inset shows the data on a log-log scale.

teractions and thus surface wetting properties, and generally, though not always, increases with increasing hydrophobicity and thus contact angle θ [107, 117, 118, 122]. Since hydrophobic surfaces possess a larger slip fluid velocity [123], we hypothesize that they also lead to a higher propulsion speed. Conversely, the no-slip approximation on hydrophilic surfaces would lead to lower speeds, see Figure 2.3A. Indeed, the advancing contact angle measured for the H_2O_2 solution by the sessile drop method agrees with this hypothesis: θ is 46 ($\pm$ 9)^o, 51 ($\pm$ 3)^o, and 100 ($\pm$ 3)^o, for glass, PE, and PDMS (as in [124]), respectively. PE is normally hydrophobic, thus a modification has been performed by the supplier.

To further test this hypothesis, we modulated the hydrophilicity of the employed substrates and repeated the experiments. We increased the hydrophilicity of glass by either a cleaning procedure ($\theta = 29.5 \pm 3^o$) or treatment with HCl [125] ($\theta = 13 \pm 3^o$) and we observed a concomitant speed decrease by 30% and 45%, respectively. Conversely, when we rendered the glass more hydrophobic ($\theta = 80 \pm 2^o$), we found that speed increased by 28% compared to untreated glass. Similar behavior was seen on PDMS that was rendered hydrophilic through UV-ozone treatment [126, 127] ($\theta = 37 \pm 7^o$): colloids propelled four times slower than on hydrophobic PDMS. Finally, we employed commercially available hydrophilic PS substrates ($\theta = 46 \pm 6^o$) and found $V = 0.8 \pm 0.45 \mu m/s$. We summarize these findings by plotting V as a function of θ in Figure 2.3B. The collapse of the data onto a single curve suggests that θ is the most relevant parameter while other differences among substrates, besides their effect on θ, are of lesser importance.

Next, we develop a quantitative framework for the slip-dependent propulsion speeds. For our analysis we consider that the height above the substrate remains relatively unaffected by the change of substrate, as supported by our experimental measurements of the diffusion coefficient [128–130], see both experimental details in the Methods and theoretical considerations in the Appendix. When the height is left unperturbed by varying $\cos\theta$, the dominant source of change to the propulsion speed comes from solute gradients near the substrate. As mentioned earlier, these are generated by reactions taking place on the swimmer surface and, similar to the way they cause self-propulsion, lead to an effective surface fluid velocity along the wall [63], often referred to as 'slip' velocity. This effective surface fluid velocity couples back to the

swimmer, modifying its net velocity [59, 95, 98, 131]. In the Appendix, we show that neither purely hydrodynamic coupling [102, 132, 133], solute confinement [96, 97, 99–101], nor reaction-based coupling [58] can account for the significant wall effect. Instead, our observation can be attributed to osmotic coupling [59, 63, 95, 98, 131, 134]. The osmotic coupling scales linearly with the slip-velocity parameter ξ_w, *i.e.*, the prefactor that converts solute gradients into effective hydrodynamic surface velocities [63]. Ajdari and Bocquet [111] have shown that for a partial-slip wall the result by Anderson [63] can be generalized to

$$\xi_w = (k_B T/\mu) \, \lambda_w \gamma_w \left(1 + b_w/\lambda_w\right), \tag{2.1}$$

where slippage is expressed by the slip length b_w; $b_w = 0$ for a no-slip surface and $b_w \to \infty$ for a full-slip surface. Here, we have introduced k_B the Boltzmann constant, T the temperature, μ the dynamic viscosity, λ_w a length scale for the solute-surface interactions, and γ_w a length measuring the solute excess [111]. For smooth surfaces, as we consider here, the value λ_w is left relatively unaffected by changes in θ, but $b_w \propto (1+\cos\theta)^{-2}$ and $\gamma_w \propto \sqrt{1+\cos\theta}$ [107]. This leads to the following leading-order proportionality of the measured speed with θ:

$$V \propto (1 + \cos\theta)^{-3/2}, \tag{2.2}$$

which requires that $b_w/\lambda_w \gg 1$, see also the Appendix for a more in-depth discussion on the osmotic coupling based mechanism. We use this quantitative relationship between propulsion speed and contact angle to fit the experimental data presented in Figure 2.3B. The proportionality factor A, which contains all other contributions to the speed that are slip independent, is 1.84 μm/s. The excellent agreement between data and model further quantitatively corroborates the influence of slip.

To provide additional support to our hypothesis, we test whether the above dependence persists in the presence of salt. Previous experiments employing 2 μm PS spheres showed that even 1 mM salt considerably decreases propulsion speeds [75, 76]. Although speeds for similar H_2O_2 concentration without salt were different above glass, namely around 4 μm/s [76] and 18 μm/s [75], they reduced to 0.45 and 1 μm/s, respectively, in 1 mM salt. In line with these experiments, we find that speeds
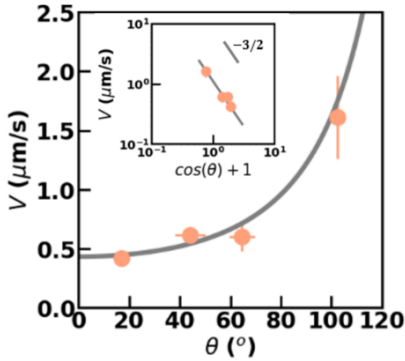
Figure 2.4: **Slip dependence of the propulsion speed V of colloidal swimmers in salt solution.** Speed in 1 mM NaCl as a function of the contact angle θ and least squares fit (solid line) with $V = A(\cos\theta + 1)^{-3/2}$ that follows from our model. The inset shows the data on a log-log scale.

above different substrates decrease with added salt, see Figure 2.4. More importantly, we observe that speeds still follow the same slip dependence. In salt solution, the proportionality factor A is 1.2 μm/s, showing a 33% decrease compared to the salt-free case. Considering that the influence of salt is complex, potentially affecting zeta potentials, separation, higher-order hydrodynamic moments or possibly more properties including bulk speeds, this decrease is not surprising. However, that the same dependence persists further supports the importance of slip, and may provide additional insights into the propulsion mechanism [75].

We emphasize that other substrate properties besides slip may affect propulsion speeds. As mentioned earlier, lowering the substrate zeta potential has been proposed to increase speeds [105]. For completeness we thus measured substrate zeta potentials using a Surface Zeta Potential Cell from Malvern by laser Doppler electrophoresis following Ref. [135] using tracers prepared as in [136], see Methods. We find zeta potentials of -38.3 $\pm$ 1.1 mV and -22 $\pm$ 0.9 mV for glass and PDMS, respectively, in line with this proposal. However, we find an even lower zeta potential, -11 $\pm$ 5 mV, for hydrophilic PDMS. Due to the low speed on hydrophilic PDMS, we conclude that the substrate zeta potential is, surprisingly, not the dominant effect. Secondly, an increase in the substrate roughness was shown to increase the speed [105]. We thus performed Atomic Force Microscopy (AFM) measurements, see Methods. The average substrate roughness Ra, is 1.5 and 5 nm, for glass and PDMS, respectively; with Ra denoting the arithmetic mean of the deviations in height from the roughness mean value. However, hydrophilic PDMS, with a roughness equal or higher [137] to untreated PDMS, featured lower speeds. We thus conclude that substrate roughness is also not the dominant effect here.

Our experiments also provide a new perspective on previous work: the speed increase previously observed on Au-coated surfaces [105] may be due to increased surface slip, since contact angles on Au are typically higher than on glass [138, 139]. Similarly, the speed decrease in [103] may be due to the hydrophilic polyelectrolyte coatings employed on the glass. Besides, our findings may explain the discrepancies in reported speeds between previous experiments. Even though glass substrates were used in all cases, glass can differ in composition, homogeneity and hydrophilicity due to different preparation, coatings, treatment and cleaning methods from the supplier or the researchers themselves, as we have also demonstrated. We also found that contact angles sometimes varied by 10° within the same type of and/or different parts of the same substrate. AFM indicated that this is likely due to inhomogeneous application or even local absence of coatings applied by the supplier. If the coating or substrate treatment is inhomogeneous or unstable, for example due to a chemical reaction with H_2O_2, a locally or temporally different substrate slip can be observed. For example, we found a 15° increase in contact angle for the PS substrate before and after being exposed to H_2O_2 for several hours.

Conclusions

Our work points out that nearby walls, though often unconsidered, can significantly impact catalytic microswimmer speeds. Specifically, we find that propulsion speed near a wall is influenced by the wall slip boundary condition. This quantitatively follows from theoretical predictions on the basis of an osmotic coupling mechanism, indicating further control and understanding of the behavior of self-propelled particles. In future work, it would be interesting to investigate if slip affects other features of active motion as well, such as the orientation of active particles with respect to the wall [140]. The here discussed slip dependence of the propulsion speed should not only be relevant for catalytic swimmers but any microswimmer that creates a fluid flow in the vicinity of a substrate.

Acknowledgements

I am grateful to our collaborator Joost de Graaf for developing the osmotic coupling-based mechanism presented here and for much useful discussions. I gratefully acknowledge Rachel Doherty for providing the TPM spheres as well as for help with AFM measurements, contact angle measurements, and substrate functionalizations. I thank Malvern for providing the Surface Zeta Potential Cell and particularly Sandra Remijn for discussions and help with substrate zeta potential measurements. I thank Federica Galli for showing me how to use the AFM, for assisting with AFM measurements and for helpful discussions. I thank Nikos Oikonomeas and Ruben Verweij for help with python routines.

Methods

Synthesis of TPM colloids. Carboxylated 3-(trimethoxysilyl)propyl methacrylate (TPM) spheres with diameter 2.7 μm and polydispersity in size 2.37% were prepared following a one-pot surfactant-free synthesis protocol extended from Ref. [108]. In short, itaconic acid (ITA, Sigma Aldrich) was weighed into a plastic beaker. 30g of MilliQ water (18.2 MΩ cm resistivity, obtained using a Millipore Filtration System Milli-Q Gradient A10) was added and the pH was adjusted to 10.8 with NH_3 (28-30%). The solution was stirred at 300 rpm until ITA was fully dissolved. 900 μL TPM oil (Sigma Aldrich, 98%) was rapidly injected into the stirred solution, which was then covered with parafilm. After 4 h, 100 mg azobis(isobutyronitrile) (AIBN, Sigma Aldrich, $\geq$ 98%) was added. In total the emulsion was stirred for 5 h prior to heating in an oil bath at 80 ^{o}C under rotation at 50 rpm for 2.5 h. The colloids were washed and stored in MilliQ. The resulting spheres have a zeta potential of -70 $\pm$ 2 mV in MilliQ (pH 5.5). Their density is 1.31 kg/L [108].

Preparation of Pt/TPM colloids. TPM spheres were spin coated from ethanol on glass slides at sub-monolayer concentrations and subsequently sputter coated from above with a 4.9 nm Pt/Pd (80/20, MicrotoNano70-PPS708) layer via physical vapor deposition using a standard sputter coating system (Cressington 208HR High Resolution Sputter Coater). During deposition, the stage was rotated at a constant speed to ensure even Pt distribution. The Pt/TPM colloids were redispersed in 5 mM NaOH by 5

min sonication and were subsequently washed and stored in MilliQ water. This method produced single particles. The Pt/TPM spheres have a zeta potential of -55 $\pm$ 2 mV in MilliQ water.

Substrate preparation. *Glass* substrates were purchased from VWR (631-1584 25mm No1) and were used as received unless stated otherwise. They were made of borosilicate glass and were subsequently coated with a Schott's D263M coating by the supplier. According to the supplier, these cover glasses are more hydrophobic than typical soda lime glasses. The measured contact angle for 10% H_2O_2 is $44^o \pm 9^o$. *Hydrophilic glass* was prepared by sonicating the glass substrates for 20 min in acetone, followed by 30 min sonication in ethanol and drying in the oven at 80 ^{o}C for 10 min. The contact angle for 10% H_2O_2 is $30^o \pm 3^o$. *Highly hydrophilic glass* was prepared by immersing the glass substrates in a 1:1 mixture of methanol and hydrogen chloride (37%) for 30 min, followed by thoroughly rinsing with MilliQ water and drying with N_2 [125]. The contact angle for 10% H_2O_2 is $13^o \pm 4^o$. *Hydrophobic glass* was prepared by first immersing glass substrates in 2% Hellmanex while stirring for 30 min. The substrates were then rinsed with MilliQ water and immersed in ethanol for 20 min and dried in the oven at 150 ^{o}C for 30 min. The dried glasses were then immersed for 20 s in 50 g xylene and 2.9 mL surfasil, for 20 s in xylene and for 60 s in methanol and were dried in the oven at 150 ^{o}C for 30 min. The contact angle for 10% H_2O_2 directly after preparation is $68^o \pm 5^o$. *PDMS* substrates were prepared similarly to [126] using the PDMS kit Sylgard-184 (Dow Corning). The base silicon elastomer and curing agent were mixed at a 5:1 ratio. The mixture was placed in a vacuum desiccator for 1 h to remove trapped bubbles due to agitation, and was then drop casted and flattened on glass. After 45 min in the desiccator, the substrates were dried in the oven at 120 ^{o}C for 3 h. We verified that the contact angle for water on these substrates was 100°, as stated by the supplier and measured elsewhere [124]; also for 10% H_2O_2, it is $100^o \pm 3^o$. *Hydrophilic PDMS* was prepared by UV-ozone treatment of the PDMS substrates [126, 127] for 60 min using a UVO cleaner (Jelight Company Inc. No 42A-220). This treatment converts the PDMS surface into a silica-like surface, see Ref. [126] for a detailed study on surface properties. The resulting contact angle for water after 60 min treatment was $37^o \pm 7^o$, close to values measured in the literature after similar treatment [127], and indeed close to the contact angle of $30^o \pm 3^o$ that we measured here

for water on clean glass. We note that we perform our experiments within 1 h after surface treatment during which time the substrates remain hydrophilic, see Ref. [127] for the timescale of the hydrophobic recovery of PDMS. *PE* substrates were purchased from ibidi GmbH (μ-slide 8 Well ibiTreat No 80826) and were used as received. These substrates are made from a polyethylene derivative and are subsequently plasma treated by the supplier. The supplier stated that the plasma treatment leads to a permanent change in the substrate properties, however there may be some surface inhomogeneities. The contact angle for 10% H_2O_2 is $51^o \pm 3^o$. *PS* petri-dishes were purchased from Sarstedt and were used as received. The supplier has introduced hydrophilic groups into the surface via a special treatment of the PS. The contact angle for 10% H_2O_2 is $46^o \pm 6^o$.

Imaging and Tracking. TPM/Pt colloids were dispersed in 10% H_2O_2 in MilliQ water at dilute particle concentration ($\approx 10^{-7}$ v/v). Their motion was recorded with a 60x ELWD air objective (NA 0.7) mounted on an inverted Nikon Eclipse Ti microscope. 25 s movies were acquired over the xy plane at 19 frames per second. All measurements were performed in the dark and within the first hour after sample preparation to avoid photocatalytic decomposition of the H_2O_2 [75] and potential changes in the slip of the substrate due to reaction with H_2O_2. At least 70 colloids were imaged and analyzed for all substrates. Additional 30 s movies of the TPM/Pt colloids were taken at 19 frames per second in water, and water containing 1 mM NaCl. Tracking was performed using the python tracking algorithm trackpy that is available online [141].

Data Analysis. The translational diffusion coefficient, D_T, of each TPM/Pt colloid in water above each substrate was extracted by fitting its mean squared displacement (MSD) with $\Delta r^2 = 4D_T\Delta t$, for lag times smaller than 1 s. The diffusion coefficients were then averaged

Substrate	Glass	PDMS	PE	Glass H/ilic
D_T (μm^2/s)	0.099	0.105	0.098	0.096
Error (μm^2/s)	0.005	0.005	0.008	0.006
Substrate	PDMS H/ilic	Gl. H/obic	Gl. Highly H/ilic	PS
D_T (μm^2/s)	0.091	0.098	0.090	0.110
Error (μm^2/s)	0.003	0.007	0.003	0.003

Table 2.1: Translational diffusion coefficient D_T of the Janus colloids above each substrate in water. The diffusion coefficient D_{bulk} is 0.17 μm^2/s.

Substrate	Glass	PDMS	PE	Glass H/ilic	
Shape	0.68	0.56	1.09	0.45	
Location	0.49	0.08	0.71	0.35	
Scale	0.87	3.75	0.46	0.52	
Substrate	PDMS H/ilic	Gl. H/obic	Gl. Highly H/ilic	PS	
Shape	0.67	0.61	0.37	1.03	
Location	0.51	0.44	0.22	0.28	
Scale	0.26	1.24	0.41	0.87	

Table 2.2: Moments of the speed distributions on all substrates as obtained from the log-normal fit.

to obtain the corresponding D_T above each substrate, see Table 2.1 where the reported error is the standard error, calculated from the standard deviation of the corresponding D_T divided by $\sqrt{N-1}$ with N the number of colloids for each substrate. The diffusion coefficient in bulk is 0.17 μm^2/s, obtained from $D_{bulk} = \frac{k_B T}{6\pi\eta\alpha}$. Colloid speeds in the active state were extracted from fitting the first seven data points, corresponding to Δt 0.4 s, of their MSDs in H_2O_2 with the expression

$$\Delta r^2 = 4D\Delta t + V^2 \Delta t^2, \tag{2.3}$$

where $\Delta t \ll \tau_R$. Here, τ_R is the characteristic time scale for the particle to undergo rotational diffusion and can be written as $\tau_R = 1/D_{R,bulk}$, with $D_{R,bulk}$ the bulk rotational diffusion coefficient $D_{R,bulk} = \frac{k_B T}{8\pi\eta R^3}$, η the viscosity, k_B the Boltzmann constant, and T the absolute temperature. There is some confusion within the literature concerning Eq. (2.3). Bechinger *et al.* [106] note that this form is incorrect and suggest a factor two should be added to the expression provided by Howse *et al.* [30], *i.e.*, the form provided in Eq. (2.3). The reason for this confusion lies in the fact that Ref. [30] reports a 2D projected MSD for active Brownian particles. Equation (13) from Bechinger *et al.* [106], which provides the full MSD for arbitrary Δt, is instead derived for in-plane motion and rotation of the swimmer *only* about the out-of-plane axis. However, there is a subsequent typo in Ref. [106], which leads to a superfluous factor of 2 in their equivalent of Eq. (2.3), as can be readily seen by taking the Taylor series of their Eq. (13). The short-time diffusion expression by Howse *et al.* [30] is thus internally consistent. Moreover, it coincides with the expression that the authors of Ref. [106] should have obtained for their short-time dynam-

ics. The route followed by Bechinger *et al.* [106] is more appropriate, as our particles are indeed constrained in their reorientation. Lastly, on this topic, we address a similar observation on the correctness of the Howse *et al.* result made in Ref. [142], where the authors provide yet another form of the MSD and consequently Eq. (2.3). This is because these authors are interested in systems for which the swimmer moves in plane, but is presumably able to have an orientation out of the plane; we are not interested in this scenario here. Generally, care needs to be taken in judging which of the three reported expressions is most applicable to the situation studied experimentally. It would be most appropriate to re-derive these from the applicable underlying microscopic dynamics on a case-by-case basis, as only Bechinger *et al.* [106] provide the relevant equations of motion.

Examples of three individual colloid MSDs above three different substrates are shown in Figure 2.5A. To obtain the speed for each colloid, we first fit all colloid MSDs above a specific substrate with both D and V as open parameters. We then use the averaged D value for the substrate as a fixed parameter to obtain V for each colloid. We note that even though the high frame rate allows us to access the short-time behavior, the long-time behavior — or else, the enhanced diffusion regime — is not recovered from our datasets due to the relatively short duration of our measurement. The speed distributions on the different substrates are asymmetric (tail on the right), see Figure 2.5B as an example of the PDF of speeds obtained from fifty individual colloids on hydrophilic glass. We fit the distributions with a log-normal distribution following Goldstein, Lauga, and collaborators [109]. We first performed a Kolmogorov-Smirnov (K-S) test for the goodness of fit, using the statistics package that is build in Python's scipy. From the obtained p-values and the observed agreement between theoretical fit and data, we concluded that the log normal fits the data adequately well. From the fit we obtain the moments of the distributions, see summary of those values in Table 2.2, which we use to determine parameters of the distributions, such as the standard deviation. Due to the distributions being asymmetrical, the peak corresponds to the most frequent value and is therefore representative of the distributions at hand. We therefore determine the fitted peak position of the speed, which takes into account the full shape of the distribution. The corresponding peak values are plotted in Figure 2.3B. The reported error corresponds to the standard error $\frac{\sigma}{\sqrt{N-1}}$, with σ the standard deviation of the distribu-

tion and N the number of colloids. Finally, we extract the characteristic time scale for rotation τ_R from the velocity autocorrelation function following Ref. [110]. We find no correlation between τ_R and the solution contact angle on the different substrates, see Figure 2.5C. We note that on all substrates a few percent of the particles irreversibly adsorbed, except for the PS and highly hydrophilic glass where about 30% and 80% of the particles adsorbed, respectively. Only speeds from colloids with non-zero speeds are included in the PDFs. Moreover, only colloids that do not interact with other colloids are included in the PDFs, since solute gradients in such case may interact and affect the velocities. In addition, colloids with chiral trajectories are not included in the analysis; such colloids are rarely encountered in our samples. We note that for the salt experiments it is hard to obtain sufficient trajectories because sticking of particles increases considerably for all samples/substrates; moreover, Brownian colloids, which also increase with salt, are excluded. Due to having fewer active particles, we cannot plot speed distributions, and therefore report average velocities from arithmetic means in Figure 2.4. However, the K-S test that we perform on the biggest data set showed that the log-normal distribution in principle still fits the data also in salt.

Surface Zeta Potential. Zeta potential measurements were performed with a Malvern Zetasizer Nano ZS, which measures electrophoretic
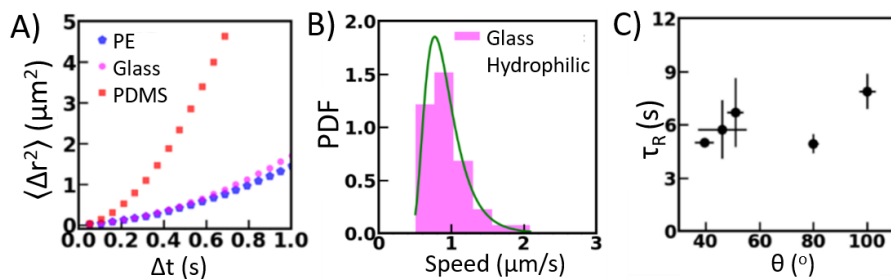
Figure 2.5: A) Typical MSD examples from three individual colloids measured on PE, Glass and PDMS in H_2O_2. B) PDF of colloid speed on hydrophilic glass. The data is fitted with a log-normal distribution. The moments obtained from the fit are shown in Table 2.2. Using these, in addition to the fitted peak position i.e. most frequent speed (0.8 µm/s), we determine the variance (0.078) and standard deviation (0.28 µm/s). C) Averaged τ_R extracted from the decorrelation of the colloid velocity vectors following [110] as a function of contact angle.

mobility of colloidal particles with laser doppler micro-electrophoresis. The zeta potential of the colloids under study was measured in water as well as in acidic pH conditions. In short, we insert a dilute solution of charged colloids in a cell that has an electrode at each end and apply a voltage, causing the colloids to move to the oppositely charged electrode. The resulting phase shifts of the laser light due to the colloid motion are measured by a laser interferometric technique called Phase Analysis Light Scattering, yielding the colloid velocity and electrophoretic mobility. The zeta potential is obtained from the electrophoretic mobility using the Henry equation and the Smoluchowski approximation $\mu = \frac{\epsilon_r \epsilon_0}{\eta} \zeta$, which are incorporated in the Zetasizer.

To measure the substrate zeta potential, the substrates under study were mounted on a planar cell custom made by Malvern for surface measurements. We measured the electrophoretic mobility of charged tracer particles at various distances from the substrate upon applying an electric field. From the tracer electrophoretic mobilities as a function of displacement, the corresponding zeta potentials were obtained through Smoluchowski's equation as a function of displacement and, in turn, the zeta potential at zero displacement (intercept) was extrapolated. The substrate zeta potential was then obtained according to Ref. [135]. Those measurements

Figure 2.6: **Substrate zeta potential control experiments.** Zeta potential of glass at various acidic pH conditions, in good agreement with streaming zeta potential measurements [143].

were performed using 1 μm carboxylated polystyrene colloids as tracers, prepared following a surfactant-free dispersion polymerization protocol, see Ref. [136]. Due to bubble formation at the electrodes in the presence of H_2O_2, all experiments were performed in aqueous HCl. Control experiments for the zeta potential of glass as function of pH (Figure 2.6) were performed in aqueous HCl with pH values equivalent to those at experimental conditions of 0.5-10% H_2O_2. After obtaining good agreement with
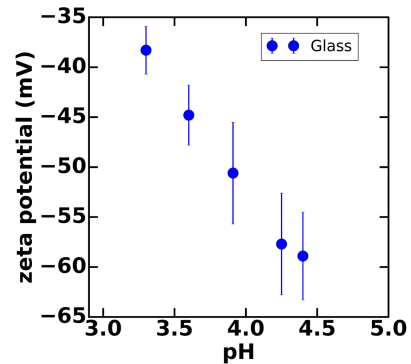
streaming zeta potential measurements, we performed the PDMS zeta potential measurements reported in the Results and Discussion section.

Atomic Force Microscopy.   Measurements were performed with a JPK Nano Wizard 3 (Ultra Speed) AFM in air, using Opus 240AC-NA probes. The measured frequency and stiffness of the probes were 75 kHz and 1.3 N/m, respectively. Images of the glass and PS substrates were acquired in AC mode, a dynamic contact mode otherwise known as tapping mode. A typical image of a glass substrate used in this work is shown in Figure 2.7: we presume that the spherical nanoparticles seen on the glass are part of the coating applied by the supplier, see Substrate Preparation. A typical image of the PS surface is also shown in Figure 2.7: we presume that the fiber-like surface is either a coating as part of the special treatment that the supplier uses to render the PS hydrophilic, or polishing marks/scratches on the surface to make it flat during the preparation. To avoid harming the surface, images of PDMS were acquired in QI (quantitative imaging) mode, which allows better vertical force control than AC mode and applies no lateral forces on the sample and is thus more suited for softer samples. It is a force curve based mode that provides three dimensional images by measuring the interaction between tip and surface while the tip moves vertically towards the surface, providing an approach and a retract force curve pixel by pixel. From the 3-dimensional images and height profiles, the Ra roughness was directly extracted using the JPK data-processing software version 6.1. The Ra roughness values for glass and PDMS are found under the Results and Discussion section. The Ra roughness for PS is 2.5 nm. The Ra is defined as the arithmetic mean of the deviations in height from the roughness mean value and is given by $Ra = \frac{1}{n} \sum_{i=1}^{n} |y_i|$, where y is the vertical distance from the mean. In air
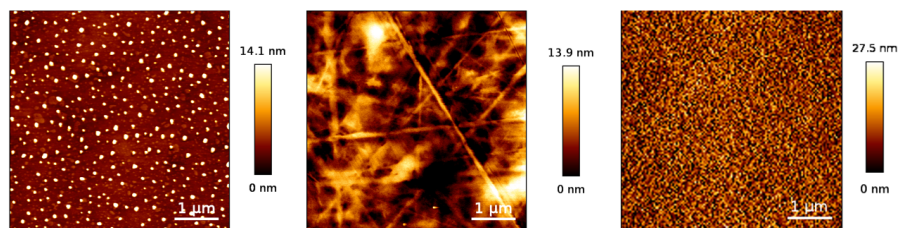

Figure 2.7: From left to right: representative AFM images of the glass, PS and PDMS substrates under study.

and with the same probe we observed from the shape of the approach curves that the stiffness increases from PDMS to glass. However, the stiffness of the PDMS should not be affected by the surface treatment that yields it hydrophilic. Thus, if substrate stiffness affected colloid speeds, speeds on PDMS and hydrophilic PDMS would not be as different.

Contact Angle Measurements. Images were taken with a Canon EF-S 60mm f/2.8 Macro USM lens mounted on a Canon EOS 500D Digital SLR Camera with back-lighting. Water droplets with volumes between 1 and 10 µL were placed on the various substrates. To determine the variation of contact angle for a specific surface, multiple droplets were imaged on the surface. To determine the spread in the contact angle for a certain material, droplets were imaged on different surfaces. These processes were repeated also for droplets containing 10% H_2O_2, 1 mM NaCl, and 10% H_2O_2 with 1 mM NaCl. All images were taken within seconds after droplet placement. The static contact angles were determined using ImageJ. The contact angle for a specific drop is typically determined with an error of less than 1°. Values reported in Figure 2.3B and under Substrate Preparation, correspond to averaged values from several individual water droplets containing 10% H_2O_2. Values reported in Figure 2.4 correspond to water droplets containing 10% H_2O_2 with 1 mM NaCl. Corresponding errors always denote standard deviations.

Appendix: Mechanism for osmotic coupling-induced speed variation

Understanding the effect of the wetting properties of the wall on the motion of a catalytically propelled swimmer is nontrivial. However, as we will show here, osmotic coupling leads to $V \propto (1 + \cos\theta)^{-3/2}$ under certain conditions, thus providing a plausible explanation for our experimental result. We will also discuss other potential mechanisms and explain why these are less likely to account for the significant wall effect.

Relation between slip and contact angle

Before we proceed with our analysis, it is convenient to (re)introduce the concept of slip and contact angle from the Results and Discussion. A hydrodynamic slip boundary condition on a wall (at $z = 0$) is defined as

$$b\frac{\partial}{\partial z}\boldsymbol{u}_i(x, y, z = 0) = \boldsymbol{u}_i(x, y, z = 0), \tag{2.4}$$

where z measures distance normal to a wall, and x and y are orthogonal co-planar coordinates. The fluid velocity is given by $\boldsymbol{u}$ and the subscript $i = x, y$ indicates that the boundary condition is applicable to the co-planar components of the flow vector. Finally, b denotes the slip length, which is zero for a no-slip surface and divergent for a full-slip surface. Regardless of the value of b, the fluid velocity normal to the boundary is characterized by a no-penetration condition: $\boldsymbol{u}_z(x, y, z = 0) = 0$. We do not consider patterned surfaces here, in line with our AFM measurements of the experimental surfaces, see Methods, which means that we can use a single slip value that is homogeneous along the surface.

Huang *et al.* [107] have argued that the following quasi-universal relation between slip b and contact angle θ holds:

$$b \propto (1 + \cos\theta)^{-2}, \tag{2.5}$$

where θ is the angle between the surface and a wetting droplet of water in air. The no-slip condition is implied to hold at $\theta = 0$, and the prefactors of the proportionality may be appropriately chosen to achieve this [107].

Diffusion coefficient near surfaces

The surface-to-surface separation between the colloid and the wall δ is important for hydrodynamic and chemical coupling. We therefore analyze its value in this section. It is natural to think that a variation in swim speed stemming from modifying the wall properties may be caused by associated height variations. Such a height change could be a secondary effect of changing the wall's chemical properties, for instance, through changing the electrostatic repulsion. However, it will turn out that this idea does not match with our experimental results.

We find that the separation δ is comparable to the particle radius R. We gain this insight from the experimentally measured diffusion coefficient of our Pt-coated particles in water, see Methods for experimental details and values. The diffusion coefficients are similar within error above all substrates and therefore similarly different from the diffusion coefficient for free diffusion in the bulk. Our results are in agreement with predictions, see for example Ref. [128], on the hydrodynamic mobility of a passive particle moving close to a no-slip wall. We refer to Faxen's theoretical prediction for the near-wall in the plane parallel to the wall diffusion, which has been experimentally proven in Ref. [129] and [130], and is given by $\frac{D}{D_{bulk}} = 1 - \frac{9}{16}\gamma + \frac{1}{8}\gamma^3 - \frac{45}{256}\gamma^4 - \frac{1}{16}\gamma^5$ with $\gamma = R/(\delta + R)$. Faxen's law applies to a no-slip condition, however we are still probing here small departures in terms of slip from this condition. The contact angles that we measure are in the range between 15° and 100°, implying that the corresponding slip lengths, calculated by Eq. 2.5, change by roughly a factor of 5. The measured translational diffusion coefficients remain constant upon a variation in slip of that order, and show a reduction of roughly a factor of 2 compared to free diffusion in bulk. Figure 3.1 in Ref. [123], shows the effect of the slip on the force acting on a translating sphere as function of separation distance; the effect on the diffusion coefficient is directly related to the effect on the force, therefore this figure can be used to gauge the effect of the slip on the diffusion coefficient as function of separation distance. To understand the changes in the distance with slip, we look horizontally in the above-mentioned figure — for the here constant diffusion coefficient — and read the separation gap size that would correspond to the changes in separation distance based on the conditions that follow from our measurements. We conclude that for a factor of 2 reduction compared to the bulk value, in combination with the factor 5

change in slip, the variation in the separation will be minimal. Since diffusion coefficients are similarly reduced, we use the average value above the various substrates and find that the separation δ in the Brownian state corresponds to $\delta \sim 0.4R$. Overall, the measured constancy of the passive diffusion coefficients with θ is an indicator that there is limited variation in δ with changes to the wall properties.

Osmotic coupling mechanism

Osmotic coupling can directly affect the speed upon changing the wall, even for fixed δ. We here focus on this mechanism and discuss how such a coupling may give rise to the observed trend. We assume, for convenience, neutral self-diffusiophoresis and homogeneous surface properties for both the wall and the colloid. The properties of the wall and swimmer may be different and we will distinguish these by subscripts w and s, respectively. The discussion is analogous for self-electrophoretic mechanisms, with the minor exception that the Debye length is typically considerably larger than the one associated with non-electrostatic molecular interactions.

Uspal *et al.* [95] have investigated osmotic coupling near a no-slip wall. However, adopting their result is not entirely trivial, as the derivation therein makes explicit use of the fundamental hydrodynamic solutions near a no-slip wall. It is relatively straightforward to compute the Stokeslet for a full-slip wall [144]. However, this limit is problematic for other reasons, as ξ_w will turn out to diverge due to its dependence on θ. The expressions for the Greens functions near a wall with intermediate slip values are convoluted [145] and do not provide significant additional insight beyond what can be obtained through scaling arguments.

Referencing [95], we observe that the osmotic contribution to the speed $\propto (R + \delta)^{-3}$ for no-slip surfaces; this scaling will hold even for partial or full slip. Thus, we may write

$$V \approx V_{other} + \frac{R^3}{(R + \delta)^3} V_{osm.},$$ (2.6)

where $V_{osm.}$ is a proportionality constant that measures the impact of osmotic flow along the wall on the speed of the swimmer above it. The

velocity V_{other} accounts for confinement effects and is here assumed constant with variation of θ, because the height is assumed constant. Both V_{other} and $V_{osm.}$ depend on R, however, only $V_{osm.}$ is strongly dependent on θ. Applying the standard diffusiophoretic theory [63], we have that $V_{osm.} \propto \xi_w / D_{sol.}$ with $D_{sol.}$ the solute diffusion coefficient. Ajdari and Bocquet [111] have shown that for a partial-slip wall the coupling parameter may be written as Eq. (2.1), i.e. $\xi_w = (k_B T / \mu) \lambda_w \gamma_w (1 + b_w / \lambda_w)$, with k_B the Boltzmann constant, T the temperature, λ_w a length scale for the solute-surface interactions, γ_w a length measuring the solute excess, and b_w the hydrodynamic slip length of the wall. This expression reduces to the no-slip result for $b_w = 0$. Note that typically $b_w \gg \lambda_w, \gamma_w$ [111], implying that the dominant effect of changing the wall comes from the hydrodynamic slip this induces. The value λ_w is left relatively unaffected by changes in the wall, as the interaction length scale is molecular $\approx 1\,\text{Å}$ for neutral solutes. However, γ_w will vary as it depends on details of the molecular interactions between solutes and wall, which are key to determining wetting (and slip). Following Huang *et al.* [107], we have

$$\gamma_w \propto \sqrt{1 + \cos\theta}, \tag{2.7}$$

and for b_w we can use Eq. (2.5). Isolating the dominant dependence on θ, we obtain the following proportionality

$$V \propto V_{osm.} \propto \frac{1}{(1 + \cos\theta)^{3/2}}, \tag{2.8}$$

whenever $b_w \gg \lambda_w, \gamma_w$, such that the slip-length term dominates.

Implications of the mechanism and other considerations

Equation (2.8) has some interesting consequences and caveats in relation to our experimental data. First, the presence of the factor 1 in the numerator to Eq. (2.8) allowed us to capture the finite (extrapolated) speed at $\theta = 0$ and the global trend well, without requiring an offset to Eq. 2.8. That is, a nearly negligible offset best fits the data. The implication is that the prefactors and separation δ in Eq. (2.6) are such that for a no-slip surface there is some (fortuitous) cancellation of terms that eliminate the

V_{other} contribution to the speed. This could be an expression of a competition between confinement, bulk, and osmotic effects, which may have opposite signs. It is difficult to make strong statements in this regard without knowing more about the specifics of the propulsion mechanism.

A most interesting feature of Eq. (2.8) is the potential for a divergence of the speed of a self-propelled particle near a full-slip surface. This is counter intuitive as for a dragged passive sphere the mobility enhancement with respect to bulk is only a factor 1.37 [123, 146] in the full-slip case. The reason for this is that the surface velocity generated by the osmotic coupling can become very significant, as there is a divergent separation in length scales between the atomic interactions that force the fluid λ_w and the hydrodynamic slip length b_w as θ approaches $180°$. Such a divergence does not occur in a real system as the effect of enhanced surface speed would either push the solute concentration out of the low-Péclet regime where solute diffusion dominates its advection by the fluid, or modulate the swimmer height; both effects being self-limiting in nature.

Lastly, we discuss other arguments for describing our findings, such as purely hydrodynamic coupling and solute-species confinement. By purely hydrodynamic coupling we mean the modification of the (bulk) flow field around the swimmer through the presence of the wall, but in absence of the osmotic effect. This type of coupling has been investigated in detail for simple swimmer models, *e.g.*, see Ref. [132]. Flow-mediated interactions give rise to attraction and repulsion for pusher and puller swimmers, respectively, and may also lead to swimmer reorientation [102, 132, 133]. At a constant, yet small value of $\delta \lesssim R$, hydrodynamic slip can modify the mobility of a passive particle substantially [123, 146]. However, a purely hydrodynamic effect is unlikely to describe our experiment, because at a fixed δ boundaries perturb the parallel motion of an active particle less than that of a passive one. The former has a leading-order dipolar flow-field decay [132], while the latter has a leading-order monopolar decay, explaining the difference. It is straightforward to demonstrate that within far-field theory the effect is less than 10% of the bulk speed for a squirmer-type swimmer [147, 148] moving parallel to the wall, even for small δ. We also consider solute-species confinement in the gap between wall and swimmer, which perturbs concentration gradients along the colloid surface, affecting the colloid slip velocity and thus its speed; this effect

comes on top of any purely hydrodynamic change of the velocity. This coupling has already been studied [96, 97, 99–101]. Yet, under the fixed height assumption the effect of this mechanism should be limited. This is because the Péclet number typically is small and the solute species are not substantially impacted by changes in the hydrodynamic flow field, due to wall modification. Considering the above, we believe that the osmotic coupling scenario is the most likely candidate for describing our observations.

3

Diffusion-Based Analysis for Wall Distance Determination

Abstract

Microswimmers typically move near walls that can strongly influence their motion. However, direct experimental measurements of swimmer-wall separation remain elusive to date. In this chapter, we determine this separation for model catalytic microswimmers from the height dependence of the passive component of their mean-squared displacement. We find that swimmers exhibit "ypsotaxis", a tendency to assume a fixed height above the wall for a range of salt concentrations, swimmer surface charges, and swimmer sizes. Our findings indicate that ypsotaxis is activity-induced, posing restrictions on future modeling of their still debated propulsion mechanism.

Introduction

Confining surfaces, such as planar walls, have a far-reaching impact in the microswimmer world, often ensuring microswimmer function and survival [18]. Encounters with surfaces give rise to accumulation, as seen for sperm [149], algae [150] and bacteria [151], and enable the formation of bacterial biofilms that facilitate their spreading, cooperation, and capture of nutrients [152–154]. Moreover, surfaces can significantly modify swimming trajectories; *e.g.*, bacteria often exhibit circular motion with direction controlled by the boundary condition [90–93], in stark contrast to their run-and-tumble motion in bulk.

Striking surface effects are not only found in biological systems, but are also present for synthetic microswimmers [59–61, 103, 105, 155, 156]. Model catalytic colloidal swimmers exhibit autonomous directed motion due to self-generated chemical gradients [83]. Recently, neighboring walls were shown to significantly alter the magnitude of their swim speeds [103, 105, 155, 156]. This revealed that walls play a far greater than previously expected role on self-propulsion, providing a path towards resolving seemingly conflicting experimental observations. For example, speed differences under similar conditions may stem from the phoretic interplay between the hydrodynamic boundary condition on the wall and the out-of-equilibrium chemical species generated by the swimmer [157]. Current models predict a wide range of behaviors close to walls, including hovering, sliding, forward and/or backward propulsion [58, 59, 95–102, 131–133, 158, 159]. This diversity is partly due to the complexity of and uncertainties in the propulsion mechanism, and partly due to the hydrodynamic and numerous phoretic couplings that wall proximity can introduce. Thus, quantitative insight into swimmer-wall separation is pivotal to pinpointing missing details of the propulsion mechanism, and in turn tailoring swimming behaviors, *e.g.*, for guiding microswimmers in complex environments.

To date, no reported experiment has directly measured swimmer-wall separations. However, based on qualitative observations, separations are anticipated to be smaller than the swimmer size [60, 75], even as small as a few tens of nm [113, 114]. Such separations cannot be directly resolved by standard optical microscopy [113], which is why holographic

microscopy has been proposed [105], as it yields three-dimensional positions of spherical particles with high precision [160]. However, fitting holograms of spheres half-coated with a metal is computationally expensive, especially when studying dynamics, since discrete dipole approximations have to be employed in the numerical calculations to obtain their positions [161]. Furthermore, inhomogeneities in the metal coating introduce additional fit parameters and uncertainties in determining particle positions. Another way to measure small particle-wall separations is Total Internal Reflection Microscopy, which yields separations from the scattering of evanescent waves off of particles close to a wall [162]. Here too, the asymmetric coating interferes with interpreting the result and obtaining accurate measurements. Hence, a novel measuring approach is needed.

In this chapter, we present a novel and straightforward method for obtaining microswimmer-wall separations *in situ*. We determine the translational diffusion coefficient of the swimmer from mean-squared displacement curves, and obtain the height from its theoretically predicted dependence on swimmer-wall separation. Our method can be applied to most synthetic microswimmers, and may be extended to a range of swimming microorganisms, moving parallel to walls. We applied it here to catalytically propelled model microswimmers. Besides the fuel concentration, we systematically varied additional parameters known to affect self-propulsion, as well as particle-wall separations in passive systems: the salt concentration in solution, swimmer size, and swimmer zeta potential. We were thereby able to gain unprecedented insights into their effect and the presence of a wall on the swimming behavior.

Results and Discussion

We obtained microswimmer-wall separations from experimental measurements of the separation-dependent translational diffusion coefficient, D, of the microswimmers. D as well as propulsion speeds V were extracted from mean square displacements (MSDs) following Ref. [30, 106]. Briefly, we fitted the short-time regime ($\Delta t \ll \tau_R$) of the MSDs with $\Delta r^2 = 4D\Delta t + V^2\Delta t^2$ [30]; τ_R is the rotational diffusion time, $\tau_R = 1/D_{R,bulk}$, with $D_{R,bulk} = \frac{k_B T}{8\pi\eta R^3}$ the bulk rotational diffusion coefficient, R the radius, η the viscosity, k_B the Boltzmann constant, and

T the absolute temperature. The first term corresponds to the passive diffusion contribution that is usually obscured by the activity-induced, short-time ballistic behavior [106], but may be obtained with sufficient statistics. Reliable measurements require frame-rate adjustment, such that the regime where both diffusion and activity contribute to the MSD can be resolved. See Methods for tracking and MSD calculation details.

To calculate the particle-wall separation, h, see also Figure 3.1, we first consider the ratio $d = D/D_{bulk}$, with $D_{bulk} = \frac{k_B T}{6\pi\eta R}$ the bulk diffusion constant. For $d \gtrsim 0.6$, the well-known prediction by Faxén [129, 130, 163, 164]: $d(h) = 1 - \frac{9}{16}\gamma + \frac{1}{8}\gamma^3 - \frac{45}{256}\gamma^4 - \frac{1}{16}\gamma^5$, with $\gamma = R/(h+R)$, can be used to extract h. For $d \lesssim 0.4$ a lubrication theory result, $d(h) = -\frac{1}{\frac{8}{15}\log\left(\frac{h}{R}\right)-0.9588}$, is more appropriate [128, 165]. In the intermediate ($0.4 \lesssim d \lesssim 0.6$) regime, applicable to most of our experiments, we interpolate the combined numerical data by O'Neill [165] and Kezirian [123], see Methods for the $d(h)$ relation. Here, we fitted for h using the interpolated expression.
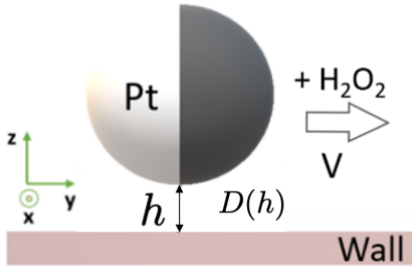

Figure 3.1: **Schematic of the experiment.** We obtain the swimmer-wall separation, h, from the measured translational diffusion coefficient, D, of the swimmer and its theoretically predicted dependence on wall separation.

In all experiments, we used monodisperse TPM colloids [108] half-coated with a thin Pt layer $\approx$ (4.5 $\pm$ 0.2) nm at dilute concentration. In water, colloids exhibited passive Brownian motion, while dispersion in 10% H_2O_2 rendered them active through a catalytic process. Colloids quickly reached the lower glass wall and continued to move adjacent to it, see Figure 3.1 for a schematic representation.

To demonstrate the effectiveness of our method, we first carried out control experiments in water. In these cases, D was acquired from fitting MSDs with $\Delta r^2 = 4D\Delta t$. Figure 3.2A shows that the extracted separation corresponds well to a theoretical prediction based on a balance of electrostatic repulsion and gravity [166, 167], see Appendix I. That is, we recovered the expected decrease in separation with increasing salt concentration: salt increases the solution's ionic strength, thereby effectively
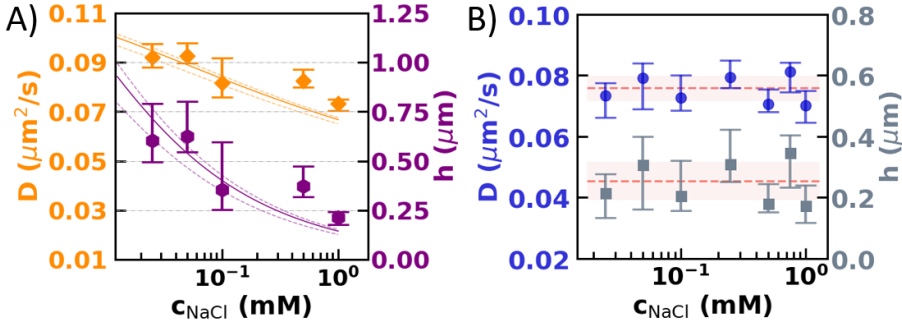
Figure 3.2: **Salt-dependent motion above the wall:** Effect of salt concentration c_{NaCl} on the motion of (2.77 ± 0.08) µm colloids with (4.4 ± 0.2) nm Pt. All reported values are medians, error bars denote first quartiles. A) Diffusion coefficient (orange) and separation (purple) in the Brownian state in water with c_{NaCl}. Lines show theoretical predictions based on balancing electrostatics and gravity, see Appendix I. B) Diffusion coefficient (blue) and separation (grey) in the active state in 10% H_2O_2 with c_{NaCl}. Dotted lines indicate mean values.

screening the charge on the particle and wall. This reduces the Debye length, *i.e.*, the distance over which surface charges act, bringing the colloids closer to the wall. To verify our method further, we compared separations resulting from our diffusion coefficient-based method to those directly measured with digital in-line holographic microscopy for uncoated silica spheres with well-known size and refractive index [168], see also chapter 5. The good agreement between the two methods confirms that we indeed recover colloid-wall separations with our diffusion-based method despite using a computed rather than a measured D_{bulk} value.

Having established the validity of our method, we employed it to our catalytic swimmers. First, we studied the effect of salt concentration in solution. For these experiments, we used TPM spheres of (2.77 ± 0.08) µm diameter half-coated with (4.4 ± 0.2) nm Pt. Surprisingly, in active systems we found a behavior completely unlike that of passive systems in Figure 3.2A. For the same particles and salt concentration range, D and h remain constant within measurement precision, see Figure 3.2B. Particles propel themselves parallel to the wall at constant separations of (0.25 ± 0.06) µm.

At the same time, we found a decrease in speed with increasing salt concentration, see Figure 3.3, where the line represents the least-squares fit with $V = A + (B/(C + c_{NaCl}))$. This expression follows from a salt-gradient based contribution to the observed speed [75], with A the remaining speed in the limit of high salt, B a prefactor, and C the ion concentration already present in the medium. From the fit we find (0.35 ± 0.09) µm/s and (0.09 ± 0.07) mM, for A and C, respectively. The fitted C value agrees reasonably well with the background ion concentration (0.008 mM) we obtained from electrical conductivity measurements [169] for 10% H_2O_2 (2.7 µS/cm, Ilium technology, Model 2100 Conductivity Meter) assuming hydrogen ions as the dominant ion species. We return to this salt gradient below.
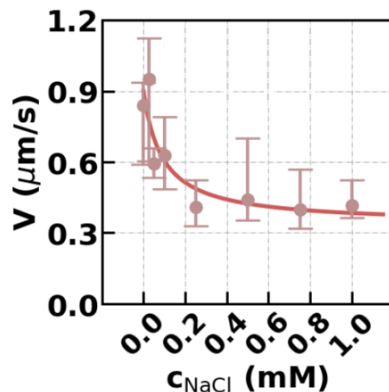

Figure 3.3: **Salt-dependent propulsion speed above the wall.** Speed decrease in 10% H_2O_2 with c_{NaCl}. Solid line is a least-squares fit with $V = A + (B/(C + c_{NaCl}))$, where A is the remaining speed in high salt, B a prefactor, and C the ion concentration already present in solution, following from ionic diffusioosmosis along the wall, see Appendix II.

Second, we explored the effect of colloid zeta potential, ζ, the electric potential at the colloid's surface. We used (2.70 ± 0.06) and (2.77 ± 0.08) μm diameter colloids with different surface functionalizations [136] and thus different ζ. The reported ζ correspond to those of the parent colloids, see Methods for characterization, before adding the Pt coating. We therefore use the adjective "base" and a subscript "b", *i.e*, ζ_b, to indicate that we know only the zeta potential of the uncoated colloid, and not that of the swimmer. We note that passive colloids with $\zeta_b > -12$ mV were typically stuck on the negatively charged wall, see also Methods (Figure 3.7B).

However, for the active system, we found that wall separation remained unaffected for the entire (wide) range of ζ_b under study, see Figure 3.4A. In all cases, particles moved at (0.24 ± 0.04) µm from the wall, which matches the separations measured for different salt concentrations. Unexpectedly, as we will return to, the colloids self-propelled not only at a constant h when varying ζ_b, but also at quantitatively comparable speeds
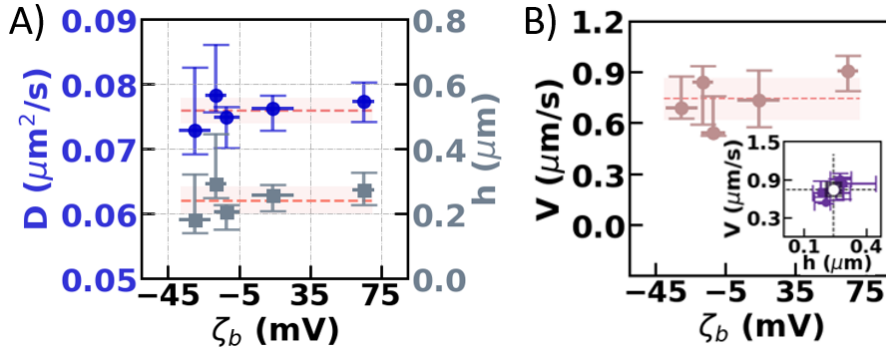
Figure 3.4: **Swimmer base zeta potential dependence of propulsion above the wall.** The base zeta potential, ζ_b, of TPM colloids with diameters between (2.70 ± 0.06) and (2.77 ± 0.08) µm, and Pt coating thicknesses $\approx (4.4 \pm 0.2)$ nm, was varied through surface functionalization. All reported values are medians, error bars denote first quartiles, and dotted lines represent mean values. A) Diffusion coefficient (circles) and separation (squares) with ζ_b. B) Speed for the same ζ_b range as in (A). The inset shows propulsion speed with separation (purple circles), with the write circle marking the intersection of mean values.

V, see Figure 3.4B. We can indeed collapse the data by plotting V as a function of h, see the inset in Figure 3.4B, further demonstrating that ζ_b does not affect the swimming behavior. We note that the direction of motion was away from the Pt cap both for positive and negative ζ_b.

Third, we focused on swimmer size, another parameter known to affect swim speeds [58]. We performed experiments using TPM spheres with a wide range of radii, but with similar Pt coating thicknesses and ζ_b, see Methods. We found that diffusion coefficient decreases with swimmer size, see Figure 3.5A, where the solid line represents the least-squares fit with $D = a/R^b$ ($a = 0.120 \pm 0.004$ µm^3/s, $b = 1.3 \pm 0.2$). The inset shows the measured swim speeds together with a fit of the expected scaling $V = a/R$ [58] ($a = 2.2 \pm 0.4$ µm^2/s). Strikingly, swimmer-wall separation remained relatively constant with R, see Figure 3.5B; the dashed line shows the mean separation of (0.32 ± 0.08) µm.

The above experiments reveal that our swimmers exhibit "ypsotaxis": a tendency to assume a specific height for a wide range of parameters. Remarkably, the height appears independent of salt concentration, ζ_b,

and even size, running not only counter to our intuition for passive systems but also to features of common self-propulsion mechanisms. For our Pt-coated swimmers, this robust separation distance was found to be (0.27 ± 0.11) µm on average, in line with the observation that micron-sized catalytic swimmers do not self-propel over steps of a few hundred nanometers [60]. Such a height is further consistent with wall-dependent speeds [103, 105, 155, 156], for which wall separation must not substantially exceed the swimmer size to ensure strong osmotic coupling [59, 95, 100]. The wide range of swimmer sizes employed here showed that buoyancy is not the prime contributor to ypsotaxis. This is further underpinned by our observation of swimmers moving along the top wall, upon inversion of the sample holders, for a period of time. We hypothesize that ypsotaxis is instead primarily caused by phoretic and osmotic flows, *i.e.* it is activity-driven.

To test for this, we performed experiments using (2.23 ± 0.11) µm diameter TPM spheres with (4.5 ± 0.2) nm Pt for various H_2O_2 concentrations, and hence degrees of activity. Indeed, we found that diffusion coefficient and thus swimmer-wall separation not only decreases rapidly with increasing fuel concentration from the Brownian 0% H_2O_2 state (inset and
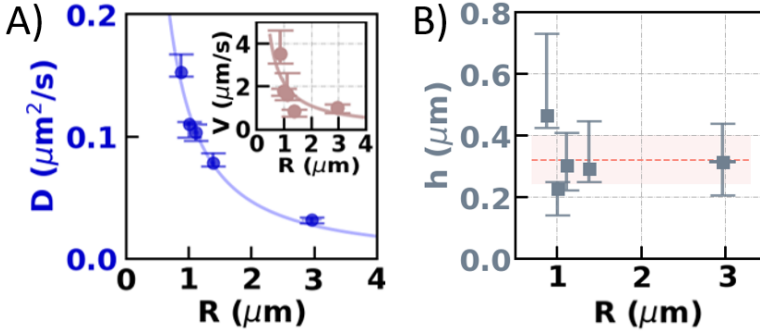
Figure 3.5: **Swimmer size-dependent propulsion above the wall.** All reported values are medians, error bars denote first quartiles. Variation of the radius, R, of active TPM spheres with similar ζ_b and Pt (coating thickness $\approx 4.5 \pm 0.2$ nm) affects A) the diffusion coefficient and B) swimmer-wall separation. The inset in (A) shows the propulsion speed with R. The solid lines in (A) are fits with a/R^b (main panel) and the expected a/R following from Ref. [58] (inset). The dotted line in (B) shows the mean separation $(0.32 \pm 0.08 \, \mu m)$.
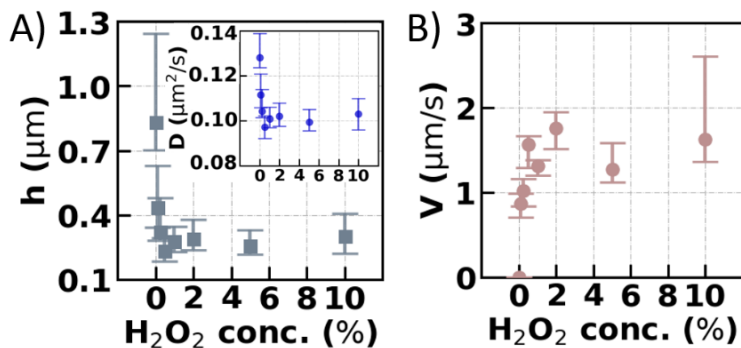
Figure 3.6: **Activity-induced ypsotaxis**. A) Swimmer-wall separation h with increasing H_2O_2 (fuel) concentration. The inset shows the corresponding diffusion coefficient D for the same concentration range. B) Speed V for the same fuel concentration range as in (A); the trend is similar to that of Refs. [30, 56]. Experiments were performed using (2.23 ± 0.11) µm diameter TPM spheres with (4.5 ± 0.2) nm Pt. All reported values are medians, error bars denote first quartiles.

main panel of Figure 3.6A, respectively), but also plateaus beyond 0.25% H_2O_2. Similarly, the speed also increases sharply and then plateaus above 0.25% H_2O_2 (Figure 3.6B). These observations imply that the constant separation is induced by the activity, thereby confirming our hypothesis on the origin of ypsotaxis. In Appendix III, we argue that said origin also causes the active alignment of catalytic swimmers with respect to the wall [59, 60, 81].

Our results provide new insights into the debated nature of the propulsion mechanism [76]. Current thinking favors self-electrophoresis [75, 89], *i.e.*, motion generated *via* self-generated ionic currents, as simple salts are known to greatly decrease propulsion speeds. The lack of speed variation with ζ_b, however, is not commensurate with this or other ion-based propulsion mechanisms typically scaling with ζ or ζ^2, see [74]. A possible explanation is that a different ζ at the Pt cap dominates the swimmer's behavior.

However, speed variation with salt — typically indicative of a change in activity — is not readily reconciled with a constant h which is also activity-driven, even if the cap's ζ dominates. Drawing upon our previous work [155], we provide an alternative wall-centric explanation. Suppose that the swimmer's bulk speed is unaffected by adding salt. The

swimmer's effective near-wall speed may still vary, provided salt impacts the osmotic counterflow induced by the swimmer-generated chemical species interacting with the wall [155]. Our fit in Figure 3.3 reveals that the osmotic contribution to the speed bears the hallmarks of ionic diffusion [63]. This requires a net-neutral gradient of ions with different electric mobilities to be involved, often referred to as a salt gradient. This salt gradient might originate from the chemical dissociation reactions in the long-range H_2O_2 gradient with the wall [74], stemming from fuel consumption at the Pt cap. This model would have the right features to show an ionic diffusioosmosis along the wall, see Appendix II for details.

Conclusions

In this chapter, we established a novel method for measuring swimmer-wall separations utilizing the height dependence of the diffusive component of their mean-squared displacement. We found that catalytic model microswimmers propel at roughly fixed heights of few hundred nanometers from planar walls. Our work further showed that nearby walls could be dominant factors in controlling swim speeds, *i.e.*, ion-induced flow may only play a role at the wall and not at the swimmer surface. This would necessitate a paradigm shift in modeling experimental observations and in identifying the still missing details of their propulsion mechanism. Our method can be readily applied to other types of spherical microswimmers moving parallel to walls, and may be extended to different swimmer shapes as well. We are confident that further application of our method will provide novel insights on the impact of confining surfaces in the microswimmer world and, in turn, facilitate predicting swimming behaviors in complex environments.

Methods

In this section, we provide additional details on particle preparation and characterization as well as describe the methods by which we obtained and processed MSD curves to subsequently infer the particle height.

Synthesis of bare TPM colloids. The bare TPM spheres used in Figures 3.2-3.6 were obtained from the one-pot surfactant-free synthesis protocol of Ref. [108]. In short, 30.0 g of a fresh stock solution of MilliQ water (18.2 MΩ cm resistivity, Filtration System Milli-Q Gradient A10) was weighed into a plastic beaker; the pH of the water was adjusted to 10.80 with ammonium hydroxide (28-30%, Sigma-Aldrich), and the solution was then stirred at 300 rpm. 900 µL TPM (98%, Sigma Aldrich) was rapidly injected into the water and the solution was covered with parafilm. After 20 min, the stirring speed was reduced and maintained at 200 rpm. After 2 h, 100 mg of azobis(isobutyronitrile) ($\geq$ 98%, Sigma-Aldrich) was added to the emulsion. The suspension was stirred a total of 2.5 h before heating in an oil bath at 80 °C under rotation of 50 rpm for another 2.5 h. The diameters of the colloid batches obtained with this protocol are found in Table 3.1. Different syntheses resulted in monodisperse spheres with diameters varying from 1.75 to 2.77 µm; size variation between syntheses is expected. The largest employed colloid batch was obtained through addition of the dye fluorescein isothiocyanate isomer I ($\geq$ 90%, Sigma-Aldrich) following Ref. [108]. Bare TPM particles are negatively charged in MilliQ water (pH 5.5), see also Table 3.1. In water at pH 3.3, the zeta potential increases indicating that the particles are less negatively charged than at pH 5.5.

Synthesis of carboxylated TPM colloids. Carboxylated TPM (TPM-COOH) spheres of diameter 2.70 ± 0.06 µm were prepared as in [155].

Amine functionalization of bare TPM colloids. Bare TPM spheres were modified with amine (NH$_2$) groups by silanization, resulting in positive colloid surface charges. Briefly, 14 mL ethanol (EtOH, Sigma-Aldrich), 3 mL NH$_3$ and 100 µL 3-aminopropyl triethoxysilane (APS, $\geq$ 98%, Sigma-Aldrich) were added in a glass vial and mixed at 300 rpm. 1 mL of 1% w/v TPM spheres in EtOH was subsequently added in the solution, which was then covered with parafilm. After stirring for 24 h, the particles were thoroughly washed in EtOH and subsequently in water.

NeutrAvidin-PEG-functionalization of carboxylated TPM colloids. The surface of the TPM-COOH spheres was functionalized with NeutrAvidin (Molecular Probes) and poly(ethylene) glycol (PEG), following the surfactant-free coating protocol established in Ref. [136]. Briefly, 13.8 mg EDC (1-Ethyl-3-(3-dimethylaminopropyl) carbodiimide hydrochloride, 99%, Carl Roth) and 4.6 mg NHS (N-Hydroxysulfosuccinimide sodium salt, 98%, Sigma-Aldrich) were dissolved in 1 mL water, previously kept at 4 °C. 250 µL of this solution was added in a 500 µL water solution containing 1% TPM-COOH spheres, previously kept at 4 °C; the solution was vortexed for 30 min at 4 °C. Subsequently, the pH was adjusted to 8.60 with 7.5 µL 0.2 M sodium hydroxide (NaOH, 98.5%, Acros Organics). 400 µL PEG (M_w = 2000, Alpha Aesar), taken from a 500 µL water solution containing 20 mg PEG, was added in the TPM-NHS particle solution. After vortexing for 48 h at 4 °C, the resulting PEG-coated particles (TPM-PEG) were thoroughly washed and stored in water. To check whether the PEG coating was successful, the TPM-PEG spheres were vortexed for 1 h in 2 M NaCl, after which aggregation was not observed. Moreover, we checked the bare zeta potentials (ζ_b) before and after PEG coating. In water, the original TPM-COOH spheres were measured to have $\zeta_b = -70 \pm 9$ mV while the TPM-PEG spheres had $\zeta_b = -40 \pm 7$ mV. This further indicated the presence of the PEG layer which shielded the COOH groups. The bare zeta potential decrease agrees with the one measured in Ref. [136] for 1 µm colloids after coating. The remaining negative surface charge is probably caused by unreacted COOH groups, as also mentioned by the authors of Ref. [136]. Note that in the acidic pH conditions of Figure 3.4 (pH 3.3), the bare zeta potential of the TPM-COOH spheres dramatically decreases to $\zeta_b = -12 \pm 7$ mV, which is expected since binding with hydrogen will neutralize the COOH groups. At the same time, the bare zeta potential of the TPM-PEG spheres is affected much less ($\zeta_b = -30 \pm 9$ mV) at pH 3.3.

Pt coating. All spheres were spin coated from ethanol dispersions on flat glass slides at sub-monolayer concentrations and subsequently sputter coated with Pt/Pd (80:20) from above, as described previously in the Methods of chapter 2. Thicknesses for all employed batches are shown in Table 3.1. These were determined electronically from the mass and the density of the deposited material using the Cressington Thickness Monitor, which measures thicknesses with resolution of order 0.2 nm. Note

that all particles have similar Pt thicknesses within error which ensures that any differences in observed behaviors do not arise from the thickness of the coating. After deposition the TPM/Pt colloids were redispersed in water (bare TPM and TPM-PEG spheres), or water containing 5 mM HCl (TPM-NH$_2$ spheres) or water containing 5 mM NaOH (TPM-COOH spheres) by sonication. Sonication typically took place for 10 to 20 minutes, during which time no Pt flakes were released from the glass slides in the solution. The colloids were subsequently washed and stored in water. Redispersion produced well-dispersed particles.

σ (µm)	PD (%)	surface groups	ζ_b (mV) pH 5.5
2.77 ± 0.08	2.8	-	- 41 ± 9
2.70 ± 0.06	2.2	COOH	- 70 ± 9
2.70 ± 0.06	2.2	PEG	- 40 ± 7
2.77 ± 0.08	2.8	NH$_2$	—
2.77 ± 0.08	2.8	NH$_2$	—
1.75 ± 0.06	3.4	-	- 44 ± 7
2.01 ± 0.06	3.0	-	- 39 ± 7
2.23 ± 0.11	5.0	-	- 44 ± 9
5.94 ± 0.31	5.2	-	- 53 ± 10

σ (µm)	ζ_b (mV) pH 3.3	Pt (± 0.2 nm)	Fig.
2.77 ± 0.08	-18 ± 6	4.4	3.2-3.5
2.70 ± 0.06	- 12 ± 7	4.3	3.4
2.70 ± 0.06	- 30 ± 9	4.3	3.4
2.77 ± 0.08	+ 14 ± 12	4.3	3.4
2.77 ± 0.08	+ 65 ± 6	4.4	3.4
1.75 ± 0.06	—	4.7	3.5
2.01 ± 0.06	—	4.5	3.5
2.23 ± 0.11	—	4.5	3.5-3.6
5.94 ± 0.31	—	4.5	3.5

Table 3.1: Overview of colloid properties for all batches employed in this chapter. Top from left to right, the columns provide: the diameter σ, the size polydispersity (PD) in percent, the groups (if any) present on the colloid surface after functionalization, the *bare* zeta potential ζ_b at pH 5.5. Bottom from left to right, the columns provide: the *bare* zeta potential ζ_b at pH 3.3, the thickness of the sputter-coated Pt layer, and the figure in which each colloid batch was used.

Colloid Zeta Potential Measurements. Measurements were performed at all times on the parent, i.e. uncoated, colloids using a Malvern Zetasizer Nano ZS, which measures the electrophoretic mobility of charged colloidal particles with laser doppler micro-electrophoresis. The colloid zeta potential is obtained from the electrophoretic mobility using Henry's equation [170] and the Smoluchowski approximation $\mu = \frac{\epsilon_r \epsilon_0}{\eta} \zeta$, incorporated in the Zetasizer's software. Typically, we performed 12-15 runs to obtain an accurate measurement of the zeta potential in water. Such measurements were then repeated two to five times for each batch. The results are reported in Table 3.1, showing that colloids of different sizes employed in Figure 3.5 have comparable zeta potentials. To determine potential differences in swimmer-wall separation and speed due to the swimmer zeta potential in Figure 3.4, we would have to determine the zeta potentials under conditions similar to the swimming experiments, *e.g.*, in H_2O_2. However, due to bubble formation at the electrodes of the cell measurements in H_2O_2 were not feasible. Since zeta potentials are set by the pH, the zeta potentials in Figure 3.4 were measured in water at pH 3.3 obtained by addition of HCl. This pH value is equivalent to that of the H_2O_2 solution.

Imaging and Tracking. In all swimming experiments, TPM/Pt colloids were dispersed in 10% aqueous H_2O_2 solution at dilute particle concentration ($\approx 10^{-7}$ v/v). Their motion was recorded above glass walls (glass cover slips, purchased from VWR and used as received) with a 60x oil objective (NA 1.4) mounted on an inverted Nikon Eclipse Ti microscope. 30 s movies were acquired in the xy-plane at a frame rate of 19 fps to allow access to short time scales. All measurements were performed in the dark to avoid photocatalytic decomposition of H_2O_2 and typically within the first hour after sample preparation to avoid depletion of H_2O_2 [75] and potential changes in substrate slip due to reaction with H_2O_2 [155]. Additional movies of the motion of TPM/Pt colloids were taken at 5 fps in water and water with pH 3.3, adjusted using HCl to match the pH of the swimming experiments in 10% H_2O_2. The duration of the control movies was adjusted with respect to the colloid size under study to ensure that motion was randomized: particles with diameter smaller than 2 µm were measured for 3 min, while particles with diameters between 2 and 3 µm were measured for 4 min, and particles with diameter 5.94 µm were measured for 6 min. Tracking was performed using Trackpy [141].

Fitting colloid-wall separations. In the Brownian (inactive) state, *i.e.*, in water without H_2O_2, the translational diffusion coefficient, D, of each TPM/Pt colloid was extracted by fitting individual MSD curves with $\Delta r^2 = 4D\Delta t$, where Δt is the lag-time. MSD calculation was performed using existing routines within Trackpy [141]. We typically fitted lag-times shorter than 2 s, for which we verified that the MSD data grew linearly in time; the power-law fit that we performed consistently yielded exponents of order 1 within these lag-times. For each distribution of D values, we extracted the median value and first quartiles. The reason for taking the median is to account for the asymmetry in the obtained distributions, primarily due to the presence of the wall; see Figure 3.7A for an example of the distribution of D values from 40 individual TPM/Pt colloids in water (colloid diameter 2.23 ± 0.11 μm). These measures gave the most satisfactory results in general in comparison with theory, see Figure 3.2A, to which we come back in Appendix I. We further checked in these control measurements that in-plane diffusion was random by additionally examining the MSDs in x and y directions separately. Extracting the corresponding diffusion coefficients revealed that these quantitatively agreed (values differ by less than 10%), confirming their random motion. We performed control experiments for colloids with different zeta potentials. As the zeta potential of the parent colloid ζ_b became more positive, the particles became irreversibly stuck on the glass wall, as expected. However, that
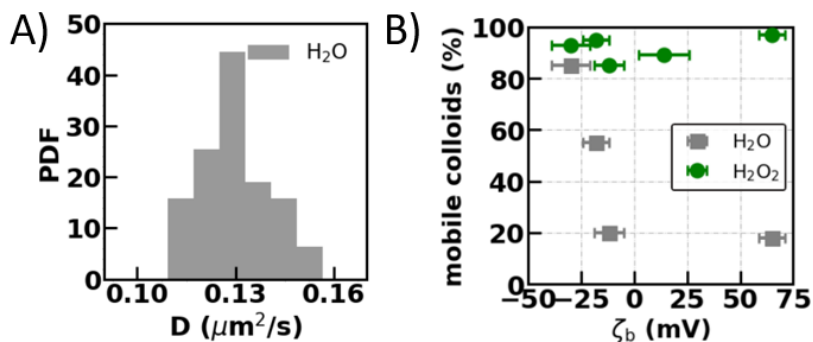

Figure 3.7: A) Distribution of translational diffusion coefficients D from 40 colloids (batch diameter 2.23 ± 0.11 μm) in the passive state in water. B) Fraction of mobile particles observed for colloids with a wide range of base zeta potentials ζ_b in the passive (H_2O, squares) and active (H_2O_2, circles) state at pH 3.3.

was not the case for the same particles in the active state. Figure 3.7B shows the fractions of mobile particles in the corresponding samples. For the experiments with positively charged parent colloids in their passive states, we still find a small percentage of mobile colloids. This is possibly due to the negatively charged Pt cap at pH 3.3.

In the active state, *i.e.*, in the H_2O_2 solution, D as well as the swim speed V were extracted from individual MSD curves using Eq. (2.3), the applicability of which we have already discussed in chapter 2. Returning to the fit expression given by Eq. (2.3), we are justified in using $D_{R,bulk}$ to evaluate τ_R, even close to a wall, since in-plane rotational motion is far less affected by the presence of a wall than out-of plane rotation, see Figs. 7 and 8 of Ref. [171]. Generally, rotation is influenced far less than translation, due to the more rapid decay of the associated hydrodynamic mode [128, 171]. In addition, Eq. (2.3) does not directly depend on τ_R. For each MSD curve, we performed a two parameter fit for D and V simultaneously. Figure 3.8A shows that if the passive component is omitted from the fit, the data is not fitted accurately with $V^2 \Delta t^2$ alone (dashed line). However, the fit that does include the passive diffusion contribution $4D\Delta t$ follows the data perfectly (solid line). For the ≈ 2.7 μm diameter particles, MSDs were fitted up to lag-times of 0.4 s, as in chapter 2. For the 1.75 μm, 2.0 μm, 2.23 μm, and 5.94 μm diameter particles, MSDs were fitted up to lag-times of 0.22 s, 0.3 s, 0.35 s, and 0.6 s, respectively. The asymmetric nature of the V [155] and D distributions let us to extract and report median values in the Results and Discussion section. Asymmetry is expected when there are long-range, out-of-equilibrium interactions that couple to the wall. The wall distorts the flows and molecular gradients surrounding the swimmer, leading to an asymmetry in coupling between approaching and moving away from the wall, *i.e.*, this leads to an effective potential. Thus, asymmetry is an intrinsic property of our system, not a statistical one. Due to the skewed nature of the PDF, median values more accurately represent the average swim speed than means would. Figure 3.8B shows an example of such a distribution of D values obtained in the active state. Next, for each of our median values for D, we computed the reduced diffusion coefficient D/D_{bulk} using the bulk diffusion coefficient using $D_{bulk} = \frac{k_B T}{6\pi\eta R}$. This ratio, as we detail in the following section, corresponds to an established ratio of gap height h over particle radius R. We used the fitted value for D/D_{bulk} to extract the corre-
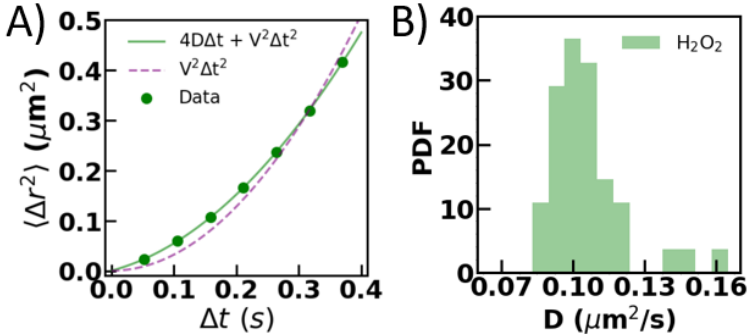
Figure 3.8: A) MSD curve for an individual colloid in the active state (data shown in green circles) fitted with $\Delta r^2 = 4D\Delta t + V^2\Delta t^2$ (green solid line) and $\Delta r^2 = V^2\Delta t^2$ (purple dashed line). B) Distribution of D coefficients from 40 colloids in the active state in H_2O_2 (colloid batch same as in Figure 3.7A), showing that the values are not normally distributed.

sponding h/R and associated first quartiles, see the following section for a discussion of the fitting. Lastly, we employed holographic microscopy to verify the accuracy of our approach. We measured the height distribution of Brownian 1 μm silica spheres with well-known refractive index in water [168] and found good agreement with the heights extracted following the here described diffusion-coefficient based method, as we detail in chapter 5, see also Figure 5.3 for a comparison to our prediction.

Height dependence of the diffusion coefficient. The Brownian motion of spherical particles immersed in a fluid near a plane wall has drawn the attention of the experimental community as a means to determine the gap height h between the particle and wall [129, 130]. This means of determining h relies on the hydrodynamic mobility, *i.e.*, the coupling between an applied force on the sphere and its observed speed, being substantially reduced by the presence of a wall [128]. Here, we briefly cover expressions found in the literature to approximate this reduction and how we combined these to fit for the height in our work. We will also indicate why activity and to a large extent wall wetting properties can be ignored.

The most commonly used expression for the effect of hydrodynamics on the mobility, or equivalently the gap-height-dependent diffusion $D(h)$ of a spherical particle above a *no-slip* wall ($\boldsymbol{u} = \boldsymbol{0}$ at the wall, with $\boldsymbol{u}$ the

fluid velocity) was derived by Faxén [163, 164] and reads

$$\frac{D(h)}{D_{bulk}} = 1 - \frac{9}{16}\gamma + \frac{1}{8}\gamma^3 - \frac{45}{256}\gamma^4 - \frac{1}{16}\gamma^5, \tag{3.1}$$

where $\gamma = R/(h + R)$ and the quadratic term drops out on the ground of symmetry. This expression was obtained using the method of reflections — applicable to the low-Reynolds-number regime that holds for our experiment, in which viscous dissipation dominates inertia. The limited number of reflections used in Faxén's derivation implies that expression (3.1) holds only for sphere-wall separations $h \gtrsim R$, see Figure 3.9A. For very small sphere-wall separations $h/R \ll 1$, results from lubrication theory apply as derived by Goldman, Cox, and Brenner [128]:

$$\frac{D(h)}{D_{bulk}} = -\frac{1}{\frac{8}{15}\log\left(\frac{h}{R}\right) - 0.9588}, \tag{3.2}$$

where the factor 0.9588 is a gauge that was applied to match the numerical data by O'Neill [165] in the near-field regime. Figure 3.9A shows the lubrication prediction and the O'Neill data. For completeness, we present additional numerical data obtained in the 1990s by Kezirian [123], which span the entire range, in the same figure. The $D(h)/D_{bulk}$ ratios obtained from our MSDs ($D(h)/D_{bulk} \approx 0.5$), mostly fell in the region between the respective ranges of applicability of the Faxén and lubrication expressions. From the comparison to the numerical data [123, 165] in Figure 3.9A, we notice that for $D(h)/D_{bulk} \lesssim 0.4$ Faxén's expression should not be trusted and the same holds for the lubrication expression for $D(h)/D_{bulk} \gtrsim 0.6$. In the overlapping range $0.4 \lesssim D(h)/D_{bulk} \lesssim 0.6$, both expressions give a 'reasonable' approximation of the ratio $D(h)/D_{bulk}$, *i.e.*, an accuracy of about 20% when establishing h is to be expected, with the former overestimating and the latter underestimating h. Analytic expressions that cover the range of interest to us do not exist, and for practical purposes it is cumbersome to perform the necessary numerical calculations for each obtained data point [123, 165]. We therefore complemented these expressions by a third-order interpolation to the log-log variant of the combined numerical data by O'Neill [165] and Kezirian [123]. This approach led to the black dashed curve shown in Figure 3.9A which can
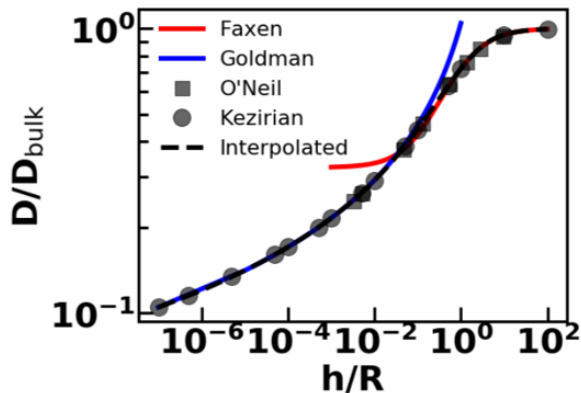
Figure 3.9: The change in the effective translational diffusion coefficient D — in terms of the bulk diffusion coefficient D_{bulk} — for a sphere with radius R as a function of the gap height h between the wall and the sphere surface. Log-log representation of various literature predictions and our own interpolated curve (dashed black) for a no-slip wall. The solid red curve corresponds to Faxén's prediction in Eq. (3.1) [163], the solid blue curve to the Goldmann, Cox, and Brenner result of Eq. (3.2) [128], the grey squares to the numerical results by O'Neill [165], while the grey circles to the numerical results of Kezirian [123].

generally be used to improve other experimental measurements of the height using our diffusion-based analysis approach. While our measured ratios fall inside the near-field regime of hydrodynamic interaction, where we need to resort to numerical results, this region fortuitously has significant sensitivity to variation in gap height, see Figure 3.9A. Thus, we were able to obtain accurate height measurements.

Appendix I: Balance between electrostatics and gravity in the passive system

Here, we introduce the Poisson-Boltzmann-based expressions and underlying assumptions for the salt-dependence of the height for a passive particle, which was used to determine the theory curves in Figure 3.2A. The solid and dotted orange curves in Figure 3.2A show the theoretical predictions that result from balancing electrostatics and gravity between colloids and wall in water. We make use of Poisson-Boltzmann expressions for the electrostatic repulsion rather than their linearized versions (Debye-Hückel). This is because the values of the zeta potentials of either surface are the least well-known quantities in our system. We consequently varied the zeta potentials over a reasonable range to estimate their effect, wherein we departed from the linear regime. Following, amongst others, Flicker and Bike [166] and Rashidi and Width [167] we arrive at the following force balance

$$\frac{4}{3}\pi \left(\rho_p - \rho_f\right) g R^3 = \kappa B \exp\left(-\kappa h\right). \tag{3.3}$$

where the left-hand side represents the buoyant force, with the fluid mass density $\rho_f = 0.99 \ 10^3$ kg m^{-3}, the TPM particle mass density $\rho_p = 1.314 \ 10^3$ kg m^{-3} [108], the local gravitational acceleration $g = 9.81$ m s^{-2}, and the particle radius $R = 1.4$ µm. The right-hand side of Eq. (3.3) represents electrostatic repulsion [1] with

$$\kappa = \sqrt{\frac{2e^2 C_{salt}}{\epsilon_0 \epsilon_f k_B T}}, \tag{3.4}$$

$$B = 64\pi\epsilon_0\epsilon_f R \left(\frac{k_B T}{e}\right)^2 \tanh\left(\frac{e\zeta_{wall}}{k_B T}\right) \tanh\left(\frac{e\zeta_{part}}{k_B T}\right). \tag{3.5}$$

Equation (3.4) provides the inverse Debye screening length κ with e the elementary charge, $C_{salt} = C_{pH} + c_{NaCl}$ the salt concentration, which can be decomposed into a base conductivity contribution $C_{pH} = 3.16$ µM, the ion concentration calculated from the pH of the solution through $C_{pH} =$

---

[1]N.B. Flicker and Bike appear to use Gaussian units, as their B expression is missing a factor 4π with respect to Eq. (3.5).

$10^{(-pH)}$ for pH 5.5, and the amount of added sodium chloride c_{NaCl}, ϵ_0 the vacuum permittivity, $\epsilon_f = 80$ the relative dielectric constant of the fluid, k_B the Boltzmann constant, and $T = 300$ K the temperature. Equation (3.5) provides the electrostatic charge parameter, with ζ_{wall} and ζ_{part} the estimated zeta potential of the wall and particle, respectively. We took $\zeta_{wall} = \zeta_{part} = -50$ mV to compute the central solid line and $\zeta_{wall} = \zeta_{part} = -25$ mV and -75 mV for the lower and upper dashed lines in Figure 3.2A, respectively. By making these choices, there are no free parameters left and the equilibrium height may be extracted as a function of c_{NaCl}. Note that, given these reasonable zeta potential choices, the fit is excellent and appears to be mostly insensitive to the exact value of the zeta potential and more sensitive to the salt concentration. Examining the properties of the equation system further revealed that it is most sensitive to $(\rho_p - \rho_f)$; the fit may thus be improved by relaxing the constraint on ρ_p, though for this we are constrained by the literature [108].

Appendix II: Ionic diffusio-osmosis along the wall, rather than the swimmer

Here, we provide additional arguments in favor of ionic diffusiooosmosis along a wall. There are various self-propulsion mechanisms that have been considered for Pt-coated Janus swimmers in H_2O_2, *e.g.*, see Ref. [74] for a brief overview. Most of the theory concerning mechanisms has focused on self-propulsion in bulk, ignoring the wall due to the symmetry break that it introduces, which hinders solving the associated Stokes-Poisson-Nernst-Planck equations in an analytic manner. There are, however, a large number of (numerical) studies of this more complicated geometry [95–97, 99–101, 158], but their focus is more often on the richness of behavior that simple models for self-propulsion can produce, by accounting for this symmetry break, rather than the propulsion mechanism. Turning to the experimental result, we observe that the lack of observed speed change when varying ζ_b in Figure 3.4B provides a potential clue that ionic effects are not dominating the dynamics of the swimmer itself. This is because both electrophoresis and ionic diffusiophoresis typically have linear proportionality in the zeta potential of the surface; the latter potentially even possessing a quadratic dependence on ζ_b [63]. In elec-

trophoresis, propulsion is a result of ions moving in a (self-induced) electric field coupling to a surface potential (or charge). Ionic diffusiophoresis is conceptually similar, but in this case the electric field is locally generated when there is a salt gradient in response to a difference in ion diffusion rates. Ionic diffusiophoresis can be the result of a Pt-based reaction that splits a neutral molecule into two charged species, *e.g.*, $H_2O_2 \rightarrow HO_2^-$ + H^+. Brown and co-authors have on separate occasions argued against neutral self-diffusiophoresis and ionic diffusiophoresis as viable candidates for self-propulsion *in bulk* [74, 75]. For both mechanisms, the numbers do not seem to be commensurate with the experimentally observed propulsion velocities. These calculations together with our observed lack of ζ_b-dependence of the swim speed leads us to conclude that other mechanisms may need to be considered to understand the motion of Pt-coated colloids. In modeling catalytic swimmers, the above observation could necessitate a return to a regular diffusiophoretic variant of H_2O_2 self-propulsion *in bulk* or a variation on the recently pitched 'rocket propulsion' [172] (presently it does not possess appropriate scaling with radius to describe our experiment) or even an, as of yet, unknown mechanism.

Nonetheless, there are clues that ions are important. Our experiments in which we vary the salt concentration showed a marked decrease of the observed swim velocity as a function of c_{NaCl}, in line with previous observations in the literature [75, 76]. We have shown in Figure 3.3 that our data is fitted well using the expression

$$V = A + \frac{B}{C + c_{\text{NaCl}}}, \tag{3.6}$$

where V is the observed swim speed, and A, B, and C are fit constants, representing the remaining speed in the limit of high salt A, a concentration-to-speed conversion factor B, and the ion concentration already present in the medium C. Of the interfacial transport mechanisms described by Anderson [63], only the one based on ionic diffusion scales with $\kappa^{-2} \propto (C + c_{NaCl})^{-1}$. In addition, from our fit procedure we obtain the reasonable numbers 0.35 ± 0.09 μm/s, 0.05 μm mM/s, and 0.09 ± 0.07 mM, for A, B and C, respectively. In view of the above discussion, we thus interpret the fit in Eq. (3.6) as representing a term that governs bulk and non-ionic wall effects on

self-propulsion (A) and a term that describes an ionic diffusioosmosis along the wall (a combination of B and C). The latter generates a fluid flow along the wall, which acts on the swimmer and opposes its self-propulsion. The presence of a diffusioosmotic contribution implies that the reactions on the Pt surface must generate a salt gradient [74], *i.e.*, there must be a gradient of oppositely charged ionic species that differ in their electrophoretic mobility, though the exact nature of the involved ions remains speculative. This leads to an alternative interpretation of the swimming direction reversals through the addition of the ionic surfactant cetyltrimethylammonium bromide (CTAB) observed by Brown and Poon [75]. CTAB is known to affect the zeta potential and contact angle of surfaces. However, we have shown that changing ζ_b does not strongly impact the observed swim speed. We therefore argue in favor of a wall effect. That is, the reversal observed in Ref. [75] may be generated at the wall, through the adsorption of CTAB which impacts the induced osmotic flow. If there is indeed a sizeable effect of the wall, this sets a limit to the amount of bulk recombination of ionic species generated by the surface reactions [74] that can occur. That is, if ions are created at the surface of the swimmer, then they should not recombine before interacting with the wall. However, the recombination length was estimated to be 70 nm under typical experimental conditions [74], as is the case here; a length that is much smaller than the gap height. In addition, there is experimental evidence [173] that swimmers that move using ionic diffusion experience a limited near-wall effect on propulsion speed, though systematic variation of the wall zeta potential was not attempted in these systems. This speaks in favor of a relatively small recombination length, although the AgCl system in Ref. [173] is notably different from the H_2O_2-fueled swimmers employed by us.

The H_2O_2 gradient itself is, however, sufficiently long-ranged to bridge the gap between the swimmer and the wall. In addition, through dissociation reactions taking place in the bulk, involved in the association-dissociation equilibrium of $H_2O_2 \rightleftharpoons H^+ + HO_2^-$ [74], this H_2O_2 gradient leads to ionic gradients along the surface of the wall. This in turn can induce an ionic diffusioosmosis along the wall. However, it should be noted that generally the above reactions favor the associated state. Any ionic contribution resulting from dissociation is therefore weak compared to situations where H_2O_2 is forced to dissociate into its charged

constituents, which could take place on the Pt cap, as argued by Brown *et al.* [74]. These authors therefore disregarded dissociation of H_2O_2 as a viable self-propulsion mechanism for colloidal swimmers, since the associated gradients and consequently the speed are limited by the size of the swimmer. However, the gradient along the wall has a much larger surface to act over, which could lead to a more substantial contribution, even if the effect contributes little to self-propulsion itself. Lastly, while on the topic of speeds, we should comment on the inverse scaling of speed with size found for our swimmers, as previously reported by Ebbens *et al.* [58]. These authors made their observations away from walls, in the middle of the cuvettes they use. Therefore, the observed speed change in our system, when making an analogous change in radius, can most likely be attributed to the way the propulsion *in bulk* is influenced by the size of the swimmer, rather than due to an interaction with the wall. That is to say, the trend in the speed is not strongly influenced by aspects of the gap between the swimmer and wall, such as the local curvature. This speaks in favor of wall-based speed modification on scales larger than the gap height, *e.g.*, one governed by the gradient in H_2O_2. Note that it is unclear if the absolute value is modified with respect to the bulk speed based on our experimental data. Bulk measurements would be a next logical step in determining the full extent of the impact of the wall, possibly following the approach outlined in Ref. [173]. If a H_2O_2-gradient based ionic diffusioosmosis along the wall can be shown in this manner, more insight into the reaction specifics taking place at the Pt cap and the manner of self-propulsion may be gained.

Appendix III: Activity-induced ypsotaxis

Our experiments showed that TPM/Pt swimmers moving along a wall tend toward a constant height, a property that we refer to as ypsotaxis. This coincides with the speed of the swimmer plateauing when varying the H_2O_2 concentration, see Figure 3.6, strongly indicating that ypsotaxis is activity driven. At the same time, the chemical swimmers show a tendency to align their propulsion parallel to the wall [59, 81]. Das *et al.* [59] introduced a simple model for describing this orientational quenching, which we will now comment upon in relation to our work. Das *et al.* considered the contribution of several effects to orientational

quenching, including hydrodynamic interactions and electro- and diffusio-phoretic coupling. Estimating the relative contribution of each term, they concluded that a hydrodynamic coupling between swimmer and wall best explained their experimental observation, when the swimmer is propelled by a self-electrophoretic mechanism. However, combining our present results with our previous result on the effect of the contact angle of the nearby wall [155], we have shown that: (i) Phoretic flows along the wall can substantially influence the swimmer's dynamics. (ii) These flows are likely due to ionic diffusiophoresis. (iii) The mechanism of self-propulsion is probably not entirely commensurate with self-electrophoresis.

We found that h is roughly constant for the various sizes that we considered. This, however, does not mean that we expect this result to hold indefinitely. Very small swimmers have a tendency to reorient substantially and could (and have been observed) to move away from the wall more readily. Yet, surprisingly, a constant height approximation seems to capture the data well over the range of swimmer sizes for which we could conduct experiments. Over this range, the buoyant force changes by a factor of nearly 40, as the buoyant mass scales with R^3, not even factoring the weight of the larger (dense) Pt cap. It therefore seems unlikely that ypsotaxis is a result of a balance between gravity and an activity-related effect. Calculations on self-diffusiophoretic [58] and self-electrophoretic [74] swimming both predict a different scaling of swim speed with size that is not R^3, casting further doubt on such a balance. The subdominance of buoyancy was further underpinned by experiments showing that the self-propelled particles can, for a time, move along the top surface of an inverted sample cell. Here, gravitational contributions are pointing in the opposite direction with respect to the surface normal, yet the phoretic/osmotic contributions maintain their orientation with respect to the surface. Nonetheless, we should point out that previous experiments support a greater separation between less dense swimmers and the wall [61, 75]. That is, their swimmers have $D \approx D_{bulk}$, while our TPM swimmers (a substantially denser material) attain $D \approx 0.5D_{bulk}$, which speaks for a limited gravitational effect, but clearly not a dominant one. Das *et al.* argued that their orientational quenching was a consequence of the activity only. Based on our Figure 3.6 we can extend this conclusion

to ypsotaxis and we can even go further and suggest a common origin. It is, at present, unclear how activity would lead to a constant self-propulsion height with the observed variation of self-propulsion speed, as we have undercut the self-electrophoretic argument by Das *et al.* for this mechanism. We leave the exact way in which this happens open to future investigation, as without further experimental evidence in favor of a specific self-propulsion mechanism there remain too many free parameters to solve the problem. Nonetheless, our experimental evidence in favor of a constant height is strong and should serve to bound future modeling.

4

Activity-Induced Interactions Along One-Dimensional Paths

Abstract

Cooperation in biological microswimmers is crucial for their survival as it facilitates adhesion to surfaces, formation of hierarchical colonies, efficient motion, and enhanced access to nutrients. Synthetic microswimmers however currently lack truly cooperative behavior that originates from activity-induced interactions. Here, we demonstrate that catalytic microswimmers show a variety of cooperative behaviors along one-dimensional paths. We show that their speed increases with the number of swimmers, while the activity induces a preferred distance between swimmers. Using a minimal model, we ascribe this behavior to an effective activity-induced potential that stems from a competition between chemical and hydrodynamic coupling. These interactions further induce active self-assembly into trains as well as compact chains that can elongate, break-up, become immobilized and remobilized. We identify the crucial role that environment morphology and swimmer directionality play on these highly dynamic chain behaviors. These activity-induced interactions open the door towards exploiting cooperation for increasing the efficiency of, as well as provide temporal and spatial control over, microswimmer motion, thereby enabling them to perform intricate tasks inside complex environments.

Introduction

Many microorganisms crucially rely on cooperation for their survival and thriving. Cooperation greatly enhances microorganism motility and overall motion efficiency [18] and often leads to the formation of organized, complex colonies. For example, spermatozoa self-assemble into train-like structures to enhance fertilization [174], *Volvox* algae form colonies to propel and facilitate fluid flows with nutrients and chemical messengers [175] and cancer cells secrete chemicals to communicate and promote tumour growth [176]. Similarly, bacteria cooperate to enhance surface adhesion [177] during biofilm formation which increases their resistance to environmental stresses and drugs, their spreading, and the efficiency of nutrient capture [177–179]. At high densities, bacterial colonies again rely on cooperation to form swarms with large-scale dynamic patterns, such as whirls and jets, to expand and to explore their surroundings while simultaneously reducing their competition for nutrients [180, 181]. These vital behaviors are achieved by exploiting interactions based on hydrodynamic and steric effects [182] as well as chemical signaling, called quorum-sensing [183].

Similar to their biological counterparts, synthetic swimmers are also capable of performing directed motion inside liquid environments [184], even under realistic conditions such as inside patterned [33, 59–61, 114, 185–190] and biological environments [161, 191, 192]. Consequently, they offer exciting opportunities as they open new routes for precise motion control and, hence, a wide range of applications on the microscale [184]. In the future, these swimmers may be deployed to perform complicated tasks such as *in vivo* drug delivery and repair [193, 194] inside complex and crowded environments [48, 106], e.g. in living organisms and lab-on-a-chip devices [195, 196].

Drawing inspiration from biological systems and their efficiency-increasing strategies, it is desirable that the aforementioned tasks are performed not only on the single but on the multi-swimmer level [43, 45]. For instance, if employed in drug delivery, collections of swimmers may reach the desired target faster or deliver a higher dosage [197]. Cooperative behavior and communication between the microswimmers could furthermore enable different types of delivery in which, for example, dosages are applied at specific times or time intervals [13].

Although *collective* effects, such as enhanced aggregation, cluster and crystal formation, ordering and phase separation, have been observed for synthetic systems in 2- and 3-dimensions [25, 44, 198, 199], these effects can in principle be explained by volume exclusion and persistent motion of the swimmer [18, 198, 199] and thus do not require *cooperation*; with the latter typically relying on information exchange to enhance the efficiency of their behavior. Even the exciting recently observed corralling of passive particles by swarms of light-driven synthetic swimmers was explained purely by geometric arguments [200], and the formation of self-spinning microgears [201] and active colloidal molecules [202] required external fields for their assembly and/or propulsion. While cooperation is a type of collective effect, the inverse is not true. That is, the collective behavior and motion of synthetic microswimmers at higher densities does not necessarily signify that they collaborate and cooperate in the same sense as biological swimmers, which employ signaling and sensing, do.

In this chapter, we demonstrate that catalytic model microswimmers exhibit a wealth of activity-induced interactions along closed 1-dimensional paths. Single swimmers move at stable speeds independent of path curvature. We furthermore find that multiple swimmers along the same path exhibit cooperation. That is, their speed increases with the number of swimmers while their activity induces a preferred distance between them. We show that swimmer cooperation originates from a combination of steric effects and hydrodynamic and chemical couplings. Lastly, we demonstrate rich locomotion behavior induced by chain fission and fusion, which has only been considered theoretically in the context of magnetic swimmers [203]. We reveal that chain formation and breakup can be tuned using the local curvature of the path.

Results and Discussion

To study their dynamic behavior and interactions, we confine catalytic swimmers to 1-dimensional tracks by exploiting their strong affinity for surfaces [59–61, 155, 157]. This affinity stems from their propulsion mechanism, which is based on an asymmetric catalytic decomposition of H_2O_2 on their Pt-coated hemisphere [42]. We equip planar substrates with

designed 3D micro-printed posts, thereby effectively creating preferred 1-dimensional environments around the posts, where the swimmers can be in close vicinity to both posts and substrates [59–61]. See Figure 4.1 for an example of our experimental setups featuring circular posts. The H_2O_2 decomposition reaction here creates gradients in solute molecules which act over the swimmer surfaces, posts and substrate, inducing phoretic and osmotic flows thereby causing swimmer capture [155, 157]. That is, when a swimmer encounters a post, it quickly gets captured into motion along it and is retained there for long times.

Once attached to a circular post, our swimmers with diameters of (2.00 ± 0.05) µm and Pt coating thicknesses of (4.7 ± 0.2) nm moved with equal probability in either the clockwise or counterclockwise direction, without switching direction. Single swimmers as well as multiple swimmers with the same direction of motion on a given post, orbited their posts with approximately constant speed. We highlighted these swimmers by coloring their corresponding posts

Figure 4.1: **Catalytic microswimmers in patterned environments.** Light microscopy image showing catalytic swimmers in one of our experimental setups featuring circular 3D micro-printed posts on planar substrates. Coloring is used to distinguish the stationary posts from the swimmers, and indicates whether the attached swimmers were mobile (red) or immobile (blue posts). Scale bar is 20 µm.

in red in Figure 4.1. These swimmers continued their orbiting motion for at least 30 min in our experiments, during which we did not see them leave. However, swimmers that moved in opposing directions on a given post hindered each others motion and were immobilized. We indicated
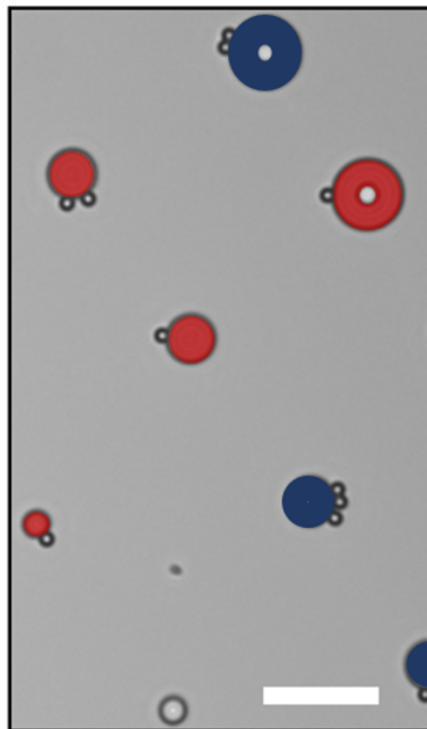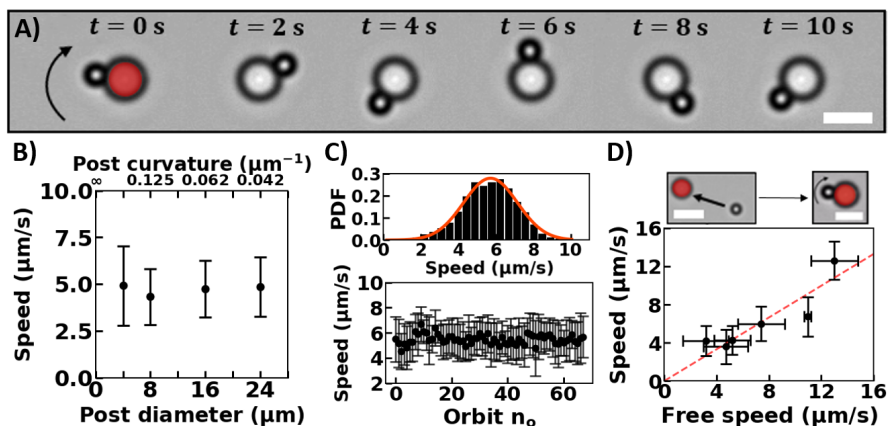
Figure 4.2: **Catalytic microswimmer motion along circular posts: single particle orbiting. A)** Time series of light microscopy images of a (2.00 ± 0.05) µm diameter swimmer orbiting a 4 µm diameter post, with the arrow denoting its constant direction of motion. Scale bar is 5 µm. **B)** Propulsion speed along the post as a function of post diameter. All data were taken at otherwise fixed experimental conditions. **C)** Bottom: propulsion speed as a function of number of orbits of the particle shown in (A). Measurement duration was 4 min. Top: same data plotted as a probability density, showing that speed in orbit follows a Gaussian distribution. **D)** Propulsion speed for the same swimmers before orbiting, i.e. "Free speed" along the planar substrate, plotted against the speed in orbit. The dashed line is a least-squares fit with $y = ax$ and $a = 0.83 \pm 0.08$, in agreement with Ref. [114].

these immobilized clusters by coloring their adjacent posts blue in Figure 4.1.

Surprisingly, long-term capture around posts happens even when post size is comparable to the swimmer size, see *e.g.* Figure 4.2A for a swimmer orbiting a 4 µm diameter post. This is in stark contrast with simulations on model squirmers [159, 204], which are often used to approximate synthetic swimmers such as ours. For model squirmers, capture has only been proposed for posts of sizes several times larger than the squirmer [204]. Moreover, simulations for the orbiting of a squirmer around a sphere predict a relation between curvature and squirmer speed, as can be readily obtained from the data in Ref. [159].

To test these predictions, we track the swimmers in time and extract their speed in orbit using python routines [141]. We find that post curvature does not influence the propulsion speeds of our catalytic swimmers, at least not for the range studied here (Figure 4.2B). These discrepancies between our experiments and simulations imply that catalytic swimmers are different from pure squirmers, probably due to their propulsion mechanism and to the long-range solute gradients that act across substrate and posts [155, 157].

Despite orbiting short tracks, we find that propulsion speed in orbit is rather stable in Figure 4.2C, which shows that speed in orbit follows a Gaussian distribution. Note that the presence of the post itself does not have a considerable effect on propulsion speed: the speed of a swimmer in orbit is only slightly reduced with respect to its "free" speed parallel to the substrate alone in Figure 4.2D. The dashed line is a least-squares fit with $y = ax$ where a is (0.83 ± 0.08), in line with the slope obtained previously for bimetallic microrods [114]. These findings point out that any hydrodynamic and/or phoretic coupling to the post leads to a sub-dominant contribution to the speed.

Intriguing effects take place when multiple swimmers orbit the same post: the swimmers move with seemingly equal speeds while also maintaining roughly constant distances, see Figure 4.3. This constancy in speed and distance appears both for two (Figure 4.3A, B) and three comoving swimmers (Figure 4.3C) and is independent of the post curvature (Figure 4.3D). More quantitatively, we find that swimmers that orbit the same post in fact have almost the same speed distribution, independent of the particle number and post size, see Figure 4.4A for the distributions of three swimmers on a 4 μm post and Appendix I for additional data.

Even more strikingly, speed increases with the number of swimmers in orbit, as shown in Figure 4.4B for posts with 4 and 8 μm diameters. That is, two particles orbit faster than one and, in turn, three particles orbit faster than two: under otherwise fixed conditions, speed increases by $\approx 20\%$ and 60% for two and three comoving swimmers on 4 μm posts, respectively, and by $\approx 40\%$ for two comoving swimmers on the 8 μm post, in comparison to single swimmers. Interestingly, for our system there is no significant speedup of a pair of particles with respect to a separated third particle moving along the post. This contrasts strongly with the result of
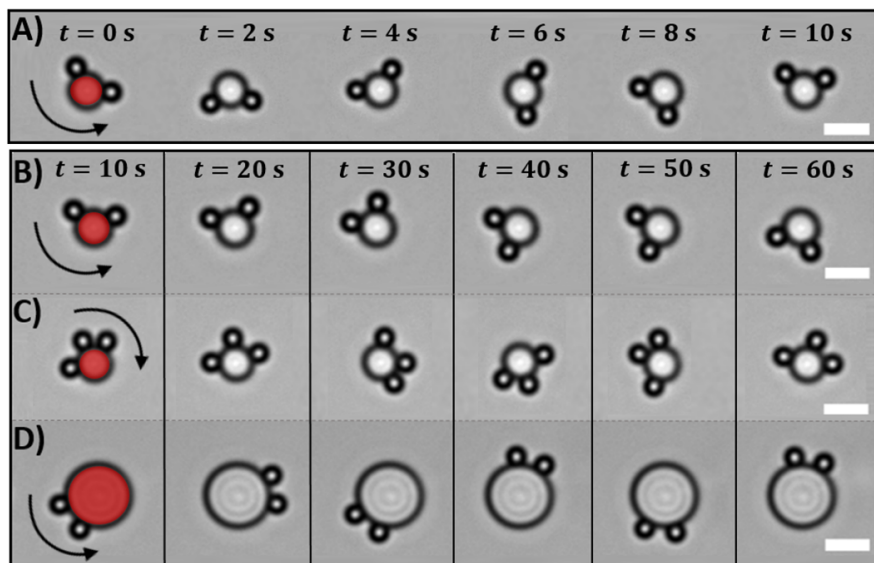
Figure 4.3: **Multiple microswimmers orbiting circular posts.** Red color has been added to distinguish the stationary posts from the orbiting swimmers. Scale bars are 5 µm. Sequence of light microscopy images showing orbiting of **A, B)** two and **C)** three swimmers around a 4 µm diameter post, and **D)** two swimmers around an 8 µm diameter post. Each column in panels (B)-(D) shares the same timestamp, indicated in (B).

passive, driven particles in a toroidal optical trap [205–207], where pair formation and breaking is observed. That is, two driven particles overtake a third, which then leads to a fracture of the triplet with the two lead particles moving off, a result that can be understood using hydrodynamic theory [205–207].

Our findings thus strongly suggest *cooperative motion* of the swimmers. Chemical gradients of swimmers in close proximity interact, thereby causing multi-bound states and a collective speedup. This speedup is independent of the post size for the here considered 4 and 8 µm posts, see Figure 4.4B. The dashed line represents a least squares fit with $y = \alpha x + b$, with α (1.6 ± 0.2) µm/s and b (2.9 ± 0.4) µm/s, implying a linear relationship between the number of swimmers and the collective speedup. This observation of a speedup as well as the seemingly constant swimmer distance in Figure 4.3, is surprising in view of the
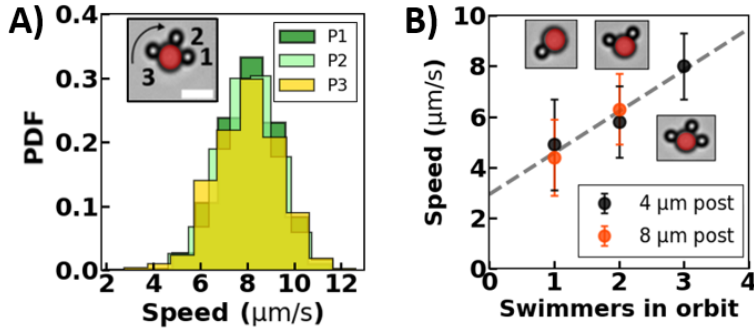
Figure 4.4: **Speed of comoving swimmers.** **A)** The PDFs of propulsion speed in orbit for three swimmers on the same post are almost identical. **B)** Average propulsion speed as a function of the number of swimmers in orbit for two post sizes, showing that speed increases with the number of comoving swimmers for both post sizes in a similar fashion. All measurements were taken under the same experimental conditions. The dashed line is a least squares fit with $y = \alpha x + b$, with α and b being (1.6 ± 0.2) µm/s and (2.9 ± 0.4) µm/s, respectively.

distribution in speed that single swimmers exhibit and implies that swimmers experience a coupling that adjusts their speed. To understand the origin of this behavior, we will now quantify swimmer distances and test for correlations of the speeds of pairs of comoving swimmers.

We quantify the arc distance, ℓ, between comoving swimmers as depicted in Figure 4.5A. We measure the distances between various swimmer pairs, on differently sized posts and with different number of attached swimmers, see the inset of Figure 4.5B. In all cases, we find that swimmers orbit the posts at a preferred distance (Figure 4.5B), in line with our expectations based on Figure 4.3. Specifically, the average distance measured over a 4 min time interval is (5.3 ± 1.4) µm and (4.2 ± 0.5) µm for two swimmers on a 4 and 8 µm post, respectively, and (3.8 ± 0.3) µm and (4.3 ± 0.4) µm between the front-middle and middle-back swimmers of a three-swimmer system on a 4 µm post, respectively. We notice that swimmers never approach closer than a minimum distance of (3.0 ± 0.1) µm. In addition, the arc distances show similar distributions, albeit with different peak values and widths.

These common features raise the question whether the constancy in the distance stems from correlations between the speeds of the comoving
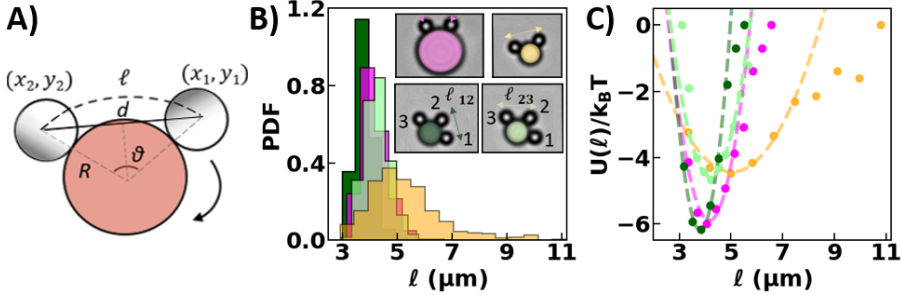
Figure 4.5: **Interactions of comoving swimmers: experiment. A)** Representation of the arc distance. **B)** PDF of the arc distance between comoving swimmers, showing that swimmers assume a relatively constant distance in orbit with minimum center-to-center distance ≈ 3 μm. Measurement duration is ≈ 4 min. The inset shows snapshots of swimmer pairs in orbit, color-coded so that each color marks the corresponding swimmer pair in panels (B, C). **C)** Potential energy in terms of thermal energy, as obtained from the swimmer distances in (B) using the Boltzmann distribution. The dashed lines represent least-squares fits with $y = \frac{1}{2}k(x - x_0)^2 + y_0$. All fitted parameters are listed in Appendix I.

swimmers. However, a closer examination reveals that speeds always vary independently of one another, see the scatter plot of the speeds of two comoving swimmers along an 8 μm post, $V_1(t)$ vs $V_2(t)$, where t is time in Figure 4.6 and Appendix I. Already, the symmetric shape of the plot indicates that they are not correlated, which is further supported by a Pearson correlation coefficient of 0.2. In addition, we excluded time-delayed correlations by considering the correlation between $V_1(t)$ and $V_2(t+\tau)$, see Appendix I, with τ the time between two frames. Again, the Pearson correlation coefficient was 0.1, signifying no speed correlation. Hence, there must be an alternative mechanism that can explain why the swimmers move with the same average speed and stable distance.

The random fluctuations around an average distance is reminiscent of the thermal motion of a passive particle inside a potential well. Here, this effective potential must be induced by the active state of *both* swimmers. A single active particle is not sufficient, because passive particles in the vicinity of an active particle do not get confined but are instead either dragged along the fluid flow around the active particle [112] or attracted to the active particle site [25].

Seeing that our swimmers are moving together at the same average speed, we consider their activity-confined motion in the rotating frame that comoves with the swimmers. While this is a non-inertial frame of reference and an out-of-equilibrium state, it still allows us to view our system from a simplified perspective: that of random thermal motion of each particle in a potential induced by the other. To do so, we use the Boltzmann distribution, $\text{PDF}(\ell) = \exp\left(-U(\ell)/k_B T\right)$ to extract the relative potential energy for our systems from the probability density function of their corresponding distances. This allows us to measure the probability for the system to be in a certain distance relative to the distance's energy and system

Figure 4.6: **Checking for correlation between speeds of comoving swimmers.** Scatter plot of the speeds of two swimmers comoving along a 8 μm post, see magenta-colored post in Figure 4.5B, showing that swimmer speeds are not correlated.

temperature in Figure 4.5C, where the relative energy is $U(\ell)/k_B T = -\log(\text{PDF}(\ell)) + U/k_B T$, with $U/k_B T$ an arbitrary reference state, set such that the relative energy goes to 0 at infinite distances.

The shape of the resulting effective potentials close to the minimum resembles a harmonic function and, hence, we fit them with $y = \frac{1}{2}k(x - x_0)^2 + y_0$ using a least-squares fit. This provides us with the depth of the potential wells y_0, the preferred distance x_0, and the interaction strength k, see Appendix I for values. Interestingly, the confinement seems to weaken with increasing preferred distance of the swimmers, which would be in line with the intuitive picture of interacting solute gradients. However, the larger preferred swimmer separation and lower interaction strength might also be due to a difference in one of the participating swimmers.

Let us now turn to the origin of this activity-induced interaction. In view of our recent work [155, 157], we hypothesize that there is a short-ranged repulsion, due to the pusher-type nature of the propulsion mechanism, and a long-ranged attraction, due to osmotic flows along the substrate. To lowest order, the former interaction induces an *outward* directed
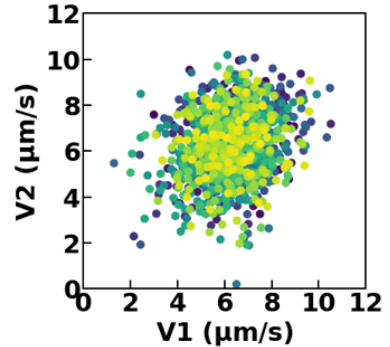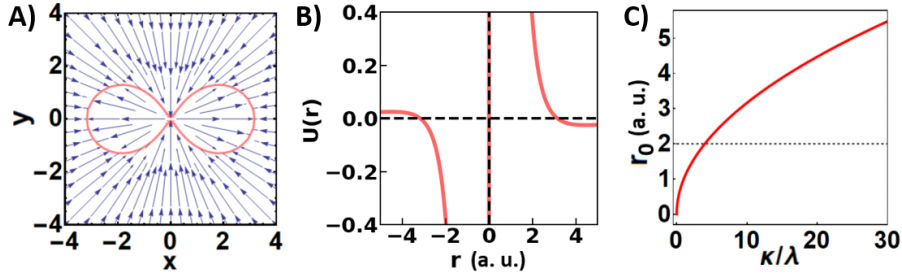
Figure 4.7: **Interactions of comoving swimmers: modeling.** Effective separation between swimmers based on hydrodynamic and osmotic balance. **A)** The balance between an inward osmotic flow along the wall and an outward pusher-type dipolar flow away from the swimmer leads to a curve of zero velocity depicted in red. **B)** Two swimmers that lie head-to-tail as in Figure 4.5A assume a fixed distance as evidenced by the x-axis intercept. The shape of the relative velocity generates an effective potential. **C)** Swimmer separation distance as a function of the ratio between the osmotic and pusher contributions, with λ and κ indicating the respective strengths of the inward and outward flows.

dipolar fluid flow along the symmetry axis of the swimmer [112] that scales as $u_{\mathrm{dip}}(r, \theta) = \kappa \left(3\cos^2\theta - 1\right)/(2r^4)$, while the latter induces an *inward* directed flow due to osmosis along the substrate [208] that scales as $u_{\mathrm{osm}}(r) = -\lambda/r^2$; the factors κ and λ indicate the respective strength of the outward and inward flows, r the radial distance — the decay accounts for the presence of a no-slip surface —, and θ the angle with respect to the swimmer's orientation.

When the two contributions balance at a finite distance, comoving swimmers can assume a stable separation, see Figure 4.7A for a vector plot of the total velocity profile $u_{\mathrm{tot}}(r, \theta) = u_{\mathrm{osm}}(r) + u_{\mathrm{dip}}(r, \theta)$. The angular dependence shows a lemniscate zero-velocity contour, which does not account for the finite size of the swimmer. Clearly, our simple argument would allow for swimmer contact at a finite angle, which can be stabilized by imposing 1-dimensional motion. Figure 4.7B shows that when aligned head to tail, there is a separation r_0 that is stable, as indicated by the slope at the intercept. For swimmers comoving in the same direction we obtain a simple expression for the separation as a balance between the inward and outward flow strength: $r_0 = \sqrt{\kappa/\lambda}$, see Figure 4.7C. Hence, this profile can indeed be recast into an effective potential, as in

Figure 4.5C. The collective speed-up observed in Figure 4.4B may thus stem from long-ranged chemical gradients leading to an enhancement of the phoretic driving mechanism, or from a collective hydrodynamic effect, such as a drag reduction for the actively-assembled dimers and trimer. Lastly, note that according to this simple model if one particle is immobilized, the second particle may approach much more closely, possibly even come into contact depending on the strengths of repulsion and self-propulsion; the latter should also hold for particles moving toward each other.

Intriguingly, we can test these predictions in our experiments, where we may be able to induce situations of close contact which would disturb the stable swimmer distance by temporarily or even permanently stopping one of the swimmers. The latter we have already observed for immobilized pairs of swimmers on the blue-colored posts in Figure 4.1. These swimmers probably moved in opposite directions before their encounter immobilized them, see Figure 4.8A for a schematic drawing. More surprisingly, we also observed immobile clusters consisting of three particles, see Figure 4.1. This implies that a third particle not only was able to approach two immobilized particles much closer than the previously observed 3 μm minimum distance, in line with our model prediction, but also that it did not remobilize the cluster despite the uneven particle number and hence presumably unbalanced forces, see Figure 4.8B.

To gain better control over the location and duration of the stops and test our hypotheses, we employed micro-printed posts with a peanut shape that feature regions of alternating positive and negative curvature. Swimmers passing through negative curvature points need time to reorient themselves to be able to move on, thereby enforcing temporary stops at precisely defined locations, see Figure 4.8D. The more curved the neck regions of these posts, the longer it takes for the swimmers to escape. In addition, these larger posts allow us to study the interactions and behavior of more than three particles.

Equivalently to our observations on the circular posts, and previous work on channels [59], we verify that swimmers with opposing directions of motion hinder each other, see the bottom edge of the peanut-shaped post in Figure 4.9A ($t=0$ s). Similarly, a third swimmer is unable to disturb
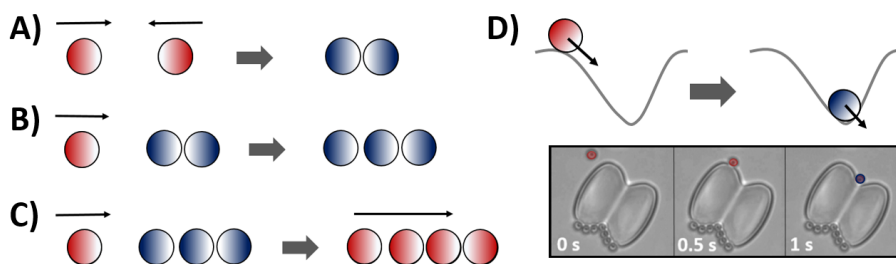
Figure 4.8: **Schematic representations of the conditions determining chain mobility.** Red and blue colors indicate mobile and immobilized swimmers, respectively. The darker hemispheres represent the Pt side, which drives motion. **A)** Two swimmers with opposing motion direction become immobile. **B)** When a third swimmer approaches the cluster, it gets in close touch and also becomes stationary. **C)** A fourth swimmer, entering from the same side as in (B), causes the chain to move again in the direction of the majority of swimmers. **D)** In highly curved neck regions, swimmers stop temporarily because a reorientation is required, see also the light microscopy image at the bottom.

this configuration and joins the immobile cluster, see bottom edge of Figure 4.9A (t=1 s), where the black-colored swimmer joins the immobile dimer. Thus, such immobilization not only happens in the negative curvature region of the neck, but also along the positive curvature regions of the rounded peanut edges. A fourth swimmer joining the immobile trimer from the right leads to a balanced situation and an immobile tetramer cluster similar to Figure 4.8A, see the red-colored swimmer in Figure 4.9A at t=2 s and t=3 s. Based on our experiment we found that a fourth swimmer is able to remobilize an immobile trimer, whenever there are three particles pointing in the same direction, see Figure 4.8C. Generally in combining chains, we find remobilization whenever the number of swimmers pointing in one direction exceeds the number of swimmers pointing in the other direction by $\Delta n = 2$. Notice, however, that swimmers pointing in the direction opposite to the net motion do not need to reorient, they are simply pushed along.

Based on the aforementioned simple conditions, we can furthermore deduce the directionalities of the swimmers in compact moving chains, either from their position or from the dynamic information of chain formation. For example, swimmers at the ends of long immobile chains always
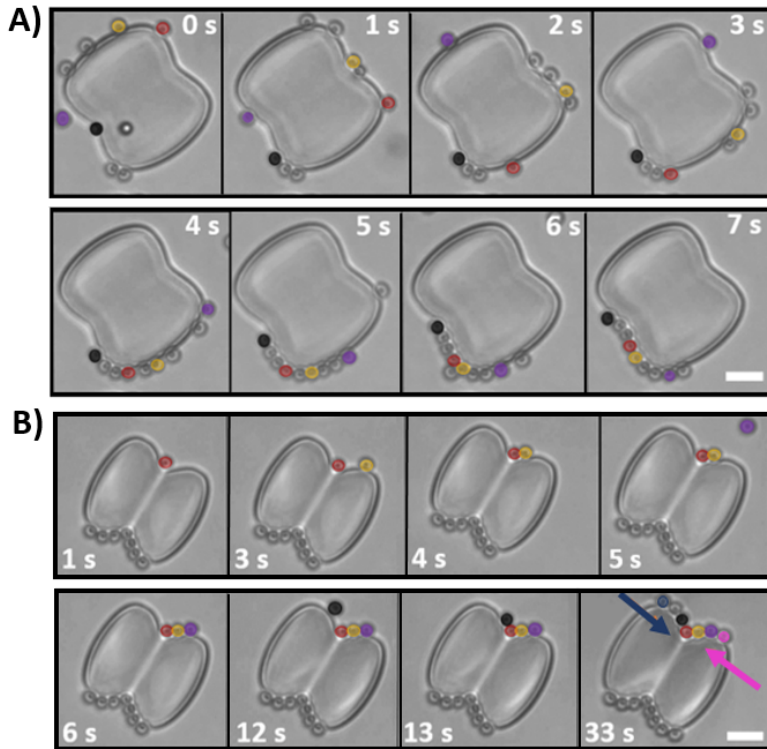
Figure 4.9: **Actively-assembled chains of microswimmers on peanut-shaped posts.** Same color marks the same swimmer throughout each time-series. **A)** Dynamic chain formation: initially, self-propelled swimmers headed by the red swimmer move clockwise in a train. After being stopped by an immobile cluster at the edge, the train becomes a compact chain that moves after further addition of swimmers. **B)** Posts with a more negative neck curvature enhance the formation of compact and immobile chains, because the necks act as accumulation sites. This time-series is a continuation of that in Figure 4.8D.

must have directions that point towards its center. Conversely, in this manner we can also predict the dynamics of a compact chain upon addition of a swimmer.

The larger size of our peanut-shaped microprinted posts enables the attachment of multiple moving swimmers that can actively interact and dynamically self-assemble and disassemble. These posts therefore allow

us to see how swimmers that move in trains along the post evolve into compact swimmer chains. For example, four swimmers that move in the same clockwise direction form a train led by the red-colored swimmer in Figure 4.9A (t=0 s). Between t=0 s and t=1 s a fifth swimmer, initially swimming on the top of the post, enters the train of co-moving swimmers from above, in front of the orange one. Interestingly, the swimmers following the red maintain stable distances while orbiting. That is, before being stopped by the immobilized cluster at the bottom-left corner, their in-between distances fluctuate around a preferred distance in accordance with our Figures 4.3, 4.5, and 4.7 findings.

Figure 4.10: **Distance between swimmers within a mobile chain.** Center-to-center distance between swimmer pairs within a chain that self-propels in the direction of swimmer "1", i.e. swimmer "1" is at the front end while swimmer "9" is at the back end, see also the light microscopy image on the right. Swimmers at the ends maintain at all times larger distances from their neighbors, in comparison to those positioned in the middle.

The immobile cluster acts as a stopping point that compacts the train of swimmers into a chain: one by one, the swimmers encounter and join the cluster in close contact, thereby creating a compact chain. Once the number of clockwise moving swimmers is at least by two greater than the number of counterclockwise moving swimmers in the immobile cluster the entire chain sets into motion. Since the majority of swimmers are moving clockwise, the clockwise direction is imposed to the chain as a whole.
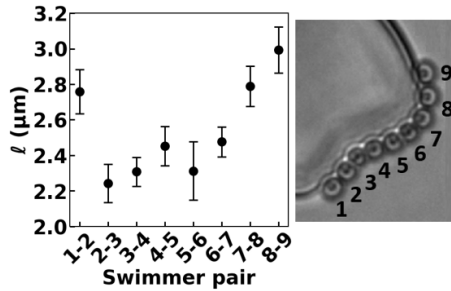
After the chain is formed and remobilized, the distance between a swimmer and its neighbor depends on its position in the chain, see Figure 4.10. Swimmers at the chain ends are further apart from their neighbors as opposed to the ones in the middle that are almost in touch. Swimmers at both ends are positioned at a center-to-center distance of $\approx (2.9 \pm 0.2)$ μm from their neighbors, unlike the swimmers within the chain that move at distances of $\approx (2.4 \pm 0.3)$ μm. For comparison, our swimmers have a diameter of (2.00 ± 0.05) μm, implying that indeed particles in the center

of the chain are almost touching. Note that the distance of the swimmer pairs at the chain ends coincides with the minimum distance found for the swimmer pairs in the spherical posts in Figure 4.5B. This observation further corroborates our hypothesis of a long-range attraction being present between the swimmers, which is balanced by a short-range repulsion. Because the attraction spans more than a single swimmer, the swimmers in the middle are more compacted than those at the end.

Contrary to the dynamic collective motion we have just described, we furthermore find that highly curved necks capture swimmers for such long times that, in fact, they act as semi-permanent stopping points. Although long chain formation is still possible, the self-assembled chains remain immobile due to the pinning of the swimmers by the neck, see Figure 4.8D and 4.9B: the motion of the red swimmer immediately stops at the neck at $t=1$ s. Thus, a highly curved neck not only prohibits collective motion, but also hinders single swimmer motion since it requires reorientation.

Besides an activity-induced self-assembly into compact chains, chains may also reorganize in time. In Figure 4.11A we follow a clockwise self-propelling chain consisting of ten swimmers. During orbiting, swimmers may leave the chain in the following ways: (1) swimmers at the chain end may leave when they reach locations of comparatively high positive or negative curvature, in line with earlier findings for individual swimmers [59, 60], which here is also likely facilitated due to the larger distances to their neighbor. That is the case for the red swimmer at $t=0$ s, which leaves the chain when it reaches the rounded peanut edge (top left). (2) Likewise, swimmers from the middle may exit when they pass through locations where curvature varies. This situation is visible both at $t=11.5$ s and $t=13.0$ s in Figure 4.11A, where a center-chain swimmer highlighted in red escapes while passing through the negatively curved neck and positively curved corner, respectively. In both cases, the chain slowed down before the escape. We speculate that escape is enhanced for swimmers with directionality that opposes the net direction of motion.

In addition to facilitating swimmer escape, locations with strong curvature variations furthermore enhance chain breakup and motion reversal, see Figure 4.11B as an example. A chain that moves clockwise slows down and becomes immobile when its middle is situated on the rounded edge. The swimmer from the middle leaves the chain while the entire chain
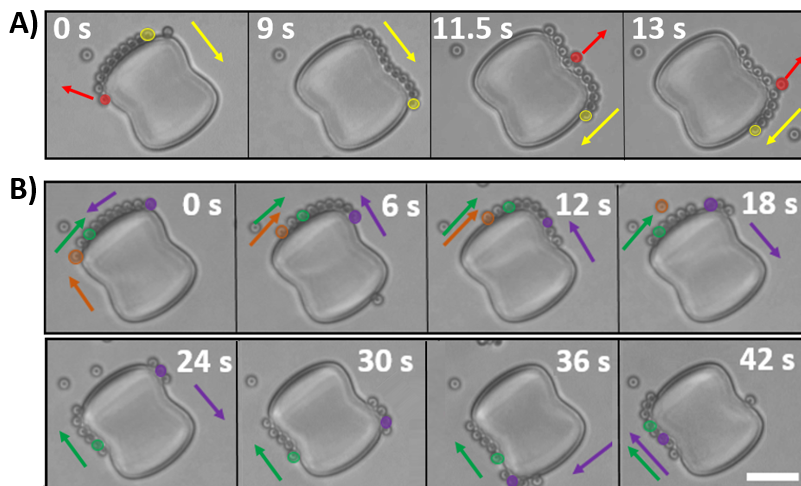
Figure 4.11: **Dynamics of actively-assembled chains: effect of post topology on chain mobility.** Each color marks the same swimmer within each time-series, except the red color in (A) which marks three different swimmers all escaping the chain; corresponding arrows denote directionality. **A)** When it reaches the rounded post edge, a swimmer escapes from the end of the self-propelled compact chain. Swimmers from the middle of the chain also escape during orbiting from the neck or the rounded post edge. **B)** Example of chain breakup: a chain self-propels in the clockwise direction and becomes immobile around the rounded post edge. Two swimmers with opposing direction are incorporated to the chain from the right, and the chain remobilizes in the opposite direction. When reaching the rounded edge, the chain end slows down, the chain breaks, and its end immobilizes. Upon arrival of new swimmers, the end remobilizes at the reverse direction eventually leading to the reformation of the entire chain at the opposite site of the neck.

remains stationary. At t=12 s two swimmers with the same counterclockwise direction as the purple swimmer enter the chain from the right. The entire chain gets remobilized and starts to move in the counterclockwise direction: when reaching the rounded edge, the end of the chain is being slowed down, then the chain breaks, leaving three swimmers immobilized on the rounded edge behind. The rest of the green-swimmer-led chain continues to move counterclockwise until it stops at the other neck side. From the stationary purple chain, one swimmer escapes and gets

remobilized in the clockwise direction by two swimmers joining. When the purple chain encounters the immobile green chain, it lifts the immobilization and the entire chain continues in the clockwise direction, in line with what we observed previously in Figure 4.9A.

Conclusions

In summary, catalytically self-propelled microswimmers show a plethora of striking collective effects along 1-dimensional paths. When moving in the same direction microswimmers "cooperate". That is, they move at a greater speed the more particles join as well as at a preferred distance, larger than a minimum distance. This activity-induced interaction can be described by an effective potential of the order of a few $k_B T$. Stopping the chain can overcome this minimum spacing of comoving swimmers, thereby leading to compact chains. These active chains show very rich dynamics themselves, with activity induced self-assembly, compaction, disassembly, breakup, and reformation. A simple rule seems to distinguish between chain mobility and immobility: mobility is achieved if the difference in the numbers of opposing swimmers is greater or equal to two. Once in contact, the notion of the potential well still persists, as distances within the self-assembled chains are not uniform, i.e. swimmers at the ends are less tightly packed. Curvature modulations of the posts allow spatial control over chain speed and reorganization, such as compaction, breakup, and immobilization, offering an exciting playground for testing efficient modes of transport. Overall, our findings unravel novel behaviors of model swimmers in 1-dimensional environments, thereby providing novel insights into activity-induced interactions. Insights into interactions and collective behavior of synthetic microswimmers are pivotal for applications that require increased swimming efficiency or directionality across different environments as well as answering fundamental questions on the 1-dimensional phase behavior of active systems.

Acknowledgements

Methods

Particles. Spherical latex particles based on polystyrene (2% cross-linked) with diameter (2.00 ± 0.05) μm, i.e. size polydispersity 2.5%, were purchased from Sigma Aldrich. Pt-half-coated particles (Pt layer thickness of (4.7 ± 0.2) nm) were produced through physical vapor deposition, as described in Ref. [155, 157].

3D printed structures. Microstructures were produced with the commercially available microprinter Photonic Professional GT of Nanoscribe which uses two-photon lithography. The microprinter was equipped with a 63X oil-immersion objective (Zeiss, NA = 1.48) and used to print the 3D structures in oil mode. Designs were performed in Autodesk Inventor and processed with Describe. The structures were printed onto glass coverslips, pre-cleaned with isopropanol, using the commercial photoresist IP-L as a pre-polymer. After printing, the structures were developed by submersion in propylene glycol methylether acrylate for 15 min, followed by gently dipping into isopropanol three times to remove the unpolymerized photoresist. The structures were subsequently dried with gentle air flow. All procedure was done under yellow light.

Imaging. Pt-half-coated particles were dispersed in a 10% aqueous H_2O_2 solution. Their motion was recorded above the planar walls with a ELWD 60x objective (S Plan Fluor, NA 0.7, zoomed at 1.5x i.e. 0.1 μm/px) mounted on an inverted Nikon Eclipse Ti microscope at a frame rate of 5 and 10 fps along the circular and peanut-shaped posts, respectively.

Analysis. Particle positions above the wall and along circular posts were obtained using the Python tracking algorithm Trackpy [141]. The speed of all particles was determined using the time derivatives of spatial displacements at consecutive frames, see inset of Figure 4.2C for the speed distribution of a single particle measured in orbit for ≈ 4 min (> 1200 frames). Along circular posts, the (arc) displacement was obtained according to Figure 4.5A. Along peanut-shaped posts, distances were obtained using the NIS-Elements Advance Research software package by Nikon.

Appendix I: Comoving swimmer speeds
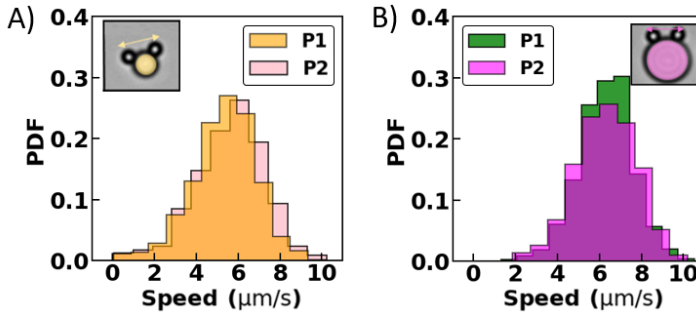
Figure 4.12: PDFs of the speeds of two swimmers moving along a **A)** 4 µm and **B)** 8 µm post. Front and back swimmers are labeled P1 and P2, respectively. Swimmers orbiting the same post have almost the same speed distribution, independent of swimmer number and post size, see Figure 4.4A for three swimmers.

Post diam. (µm)	k (k_BT/µm^2)	x_0 (µm)	y_0 (k_BT)	Curve color
4	0.8 ± 0.1	5.0 ± 0.1	-4.4 ± 0.1	orange
8	4.7 ± 0.7	4.20 ± 0.04	-5.9 ± 0.2	magenta
4	8.3 ± 0.5	3.80 ± 0.02	-6.1 ± 0.1	dark green
4	3.9 ± 0.3	4.20 ± 0.02	-4.60 ± 0.04	light green

Table 4.1: Parameters obtained from the fits in Figure 4.5C with $y = \frac{1}{2}k(x - x_0)^2 + y_0$, where k is the interaction strength, x_0 the preferred distance and y_0 the potential well depth. From left to right: post diameter, k, x_0, y_0, and the color used for each curve, see also Figure 4.5B for the corresponding swimmer pair.
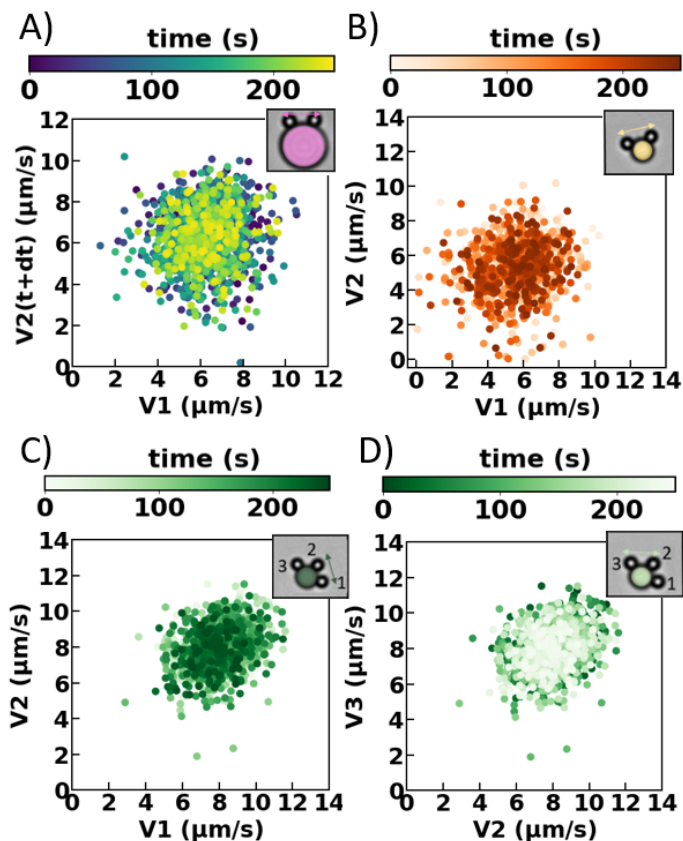
Figure 4.13: **A)** We check for time-delayed speed correlations by considering the correlation between $V_1(t)$ and $V_2(t + \tau)$, with τ the time between two frames, for the same swimmer pair as in Figure 4.6. The Pearson correlation coefficient is 0.1, signifying no correlation. Additional scatter plots of the speeds of **B)** two comoving swimmers, **C)** the front "1" and middle "2" swimmers and **D)** the middle "2" and back "3" swimmers from a three-swimmer system, along 4 μm posts, none of which show correlations.

Appendix II: Model for preferred comoving swimmer distances

Here, we provide an in-depth discussion regarding the origin of the activity-induced interaction, see also Figure 4.7. Referencing the recent work on two interacting chemical swimmers in bulk [209, 210] there is repulsion between two identical comoving swimmers in bulk. A full analysis of all possible couplings has not been attempted, so that a pure bulk hydrodynamic and chemophoretic mechanism may not be excluded. However, in view of our recent work [155, 157], we hypothesize that there is a short-ranged repulsion due to the swimming mechanism itself and a long-ranged attraction due to osmotic flows along the substrate. The attraction must be the longer ranged effect to be commensurate with the particles assembling into co-moving objects, see also Results and Discussion on chain formation. The repulsion can be related to the pusher-type nature of the self-propulsion, which induces outward directed fluid flow along the swimmer symmetry axis. When the two contributions balance at a finite distance, comoving swimmers can assume a stable separation. To show that this argument has merit, we formulated a minimal model that exhibits such a balance point.

An inward directed flow due to osmosis along the substrate [208] scales as $u_{\mathrm{osm}}(r) = -\lambda/r^2$, while a pusher-type swimmer has an outward directed flow [112] that scales as $u_{\mathrm{dip}}(r, \theta) = \kappa \left(3 \cos^2 \theta - 1\right)/(2r^4)$ (the bulk r^2 decay becomes r^4 due to proximity to a no-slip wall). The factors λ and κ indicate the respective strength of the inward and outward flow. Note that we only take the leading-order contributions for both effects in our proof of concept. Clearly, a more detailed calculation could distinguish between various forms of self-propulsion, and account for near-field effects, but this goes beyond the scope of the current investigation. For an appropriate choice of the prefactors $\lambda = 0.1\kappa$ we obtain the total velocity $u_{\mathrm{tot}}(r, \theta) = u_{\mathrm{osm}}(r) + u_{\mathrm{dip}}(r, \theta)$ profile shown in Figure 4.7B, which indeed reveals a favorable separation r_0. Generally, we have that $r_0 = \sqrt{\kappa/\lambda}$ for comoving swimmers that are pointed in the same direction, see Figure 4.7C. The slope of the velocity profile at the intercept in Figure 4.7B indicates a stable configuration. Thus, we expect that this profile can be recast into an effective potential, as was done from the distance data in the experiment, see also Figures 3C and 3D. Setting $\theta = 0$ and locally lin-

earizing $u_{\text{tot}}(r - r_0) \approx -Us$ with $U > 0$ the absolute value of the slope and $s = r - r_0$ the perturbation around the favorable separation. In the low-Reynolds number regime, a speed can be converted into a force via the mobility, i.e. $F = -6\pi\eta a U s$ in this case, with η the viscosity and a the sphere radius. The sign indicates the restorative nature of the force, with $U > 0$ as before. If F is a force deriving from an effective potential, then the potential has the shape $3\pi\eta a U s^2$, which is the origin of the harmonic potential inferred from the experiment. When one of the particles is immobilized, the second particle may approach much more closely, possibly even come into contact (depending on the strength of the repulsion versus self-propulsion), and similarly for particles moving toward each other. Lastly, turning to the speed-up of multiple particles moving in the same direction: it is important to note that $u_{\text{tot}}(r)$ describes a relative speed, and our argument is robust to a change in the net speed of the pair. Such a collective speedup may be the result of the long-ranged chemical gradients leading to an enhancement of the phoretic driving mechanism, or a collective hydrodynamic effect, such as a drag reduction for the actively-assembled dimer and trimer [206].

5

Holography as a Probe for Near-Wall Colloid Dynamics

Abstract

Geometric confinement does not only influence swimmer behaviors, as we have seen in previous chapters, but in fact, it strongly influences the behavior of all colloidal particles in liquid environments. To date, non-spherical colloid behaviors close to confining boundaries, even as simple as planar walls, remain largely unexplored. Here, we develop a method based on digital in-line holographic microscopy that allows us to measure the separation between colloids with uniform surface properties and walls. In the first part of the chapter, we employ this method on colloidal spheres, and find good agreement with our diffusion-based height analysis method described in chapter 3. In the second part, we employ our method to colloidal dumbbells of different sizes. We find that while larger dumbbells are oriented almost parallel to the wall, smaller dumbbells of the same material are surprisingly oriented at preferred angles. We determine the total height-dependent force acting on the dumbbells by considering gravitational effects and electrostatic dumbbell-wall interactions. Our modeling reveals that at specific heights both net forces and torques on the dumbbells are simultaneously below the thermal force and energy, respectively, which makes the observed orientations possible. Our results highlight the rich near-wall dynamics of nonspherical particles and may further contribute to the development of quantitative frameworks for arbitrarily shaped particle dynamics in confinement.

Introduction

The behavior of micron-sized colloidal particles under confinement has been a subject of intensive research in engineering, materials science, and soft matter physics [211]. Such particles often serve as model systems for understanding the effects of confinement on microscale processes, *e.g.* structure formation and rheology, offering quantitative insights into the behavior of biological systems [212–214]. This understanding is further desirable for various applications where confinement dictates the dynamics, ranging from improving microfluid transport in lab-on-a-chip devices [215], growing low-defect photonic crystals [216], and tuning pattern formation for materials design [217–219].

Confinement can strongly affect hydrodynamic and electrostatic (self-) interactions. These effects depend on particle-wall separation as well as particle size and shape [220]. Yet, the majority of research has focused on the behavior of spherical particles, both from a theoretical and experimental standpoint. This includes the behavior of single spheres close to a plane wall [128, 129, 221–227], between two walls [228–231] and microchannels [232, 233]. Going beyond single particle dynamics, the collective behavior of sphere clusters and dense suspensions has also been examined close to [234, 235] as well as in between walls [236], microchannels [237, 238] and confining droplets [239]. However, microparticles involved in biological processes and industrial applications typically depart from the ideal spherical shape. Since the motion of nonspherical particles is different from that of spherical ones [240–244], there is a need to study the effect of confinement on nonspherical particles [245] to gain proper understanding of both naturally occurring and technologically relevant systems. For nonspherical colloids, dynamics have typically been measured far from walls [243]. Despite predictions for axisymmetric particles [246] and simulated studies for arbitrary shapes [247, 248], the effect of particle-wall separation remains experimentally unexplored. Yet, the interplay between shape anisotropy and wall separation ought to be examined as well, to develop accurate model systems for molecular matter.

To date, a plethora of techniques has been employed for colloidal studies, including optical microscopy [249], optical tweezers [229, 250–252], light scattering [253–256], evanescent wave dynamic light scattering (EWDLS) [228, 235, 257–260], total internal reflection microscopy (TIRM) [225, 261, 262], TIRM combined with optical tweezers [263], holographic microscopy [160, 264], and holographic optical tweezers [234]. Each of these techniques has its own strengths and weaknesses, especially when it comes to measuring anisotropic particle dynamics near walls with high spatiotemporal resolution in three dimensions. For example, optical microscopy is a straightforward technique, yet lacks sensitivity to out-of-plane motion. Confocal microscopy on the other hand provides accurate three-dimensional measurements, but is relatively slow when recording

image stacks and additionally requires refractive index matching and fluorescent labelling. Optical tweezers confine particle motion and hence hinder long-term three-dimensional measurements, while light scattering determines ensemble properties and is thus difficult to interpret in the case of anisotropic particles [265]. TIRM is an elaborate technique that provides high resolution, though its range is limited to the near-wall regime, typically less than $400\,\mathrm{nm}$ from the wall [225, 261–263]. To overcome the above limitations, holographic microscopy may be employed instead, as it records both position and shape [266] with high resolution [264] also in the out-of-plane direction. In addition, it is even capable of resolving weakly-scattering objects as used in biology [160, 267–269] without the need for fluorescent labeling [270]. Moreover, while measurements are typically performed using lasers, a cost-effective holographic microscopy setup can also be constructed using an LED mounted on an existing microscope [269]. As a downside, analyzing holographic measurements may be computationally expensive which, if desired, can be compensated by implementation of a neural network [271] at the expense of some accuracy loss.

In this chapter, we establish a new method for measuring particle-wall separations based on holographic microscopy. Employing our method to spherical particles not only allows us to establish our setup and analysis, but also to additionally crosscheck our diffusion-based height analysis method of chapter 3. Subsequently, we measure colloidal dumbbell dynamics above a planar wall, a simple model system that enables the study of the effects of shape anisotropy on confined dynamics. We accurately probe how particle orientation is affected by the presence of the wall, and specifically the particle-wall separation, by means of digital in-line holographic microscopy. We find that smaller dumbbells are oriented at nonzero angles with respect to the wall, while in contrast, larger dumbbells of same material are oriented mostly parallel to the wall. In all cases, we were able to identify the relation between particle orientation and particle-wall separation. We further compare our experimental findings to a minimal model for the dumbbell that combines gravitational and electrostatic dumbbell-wall interactions. We find that, despite its simplicity, the model provides qualitative insight into our observations. Our results highlight the importance of wall effects on anisotropic particle motion, and may ultimately contribute to the development of a quantitative framework for the dynamics of particles with arbitrary shapes in confinement, not fully established at present in the literature.

Results and Discussion

We employ a digital in-line holographic microscopy setup based on existing examples [269] that generates scatter patterns by a light-emitting diode (LED), see Figure 5.1A, to obtain particle holograms. A measured hologram is shown in Figure 5.1B (top). Using this setup and subsequent hologram analysis, see fitted model in Figure 5.1B, we accurately determine 3-dimensional positions (Figure 5.1C) and at the same time characterize colloidal particles, i.e. obtain particle
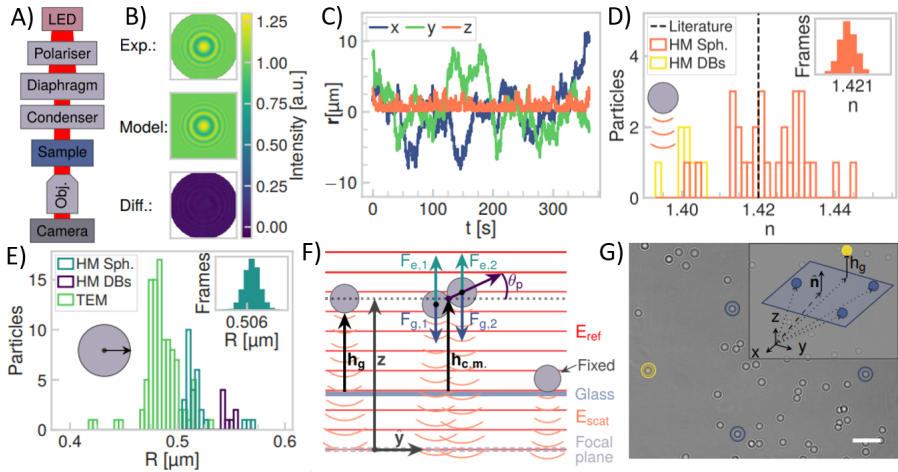

Figure 5.1: **Measuring particle-wall separations with holographic microscopy (HM).** A) Schematic of our experimental setup. Holograms are formed by the interference of the reference field E_{ref} with the scattered field E_{scat}, see also panel (F). B) Comparison of a sphere hologram measured in the experiment, the fitted model, and their residual, indicating good agreement between measurement and fitted model. C-E) Parameters extracted from our hologram analysis, see Methods for a detailed description of the fitting process. C) 3-dimensional $r(x,y,z)$ position of a single sphere in time. D) Average refractive index n obtained from fitting sphere and dumbbell holograms, with the inset showing a distribution from a single sphere measurement. E) Average radius R obtained from fitting sphere and dumbbell holograms, with the inset again showing a single sphere measurement. For comparison, we show sphere radii measured using TEM. F) We are interested in the gap height h_g, or else the center of mass (c.m.) height $h_{c.m.}$, with respect to a planar glass wall. G) The position of the wall is found by fitting a plane to the positions of at least three particles fixated on it (blue). The gap height h_g between a diffusing particle (yellow) and the wall is the distance between its measured position and its position projected on the plane along $\hat{n}$.

size (Figure 5.1D) and refractive index (Figure 5.1E). To further determine the separation between diffusing particles and walls, we analyzed simultaneously-measured holograms of particles that were diffusing above the wall and others that were fixated to the wall, as described in Figures 5.1F-G. Briefly, we use the fixated to the wall spheres as reference points for measuring the position of the wall. Specifically, at least three fixated spheres are recorded and analyzed, see blue-colored spheres in Figure 5.1G. This allows us to fit a plane to their positions, as illustrated in Figure 5.1G, and subsequently to project the position of the diffusing particle (yellow-colored particle in the same figure) to that plane. For all details on hologram analysis, particle tracking, characterization, and extraction of particle-wall separation, we point the interested reader to the Methods.

Part I: Characterization, height distribution, and near-wall diffusion of spherical particles

First, we measured the sphere dynamics above a planar wall both to assess the sensitivity of our LED-based holographic microscopy setup as well as to verify our new method of using fixed particles to accurately locate the position of the wall. Indeed, despite the simplicity of our setup, we find an excellent agreement between the measured holograms and the Mie scattering-based model, see Figure 5.1B for a direct comparison that additionally shows the residual between data and model. Moreover, in Figures 5.1D and 5.1E we show the refractive indices and particle radii obtained during characterization, respectively. Both parameters agree with expectations: the refractive index, $n_{\text{silica}} = (1.42 \pm 0.02)$ agrees with the value provided by the particle supplier (1.42) and at the same time the radius $(0.51 \pm 0.03$ µm$)$ follows our TEM results $(0.48 \pm 0.03$ µm$)$.

For high precision measurements, careful consideration should be given to the determination of both the position and local orientation of the wall, from which the gap height can be derived, as walls in experiments may be tilted. Here, we achieved such precision, see Figure 5.2A, by using at least three fixed particles that define a plane and by subsequently obtaining the position of the diffusing particle relative to said plane. Note that the position and orientation of the plane is fitted accurately to the positions of the bottom of the fixed particles, since our method also measures the radii of the fixed particles at the same time.

In Figure 5.2B, we report the distribution of gap heights between the diffusing spheres of two different sizes and the wall. We find that the height distributions can faithfully be described using established methods that combine a barometric height distribution with electrostatic interactions, see also Methods and Ref. [220]. In comparison, the height distributions of the 1.1 µm and 2.1 µm spheres feature qualitatively different behaviors. As expected,

the smaller spheres probe a wider range of gap heights, while the axial motion of the larger spheres is more confined. However, we note that the median gap height of the larger spheres is slightly greater than that of the smaller ones, which is in line with the higher surface charge that we measured for these particles using laser doppler micro-electrophoresis. The zeta potentials are (-54 $\pm$ 7) mV and (-35 $\pm$ 6) mV for the 1.1 and 2.1 µm batches, respectively. The excellent agreement that we obtained between the prediction and our experiment for different particle parameters further verifies the sensitivity of our setup. We conclude that our method of localizing the plane, and thereby the wall, using fixed control particles allows for high precision measurements of colloidal systems near walls.

Finally, to further evaluate our method, we determined the height-dependent translational diffusivity of the spheres (Figure 5.3). In the same figure, we compared our data to the theoretical prediction for translational diffusion with wall gap height [157] presented in chapter 3, which covers the entire separation range from the far-field regime captured by Faxén [163] and the near-wall regime captured by lubrication theory [128]. We find that both particle sizes follow the

Figure 5.2: **Sphere-wall gap height.** A) The z positions of a spherical particle diffusing above a wall, as well as that of the plane (directly below the particle) obtained from the positions of three spheres fixed on the wall, are plotted in time. Using the plane z position, the gap height h_g between the diffusive particle and wall is determined. B) Experimental sphere-wall gap height distributions together with a fit with the model from Ref. [220] which combines gravitational and electrostatic effects for 1.1 µm (orange, fit parameters ρ_p= 2.1 gcm^{-3}, $1/\kappa$= 107 nm, ζ_p= -41 mV) and 2.1 µm (blue, fit parameters ρ_p= 2.2 gcm^{-3}, $1/\kappa$= 207 nm, ζ_p= -52 mV) spheres.

prediction within error, with small random variations between individual measurements, demonstrating that we can accurately determine the diffusion constant across the whole range of here accessible sphere-wall gap heights.
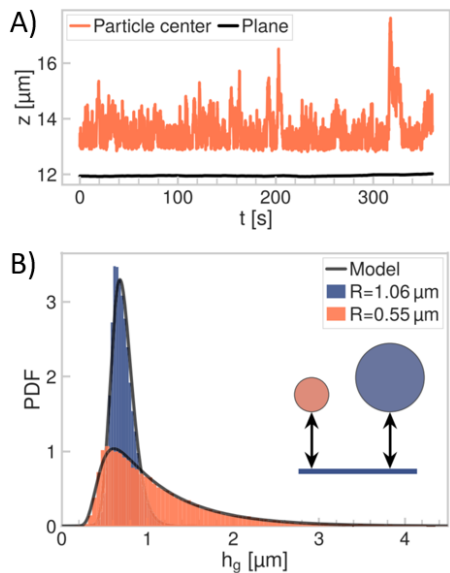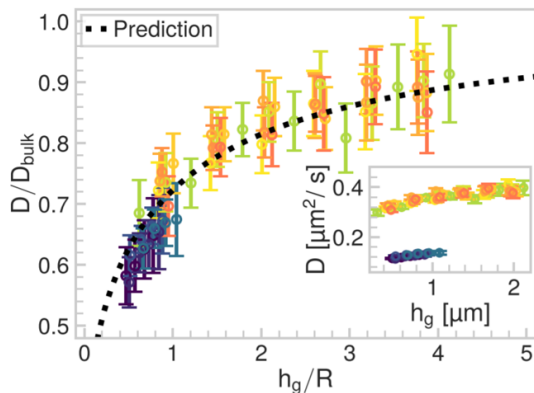
Figure 5.3: **Translational diffusion with wall separation.** Normalized translational near-wall in plane diffusion coefficient of 1.1 µm (light) and 2.1 µm (dark) spheres as function of normalized gap height. Error bars denote standard deviations. Experimental data are plotted against the theoretical prediction that follows from chapter 3, see also Ref. [157]. The inset shows the non-normalized diffusion coefficient values for both sphere sizes with gap height.

Part II: Height distribution and orientation of dumbbell particles with respect to a plane wall

Having established the validity of our setup and method, we proceeded to study the near-wall behavior of our colloidal dumbbells. These dumbbells were formed by random aggregation of two individual spheres caused by Van der Waals attraction; we expect that the spheres do not roll with respect to each other. Analogously to the spheres, we measured the three-dimensional position of dumbbells of two sizes (long axis 2.2 and 4.2 µm respectively), formed either by two 1.1 µm or two 2.1 µm spheres. We first checked the quality of our hologram analysis in Figure 5.4A and D, where the good agreement between the model and our experimental images is shown. In this model, the free parameters are the center-of-mass (c.m.) position, the dumbbell orientation, the radii, and the refractive indices of the two touching spheres comprising the dumbbell. We note that the obtained values agreed with the single spheres results (Figure 5.1D and 5.1E).

Figure 5.4B shows the positions of the 1.1 µm spheres comprising the dumbbell (dumbbell long axis 2.2 µm) as function of time, revealing that one of the spheres is positioned higher than the other in relation to the wall. Moreover, it clearly shows that twice during the duration of our 8 min measurement, the spheres drastically changed positions, *i.e.*, a flipping between upper and
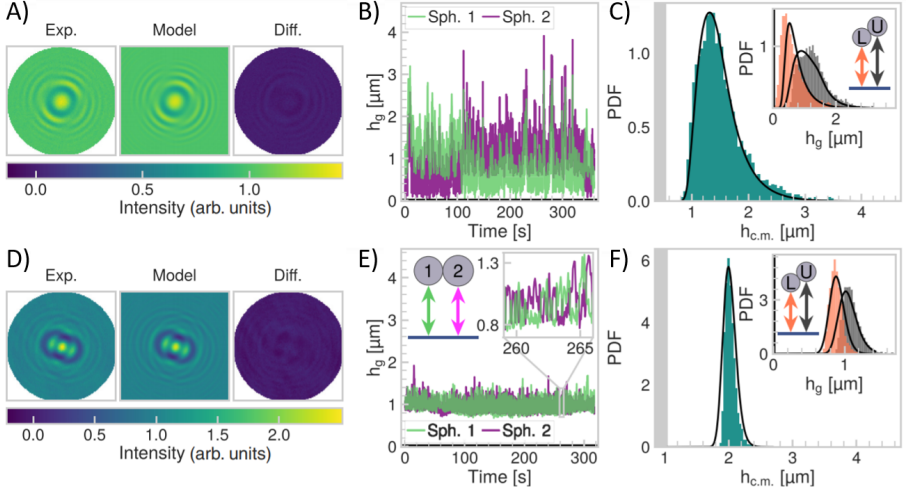
Figure 5.4: **Height distributions of colloidal dumbbells above a planar wall.**
A) Comparison of an experimental image, the fitted model and the residual for
a 2.2 µm dumbbell, the low values of which indicate the good agreement be-
tween experimental data and model. B) Gap heights for the two 1.1 µm spheres
that form the dumbbell as a function of time. C) Center of mass (c.m.) dumb-
bell height distributions (same particle as in panel B), with the corresponding
gap heights of the lower (L) and upper (U) spheres as inset. Solid lines indi-
cate the theoretical prediction of Equation 5.12 (fit parameters ρ_p= 2.0 gcm^{-3},
$1/\kappa$= 103 nm, ζ_p= -30 mV). D) Comparison of an experimental image, the fitted
model and the residual for a 4.2 µm dumbbell, the low values of which indicate
the excellent agreement between data and model. E) Gap heights for the two
touching 2.1 µm spheres that form the dumbbell as a function of time. The in-
set zooms in on a short sequence of the measurement to indicate the frequent
flipping. F) Center of mass (c.m.) dumbbell height distributions (same particle
as in panel E), with the corresponding dumbbell gap heights of the lower (L)
and upper (U) spheres as inset. Solid lines indicate the theoretical prediction of
Equation 5.12 (fit parameters ρ_p= 2.1 gcm^{-3}, $1/\kappa$= 228 nm, ζ_p= -61 mV).

lower spheres occurred. Based on the estimated rotational diffusion time
$\tau_r = 8\pi\eta R_{eff}^3/(k_B T) \approx 2$ s (with viscosity $\eta = 8.9 10^{-4}$ Pa s and the radius of
a sphere of volume equal to the dumbbell $R_{eff} = (2R^3)^{1/3} \approx 0.69$µm), this
flipping should have been observed more frequently if it were a purely diffusive
process faraway from the wall. For the larger dumbbells (long axis 4.2 µm),
which move further from the wall, we observe despite their larger size ($\tau_r \approx$
13 s), frequent flipping between the upper and lower spheres (Figure 5.4E).

By fitting the c.m. height distribution of the dumbbell, see solid black line in Figures 5.4C and F using Equation 5.12, we conclude that our simple model for a dumbbell particle near a wall describes the experimental height distribution very well. Furthermore, the fit parameters we have obtained from this fit agree with the single sphere fit parameters from the height distribution in Figure 5.2B. Additionally, we calculate the height distribution of the dumbbell gap heights of the lower (L) and upper (U) spheres, as shown in the inset of Figure 5.4C and F. Compared to the theoretical prediction from Equation 5.12, we observe a slight shift towards smaller heights for the lower and, conversely, greater heights for the upper sphere in the experiments. This may indicate that to fully describe the experimental data, higher order effects need to be taken into account, such as the distortion of the electric double layer of one sphere by the presence of the other sphere and the wall. These effects become more pronounced when the dumbbells are closer to the wall, as seen when comparing Figures 5.4C and F.

The stable and significant differences in sphere positions of Figure 5.4B, already indicated that these dumbbells are oriented at an angle relative to the wall. On the other hand, for larger dumbbells of the same material, the spheres being approximately at the same height at all times in Figure 5.4E suggested a roughly parallel orientation with the wall. We verify our observations in Figure 5.5A and 5.5D, where we visualize orientations that the dumbbells assumed during the measurements at 15 s intervals. Indeed, from the snapshots we clearly see that while flipping between lower and upper sphere did occur, the height above as well as orientation with respect to the wall remained relatively constant for the larger dumbbell, see Figure 5.5D. Conversely, the smaller dumbbell featured a richer behavior that includes notable changes in height and orientation, in addition to flipping between which of the two spheres is the lowest in Figure 5.5A.

In what follows, we further quantify our observations by calculating the angle, θ_p, between the long dumbbell axis and wall, see schematic of Figure 5.5B. Strikingly, we observe in Figure 5.5B a double-peaked structure not predicted by our model: we find no parallel orientations with respect to the wall for the the 2.2 μm dumbbell. Instead, the dumbbell is more likely to be oriented at an angle between 25 and 56 deg (median 32 deg) with the wall. In separate bright-field microscopy measurements, we verified that dumbbells of this size and material indeed show frequent out-of-plane rotations. The preferred range of orientations is robust and persists even when the dumbbell flips, *i.e.*, when the lower sphere becomes the upper sphere. The difference in peak heights in Figure 5.5B is due to the respective length of the parts of the measurement where the dumbbell assumed a negative or positive orientation. Such preferred orientations are surprising, since an angle distribution centered around zero degrees is naively expected in view of the effects of buoyancy and electrostatics, see the expected
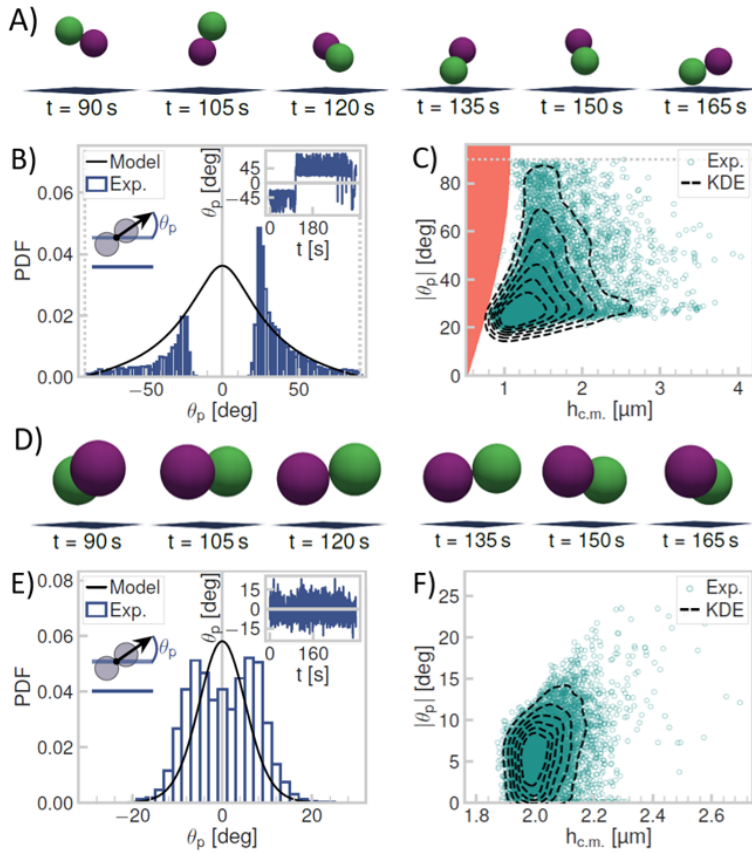
Figure 5.5: Dumbbell orientation with the wall as function of height. A) Schematics based on the experimental positions of a 2.2 μm dumbbell, showing out of plane rotations and height variations. B) Distribution of plane angles for a 2.2 μm dumbbell. The solid line indicates the expected distribution based on Equation 5.13 (same parameters as in Figure 5.4C). The inset shows the plane angle in time. C) Plane angle with c.m. height for the 2.2 μm dumbbell. The red area indicates geometrically forbidden configurations. D) Schematics based on the experimental positions of a 4.2 μm dumbbell at the same times as in (A), showing significantly fewer out of plane rotations. E) Distribution of plane angles for a 4.2 μm dumbbell. The solid line indicates the expected distribution based on Equation 5.13 (same parameters as in Figure 5.4F). The inset shows the plane angle in time. F) Plane angle with c.m. height for the 4.2 μm dumbbell. In panels C and F, the dashed lines are contour plots of the kernel density estimation, corresponding to 12.5%, 25%, 37.5%, 50%, 62.5% and 75% of the data.

distribution depicted by the solid line in Figures 5.5B and 5.5E.

Examining the larger and, hence, heavier 4.2 μm dumbbells in Figure 5.5E, we notice that these indeed have assumed mostly flat orientations with the wall, with the most probable angles ranging between 2.2 and $9.6 \deg$ (median $6 \deg$). However, the double-peak structure in the angle probability density function that we observed for the smaller dumbbells persists to some degree even for these larger particles, indicating that the increased gravitational force leads to a suppression of the interaction which causes the dumbbells to adopt a nonparallel orientation. We hypothesize that the observed angle distributions for both dumbbell sizes stem from a higher-order electrostatic effect not accounted for in our theory. However, we cannot exclude a more subtle interplay of other effects, such as buoyancy and hydrodynamics.

Naturally, the question arises whether changes in height relate to changes in dumbbell orientation. To test for this, we plot the measured angles as function of center-of-mass height. We find that for the smaller dumbbells, there is a clear preference for lower angles at low heights in Figure 5.5C, the preference for which disappears with height. That is, further from the wall the dumbbells may adopt a wider range of orientations. For the larger dumbbell, we also find a narrower distribution of angles at lower heights in Figure 5.5F. However, we note that both angle and height distributions are considerably narrower compared to those that correspond to the smaller dumbbell. At the same time, the particle-wall separation is typically greater than that of the smaller dumbbell: while the smaller dumbbell moves closely to the wall, see the red area in Figure 5.5C which indicates geometrically forbidden configurations caused by particle-wall overlap, the larger dumbbell does not come into close contact with the wall.

Theoretical considerations for preferred dumbbell orientations

To gain insight into the preferred orientations and minimal angle measured in the previous section, we extended the gravity and electrostatics model for a sphere above the wall to the dumbbell as described in the Methods. Briefly, Equations 5.8-5.9 model the dumbbell as two connected, but otherwise non-interacting, spheres by balancing electrostatic and gravitational forces. This approximation ignores the distortion of the electrostatic double layer caused by the presence of the other sphere, but allows us to probe the origin of the previously described dumbbell orientation, by examining whether the combined effects of electrostatics and gravity would result in zero force and torque solutions as function of plane angle and height above the wall.
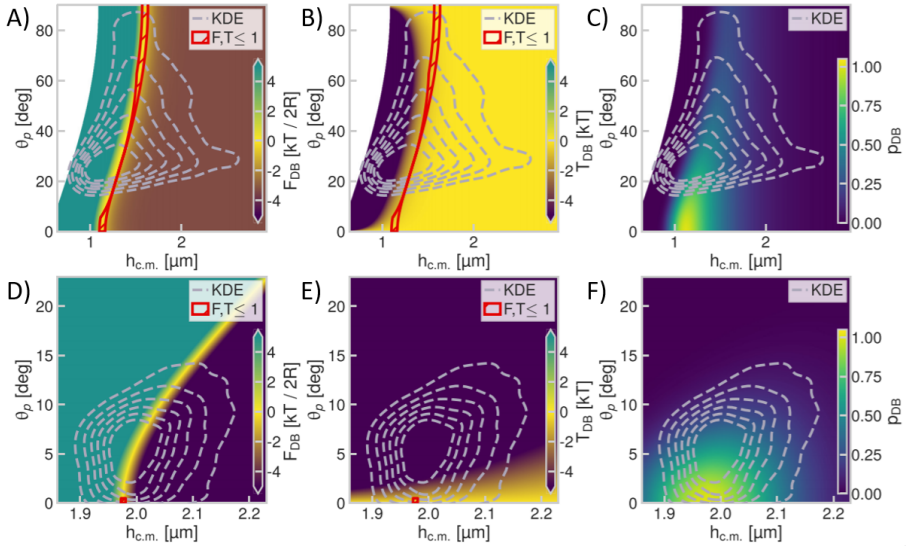
Figure 5.6: **Force and torque acting on a dumbbell by balancing electrostatics and gravity.** A) The force as a function of θ_p and $h_{\text{c.m.}}$ for the 2.2 μm dumbbell. For all orientations, there is a height range for which the net force is zero. B) The torque as function of θ_p and $h_{\text{c.m.}}$ for the 2.2 μm dumbbell. C) The probability of observing a combination of θ_p and $h_{\text{c.m.}}$ for the 2.2 μm dumbbell, as predicted by Equation 5.11 and measured in the experiments (dashed line). D) The force as a function of θ_p and $h_{\text{c.m.}}$ for the 4.2 μm dumbbell. The area where the net force is zero is smaller compared to the smaller dumbbell in (A). E) The torque as a function of θ_p and $h_{\text{c.m.}}$ for the 4.2 μm dumbbell. For the same range of angles as in (B), the torque on the larger dumbbell is considerably higher than the thermal energy for the majority of angles, causing the dumbbell to adopt a flat orientation with respect to the wall. F) The probability of observing a combination of θ_p and $h_{\text{c.m.}}$ for the 4.2 μm dumbbell. In panels A, B, D and E, the red lines indicate regions where both the force and torque are simultaneously small compared to the thermal energy, indicating a possibility of observing the dumbbell at those heights and orientations. Values outside the indicated range of the color-bars are clipped to visualize the low force and torque region relevant to the experiments, while white regions represent sterically-forbidden combinations of height and angle. Dashed lines are a contour plot of the kernel density estimation of the experimental data, see also Figure 5.5.

By applying the reduced model for the dumbbell to the experimental data, we reach a number of interesting conclusions in Figure 5.6, where we plot the results from the model. Figure 5.6A shows that the net force on the 2.2 μm dumbbell vanishes for a range of heights and orientations. That is, for each given orientation there exists a narrow distribution of heights where the force balance is zero. As expected for a particle with a larger mass, for the 4.2 μm dumbbell in Figure 5.6D the range of heights where the net force vanishes is considerably narrower compared to the 2.2 μm dumbbell of Figure 5.6A. To answer whether such configurations are expected to be stable, one must additionally consider the possibility of a reorienting torque stemming from the combined effect of gravity and electrostatics acting on the dumbbell. We expect that the interplay between the magnitude of this reorienting torque and a random torque, stemming from thermal fluctuations, causes changes in the dumbbell orientations with respect to the wall. In the case of a reorienting torque that is large in comparison to the random torque (≈ 1 kT), we expect a mostly parallel orientation with respect to the wall. In contrast, for a reorienting torque that is small compared to the random torque, we expect largely fluctuating orientations. In what follows, we examine the presence and magnitude of the reorienting torque.

Interestingly, for the smaller 2.2 μm dumbbells, a regime arises where both net forces and reorienting torques are simultaneously below the thermal force and energy, respectively, for certain combinations of dumbbell-wall separations and non-zero plane angles, as indicated by the red lines in Figures 5.6A and B. The presence of such a regime that spans throughout state space suggests that the large variations of the angle as found in Figure 5.5, evidenced also in the dashed lines of Figures 5.6A and B, are expected. This is further corroborated by the angle probability plot that follows from our model in Figure 5.6C for heights relevant to our experiment. For the largest dumbbells, our minimal modeling in Figures 5.6D-5.6F agrees well with the almost parallel orientations observed in the experiments in Figure 5.5F, which mostly fall within the high reorienting torque regime, see dashed line in Figure 5.6D.

Our minimal dumbbell model also sheds light on the relation between height and orientation observed in Figures 5.5C and 5.5F, indicated also by the dashed lines in Figure 5.6. Although the agreement is not fully quantitative, the model shown in Figures 5.6C and 5.6F predicts an increase in the most probable angle with greater heights, similar to our experiments. Moreover, the height and orientation combinations that the dumbbells experimentally adopt most often coincide with the zero net force regime and, equivalently, non-zero probabilities in Figures 5.6C and 5.6F, for both dumbbell sizes, as evidenced by the overlap between the experimental data and the areas of higher probability.

Finally, we notice that the range of experimentally observed angles for the 2.2 μm

dumbbells does not fully coincide with the range of angles that fall within the low force and torque regime from the model. For torques below the thermal energy, the model also allows for angles below $17 \deg$, which we did not observe here for these dumbbells. We note that the discrepancy between our model and experiment does not stem from a difference in size between the two spheres in the dumbbell. As can be seen in Figures 5.8 and 5.9, where we additionally account for — the here relevant — 5% dispersity in the sphere sizes, the most probable heights are only slightly shifted towards greater values. The overall dumbbell behavior that the model yields remains the same with or without polydispersity in the sphere size. We hypothesize that this discrepancy may be resolved by considering higher-order electrostatic effects. However, higher-order effects, together with the possibility of dynamic charge redistribution in the double layers which may be relevant here, cannot be described by a simple analytical model.

Conclusions

We have measured the height of colloidal particles relative to planar walls with high precision by means of holographic microscopy. The position of the wall was tracked in time by following the position of spheres fixed on its surface, thereby allowing for an accurate measurement of the location and orientation of the plane and wall. For spheres, the obtained height distributions and diffusivities as function of height are in line with well-known theoretical predictions. Going a step further, we studied the height distributions and orientations of colloidal dumbbells relative to walls. We found that smaller dumbbells assume non-parallel orientations with the wall and further examined the connection between orientation and particle-wall separation. Conversely, we found that larger dumbbells of the same material were always oriented almost parallel to the wall. Finally, we showed that, despite its simplicity, a minimal model accounting for gravity and electrostatics not only faithfully describes the dumbbell height distribution, but also predicts stable configurations for a large range of orientations and dumbbell-wall separations. However, our model predicts a larger range of stable orientations than was found in our experiment, indicating that refinements that account for higher-order electrostatic effects may need to be considered. We thus hope that our findings will encourage further investigations of near-wall particle dynamics. Our results highlight the rich dynamics that nonspherical particles exhibit in the proximity of walls and can aid in developing quantitative frameworks for arbitrarily-shaped particle dynamics in confinement.

Acknowledgements

Methods

Materials. We used spherical silica particles of diameter (1.1±0.04) µm (size polydispersity (PD) 3.7%) prepared following the method of Ref. [272]. Briefly, 0.5 mL tetraethyl orthosilicate (TEOS) diluted with 2 mL ethanol was added to a mixture of 50 mL ethanol and 10 mL ammonia (25%). The mixture was stirred magnetically for 2 h. The seed particles were grown to the desired size by adding 5 mL TEOS diluted with 20 mL ethanol during 2 h using a peristaltic pump. The dispersion was stirred overnight and washed by centrifuging and redispersing in ethanol three times. We obtained their diameter and PD from transmission electron micrographs using ImageJ [273], by fitting particle diameters with the software's built-in functions. In addition, we used (2.1±0.06) µ diameter (PD 2.8%) spherical silica particles purchased from Microparticles GmbH. In all experiments, dumbbell particles are naturally occurring aggregates of two spherical particles. All solutions were prepared with fresh ultra-pure Milli-Q water (Milli-Q Gradient A10, 18.2 MΩcm resistivity). Glass cover slips were purchased from VWR and were used as received.

Holographic setup. We employed a digital inline holographic microscopy (DIHM) setup based on existing examples [269]. Our setup made use of an inverted microscope (Nikon Ti-E) equipped with a 60X oil immersion objective (NA = 1.4). To generate a scatter pattern, we used a 660 nm light-emitting diode (LED) source (Thorlabs M660L4) at its maximum power (3120 mW, using a Thorlabs LEDD1B LED driver), mounted on the lamphouse port of the microscope instead of the standard bright-field lamp. A schematic of the setup is shown in Figure 5.1A. Prior to each measurement, we performed a Köhler illumination procedure in bright-field mode to align the diaphragm and condenser. Additionally, we employed a linear polarizer on top of the condenser to improve the quality of the holograms by enforcing a specific polarization direction.

Sample preparation and measurement details. Spherical silica particles of either 1.1 or 2.1 µm diameter were spin coated from ethanol at dilute concentration onto the glass cover slips, which fixated their position. The cover slips were then placed at the base of the sample holder, serving as the walls relative to which particle motion was measured. The fixated-to-the-wall spheres served as reference points for determining the position of said wall, see also Figure 5.1F and 5.1G as well as the discussion under Analysis of holograms. Afterwards, an aqueous dispersion of particles of the same size was added in the sample holder, which was subsequently entirely filled with water and covered at the top with a glass cover slip to prevent drift. The dispersion contained single spheres as well as small fractions of dumbbell particles that consisted of two touching spheres, see also Figure 5.1F for an illustration. The motion of all particles above the wall was recorded at a frame rate of 19 fps for at least 6 minutes.

Analysis of holograms. For all measurements, the recorded holographic microscopy images were corrected with background as well as dark-field images to minimize errors stemming from interfering impurities along the optical train. Then, for each measurement, the particle of interest was selected manually and a circular crop around its hologram was taken, see also Figure 5.1B, to reduce the amount of pixels considered during model fitting, thereby increasing computational efficiency. From the holograms, we determine the three-dimensional position, (x, y, z), the radius, R, and refractive index, n, of the spheres and dumbbells as described below.

Hologram analysis of spheres. To fit the experimental data, we performed least-squares fits of a model based on Mie scattering theory [160] using the Python package HoloPy [274], see Figure 5.1B as an example. The 3D position of the

Characterization:

1) $(x_1, y_1, z_1)|(R_e, n_e)$

2) $(n_2, z_2)|(R_e, x_1, y_1)$

3) $(R_3, z_3)|(n_2, x_1, y_1)$

Tracking:

4) $(x, y, z)|(\langle n_2 \rangle_t, \langle R_3 \rangle_t)$

Figure 5.7: **Schematic summary of the fitting steps performed to obtain the 3D position of a particle from the measured hologram analysis.** The position in time is fitted in four steps: the first three are characterization steps, in which we find the approximate 3D position (fitting step 1) as well as appropriate guesses for the refractive index n (fitting step 2) and radius R (fitting step 3). In the fourth step, we use these positions and the average n and R values to determine the 3D position accurately (fitting step 4).

particles in time was fitted in four steps, see also summary in Figure 5.7: the first three are characterization steps to find the approximate 3D position (fitting step 1) as well as appropriate guesses for the refractive index n (fitting step 2) and the radius R (fitting step 3). In the fourth step, we used these positions and the average values of the radius and refractive index to determine the 3D position accurately (fitting step 4). We will now discuss these steps in detail. The subscripts correspond to the fitting step in which each parameter was determined.

Fitting step 1) For each frame, we determined the rough particle position (x_1, y_1, z_1), using reasonable estimates for radius R_e and refractive index n_e.

Fitting step 2) For the current frame, we determined z_2 and characterized the particle refractive index n_2, while keeping the (x_1, y_1) position and the estimated radius R_e fixed. Example distributions and average values of the refractive indices obtained in this fitting step are shown in Figure 5.1D.

Fitting step 3) While keeping the (x_1, y_1) position and estimated refractive index n_2 fixed, we fitted z_3 and the radius R_3. Example distributions and average values of the radii obtained in this fitting step are shown in Figure 5.1E.

Fitting step 4) Once initial positions (x_1, y_1, z_3) and particle properties (n_2, R_3) were determined for all frames, we calculated the time-averaged over all frames properties $(\langle n_2 \rangle_t, \langle R_3 \rangle_t)$. Lastly, we performed a least-squares fit for each frame allowing (x, y, z) to vary, keeping $(n = \langle n_2 \rangle, R = \langle R_3 \rangle)$ fixed, see Figure 5.1C for an individual sphere result.

Following this procedure, we minimized unwanted correlations between (z, R, n) that can arise when allowing all parameters to vary at once during the fit. For every frame, save the initial one, we used the values of the previous frame as starting guesses to speed up the (convergence of the) analysis.

Hologram analysis of dumbbells. The steps followed to obtain particle properties and positions of the dumbbells were analogous to those of the single spheres, only modified to additionally account for determining the dumbbell orientations. The scattering pattern of the dumbbell, calculated using the T matrix (or null-field) method [275], was modelled using the Python package HoloPy [274]. We used three characterization fitting steps to find the approximate 3D position and orientation (fitting step 1) as well as appropriate guesses for refractive indices $n^{(A)}, n^{(B)}$ (fitting step 2) and the radii $R^{(A)}, R^{(B)}$ (fitting step 3). $R^{(A)}, R^{(B)}$ are the radii of the respective 'A' and 'B' spheres of the dumbbell with refractive indices $n^{(A)}, n^{(B)}$. In the fourth and final step, we used these positions, orientations and the average values of the radii and refractive indices to determine the 3D position and orientation accurately (fitting step 4). We will now discuss these steps in detail. The subscripts correspond to the fitting step in which each parameter was determined.

Fitting step 1) In this first step, we determined $(x_1, y_1, z_1, \alpha_1, \beta_1, \gamma_1)$ of the center-of-mass (c.m.), with $(R_e^{(A)}, n_e^{(A)}, R_e^{(B)}, n_e^{(B)})$ set to reasonable estimates. Here, (α, β, γ) correspond to the three Euler angles using the ZYZ convention, while (x, y, z) denote the c.m. positions and, again, numbered subscripts the fitting step in which the parameter was obtained.

Fitting step 2) We determined the refractive indices and z-position $(n_2^{(A)}, n_2^{(B)}, z_2)$ while keeping $(x_1, y_1, \alpha_1, \beta_1, \gamma_1, R_e^{(A)}, R_e^{(B)})$ fixed.

Fitting step 3) Radii and z-position $(R_3^{(A)}, R_3^{(B)}, z_3)$ were fitted while $(x_1, y_1, \alpha_1, \beta_1, \gamma_1, n_2^{(A)}, n_2^{(B)})$ were kept constant.

Fitting step 4) After determining the initial positions (x_1, y_1, z_3), orientations $(\alpha_1, \beta_1, \gamma_1)$ and particle properties $(n_2^{(A)}, n_2^{(B)}, R_3^{(A)}, R_3^{(B)})$ for all frames, we calculated the time averaged properties $(n^{(A)} = \langle n_2^{(A)} \rangle_t, n^{(B)} = \langle n_2^{(B)} \rangle_t, R^{(A)} = \langle R_3^{(A)} \rangle_t, R^{(B)} = \langle R_3^{(B)} \rangle_t)$ over all frames. Then, we performed a least-squares fit for each frame again, where we allowed $(x, y, z, \alpha, \beta, \gamma)$ to vary, keeping $(R^{(A)}, R^{(B)}, n^{(A)}, n^{(B)})$ fixed.

With this procedure, we minimize unwanted correlations that can arise between $(\alpha, \beta, \gamma, z, R^{(A)}, R^{(B)}, n^{(A)}, n^{(B)})$ when allowing all parameters to vary at the same time. For every frame, save the initial one, we used the values of the previous frame as starting guesses to speed up the analysis. On that note, we additionally restricted the differences in rotation angles between subsequent frames to be smaller than $90 \deg$. Finally, we used the open-source TrackPy implementation [276] of the Crocker-Grier algorithm [277] to link the individual sphere positions between frames into continuous trajectories, ensuring a correct and consistent orientation of the dumbbell. Because we assign specific labels to both particles in the first frame of the video, we can distinguish the particles and, in turn, between positive and negative orientations, throughout the video.

Particle-plane separation. The position and orientation of the wall was accurately determined from the 3-dimensional positions of at least three spin coated spheres that were irreversibly fixed to the wall. This served two purposes: first, to speed up the fit of the mobile particles under study by providing a reliable lower bound on their axial position and, second, to accurately determine their height from the wall. A reference point on the plane $\mathbf{r}_p = (0, 0, z_p)$ and a normal vector $\hat{\mathbf{n}}_p$, see inset of Figure 5.1G, were determined for all the fixed particles for each frame. Using $\mathbf{r}_p$ and $\hat{\mathbf{n}}_p$, the particle-plane separation along the normal vector $\hat{\mathbf{n}}_p$ was determined for the mobile spheres, see also Figure 5.2A, from $\hat{\mathbf{n}}_p \cdot (\mathbf{r} - \mathbf{r}_p) - R$, with $\mathbf{r}$ and R the position and radius of the sphere, respectively. For the dumbbells, particle-plane separation was determined using the same procedure as the individual spheres; both the c.m. height, $h_{c.m.} =$

$\hat{\mathbf{n}}_p \cdot (\mathbf{r}_{c.m.} - \mathbf{r}_p)$, above the wall is reported as well as gap heights of both lower and upper sphere. Note that, since the orientation of the dumbbell can flip, the lower (or upper) sphere is not necessarily always the same physical particle.

Sphere height distribution. To model the height distributions of the spherical particles above the wall in Figure 5.2B, we used a model that combines electrostatic and gravitational effects [166, 220] to calculate the total height-dependent force $F(h_{c.m.})$ in the z direction (see also schematic in Figure 5.1F):

$$F(h_{c.m.}) = F_e(h_{c.m.}) + F_g \tag{5.1}$$

$$F_e(h_{c.m.}) = 64\pi\epsilon\kappa R \left(\frac{k_B T}{e}\right)^2 \tanh\left(\frac{e\Psi_w}{4k_B T}\right)$$

$$\tanh\left(\frac{e\Psi_p}{4k_B T}\right) e^{-\kappa h_{c.m.}} \tag{5.2}$$

$$F_g = -\frac{4}{3}\pi R^3 (\rho_p - \rho_f) g \tag{5.3}$$

with $h_{c.m.}$ the height of the center of the sphere, $F_e(h_{c.m.})$ the force due to overlapping electric double layers of the particle and the wall, F_g the gravitational force, ϵ the dielectric permittivity of water, k_B the Boltzmann constant, $T = 300\,\text{K}$ the temperature, e the elemental charge, Ψ_p and Ψ_w the Stern potentials of the particle and wall respectively, $\rho_p \approx 2.0\,\text{g cm}^{-3}$ the particle density, ρ_f the density of water, g the gravitational acceleration and κ^{-1} the Debye length. Based on the pH of our solution (pH$\approx$5.5), we find that the solution ionic strength is approximately $I = 10^{-5.5} = 3 \times 10^{-6}\,\text{M}$. Therefore, the Debye length is expected to be $\kappa^{-1}(\text{nm}) = 0.304/\sqrt{I(M)} = 175\,\text{nm}$ [278], in good agreement with the fit values of 100 to 230 nm that we obtained by fitting Equation 5.7 and 5.11 to the experimental data for both sphere and dumbbell particles, respectively. We neglected van der Waals interactions; we used the Derjaguin approximations for F_e. For the electrostatic potential, we used the Debye-Hückel approximation,

$$\Psi(r) = \Psi_s \frac{R}{r} \exp(-\kappa(r - R)), \tag{5.4}$$

with $\Psi(r)$ the electrostatic potential at a distance r from the center of the particle and Ψ_s the Stern potential. By setting $\Psi(r = 1/\kappa)$ equal to the here measured zeta potential of the spherical particles, see values in Part I of Results and Discussion, we calculated an approximate value for the Stern potential. This we subsequently used as a starting value for the least-square fit of the model to our experimental height distributions. For the wall, we converted the zeta potential value of $-55\,\text{mV}$ [143] to an approximate Stern potential using Equation 5.4.

For ρ_p and Ψ_p we used $\pm 2\sigma$ bounds; we fixed Ψ_w to the calculated value as discussed above, and put no restrictions on κ. To calculate the expected height distribution, we first obtained the electrostatic and gravitational potential energy, $\phi_e(h_{c.m.})$ and $\phi_g(h_{c.m.})$, respectively, from the force,

$$\phi_e(h_{c.m.}) = F_e(h_{c.m.})/\kappa \tag{5.5}$$

$$\phi_g(h_{c.m.}) = -F_g h_{c.m.}, \tag{5.6}$$

which we then used to derive the appropriate Boltzmann distribution,

$$p(h_{c.m.}) = A \exp\left(-\frac{\phi_e(h_{c.m.}) + \phi_g(h_{c.m.})}{k_B T}\right), \tag{5.7}$$

up to a normalization constant A [220].

Sphere near-wall diffusion. To test the validity of our measuring approach and the accuracy of our measured gap heights above the wall, we sought to compare our measurements to theoretical predictions. To this end, and since well-established predictions exist for spheres alone, we determined the translational diffusion coefficient for our sphere measurements as function of gap height. To calculate the translational diffusion coefficient with gap height in Figure 5.3, we proceeded as follows: instead of binning particle trajectories in time leading to bins with large height variations, we split all trajectories into shorter trajectories for which the gap height stayed within a certain height range, typically binning the total height range in bins of $0.30\,\mu m$ and $0.12\,\mu m$ for the 1.1 and 2.1 μm spheres, respectively. For each height bin, the in-plane mean squared displacement ($\langle\Delta r^2\rangle$) was calculated. The in-plane translational diffusion coefficient D and its error (standard deviation), was obtained from the first data point, typically an average of at least 300 measurements, of the MSD corresponding to a lag-time Δt of 0.053 s using $\langle\Delta r^2\rangle = 4D\Delta t$.

Modeling forces and torques on the dumbbell. To elucidate dumbbell behaviors above the wall already presented in Part II of the Results and Discussion section, we extended the sphere height distribution model described above to our dumbbells. We approximated the gravitational and electrostatic forces acting on a dumbbell, by assuming that the spheres comprising the dumbbell interact with the wall individually, as though the other is not present. That is, we used the expressions from Equations 5.1-5.3 on each sphere. This approximation ignores the distortion of the electrostatic double layer caused by the presence of the other sphere, but allows us to derive predictions efficiently. The consequences of this approximation have also been discussed in Part II of the Results and Discussion.

The total force and torque acting on the dumbbell c.m. are thus given by:

$$F_{DB} = F(h_1) + F(h_2) \tag{5.8}$$

$$T_{DB} = [(\mathbf{r}_1 - \mathbf{r}_{c.m.}) \times F(h_1)\hat{\mathbf{e}}_z + (\mathbf{r}_2 - \mathbf{r}_{c.m.}) \times F(h_2)\hat{\mathbf{e}}_z] \cdot \hat{\mathbf{e}}_x \tag{5.9}$$

with h_i, $\mathbf{r}_i$ the height and position of sphere i, θ_p the angle between the long axis of the dumbbell and the wall and $\hat{\mathbf{e}}_j$ the unit vector along the $j \in [x, y, z]$ axis, see schematic of Figure 5.1F. From the force expressions acting on the individual spheres of the dumbbell, we calculated the corresponding potential energy:

$$\phi_{DB}(h_{c.m.}, \theta_p) = -2F_g h_{c.m.} + \frac{2F_e(h_{c.m.})}{\kappa} \cosh\left(\kappa R \sin \theta_p\right). \tag{5.10}$$

Equation 5.10 assumes that both spheres have the same radius. This potential can be derived with respect to the $h_{c.m.}$ to obtain the force and to θ_p to obtain the torque. We subsequently used the potential to derive the appropriate height distribution for the dumbbell c.m. $p_{DB}(h_{c.m.}, \theta_p)$ up to a normalization constant,

$$p_{DB}(h_{c.m.}, \theta_p) \propto K \exp\left[-\frac{\phi_{DB}(h_{c.m.}, \theta_p)}{k_B T}\right] \tag{5.11}$$

$$p_{DB}(h_{c.m.}) \propto \int_{-\frac{\pi}{2}}^{\frac{\pi}{2}} d\theta_p \cos(\theta_p) K \exp\left[-\frac{\phi_{DB}(h_{c.m.}, \theta_p)}{k_B T}\right], \tag{5.12}$$

$$p_{DB}(\theta_p) \propto \int_{R}^{h_{max}} dh_{c.m.} K \exp\left[-\frac{\phi_{DB}(h_{c.m.}, \theta_p)}{k_B T}\right], \tag{5.13}$$

where we evaluated Equation 5.12 by numeric integration over all possible plane angles θ_p and Equation 5.13 by numeric integration over all possible heights $h_{c.m.}$; h_{max} was set to $5\,\mu\text{m}$. K represents the particle-wall hard-core interaction potential contribution to the Boltzmann weight: $K = 1$ if both spheres of the dumbbell are above the wall; otherwise $K = 0$. We calculated the probability as a function of the lowest dumbbell gap height (i.e., separation between the wall and the bottom of the lower sphere) by substituting $h_{c.m.} = h_{g,l} + R + R \sin \theta_p$ in Equation 5.12. Equivalently, for the upper gap height, we substituted $h_{c.m.} = h_{g,u} + R - R \sin \theta_p$ in Equation 5.12 to derive its distribution.

Appendix: Model for dumbbells consisting of spheres with unequal radii - plane height and orientation probability density

Here, we derive the electrostatic and gravitational forces on a dumbbell of two unequally sized spheres of radii $R = R_1, R_2$ and use it to calculate the potential energy and probability density function in terms of center-of-mass (c.m.) height $h_{c.m.}$ and plane angle θ_p. The force $F(R, h)$ on one of the spheres is given by Eq. 5.1. The net force $F_{DB}(R_1, R_2, h_{c.m.}, \theta_p)$ is then given by

$$F_{DB} = F(R_1, h_1) + F(R_2, h_2), \tag{5.14}$$

$$h_1 = h_{c.m.} + \frac{R_2^3(R_1 + R_2)\sin\theta_p}{R_1^3 + R_2^3} \tag{5.15}$$

$$h_2 = h_1 - (R_1 + R_2)\sin\theta_p \tag{5.16}$$

Eq. 5.14 can be integrated to give the potential energy $\phi_{DB}(R_1, R_2, h_{c.m.}, \theta_p)$

$$\phi_{DB} = \phi_{DB,g} + \phi_{DB,e} \tag{5.17}$$

$$\phi_{DB,g} = -(F_g(R_1)h_1 + F_g(R_2)h_2) \tag{5.18}$$

$$\phi_{DB,e} = \frac{B(R_1)}{\kappa}\exp[-\kappa h_1] + \frac{B(R_2)}{\kappa}\exp[-\kappa h_2]. \tag{5.19}$$

This potential can be derived with respect to the $h_{c.m.}$ to obtain the force and to θ_p to obtain the torque. We subsequently used the potential to derive the appropriate height distribution for the dumbbell c.m. $p_{DB}(R_1, R_2, h_{c.m.}, \theta_p)$ up to a normalization constant,

$$p_{DB}(R_1, R_2, h_{c.m.}, \theta_p) \propto K\exp\left[-\frac{\phi_{DB}}{k_B T}\right]. \tag{5.20}$$

K represents the particle-wall hard-core interaction potential contribution to the Boltzmann weight: $K = 1$ if both spheres of the dumbbell are above the wall; otherwise $K = 0$.

We show the results of Equations 5.18-5.20 in Figures 5.8 and 5.9 for the 2.2 μm and 4.2 μm dumbbells, respectively. The individual contributions of the gravitational and electrostatic potential to the net potential energy are shown in the first and second columns, respectively, in both figures. It is clear that the electrostatic potential is not negligible compared to the gravitational potential, therefore, the height from the surface is greatly influenced by electrostatic repulsion despite the relatively short — order of 150 nm — Debye length. Using the aforementioned

equations, we have here calculated the experimentally relevant size dispersity of 5%. We have chosen the R_1, R_2 in such a way that the total mass of the dumbbell is the same as the $R_1 = R_2 = R$ case. As a convention, positive angles denote the orientation where the sphere of the smaller radius R_1 is higher than the sphere of the larger radius R_2, as given in Equations 5.15-5.16.

Compared to the case where both spheres are equal, increasing the size dispersity between the spheres by 5% has no noticeable effect on the dumbbell behavior, since the most probable heights are only slightly shifted towards greater values, as evident from the slight differences in the calculated probabilities if the right-most panel of Figures 5.8B and 5.9B. This verifies that the differences observed between our experiment and model in Figure 5.6 do not stem from differences in the size between the spheres comprising the dumbbells, as the size dispersity in our experiment is well below the 5% size dispersity considered here. This strengthens our conclusion that the discrepancy between experiment and model may stem from higher-order electrostatic effects. However, note that the equations predict that a large size dispersity, as for example in the case of a highly anisotropic dumbbell (snowman particle) for which $R_2 \approx 2R_1$, would have two effects in comparison to the $R_2 = R_1$ symmetric dumbbell: firstly, the distribution around $\theta_p = 0$ is no longer expected to be symmetric, and secondly, a larger range of both angles and c.m. heights will become accessible. Such extreme size variations are not relevant to the experiments studied in this chapter. Yet, the equations that we provide for unequal sphere sizes may serve as a useful tool for broader research studies on near-wall dynamics of anisotropic dumbbells.
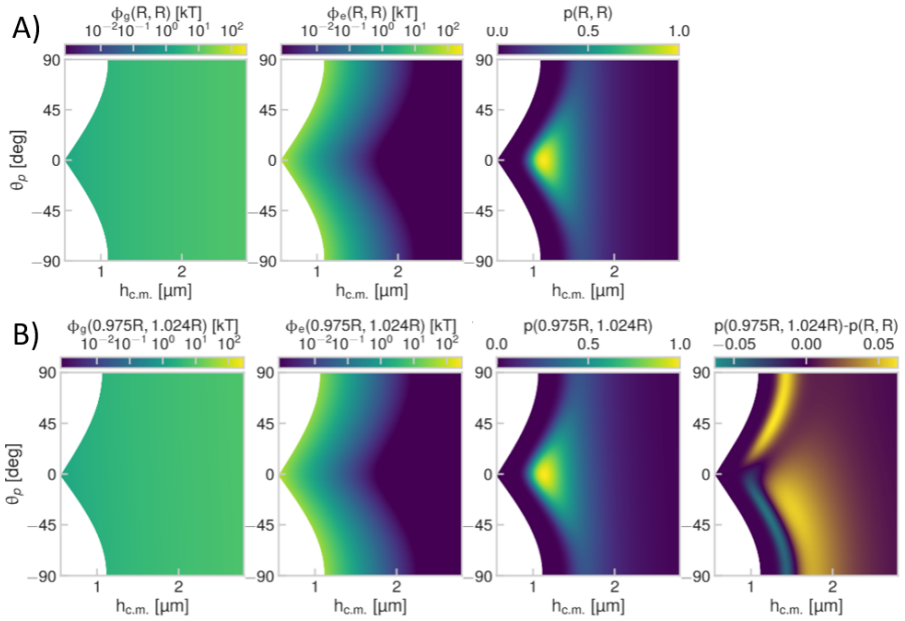
Figure 5.8: **Effect of sphere size dispersity on dumbbell PDFs: 2.2 μm dumb-bells (R= 0.54 μm).** All gravitational and electrostatic potentials were calculated according to Equation 5.18 and Equation 5.19, respectively. All probabilities were calculated according to Equation 5.20. A) Dumbbell of equal size spheres $R_1 = R_2 = R =$ with R= 0.54μm. Left to right: gravitational potential, electrostatic potential, and PDF. B) Dumbbell of spheres of unequal size $R_1 = 0.975R, R_2 = 1.024R$, with R=0.54μm as in (A). Left to right: gravitational potential, electrostatic potential, PDF, and probability difference $p(0.975R, 1.024R) - p(R, R)$ illustrating that a 5% dispersity in sphere size does not influence the behavior of the dumbbell of this size.
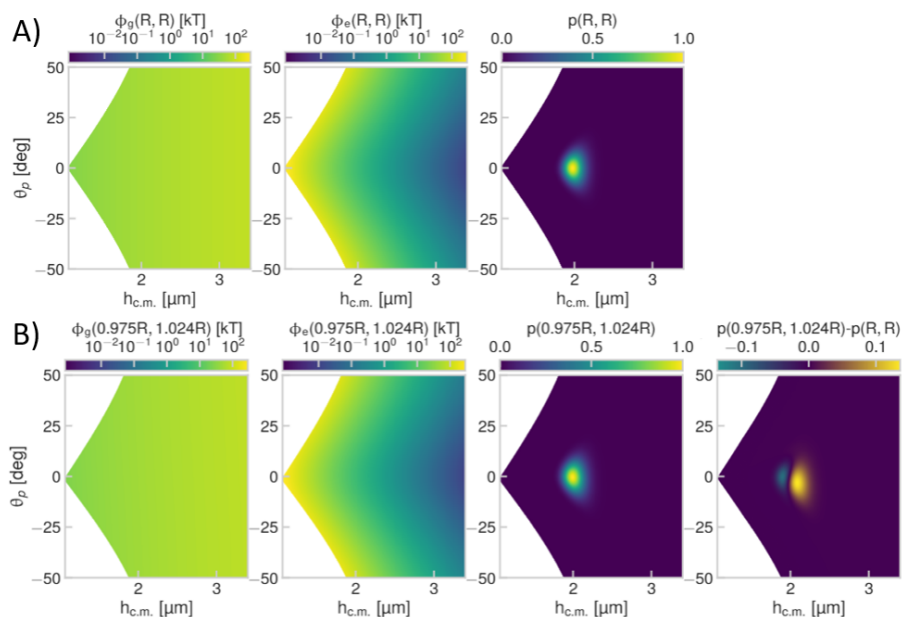
Figure 5.9: **Effect of sphere size dispersity on dumbbell PDFs: 4.2 μm dumb-bells (R= 1.04 μm).** All gravitational and electrostatic potentials were calculated according to Equation 5.18 and Equation 5.19, respectively. All probabilities were calculated according to Equation 5.20. A) Dumbbell of equal size spheres $R_1 = R_2 = R =$ with R=1.04 μm. Left to right: gravitational potential, electrostatic potential, and PDF. B) Dumbbell of spheres of unequal size $R_1 = 0.975R$, $R_2 = 1.024R$, with R=1.04 μm as in (A). Left to right: gravitational potential, electrostatic potential, PDF, and probability difference $p(0.975R, 1.024R) - p(R, R)$ again illustrating that a 5% dispersity in sphere size does not influence the behavior of the dumbbell of this size as in Figure 5.8.

6

Self-Propulsion of Symmetric and Asymmetric Dumbbells

Abstract

Biological microswimmers naturally occur in various shapes and forms. Their anisotropic shapes not only enable them to navigate complex biological environments, but have also been predicted to provide them with additional functions, such as viscotaxis and efficient swarming. Despite recent advances, research on synthetic swimmers has so far mostly been limited to spherical shapes and thus little is known about how shape affects motion in such systems. In this chapter, we study the catalytically self-propelled motion of dumbbell-shaped microswimmers near walls. We explore how shape anisotropy affects motion by fully characterizing the motion of dumbbells with different shapes, comprising symmetric, asymmetric and highly asymmetric lobes, for which the driving force is along the short dumbbell axis. We find that increasing particle asymmetry leads to circular motion. Particles move at similar translational speeds, while their angular speeds increase with particle asymmetry. In addition, we measure and compare the radius of particle trajectories to existing theory on asymmetric self-propelled particles near a wall. The good agreement that we find confirms that the radius of circular motion depends on particle shape and coating. Our findings advance the understanding of anisotropic microswimmer self-propulsion near walls and, in turn, may prove useful for increasing swimming efficiency, directionality, and motion control in patterned environments.

Introduction

Shape and motion are profoundly interconnected on the microscale. Actively self-propelled microspheres typically move in straight trajectories before their motion becomes randomized due to thermal noise. At elevated densities, such spheres [26, 44, 198] are known to exhibit activity-induced phase separation into dilute gas-like phases and dense highly dynamic cluster phases. Simulations predict that departure from the ideal spherical shape can result in various types of motions, which are hypothesized to aid in achieving precise motion control or even provide novel functionalities. For example, simulations show that by breaking swimmer symmetry, circular trajectories [84] and spiral [279] or chiral-type [280] trajectories can be obtained in two and three dimensions, respectively. In the case of particles that are asymmetric with respect to their propulsion direction, the propulsion force is predicted to lead to a velocity-dependent torque relative to the particle center-of-mass, due to a coupling between translational and orientational motion [84]. Moreover, swimmers that have non-uniaxial shapes are predicted to experience aligning torques, for example in viscosity gradients, showing that tactic behaviors may be obtained without the need for energy-consuming mechanisms [281]. Anisotropic shapes are also expected to influence swimmer interactions and collective swimmer behavior [280, 282]: for instance, torques on anisotropic swimmers are expected to influence activity-induced phase separation in active dumbbells [283] and rods [284]. Hence, answering how symmetry and shape couple to motility and motion patterns is important for understanding and ultimately controlling the behavior of single as well as collections of swimmers.

Nowadays, nonspherical swimmer shapes such as dumbbells and rods can be obtained in the laboratory through chemical synthesis, or even as we demonstrated recently [88], through 3D microprinting which allows for further flexibility in particle shape and in choosing the location of the active site on the particle. Thus, the aforementioned predictions from simulations can readily be tested in experiments employing synthetic model swimmers of nonspherical shapes.

Already, the limited number of studies on shape-dependent motion of synthetic particles have provided interesting insights into the effect of shape: 10-µm-long L-shaped particles in critical binary solvents exhibited circular trajectories near a wall upon light illumination, in agreement with predictions [84]. Along the same line, experiments on straight and bent electrophoretic microrods showed that trajectories changed from straight to circular when the particle shape changed from a straight to an L-shaped rod [85], while experiments on chemically propelled half-spheres showed a transition from straight to circular motion, in addition to changes in the particle orientation with respect to the wall with increas-

ing fuel concentration [87]. Chemically propelled prolate ellipsoids showed a transition from 3-dimensional passive Brownian motion at low fuel concentration to 2-dimensional active motion at intermediate fuel concentration and even spinning at high fuel concentration [86]. In addition, particle speed increased with ellipsoid length [86]. More recently, helical particles were found to swim slightly faster than spheres of the same cross-section and material, possibly due to the shape-induced coupling between translation along and rotation around their long axis in combination with the propulsion force that increased their rotation [88]. Finally, chemically propelled asymmetric dumbbells — with the smaller lobe being the catalyst — showed both quasi-linear as well as quasi-circular trajectories, and an increase in speed when increasing the size of the catalytic lobe [285]. However, in these experiments dumbbells were formed by sputtering Pt layers on silica spheres. These were subsequently annealed so that the Pt layer de-wet, thereby forming a sphere-like Pt particle attached onto the silica. Consequently, the size and shape of the catalytic site was highly irregular, especially when increasing the catalyst site size. Hence, to pinpoint the effect of shape on active motion, controlled experiments in which the shape is preserved while the degree of asymmetry with respect to the propulsion direction varies are highly desirable.

Here, we employ chemically synthesized symmetric and asymmetric dumbbell-shaped swimmers with well-defined shapes to gain insight into how shape contributes to the active motion. To this end, we experimentally study and fully characterize their catalytically propelled 2-dimensional motion near a wall. We find that increasing particle asymmetry leads to pronounced circular motions. Surprisingly, particles move at similar translational speeds, while their angular speeds strongly increase with particle asymmetry. We directly measured the radius of particle trajectories and, subsequently, compared our measurements to theory [84], which predicts that the radius of circular motion for asymmetric particles self-propelled near a wall solely depends on the diffusional properties of the particles determined by their shape, finding good agreement.

Results and Discussion

Through chemical synthesis, we prepared dumbbell-shaped particles with three different aspect ratios α — the ratio between the size of the larger lobe and the smaller lobe — by creating protrusions on polystyrene spheres following the method of Ref. [286]. That is, we prepared symmetric ($\alpha = 1.03 \pm 0.03$), asymmetric ($\alpha = 1.6 \pm 0.1$), and highly asymmetric dumbbells ($\alpha = 2.7 \pm 0.4$). In brief, we started from the same sphere batch of seeds and created three
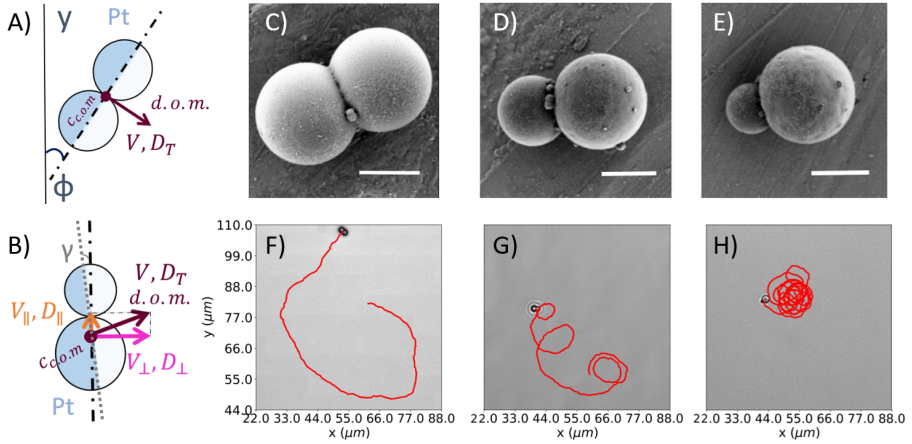
Figure 6.1: **Self-propelled motion of symmetric and asymmetric dumbbells moving in two dimensions above a wall. A-B)** Schematic representation of the motion: all dumbbells are half-coated with (4.8 ± 0.2) nm Pt. Their direction of motion, $d.o.m.$, is always away from their coating. We are interested in studying the velocity, V, and translational diffusion coefficient, D, of the dumbbell center-of-mass, $c_{c.o.m.}$. **A)** For a perfectly symmetric dumbbell with a symmetric coating, the Pt coating and hence the $d.o.m.$ is aligned perpendicular to the long dumbbell axis, see dashed line, due to the preparation method. **B)** For an asymmetric dumbbell, the coating is slightly asymmetric and forms an angle γ with respect to the dumbbell long axis, hence the $d.o.m.$ is not expected to be exactly perpendicular to its long axis. We additionally measure the motion parallel $(V_\parallel, D_\parallel)$ and perpendicular $(V_\perp, D_\perp)$ to the long dumbbell axis by projecting the displacement of its center-of-mass in the two directions, see orange and magenta vectors, respectively. The same holds for symmetric particles that are not perfectly half-coated: asymmetry in the coating will result in motion that deviates from the perpendicular to the long axis direction. **C-E)** SEM images of dumbbells with different aspect ratios, α, obtained via chemical synthesis and subsequent half-coating with Pt. The brighter particle sides indicate the coating. Scale bars are 1 µm. **C)** Symmetric dumbbells ($\alpha = 1.03 \pm 0.03$). **D)** Asymmetric dumbbells ($\alpha = 1.6 \pm 0.1$). **E)** Highly asymmetric dumbbells ($\alpha = 2.7 \pm 0.4$). **F-H)** Shape-dependent particle trajectories. A bright field image of the final position of each dumbbell is superimposed on its trajectory. The dimensions of the field of view in the microscopy images are the same. **F)** Symmetric dumbbells move in open straight trajectories, randomized by thermally induced changes in direction. Image shows a 21 s trajectory, $V = (7.2 \pm 2.1)$ µm/s, before leaving the field of view. **G)** Asymmetric dumbbells move in quasi-circular trajectories. Image shows a 25 s trajectory, $V = (7.3 \pm 2.0)$ µm/s. **H)** Highly asymmetric dumbbells move in circular trajectories. Image shows a 25 s trajectory, $V = (8.3 \pm 2.6)$ µm/s.

dumbbell batches with different sizes in their protruded spheres. The lobe sizes were (1.74±0.05) and (1.69±0.04) µm for the symmetric, (1.59±0.07) and (1.00±0.05) µm for the asymmetric, and (1.56±0.07) and (0.59±0.08) µm for the highly asymmetric dumbbells, as measured from scanning electron microscopy (SEM) images. Details on dumbbell preparation are provided in the Methods. Subsequently, we sputter coated all dumbbells from above with a (4.8±0.2) nm thick Pt coating while they laid flat on glass substrates, i.e., we half-coated the dumbbells along their long-axis direction (see Figures 6.1A-B for a schematic and Figures 6.1C-E for example SEM images). As all dumbbells laid flat on the substrate during the coating procedure, for an asymmetric dumbbell we expect, due to the size asymmetry between its two lobes, that the Pt coating will be positioned at an angle with respect to its long axis, see γ angle in Figure 6.1B. From the size ratios, we calculated γ to be 3°, 13°, and 27° for the symmetric, asymmetric, and highly asymmetric dumbbells, respectively.

To investigate the effect of shape asymmetry on self-propelled motion, we dispersed all dumbbells in 10% aqueous H_2O_2. The particles quickly sedimented to the glass substrates. We recorded their two-dimensional motion, in the direction away from their long axis, after settling above the substrate, and subsequently analyzed their motion using python routines. We found that the self-propelled trajectories depended on dumbbell morphology, see Figures 6.1E-G. Symmetric dumbbells, with $\alpha \approx 1$ as in Figure 6.1C, tended to move in straight lines at short times, see Figure 6.1F, while their motion became random at longer times due to thermal noise. Over similar timescales, particles that were asymmetric with respect to their propulsion direction, see Figures 6.1D and 6.1E, exhibited circular motion. The circularity in the trajectories became more pronounced with increasing particle asymmetry, with the highly asymmetric dumbbells typically moving in small consecutive circles, see Figures 6.1G and 6.1H for dumbbells with $\alpha \approx 1.6$ and $\alpha \approx 2.7$, respectively.

We wished to investigate whether theoretical predictions on the circularity of asymmetric particle trajectories hold for our catalytic dumbbells of different shapes near a wall. To this end, we characterized the particles' motion as a function of dumbbell shape, see Methods for details on motion analysis. First, we examined the translational components of the motion, i.e. the translational velocity, V, and diffusion coefficient, D_T. These parameters were obtained from fitting the mean-squared displacement of the dumbbell center-of-mass, determined with the software package trackpy, with $\Delta r^2 = 4D\Delta t + V^2\Delta t^2$ using the method of Ref. [30]. Surprisingly, we found that V remained rather constant with increasing aspect ratio α in Figure 6.3A. This constancy is initially unexpected, based on the well-known speed decrease of spherical particles with size [58, 157], since the overall size here decreases with increasing aspect ratio.

However, at the same time, the larger, symmetric, dumbbells have a larger surface area covered by the Pt which may compensate for the similarity in particle speeds. We also found that the translational diffusion coefficient D_T increased with α as shown in Figure 6.2D.

Due to asymmetries in either the metal coating or the dumbbell shape, motion of the dumbbell center-of-mass will slightly deviate from the motion perpendicular to the dumbbell long axis direction, as shown in the schematic of Figure 6.1B. Therefore, to gain further insight in dumbbell self-propulsion, the displacement vector of the center-of-mass is projected parallel and perpendicular to the dumbbell long axis yielding the center-of-mass displacements in the respective directions, see the orange and magenta vectors in Figure 6.1B. The parallel and perpendicular mean-squared displacements were then calculated from the respective displacements in time. By doing so, we obtained the motion parameters $(V_\perp, D_\perp)$ and $(V_\parallel, D_\parallel)$ in the parallel and perpendicular directions from parallel and perpendicular mean-squared displacement fits [30]. As in the translation speeds V, we find that the perpendicular speeds are, within error, similar for all shapes, see Figure 6.2B. Since this direction typically coincides with the direction of propulsion, this suggests that the propulsion force is also similar, in spite of the difference in dumbbell sizes and coating surface coverage. In the parallel direction, however, speed increases with aspect ratio in Figure 6.2C. The diffusion coefficients in the perpendicular, $D_\perp$, and parallel directions, $D_\parallel$ are shown in Figures 6.2E and 6.2F, respectively.

In contrast to the shape-independent translational velocity, the angular velocity, ω, strongly increases with aspect ratio, see Figure 6.2G. In addition, we find that the timescale for rotation, τ_R, obtained from the rotational diffusion coefficient, D_R, via $\tau_R = 1/D_R$, strongly decreases with aspect ratio, see Figure 6.2H. The rotational parameters ω and D_R were obtained from fitting the mean-squared angular displacement of the dumbbell following Ref. [83]. For the angular displacement, we considered the angle ϕ, defined as in Figure 6.1A. That is, we calculated the angle between the long axis of the dumbbell and a fixed angle in the laboratory frame — y axis — in time. To obtain a quantitative relation between translational and rotational velocity, we plotted V as a function of ω for individual dumbbells of each shape in Figure 6.2I. The dashed lines represent least-squares fits with $y = \beta x$. We find that the slope of the curves, which can be interpreted as a measure of curvature of the particle trajectories, decreases with aspect ratio: the respective slope, β, for the symmetric (blue), asymmetric (red) and highly asymmetric (black) dumbbells is (74 ± 11) µm, (28 ± 4) µm, and (17 ± 2) µm.

We furthermore examined the orientation of the self-propelled dumbbells, θ, in
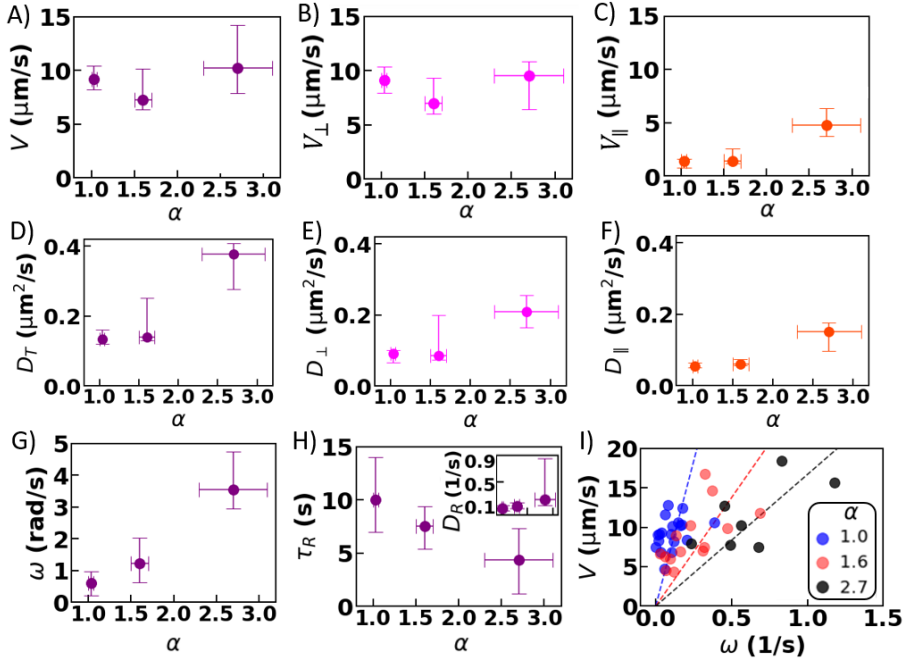
Figure 6.2: **Translational and rotational self-propelled dumbbell motion.** A-H) Dumbbell properties as function of the aspect ratio, α. Each reported value is the median of averaged values obtained from individual particles of the same α, the errors reporting first quartiles. **A)** Translational velocity, V. **B)** Translational velocity perpendicular to the dumbbell long axis, $V_\perp$. **C)** Translational velocity parallel to the long axis $V_\parallel$. **D)** Translational diffusion coefficient, D_T. **E)** Translational diffusion coefficient perpendicular to the dumbbell long axis, $D_\perp$. **F)** Translational diffusion coefficient parallel to the dumbbell long axis, $D_\parallel$. For definitions of all the above parameters see Figure 6.1B. **G)** Angular velocity, ω, obtained following Ref. [83] by fitting the mean-square angular displacement of ϕ, the angle between the dumbbell long axis and a fixed axis in the microscope frame, see Figure 6.1A for a schematic. **H)** Timescale for rotation, τ_R (main), and rotational diffusion coefficient, D_R (inset), with D_R obtained as described in (G). **I)** Translational velocity plotted against angular velocity, with the color denoting the aspect ratio. Each data point shows average values that correspond to an individual particle. Dashed lines are least-squares fits with $y = \beta x$, with β (74 ± 11) μm (blue), (28 ± 4) μm (red), and (17 ± 2) μm (black).

the particle-centered frame by considering the angle between the displacement vector of the dumbbell center-of-mass $\Delta \mathbf{r}$ in consecutive frames (d.o.m.) and the perpendicular component of the velocity, see Figure 6.3A. For a symmetric dumbbell and symmetric coating we expect the two vectors to coincide, i.e. θ to be zero. The θ values that we obtain for symmetric dumbbells that move in straight trajectories, are indeed close to 0°, while θ increases with aspect ratio, see Figure 6.3B, as expected from particle trajectories. We notice that for the symmetric and asymmetric dumbbells these angle values are similar to the calculated γ angles between the long and the Pt coating axes (see also Figure 6.1), while for the highly asymmetric dumbbells θ is higher than γ. If the apparent difference in direction of motion from the perpendicular orientation would solely stem from the asymmetric coating, we would expect that $\theta = \gamma$. However, the observed difference in Figure 6.3B, suggests that particle shape also contributes to the angular motion. Moreover, we find that θ increases with the angular particle velocity in Figure 6.3C. However, we note that translational velocity is unaffected by the orientation of the dumbbell in the particle-centered frame (Figure 6.3D).

Lastly, we study the average local curvature, LC, of particle trajectories, see Methods for details on trajectory characterization using a Savitzky Golay filter that performs polynomial curve fits to smoothen out the noise. We find that LC increases with increasing aspect ratio in Figure 6.4A, in line with our observations on particle trajectories shifting from straight to circular with increasing dumbbell asymmetry, see Figure 6.1. We additionally obtain the radius, R with $R = \frac{1}{LC}$, of particle trajectories from the average curvature values that we determined. We found that the radius of the trajectory decreases with the dumbbell
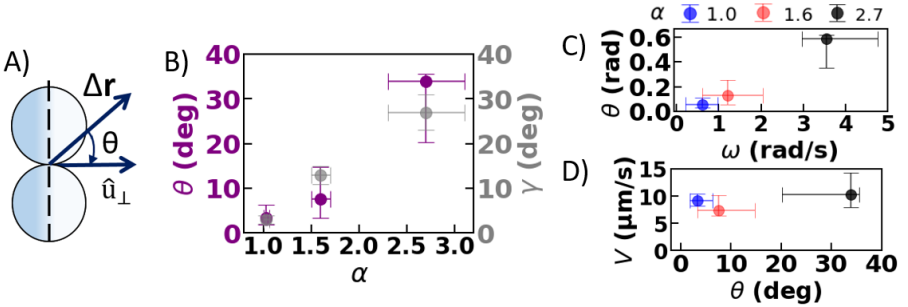

Figure 6.3: **Orientation of self-propelled dumbbells. A)** The orientation in the particle frame, θ, is the angle between the normal vector of the dumbbell long axis, and the displacement vector. **B)** Orientation θ as a function of aspect ratio, α. **C)** Orientation θ, as function of angular velocity, ω. **D)** Translational velocity, V, as function of θ. All values reported here are medians of averaged values obtained from individual particles of the same α, the errors report first quartiles.

angular velocity in Figure 6.4B. Note that the translational velocity remains un-affected by the radius of the trajectory in Figure 6.4C.

We directly compare our findings for the radius with the theoretical prediction for the radius of asymmetric particles from Ref. [84]. By taking into account the presence of a substrate using the Stokeslet close to a no-slip boundary to model the hydrodymanic interactions, Ref. [84] showed that instead of using the generalized mobility tensor for bulk motion [287], the radius of the parti-
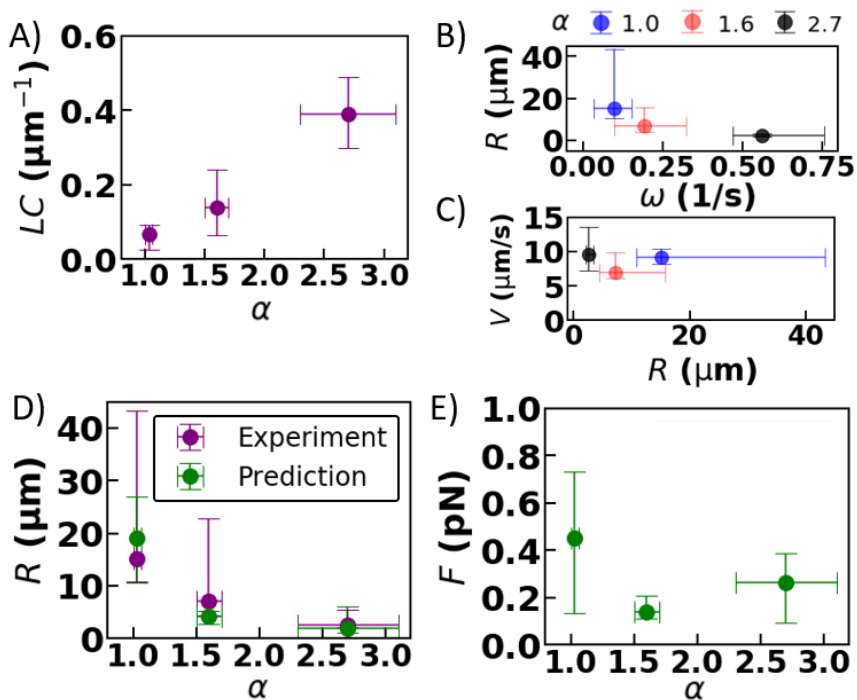

Figure 6.4: **Characterizing the trajectory of self-propelled dumbbells: local cur-vature and radius. A)** Average local curvature, LC, as function of aspect ratio, α. **B)** Radius of trajectory, R, with $R = 1/LC$, as function of angular velocity, ω. **C)** Translational velocity, V, as function of R. **D)** R with α, as measured from our experiments (purple) and as obtained using theory (green) [84]. **E)** Effective propulsion force, F, with α, for our dumbbells calculated using the theory of Ref. [84] and experimentally measured values for ω, D_R, and ℓ. All values re-ported here are medians of averaged values obtained from individual particles of the same α, errors report first quartiles.

cle trajectory near a wall may be obtained with the expression $R = |\frac{D_\perp}{\ell D_R}|$, where ℓ is the length difference between the middle of the metal coating axis and the particle center-of-mass projected on the long axis. We, thus, used this expression to calculate the predicted radius that corresponds to our dumbbells with different aspect ratios from our measured values of $D_\perp$ and D_R, see insets of Figures 6.2E and 6.2H, respectively. For the ℓ parameter, we used 0.05 μm (symmetric), 0.20 μm (asymmetric), and 0.27 μm (highly asymmetric dumbbells). These approximate values were obtained from the distance difference between the middle of the long axis of our dumbbells, the length of which was determined from SEM images, and the dumbbell center-of-mass position, see Methods for center-of-mass determination. We found a good agreement between the measured (purple points) and the predicted values (green points) for the radius in Figure 6.4D. Finally, we calculated the effective propulsion force for dumbbells of different shapes. According to Ref. [84], the force, F, near the wall is given by $F = \frac{k_B T \omega}{D_R \ell}$. By employing ω and D_R values shown in Figures 6.2G and 6.2H, respectively, and ℓ values mentioned above, we found that the propulsion force is ≈ 0.1 pN (Figure 6.4E). Together, these findings confirm the expectation that the radius of trajectory depends on particle shape, while it is independent of propulsion strength [84], although the latter is surprising due to differences in dumbbell size and Pt surface coverage.

Conclusions

We examined the motion of self-propelled dumbbells with different aspect ratios, from highly symmetric to highly asymmetric shapes. We found clear differences in dumbbell motion, which switched from straight to circular with increasing particle asymmetry, due to their asymmetric shape and coating. By fully quantifying their motion properties, we discovered that although our dumbbells propel themselves with similar translational velocity, their angular velocity strongly increases with particle asymmetry. We further measured the local curvature and corresponding radii of their trajectories, and found that the radius strongly decreases with particle asymmetry in line with our observations. Most importantly, the radii that we measured were in good agreement with theoretical predictions on asymmetric particles moving near a wall.

According to theory, the translational and rotational motion of asymmetric particles are coupled under an intrinsic force that sets the speed [84], while, due to the anisotropic shape, an additional velocity-dependent torque is generated. Our measurements on differently shaped particles, confirmed that the radius of circular motion depends on particle shape and coating [84], while it does not

depend on propulsion strength. However, that propulsion strength remained roughly the same for all considered shapes, i.e. sizes and metal surface coverage, contrasts spherical particle behaviors for which propulsion strength is found to depend on these parameters.

Overall, our findings showed that departure from the spherical shape, predominantly used in microswimmer studies, leads to significant effects on the active motion on the individual particle level. The dumbbell shapes used here may prove to be of great interest, because although they are considerably more complex than spheres, they can be modelled in simulations. A future comparison to simulations can aid in predicting their collective behavior, typically remaining experimentally largely unexplored due to limitations in fuel consumption.

Acknowledgements

Methods

Dumbbell synthesis. First, linear polystyrene (PS) spheres were synthesized by a dispersion polymerization method and crosslinked by the addition of a swelling solution containing 90:10 v:v styrene:TPM, 1.5% v/v divinylbenzene (DVB) and 2 wt% azobisisobutyronitrile (AIBN), following the protocol of Ref. [288]. Subsequently, to form the dumbbells, protrusions were created on the spheres following the method of Ref. [286]. Here, 25 mg of AIBN and 0.567 ml of 0.5% aqueous hydroquinone (HQ) were added to 3.5 ml of aqueous 2 wt% solution of poly(vinyl alcohol) (PVA) and a variable amount of monomer solution consisting of 90:10 v:v styrene:TPM. This mixture was then emulsified at 8,000 rpm for 2 min and 10,000 rpm for 30 s using an IKA Ultra-Turrax disperser. 1.5 ml of 4.9 wt% crosslinked PS was added to this emulsion while vortexing. The emulsion was bubbled with N_2 for 20 s, sealed, and rotated in the dark for 24 h. After this second swelling step, the emulsion was heated while rotating in an oil bath at 80 deg for 24 h. The size of the protrusion, and thereby the dumbbell, was controlled by controlling the swelling ratio, which is defined as the mass of the added monomer divided by the mass of the polymer colloids. The swelling ratios for the three different batches used here were 1.25, 1.5 and 2.75. The dumbbells in the resulting particle batches had a long axis of (2.2 $\pm$
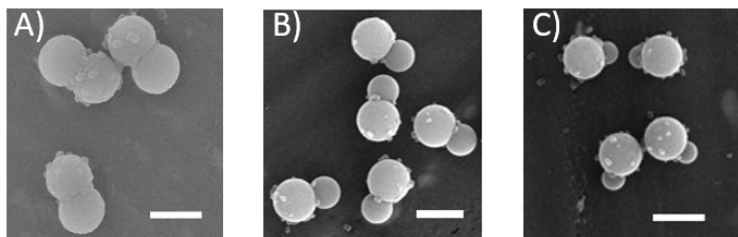
Figure 6.5: Scanning electron microscopy images of synthesized dumbbell particles, also used for particle characterization. Scale bars are 2 μm.

0.1) μm, (2.6 ± 0.1) μm, and (3.1 ± 0.1) μm, respectively, with the corresponding aspect ratios — i.e. size of the larger lobe divided by the size of the smaller lobe — being (2.7 ± 0.4), (1.6 ± 0.1), and (1.03 ± 0.03), respectively. The batch sizes and corresponding aspect ratios were measured from SEM images by sizing 27, 25, and 23 particles, respectively, see Figure 6.5 for examples.

Preparation of Pt-coated dumbbells. To prepare Pt-coated particles, we followed the same procedure as in the previous chapters, which — briefly — requires drying the particles on glass slides, sputter-coating with Pt, and redispersion in water using ultrasonication. Here, the drying process prior to Pt-coating application on the glass, in combination with the redispersion step, initially lead to adsorption and deformation of the PS/TPM dumbbell surfaces as well as to large Pt flakes being released in the samples during redispersion. We therefore took additional steps to ensure that dumbbell surfaces remained smooth at all times, and that the Pt was properly adhered on the dumbbells while it remained on the glass during redispersion. The first step was to clean the dumbbell surfaces by washing them thoroughly (x6) in MilliQ (MQ) water. The second step was to treat the glass slides on which the dumbbells were deposited, prior to Pt coating. For this, we followed a protocol from Ref. [289]: the slides were successively immersed for 1 min in six separate containers with 1 M aqueous KOH, MQ, 1% w/w aqueous poly(ethyleneimine), MQ, 1% w/w aqueous poly(styrenesulfonate) salt, and MQ. To remove excess polymer and salt, they were then cleaned (x6) in MQ and subsequently placed in MQ for 10 min, and dried with N_2. Dumbbells were subsequently either spin coated, or drop-casted and spread, from ethanol dispersions on the treated slides. To ensure a homogeneous Pt coating, we inspected proper spreading of particles on the glass slide for each batch. To ensure proper adhesion when applying the Pt coating with a Cressington sputter-coater, we first sputter coated from above a thin layer of (0.6 ± 0.2) nm of Chromium, followed by (4.8 ± 0.2) nm of Pt/Pd (80:20), while rotating the flat stage with the slides, for even Pt distribution across the slides.
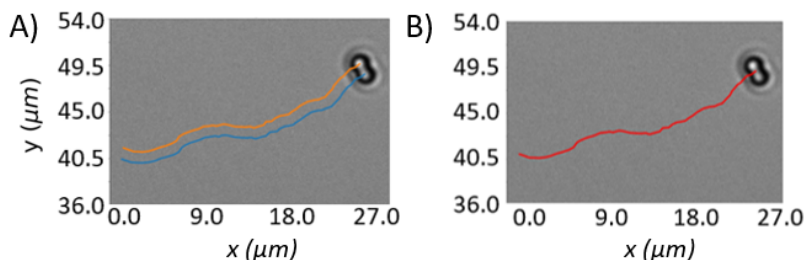
143

Figure 6.6: **Example of the two-step process performed to track the dumbbells under study. A)** The trajectories of the two lobes of the dumbbell particle over 50 frames ($\approx$ 2.6 s) of a symmetric dumbbell are shown in blue and orange. A light microscopy image of the dumbbell is superimposed at 0 s. **B)** The trajectory of the center-of-mass of the same dumbbell as in (A) during the same frames, shown in red. A light microscopy image of the dumbbell is also superimposed.

After these steps, the Pt-coated dumbbells, see Figure 6.1 as an example, were removed from the slides and redispersed in water by $\approx$ 15 min sonication. The colloids were subsequently washed and stored in water.

Imaging. Pt-coated dumbbells were dispersed in 10% aqueous H_2O_2 at dilute particle concentration. Their motion was recorded with an inverted Nikon Eclipse Ti microscope equipped with a 60x long working distance objective (S Plan Fluor ELWD, NA 0.7) and/or an 100x oil objective (APO TIRF, NA 1.49) above glass cover slips. Cover slips were purchased from VWR and used as received. For the highly asymmetric dumbbells whose imaging required a higher magnification, the zoom 1.5x setting was used (0.06 µm/px). Movies were acquired in the xy-plane at a frame rate of 19 fps typically for 25 s. For the symmetric dumbbells which tend to move in straight lines, movie duration is sometimes shorter due to them leaving the field of view. Measurements were performed in the dark and typically within the hour after sample preparation.

Tracking. Tracking was performed using Trackpy [141]. First, the two spheres comprising the dumbbells were located for each frame, and the individual sphere positions were linked in time, see Figure 6.6A. For the asymmetric dumbbells, the parameters used for tracking their comprising spheres were different, due to the different sphere sizes. The sphere locations were then used to track the center-of-mass of the dumbbell throughout the measurement, see Figure 6.6B, which due to symmetry is always located on the line that passes through the centers of the separate spheres. To determine the center-of-mass position, $c_{c.o.m.}$, the average position of the two spheres was used for the symmetric dumbbells, while for

the asymmetric dumbbells the expression $c_{c.o.m.} = \frac{m_{Sm}c_{Sm}+m_B c_B}{m_{Sm}+m_B}$ with m the sphere mass and c the position of the sphere center, was used. Subscripts "Sm" and "B" denote the small and big sphere, respectively. For similar sphere mass density, $\frac{m_{Sm}}{m_B} = \left(\frac{r_{Sm}}{r_B}\right)^3$, with r the sphere radius, and thus, $c_{c.o.m.} = \frac{c_{Sm}A^3+c_B}{A^3+1}$ with $A = r_{Sm}/r_B$.

Translational and angular velocity. After calculating the center-of-mass position in time as discussed above, we subsequently calculated the mean square displacement of the center-of-mass of the dumbbell. Its translational velocity and corresponding diffusion coefficient was subsequently calculated by fitting its short-term mean-square displacement (MSD) up to ≈ 0.2 s [30]. We cross-checked that the time derivative of the displacement method employed in chapter 4 yielded similar results, with the average velocity value obtained from the MSD method being lower by 4%, due to the MSDs containing additional information about the passive component of particle motion. To determine the angular velocity, ω, of the particles, we first extracted the orientational coordinate, ϕ, as function of time from our movies, and subsequently calculated and analyzed the mean-square angular displacement (MSAD, $\Delta\phi^2(t)$) that we obtained from Trackpy, using the Langevin description of Ref. [83]. That is, we performed a least-squares fit of the MSAD with $\Delta\phi^2(t) = 2D_R t + \omega^2 t^2$, where D_R is the rotational diffusion coefficient. From D_R we additionally obtained the rotational diffusion time, τ_R, via $\tau_R = 1/D_R$. Here, the angle ϕ in each frame is the angle between the vector that goes through the long axis of the dumbbell, and a fixed vector aligned with the reference vector (y-axis) of the microscope frame, i.e. ϕ describes the dumbbell orientation in the laboratory frame.

Local curvature of the trajectory. The (local) curvature between two points S_1 and S_2, with both points being the position of the dumbbell center-of-mass in consecutive frames, see Figure 6.7A for a schematic, is obtained by dividing the angular difference $d\beta$ between the tangent lines of points S_1 and S_2 by the path length of the curve between the two points; following Ref. [290], the curvature is calculated using the expression $LC = \frac{d\beta}{dS} = \frac{x'y''-y'x''}{(x'^2+y'^2)^{3/2}}$. The prime in this expression denotes derivation with respect to time, thus the velocity and acceleration of the center-of-mass is calculated in the x and y directions for each frame. For a straight trajectory, LC between the points along the trajectory is zero. An example center-of-mass trajectory of an asymmetric dumbbell and the corresponding LC calculated with the above expression are shown in the top panels of Figures 6.7B and 6.7C, respectively. Due to the dumbbell trajectories being influenced by Brownian motion, the resulting LC data are noisy. We thus filter out the effects of the noise by applying a Savitzky-Golay filter, see Ref. [291, 292], on the trajectory and repeat the LC calculation. The filter smoothens the data without
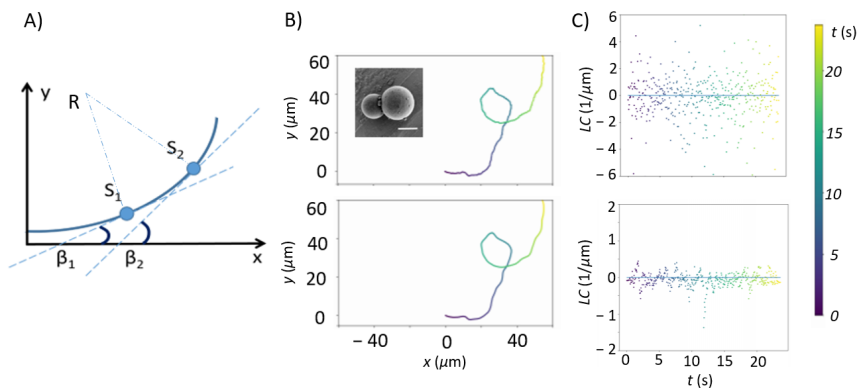
Figure 6.7: **Local curvature determination and application of Savitzky Golay (SG) filter on dumbbell trajectory. A)** The local curvature between two points along the center-of-mass trajectory is obtained from the angular difference ($\beta_2 - \beta_1$) between the tangent lines of the two points divided by the path length ($S_2 - S_1$). **B)** Trajectory without (top) and with (bottom) the SG filter of an asymmetric dumbbell (inset). **C)** Local curvature without (top) and with (bottom) the SG filter for the same dumbbell as in (B). The data in (B, C) is colorcoded with respect to time (in s) after the beginning of the measurement.

disturbing the underlying signal, see the bottom panels of Figures 6.7B and 6.7C for the filtered trajectory and corresponding LC values for the same trajectory as in the top panel. Filtering is achieved using built-in functions in python, which perform least-squares fits of a low order polynomial through subsets of the data (windows) to smoothen the dataset: the local polynomial function is fitted to the input data in the window, and a new replacement data point is calculated using the polynomial function; the process repeats for all windows.

7

Conclusions and Outlook

Biological swimmers are not only omnipresent in nature but are also instrumental in numerous processes relating to the production of food and fuel, bioremediation, and human health, and are thus of great importance for both fundamental science and industrial applications. Heavily inspired by their efficient propulsion strategies, self-regulating abilities, and adaptability within complex and crowded environments, an entire field of research has emerged in recent years aiming at developing, understanding and controlling synthetic swimmers at the microscopic scale.

To gain insights into synthetic microswimmer motion as is desirable for fundamental research and applications, in this thesis we studied the motion of synthetic model microswimmers near confining boundaries. Our model swimmers have been colloidal particles equipped with a Pt coating which covers half their surface that achieve self-propulsion in aqueous H_2O_2 environments *via* catalytic reactions taking place on the Pt. These reactions create chemical gradients which give rise to fluid flows around the particles, moving them in turn in the direction away from the Pt.

In **chapter 2**, we explored the behavior of these model swimmers near planar walls. Swimmers have the tendency to propel themselves downwards and thus quickly reach the bottom wall of their container; upon encountering the wall, they typically remain self-propelling parallel to it. Through changing the material properties of the wall, we found that walls impact their speeds. Our modeling showed that this effect can stem from the interplay between the hydrodynamic boundary condition on the wall and the chemical species produced by the reaction interacting with the wall, on the basis of an osmotic coupling mechanism. We concluded that fluid flows along the wall in conjunction with the flows along the swimmer surface are important in determining microswimmer speeds. Therefore, we proposed that wall effects can at least in part explain disparate speeds in the literature under similar conditions.

In **chapter 3**, we furthermore developed a diffusion-based height analysis to extract swimmer-wall separations. With this method, we found that microswimmers move in close proximity to the wall at gap heights of less than 300 nm, in agreement with previous observations of swimmers being stopped by steps with heights of a few hundred nanometers and with wall-dependent speed findings [103, 105, 155, 156]. In addition, we found that system parameters typically affecting the height in passive Brownian systems are less important for the active system; that is, catalytic particles tend to fixed heights thus exhibiting ypsotactic behavior. Despite the relatively unaffected height, we additionally found a speed decrease with increasing salt concentration. We proposed a wall-centric picture as an alternative to self-electrophoresis that was previously reported in

the literature: ionic diffusioosmosis along the wall stemming from long-range H_2O_2 gradients on the wall creates a flow that counteracts particle motion hence causing the speed decrease. Based on all the above, we overall concluded that walls are important factors in controlling swimmer motion and should be taken into account in future modeling.

As a next step, we exploited the swimmers' affinity for surfaces and further restricted their motion along closed one-dimensional paths in **chapter 4**. By printing secondary microstructures on the planar wall, we introduced additional geometric constrains for the swimmers which tended to accumulate on said structures. We were in turn able to identify a plethora of activity-induced interactions, caused by an effective potential stemming from a competition between chemical and hydrodynamic coupling. These interactions ranged from collective swimmer speedups for swimmers co-moving along the structures to the active assembly of swimmer chains that exhibited highly dynamic behaviors, with the latter being tunable through the local path curvature. We concluded that the concept of cooperative motion, a crucial element of biological swimmer systems, is even identifiable in synthetic active systems, opening the door towards exploiting cooperation for applications inside complex environments requiring increased swimming efficiency and directionality.

Finally, we explored the effect of swimmer shape by studying the near-wall motion of symmetric and asymmetric dumbbell swimmers. Unlike their passive state motion where preferred angles with the wall can be observed as in **chapter 5**, in the presence of activity dumbbell-shaped particles moved strictly in two dimensions in the direction perpendicular to their long axis. In **chapter 6**, we found highly tunable swimming trajectories spanning from straight-like to circular depending on the degree of particle asymmetry with respect to the propulsion direction. We concluded that, apart from employing confinement for path patterning, microswimmer shape is another promising route for tuning the directionality of active motion, allowing for different navigation strategies and control in the microscale.

Outlook:

Following the work presented in this thesis, we hereby propose routes for future research on synthetic microswimmers. We and other groups have reported on the importance of wall effects on microswimmer speeds [103, 105, 155, 156]. However, due to their gravitactic as well as ypsotactic tendencies, swimmer measurements in bulk are lacking. Such measurements could prove useful in identifying missing details of the propulsion mechanism of catalytic swimmers, as they would allow for propulsion force measurements in the absence and presence of salt near and away from walls. We have already briefly explored the

possibility of employing an optical-tweezer setup to trap such particles near the wall as well as in the bulk of the fluid. Although this approach is typically viable for non-coated particles, we were not able to efficiently utilize it on our colloids equipped with metallic caps; the reason being that once the asymmetric colloid feels the trap, the radiation pressure aligns it such that it is rapidly propelled out of the trap. However, it can still be worthwhile to attempt systematic experiments to finely tune experimental parameters such as size, metal coating thickness, coating surface coverage, or the setup itself, i.e. to adjust the trap radius through defocusing of the laser beam and laser power. Another promising possibility would be to employ acoustic levitation, see Ref. [293] for a review on acoustic propulsion. Although this technique has predominantly been employed in bimetallic nano- and microrod systems, acoustic trapping has also been utilized on polystyrene-Pt spheres which otherwise self-propelled along the air-water interface [294].

A highly interesting research avenue, of which we have only scratched the surface in our current work, is that of microswimmers inside patterned environments [106]. So far, these studies have been limited to either spherical particles or microrods. Combining our works on spherical swimmers along microprinted structures with that on symmetric and asymmetric dumbbell swimmers could yield novel insights into microswimmer interaction with boundaries; for example, we may be able to understand what is the combined effect of particle curvature and wall curvature on active motion by studying the behavior of symmetric and asymmetric dumbbells inside microprinted environments that employ structures with intricate shapes as for example in Figure 7.1A. Such effect could play a crucial role in fully unraveling the impact of confinement on microswimmer motion and, in turn, in further harnessing active particles inside, e.g., lab-on-a-chip devices, as well as aid in a deeper understanding of how biological swimmers are able to navigate complex environments.

Patterned environments may also enable researchers to go beyond single particle studies and towards unraveling collective behaviors in dense active systems, a vast research topic that remains experimentally largely unexplored especially for nonspherical synthetic swimmers. That is, environments may be patterned in controlled ways to direct the accumulation of particles with arbitrary shapes. Finally on the topic of patterning, equipping planar walls with secondary structures and once again exploiting their surface affinity may open new possibilities for exploring the three-dimensional motion of synthetic microswimmers. Apart from optical and acoustic trapping as discussed above, employing such structures can be an alternate route for guiding active particles in three dimensions, i.e. away from planar walls and towards bulk motion. In preliminary experiments using microprinted domes, see Figure 7.1B-C, we saw that spheri-

cal swimmers can follow the curvature of the dome and actively diffuse on its top. Although our bright field experiment in two dimensions would not allow for accurate particle tracking of the three-dimensional motion, fluorescent particles and microstructures could be employed instead to facilitate particle tracking, see Figure 7.1D. Overall, we believe that 3D microprinting for patterning both swimmer shapes [88] and their environments will create new opportunities for efficient swimmer utilization in future applications.

Lastly, we have so far highlighted the benefit of exploiting shape as a way to fabricate synthetic swimmers that more closely resemble their biological counterparts. Yet, the key aspect of structural flexibility and, even more so, spatiotemporal shape regulation through, e.g., segmented flexibility as is the case in biological systems, remains entirely unexplored in synthetic systems. That is, studies have focused either on rigid particles or semi-flexible particle assemblies [45, 295–297]. Recent work has shown that fully flexible structures can readily be prepared through particle functionalization with surface mobile DNA linkers, leading spherical particles functionalized with complementary linkers to assemble into structures that resemble colloidal polymers and molecules [298–300].

We explored the possibility of combining the aforementioned technique with Pt-coated particles to create self-propelling fully reconfigurable particle assemblies in H_2O_2. We prepared colloidal-joint particles with complementary motile DNA linkers following the DNA functionalization protocol using cholesterol anchors [298]. In addition, we prepared motor particles with Pt and surface-bound DNA to propel the structures using the following new strategy: as a first step, we functionalized Pt-coated particles with the protein NeutrAvidin by following the coating protocol of Ref. [136], see also the confocal image of Figure 7.1E. We applied said protocol to TPM-COOH particles that we had already half-coated with ≈ 4 nm Pt: we activated the -COOH groups on the uncoated TPM surface to form esters and then we simultaneously coated them with fluorescently-labelled Neutravidin as well as we covalently-attached a polymer layer for stability. The green patches in Figure 7.1E correspond to the NeutrAvidin used in the experiment, indicating that half the particles' surface was coated after functionalization. We also verified that the NeutrAvidin had indeed correctly coated their TPM and not their Pt sides, as they moved towards their fluorescent and away from their non-fluorescent side in H_2O_2. Subsequently, we attached surface-bound DNA on the Neutravidin following the procedure described in Ref. [298] for functionalizing colloidal particles with bound linkers. The result is shown in Figure 7.1F, where the red patch denotes the fluorescently-labelled DNA. The DNA that we used was double stranded, prepared by hybridizing the strands named as D and E in Ref. [298], and had a biotin anchor. We chose this DNA for visualization purposes as it contrasted with the dye of the NeutrAvidin, as well as because it was
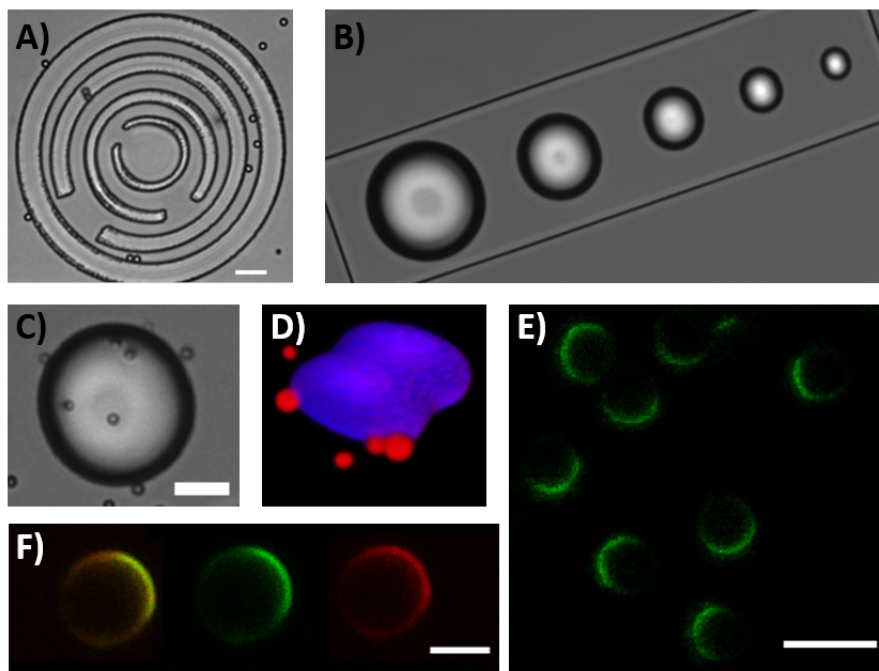
Figure 7.1: **Experiments towards microswimmers in complex environments and flexible microswimmers.** **A)** Nonspherical swimmer behavior could be studied inside intricate geometries, such as mazes, which can be readily obtained through 3D-microprinting, to potentially provide novel insights into the effect of confinement. Scale bar is 10 µm. **B)** Microprinted domes as a way to study three-dimensional motion of synthetic swimmers. **C)** Bright field microscopy image showing that active particles can follow the curvature of the dome and swim on its top. Scale bar is 10 µm. **D)** Fluorescent particles (red) and microstructures (blue) can be employed to facilitate particle tracking in three-dimensional experiments. The confocal image was reconstructed from a z-stack using commercial software. A-D) These experiments were performed in collaboration with Melissa Rinaldin. **E)** Pt half-coated particles after functionalization with fluorescent NeutrAvidin (green patches) following Ref. [136]. Scale bar is 5 µm. **F)** Particle functionalized with fluorescent NeutrAvidin and DNA bound to the NeutrAvidin imaged with green and red channels simultaneously (left), the green channel showing the NeutrAvidin (middle), and the red channel showing the fluorescently-labelled DNA (right). Scale bar is 2 µm. Such functionalized Pt-coated particles can subsequently be used for self-assembly purposes, for example as parts in flexibly linked colloidal structures.

complementary to the mobile DNA linkers used for the flexible structures.

Although motor particles were successfully prepared and could in principle be integrated into the flexible structures, we noted that salt — important for the stability of the flexible structures — diminished their velocity. As a consequence, the resulting structures would not self-propel. We concluded that combining these components was not feasible (as they were). However, we propose here that self-propelled flexible structures could be obtained in future research if either system component is modified.

The *first* possibility would be to use an assembly strategy that yields stable colloidal polymers without salt, while at the same time preserving the flexibility of the assembled structure. To this end, we propose that the self-assembly method with surface-mobile biotin linkers of Ref. [301] can be employed. The desired flexible colloidal polymer structures can then be obtained by exploiting the high specificity of biotin-NeutrAvidin bonds. This approach could subsequently also employ the half NeutrAvidin-coated and half Pt-coated particles of Figure 7.1E: after incorporation to one end of the flexible colloidal polymer, the catalytic particle could act as the structure's active motor element and push the polymer forward in H_2O_2 provided also that H_2O_2 does not affect the structural integrity and quality of the bilayer on the flexible structure.

The *second* possibility would be to use a propulsion mechanism that does not rely on the catalytic decomposition of H_2O_2 and hence is unaffected by salt. For example, thermophoretic swimmers, i.e. Au-coated particles propelled in water due to asymmetric heating, and/or acoustically propelled swimmers, maintain their propulsion even in high ionic strength solutions. Swimmers such as these could thereby serve as the active elements that propel the flexible colloidal structures assembled through surface-mobile DNA linkers. We note that the latter, i.e. eliminating H_2O_2 as a fuel, would be best in terms of biocompatibility for future applications: e.g., acoustic propulsion is not only unaffected by salt, but is also nontoxic and biocompatible, and hence more appropriate for biomedical microrobots [293].

Bibliography

[1]   Ran Nathan et al. "A movement ecology paradigm for unifying organismal movement research". In: *PNAS* 105 (2008), pp. 19052–19059. DOI: 10.1073/pnas.0800375105.

[2]   William Bialek et al. "Statistical mechanics for natural flocks of birds". In: *PNAS* 109 (2012), pp. 4786–4791. DOI: 10.1073/pnas.1118633109.

[3]   Daniel S. Seara et al. "Entropy production rate is maximized in non-contractile actomyosin". In: *Nat Commun* 9 (2018), p. 4948. DOI: 10.1038/s41467-018-07413-5.

[4]   Antoine Bricard et al. "Emergent vortices in populations of colloidal rollers". In: *Nat Commun* 6 (2015), p. 7470. DOI: 10.1038/ncomms8470.

[5]   M. C. Marchetti et al. "Hydrodynamics of soft active matter". In: *Rev. Mod. Phys.* 85 (2013), p. 1143. DOI: 10.1103/RevModPhys.85.1143.

[6]   Francesco Ginelli. "The Physics of the Vicsek model". In: *Eur. Phys. J. Special Topics* 225 (2016), pp. 2099–2117. DOI: 10.1140/epjst/e2016-60066-8.

[7]   M. Reza Shaebani et al. "Computational models for active matter". In: *Nature Reviews Physics* 2 (2020), pp. 181–199. DOI: 10.1038/s42254-020-0152-1.

[8]   Sriram Ramaswamy. "The Mechanics and Statistics of Active Matter". In: *Annu. Rev. Condens. Matter Phys.* 1 (2010), pp. 323–345. DOI: 10.1146/annurev-conmatphys-070909-104101.

[9]   G. De Magistris and D. Marenduzzo. "An introduction to the physics of active matter". In: *Physica A* 418 (2015), pp. 65–77. DOI: 10.1016/j.physa.2014.06.061.

[10]   Nature. *"Active Matter"*. 2019. URL: https://www.nature.com/collections/hvczfmjfzl.

[11] Soft Matter RCS. *"Active Matter"*. 2019. URL: https://pubs.rsc.org/en/journals/articlecollectionlanding?sercode=sm&themeid=103bdf9d-d5bc-470f-929d-69a63949f318.

[12] Roland G Winkler Gerhard Gompper and et al. "The 2020 motile active matter roadmap". In: *J. Phys.: Condens. Matter* 32 (2020), p. 193001. DOI: 10.1088/1361-648X/ab6348.

[13] Alan C. H. Tsang et al. "Roads to Smart Artificial Microswimmers". In: *Adv. Intell. Syst.* 2 (2020), p. 1900137. DOI: 10.1002/aisy.201900137.

[14] Daniel J Webre, Peter M Wolanin, and Jeffry B Stock. "Bacterial chemotaxis". In: *Current Biology* 13 (2003), R47–49. DOI: 10.1016/S0960-9822(02)01424-0.

[15] Benjamin M. Friedrich and Frank Jülicher. "Chemotaxis of sperm cells". In: *PNAS* 104 (2007), pp. 13256–13261. DOI: 10.1073/pnas.0703530104.

[16] Osborne Reynolds. "An experimental investigation of the circumstances which determine whether the motion of water shall be direct or sinuous, and of the law of resistance in parallel channels". In: *Philosophical Transactions of the Royal Society* 174 (1883), pp. 935–982. DOI: 10.1098/rstl.1883.0029.

[17] E. M. Purcell. "Life at low Reynolds number". In: *American Journal of Physics* 45 (1977), p. 3. DOI: 10.1119/1.10903.

[18] Jens Elgeti, Roland G. Winkler, and Gerhard Gompper. "Physics of Microswimmers - Single Particle Motion and Collective Behavior". In: *Rep. Prog. Phys.* 78 (2015), p. 056601. DOI: 10.1088/0034-4885/78/5/056601.

[19] Netta Cohen and Jordan H Boyle. "Swimming at low Reynolds number: a beginners guide to undulatory locomotion". In: *Contemporary Physics* 51 (2010), pp. 103–123. DOI: 10.1080/00107510903268381.

[20] Eric Lauga and Thomas R Powers. "The hydrodynamics of swimming microorganisms". In: *Rep. Prog. Phys.* 72 (2009), p. 096601. DOI: 10.1088/0034-4885/72/9/096601.

[21] Wen Yin et al. "Biofilms: The Microbial "Protective Clothing" in Extreme Environments". In: *Int J Mol Sci* 20 (2019), p. 3423. DOI: 10.3390/ijms20143423.

[22] Guido Panzarasa et al. "Transient supramolecular assembly of a functional perylene diimide controlled by a programmable pH cycle". In: *Soft Matter (Communication)* 16 (2019), pp. 591–594. DOI: 10.1039/C9SM02026H.

[23] Charlie Gilbert et al. "Living materials with programmable functionalities grown from engineered microbial co-cultures". In: *bioRxiv* (2019). DOI: 10.1101/2019.12.20.882472.

[24] H.-W. Huang et al. "Adaptive locomotion of artificial microswimmers". In: *Sci. Adv.* 5 (2019), eaau1532. DOI: 10.1126/sciadv.aau1532.

[25] Jeremie Palacci et al. "Living Crystals of Light-Activated Colloidal Surfers". In: *Science* 339 (2013), pp. 936–940. DOI: science.1230020.

[26] Alexander P. Petroff, Xiao-Lun Wu, and Albert Libchaber. "Fast-Moving Bacteria Self-Organize into Active Two-Dimensional Crystals of Rotating Cells". In: *Phys. Rev. Lett.* 114 (2015), p. 158102. DOI: 10.1103/PhysRevLett.114.158102.

[27] Alexander P. Petroff et al. "Biophysical basis for convergent evolution of two veil-forming microbes". In: *R. Soc. open sci.* 2 (2015), p. 150437. DOI: https://doi.org/10.1098/rsos.150437.

[28] Ada-Ioana Bunea and Rafael Taboryski. "Recent Advances in Microswimmers for Biomedical Applications". In: *Micromachines* 11 (2020), p. 1048. DOI: 10.3390/mi11121048.

[29] Cynthia Richard, Juliane Simmchen, and Alexander Eychmüller. "Photocatalytic Iron Oxide Micro-Swimmers for Environmental Remediation". In: *Zeitschrift für Physikalische Chemie* 232 (2018), pp. 747–757. DOI: 10.1515/zpch-2017-1087.

[30] Jonathan R. Howse et al. "Self-Motile Colloidal Particles: From Directed Propulsion to Random Walk". In: *Phys. Rev. Lett.* 99 (2007), p. 048102. DOI: 10.1103/PhysRevLett.99.048102.

[31] Walter F. Paxton et al. "Catalytic Nanomotors: Autonomous Movement of Striped Nanorods". In: *J. Am. Chem. Soc.* 126 (2004), pp. 13424–13431. DOI: 10.1021/ja047697z.

[32] Hong-Ren Jiang, Natsuhiko Yoshinaga, and Masaki Sano. "Active Motion of a Janus Particle by Self-Thermophoresis in a Defocused Laser Beam". In: *Phys. Rev. Lett.* 105 (2010), p. 268302. DOI: 10.1103/PhysRevLett.105.268302.

[33] Giovanni Volpe et al. "Microswimmers in patterned environments". In: *Soft Matter* 7 (2011), pp. 8810–8815. DOI: 10.1039/C1SM05960B.

[34] Mojca Vilfan, Natan Osterman, and Andrej Vilfan. "Magnetically driven omnidirectional artificial microswimmers". In: *Soft Matter* 14 (2018), pp. 3415–3422. DOI: 10.1039/C8SM00230D.

[35] Daniel Ahmed et al. "Artificial Acousto-Magnetic Soft Microswimmers". In: *Adv. Mater. Technol.* 2 (2017), p. 1700050. DOI: 10.1002/admt.201700050.

[36] K. Jagajjanani Rao et al. "A Force to Be Reckoned With: A Review of Synthetic Microswimmers Powered by Ultrasound". In: *Small* 11 (2015), pp. 2836–2846. DOI: 10.1002/smll.201403621.

[37] Xiaolei Peng et al. "Opto-thermoelectric microswimmers". In: *Light Sci Appl* 9 (2020), p. 141. DOI: 10.1038/s41377-020-00378-5.

[38] Alexandre Morin et al. "Distortion and destruction of colloidal flocks in disordered environments". In: *Nature Phys* 13 (2017), pp. 63–67. DOI: 10.1038/nphys3903.

[39] Kilian Dietrich et al. "Microscale Marangoni Surfers". In: *Phys. Rev. Lett.* 125 (2020), p. 098001. DOI: 10.1103/PhysRevLett.125.098001.

[40] Sijia Wang and Ning Wu. "Selecting the Swimming Mechanisms of Colloidal Particles: Bubble Propulsion versus Self-Diffusiophoresis". In: *Langmuir* 30 (2014), pp. 3477–3486. DOI: 10.1021/la500182f.

[41] Chenyu Jin, Carsten Krüger, and Corinna C. Maass. "Chemotaxis and autochemotaxis of self-propelling droplet swimmers". In: *PNAS* 114 (2017), pp. 5089–5094. DOI: 10.1073/pnas.1619783114.

[42] Ramin Golestanian, Tanniemola B. Liverpool, and Armand Ajdari. "Propulsion of a Molecular Machine by Asymmetric Distribution of Reaction Products". In: *Phys. Rev. Lett.* 94 (2005), p. 220801. DOI: 10.1103/PhysRevLett.94.220801.

[43] Wei Gao et al. "Organized Self-Assembly of Janus Micromotors with Hydrophobic Hemispheres". In: *J. Am. Chem. Soc.* 135 (2013), pp. 998–1001. DOI: 10.1021/ja311455k.

[44] I. Theurkauff et al. "Dynamic Clustering in Active Colloidal Suspensions with Chemical Signaling". In: *Phys. Rev. Lett.* 108 (2012), p. 268303. DOI: 10.1103/PhysRevLett.108.268303.

[45] Songbo Ni et al. "Hybrid colloidal microswimmers through sequential capillary assembly". In: *Soft Matter* 13 (2017), pp. 4252–4259. DOI: 10.1039/C7SM00443E.

[46] Jizhuang Wang et al. "Light-Driven Micro/Nanomotor for Promising Biomedical Tools: Principle, Challenge, and Prospect". In: *Acc. Chem. Res* 51 (2018), pp. 1957–1965. DOI: 10.1021/acs.accounts.8b00254.

[47] Renfeng Dong et al. "Photocatalytic Micro/Nanomotors: From Construction to Applications". In: *Acc. Chem. Res* 51 (2018), pp. 1940–1947. DOI: 10.1021/acs.accounts.8b00249.

[48] S. J. Ebbens. "Active colloids: Progress and challenges towards realising autonomous applications". In: *Current Opinion in Colloid and Interface Science* 26 (2016), pp. 14–23. DOI: 10.1016/j.cocis.2015.10.003.

[49] Wei Wang et al. "From One to Many: Dynamic Assembly and Collective Behavior of Self-Propelled Colloidal Motors". In: *Acc. Chem. Res.* 48 (2015), pp. 1938–1946. DOI: 10.1021/acs.accounts.5b00025.

[50] Jie Zhang et al. "Active colloids with collective mobility status and research opportunities". In: *Chem. Soc. Rev.* 46 (2017), p. 5551. DOI: 10.1039/c7cs00461c.

[51] Tania Patino et al. "Fundamental Aspects of Enzyme-Powered Micro- and Nanoswimmers". In: *Acc. Chem. Res.* 51 (2018), pp. 2662–2671. DOI: `10.1021/acs.accounts.8b00288`.

[52] Pierre Illien, Ramin Golestanian, and Ayusman Sen. "'Fuelled' motion: phoretic motility and collective behaviour of active colloids". In: *Chem. Soc. Rev.* 46 (2017), p. 5508. DOI: `10.1039/c7cs00087a`.

[53] Yang Wang et al. "Bipolar Electrochemical Mechanism for the Propulsion of Catalytic Nanomotors in Hydrogen Peroxide Solutions". In: *Langmuir* 22 (2006), pp. 10451–10456. DOI: `10.1021/la0615950`.

[54] Stephen J. Ebbens and David Alexander Gregory. "Catalytic Janus Colloids: Controlling Trajectories of Chemical Microswimmers". In: *Acc. Chem. Res.* 51 (2018), pp. 1931–1939. DOI: `10.1021/acs.accounts.8b00243`.

[55] Richard J. Archer et al. "A Pickering Emulsion Route to Swimming Active Janus Colloids". In: *Adv. Sci.* 5 (2017), p. 1700528. DOI: `10.1002/advs.201700528`.

[56] Manoj Manjare et al. "Hydrophobic catalytic Janus motors: Slip boundary condition and enhanced catalytic reaction rate". In: *Applied Physics Letters* 104 (2014), p. 054102. DOI: `https://doi.org/10.1063/1.4863952`.

[57] Brooke W. Longbottom and Stefan A. F. Bon. "Improving the engine power of a catalytic Janus-sphere micromotor by roughening its surface". In: *Scientific Reports* 8 (2018), p. 4622. DOI: `10.1038/s41598-018-22917-2`.

[58] Stephen Ebbens et al. "Size dependence of the propulsion velocity for catalytic Janus-sphere swimmers". In: *Phys. Rev. E* 85 (2012), p. 020401. DOI: `10.1103/PhysRevE.85.020401`.

[59] Sambeeta Das et al. "Boundaries can steer active Janus spheres". In: *Nat. Commun.* 6 (2015), p. 8999. DOI: `10.1038/ncomms9999`.

[60] Juliane Simmchen et al. "Topographical pathways guide chemical microswimmers". In: *Nat. Commun.* 7 (2016), p. 10598. DOI: `10.1038/ncomms10598`.

[61] Aidan T. Brown et al. "Swimming in a crystal". In: *Soft Matter* 12 (2016), pp. 131–140. DOI: `10.1039/c5sm01831e`.

[62] Ming You et al. "Intelligent Micro/nanomotors with Taxis". In: *Acc. Chem. Res* 51 (2018), pp. 3006–3014. DOI: 10.1021/acs.accounts.8b00291.

[63] John L. Anderson. "COLLOID TRANSPORT BY INTERFACIAL FORCES". In: *Ann. Rev. Fluid Mech.* 21 (1989), pp. 61–99. DOI: 10.1146/annurev.fl.21.010189.000425.

[64] Jeffrey L. Moran and Jonathan D. Posner. "Phoretic Self-Propulsion". In: *Annu. Rev. Fluid Mech.* 49 (2017), pp. 511–540. DOI: 10.1146/annurev-fluid-122414-034456.

[65] Richard A. Archer et al. "Motion of a particle generated by chemical gradients Part 1. Non-electrolytes". In: *J. Fluid Mech.* 117 (1982), pp. 107–121. DOI: 10.1017/S0022112082001542.

[66] J. F. Brady. "Particle motion driven by solute gradients with application to autonomous motion: continuum and colloidal perspectives". In: *J. Fluid Mech.* 667 (2011), pp. 216–259. DOI: 10.1017/S0022112010004404.

[67] Sébastien Michelin and Eric Lauga. "Phoretic self-propulsion at finite Péclet numbers". In: *J. Fluid Mech.* 747 (2014), pp. 572–604. DOI: 10.1017/jfm.2014.158.

[68] R Golestanian, T B Liverpool, and A Ajdari. "Designing phoretic micro- and nano-swimmers". In: *New J. Phys.* 9 (2007), p. 126. DOI: 10.1088/1367-2630/9/5/126.

[69] Howard A. Stone and Aravinthan D. T. Samuel. "Propulsion of Microorganisms by Surface Distortions". In: *Phys. Rev. Lett.* 77 (1996), p. 4102. DOI: 10.1103/PhysRevLett.77.4102.

[70] Kun-Chun Lee and Andrea J. Liu. "New Proposed Mechanism of Actin-Polymerization-Driven Motility". In: *Biophysical Journal* 95 (2008), pp. 4529–4539. DOI: 10.1529/biophysj.108.134783.

[71] Richard P. Sear. "Diffusiophoresis in Cells: A General Nonequilibrium, Nonmotor Mechanism for the Metabolism-Dependent Transport of Particles in Cells". In: *Phys. Rev. Lett.* 122 (2019), p. 128101. DOI: 10.1103/PhysRevLett.122.128101.

[72] Alexandra E. Frankel and Aditya S. Khair. "Dynamics of a self-diffusiophoretic particle in shear flow". In: *Phys. Rev. E* 90 (2014), p. 013030. DOI: 10.1103/PhysRevE.90.013030.

[73] Nima Sharifi-Mood, Joel Koplik, and Charles Maldarelli. "Diffusiophoretic self-propulsion of colloids driven by a surface reaction: The sub-micron particle regime for exponential and van der Waals interactions". In: *Physics of Fluids* 25 (2013), p. 012001. DOI: 10.1063/1.4772978.

[74] Aidan T. Brown et al. "Ionic screening and dissociation are crucial for understanding chemical self-propulsion in polar solvents". In: *Soft Matter* 13 (2017), pp. 1200–1222. DOI: 10.1039/c6sm01867j.

[75] Aidan Brown and Wilson Poon. "Ionic effects in self-propelled Pt-coated Janus swimmers". In: *Soft Matter* 10 (2014), pp. 4016–4027. DOI: 10.1039/c4sm00340c.

[76] S. Ebbens et al. "Electrokinetic effects in catalytic platinum-insulator Janus swimmers". In: *EPL* 106 (2014), p. 58003. DOI: 10.1209/0295-5075/106/58003.

[77] Philip M. Wheat et al. "Rapid Fabrication of Bimetallic Spherical Motors". In: *Langmuir* 26 (2010), pp. 13052–13055. DOI: 10.1021/la102218w.

[78] Jeffrey L. Moran and Jonathan D. Posner. "Role of solution conductivity in reaction induced charge auto-electrophoresis". In: *Physics of Fluids* 26 (2014), p. 042001. DOI: 10.1063/1.4869328.

[79] Elaine Lay Khim Chng, Guanjia Zhao, and Martin Pumera. "Towards biocompatible nano/microscale machines: self-propelled catalytic nanomotors not exhibiting acute toxicity". In: *Nanoscale* 6 (2014), p. 2119. DOI: 10.1039/c3nr04997c.

[80] Richard A. Archer et al. "pH-Responsive Catalytic Janus Motors with Autonomous Navigation and Cargo-Release Functions". In: *Adv. Funct. Mater.* 30 (2020), p. 2000324. DOI: 10.1002/adfm.202000324.

[81] Stephen J. Ebbens and Jonathan R. Howse. "Direct Observation of the Direction of Motion for Spherical Catalytic Swimmers". In: *Langmuir* 27 (2011), pp. 12293–12296. DOI: 10.1021/la2033127.

[82] R. J. Archer, A. I. Campbell, and S. J. Ebbens. "Glancing angle metal evaporation synthesis of catalytic swimming Janus colloids with well defined angular velocity". In: *Soft Matter* 11 (2015), p. 6872. DOI: 10.1039/c5sm01323b.

[83] Stephen Ebbens et al. "Self-assembled autonomous runners and tumblers". In: *Phys. Rev. E* 82 (2010), 015304(R). DOI: `10.1103/PhysRevE.82.015304`.

[84] Felix Kümmel et al. "Circular Motion of Asymmetric Self-Propelling Particles". In: *Phys. Rev. Lett.* 110 (2013), p. 198302. DOI: `10.1103/PhysRevLett.110.198302`.

[85] Dugyala Venkateshwar Rao et al. "Self-propulsion of bent bimetallic Janus rods". In: *J. Phys. D: Appl. Phys.* 52 (2018), p. 014002. DOI: `10.1088/1361-6463/aae6f6`.

[86] Onajite Shemi and Michael J. Solomon. "Self-Propulsion and Active Motion of Janus Ellipsoids". In: *Phys. Chem. B* 122 (2018), pp. 10247–10255. DOI: `10.1021/acs.jpcb.8b08303`.

[87] Yogesh Shelke et al. "Transition from Linear to Circular Motion in Active Spherical-Cap Colloids". In: *Langmuir* 35 (2019), pp. 4718–4725. DOI: `10.1021/acs.langmuir.9b00081`.

[88] R. P. Doherty et al. "Catalytically propelled 3D printed colloidal microswimmers". In: *Soft Matter* 16 (2020), p. 10463. DOI: `10.1039/D0SM01320J`.

[89] Yahaya Ibrahim, Ramin Golestanian, and Tanniemola B. Liverpool. "Multiple phoretic mechanisms in the self-propulsion of a Pt-insulator Janus swimmer". In: *J. Fluid Mech.* 828 (2017), pp. 318–352. DOI: `10.1017/jfm.2017.502`.

[90] Willow R. DiLuzio et al. "Escherichia coli swim on the right-hand side". In: *Nature* 435 (2005), pp. 1271–1274. DOI: `10.1038/nature03660`.

[91] Eric Lauga et al. "Swimming in Circles: Motion of Bacteria near Solid Boundaries". In: *Biophysical Journal* 90 (2006), pp. 400–412. DOI: `10.1529/biophysj.105.069401`.

[92] Laurence Lemelle et al. "Counterclockwise Circular Motion of Bacteria Swimming at the Air-Liquid Interface". In: *JOURNAL OF BACTERIOLOGY* 192 (2010), pp. 6307–6308. DOI: `10.1128/JB.00397-10`.

[93] Diego Lopez and Eric Lauga. "Dynamics of swimming bacteria at complex interfaces". In: *Physics of Fluids* 26 (2014), p. 071902. DOI: `10.1063/1.4887255`.

[94] Hua Ke et al. "Motion Analysis of Self-Propelled Pt-Silica Particles in Hydrogen Peroxide Solutions". In: *J. Phys. Chem. A* 114 (2010), pp. 5462–5467. DOI: 10.1021/jp101193u.

[95] W.E. Uspal et al. "Guiding catalytically active particles with chemically patterned surfaces". In: *Phys. Rev. Lett.* 117 (2016), p. 048002.

[96] M. N. Popescu, S. Dietrich, and G. Oshanin. "Confinement effects on diffusiophoretic self-propellers". In: *J. Chem. Phys.* 130 (2009), p. 194702. DOI: 10.1063/1.3133239.

[97] D. G. Crowdy. "Wall effects on self-diffusiophoretic Janus particles: a theoretical study". In: *J. Fluid Mech.* 735 (2013), pp. 473–498. DOI: 10.1017/jfm.2013.510.

[98] T.-Y. Chiang and D. Velegol. "Localized Electroosmosis (LEO) Induced by Spherical Colloidal Motors". In: *Langmuir* 30 (2014), pp. 2600–2607. DOI: 10.1021/la402262z.

[99] W. E. Uspal et al. "Self-propulsion of a catalytically active particle near a planar wall: from reflection to sliding and hovering". In: *Soft Matter* 11 (2015), pp. 434–438. DOI: 10.1039/c4sm02317j.

[100] Y. Ibrahim and T. B. Liverpool. "The dynamics of a self-phoretic Janus swimmer near a wall". In: *Eur. Phys. Let.* 111 (2015), p. 48008. DOI: 10.1209/0295-5075/111/48008.

[101] Ali Mozaffari et al. "Self-diffusiophoretic colloidal propulsion near a solid boundary". In: *Phys. Fluids* 28 (2016), p. 053107. DOI: 10.1063/1.4948398.

[102] Zaiyi Shen, Alois Würger, and Juho S. Lintuvuori. "Hydrodynamic interaction of a self-propelling particle with a wall. Comparison between an active Janus particle and a squirmer model". In: *Eur. Phys. J. E* 41 (2018), p. 39. DOI: 10.1140/epje/i2018-11649-0.

[103] Wei M. et al. "Catalytic Micromotors Moving Near Polyelectrolyte-Modified Substrates: The Roles of Surface Charges, Morphology, and Released Ions." In: *ACS Appl Mater Interfaces* 10 (2018), pp. 2249–2252. DOI: 10.1021/acsami.7b18399.

[104] J. Palacci et al. "Light-activated self-propelled colloids". In: *Phil. Trans. R. Soc. A* 372 (2014), pp. 2249–2252. DOI: 10.1098/rsta.2013.0372.

[105] A. L. Holterhoff, M. Li, and J. G. Gibbs. "Self-Phoretic Microswimmers Propel at Speeds Dependent upon an Adjacent Surface's Physicochemical Properties". In: *J. Phys. Chem. Let.* 9 (2018), pp. 5023–5028. DOI: 10.1021/acs.jpclett.8b02277.

[106] Clemens Bechinger et al. "Active particles in complex and crowded environments". In: *Rev. Mod. Phys.* 88 (2016), p. 045006. DOI: 10.1103/RevModPhys.88.045006.

[107] David M. Huang et al. "Water Slippage versus Contact Angle: A Quasiuniversal Relationship". In: *Phys. Rev. Lett.* 101 (2008), p. 226101. DOI: 10.1103/PhysRevLett.101.226101.

[108] C. van der Wel et al. "Preparation of Colloidal Organosilica Spheres through Spontaneous Emulsification". In: *Langmuir* 33.33 (2017), pp. 8174–8180. DOI: 10.1021/acs.langmuir.7b01398.

[109] Maciej Lisicki et al. "Swimming eukaryotic microorganisms exhibit a universal speed distribution". In: *eLife* (2019). DOI: 10.7554/eLife.44907.

[110] Xiaolu Wang et al. "Enhanced active motion of Janus colloids at the water surface". In: *Soft Matter* 11 (2015), p. 7376. DOI: 10.1039/C5SM01111F.

[111] Armand Ajdari and Lydéric Bocquet. "Giant Amplification of Interfacially Driven Transport by Hydrodynamic Slip: Diffusio-Osmosis and Beyond". In: *Phys. Rev. Let.* 96 (2006), p. 186102. DOI: 10.1103/PhysRevLett.96.186102.

[112] A. I. Campbell et al. "Experimental Observation of Flow Fields Around Active Janus Spheres". In: *Nature Communications* 10 (2019), p. 3952. DOI: 10.1038/s41467-019-11842-1.

[113] Daisuke Takagi et al. "Dispersion of Self-Propelled Rods Undergoing Fluctuation-Driven Flips". In: *Physical Review Letters* 10 (2013), p. 038301. DOI: 10.1103/PhysRevLett.110.038301.

[114] D. Takagi et al. "Hydrodynamic capture of microswimmers into sphere-bound orbits". In: *Soft Matter* 10 (2014), p. 1784. DOI: 10.1039/c3sm52815d.

[115] Vincent S. J. Craig, Chiara Neto, and David R. M. Williams. "Shear-Dependent Boundary Slip in an Aqueous Newtonian Liquid". In: *Phys. Rev. Lett.* 87 (2001), p. 054504. DOI: 10.1103/PhysRevLett.87.054504.

[116] J. Baudry et al. "Experimental Evidence for a Large Slip Effect at a Nonwetting Fluid-Solid Interface". In: *Langmuir* 17 (2001), pp. 5232–5236. DOI: 10.1021/la0009994.

[117] Bharat Bhushan, Yuliang Wang, and Abdelhamid Maali. "Boundary Slip Study on Hydrophilic, Hydrophobic, and Superhydrophobic Surfaces with Dynamic Atomic Force Microscopy". In: *Langmuir* 25.14 (2009), pp. 8117–8121. DOI: 10.1021/la900612s.

[118] L. Bocquet and J.-L. Barrat. "Flow boundary conditions from nano- to micro-scales". In: *Soft Matter* 3 (2007), pp. 685–693. DOI: 10.1039/b616490k.

[119] R. Pit, H. Hervet, and L. Léger. "Direct Experimental Evidence of Slip in Hexadecane: Solid Interfaces". In: *Phys. Rev. Lett.* 85 (2000), pp. 980–983. DOI: 10.1103/PhysRevLett.85.980.

[120] C. Cottin-Bizonne et al. "Nanorheology: An investigation of the boundary condition at hydrophobic and hydrophilic interfaces". In: *Eur. Phys. J. E* 9 (2002), pp. 47–53. DOI: 10.1140/epje/i2001-10112-9.

[121] Yingxi Zhu and Steve Granick. "Rate-Dependent Slip of Newtonian Liquid at Smooth Surfaces". In: *Phys. Rev. Lett.* 87 (2001), p. 096105. DOI: 10.1103/PhysRevLett.87.096105.

[122] B. Siboulet et al. "Water self-diffusion at the surface of silica glasses: effect of hydrophilic to hydrophobic transition". In: *Molecular Physics* 111 (2013), pp. 3410–3417. DOI: 10.1080/00268976.2013.861084.

[123] M.T. Kezirian. "Hydrodynamics with a wall-slip boundary condition for a particle moving near a plane wall bounding a semi-infinite viscous fluid". PhD thesis. Massachusetts Institute of Technology, 1992.

[124] Ville Jokinen, Pia Suvanto, and Sami Franssila. "Oxygen and nitrogen plasma hydrophilization and hydrophobic recovery of polymers". In: *BIOMICROFLUIDICS* 6 (2012), p. 016501. DOI: `10.1063/1.3673251`.

[125] J.J. Cras et al. "Comparison of chemical cleaning methods of glass in preparation for silanization". In: *Biosensors and Bioelectronics* 14 (1999), pp. 683–688. DOI: `10.1016/S0956-5663(99)00043-3`.

[126] K. Efimenko, W. E. Wallace, and J. Genzer. "Surface Modification of Sylgard-184 Poly(dimethyl siloxane) Networks by Ultraviolet and Ultraviolet/Ozone Treatment". In: *J. Coll. and Interf. Sci.* 254 (2002), pp. 306–315. DOI: `10.1006/jcis.2002.8594`.

[127] A. Oláh, H. Hillborg, and G. J. Vancso. "Hydrophobic recovery of UV/ozone treated poly(dimethylsiloxane): adhesion studies by contact mechanics and mechanism of surface modification". In: *Applied Surface Science* 239 (2005), pp. 410–423. DOI: `10.1016/j.apsusc.2004.06.005`.

[128] A.J. Goldman, R.G. Cox, and H. Brenner. "Slow viscous motion of a sphere parallel to a plane wall-I Motion through a quiescent fluid". In: *Chem. Eng. Sci.* 22 (1967), p. 637.

[129] P. Sharma, S. Ghosh, and S. Bhattacharya. "A high-precision study of hindered diffusion near a wall". In: *Appl Phys Let* 97 (2010), p. 104101. DOI: `10.1063/1.3486123`.

[130] Chungil Ha, H. D. Ou-Yang, and Hyuk Kyu Pak. "Direct measurements of colloidal hydrodynamics near flat boundaries using oscillating optical tweezers". In: *Physica A* 392 (2013), pp. 3497–3504. DOI: `10.1016/j.physa.2013.04.014`.

[131] M.N. Popescu et al. "Effective Interactions between Chemically Active Colloids and Interfaces". In: *Acc. Chem. Res.* 51 (2018), p. 2991. DOI: `10.1021/acs.accounts.8b00237`.

[132] S.E. Spagnolie and E. Lauga. "Hydrodynamics of self-propulsion near a boundary: predictions and accuracy of far-field approximations". In: *J. FLuid Mech.* 700 (2012), p. 105. DOI: `10.1017/jfm.2012.101`.

[133] J.S. Lintuvuori et al. "Hydrodynamic oscillations and variable swimming speed in squirmers close to repulsive walls". In: *Soft Matter* 12 (2016), p. 7959. DOI: `10.1039/C6SM01353H`.

[134] H.J. Keh and S.B. Chen. "Electrophoresis of a colloidal sphere parallel to a dielectric plane". In: *J. Fluid Mech.* 194 (1988), p. 377. DOI: `10.1017/S0022112088003039`.

[135] J. C. W. Corbett et al. "Measuring surface zeta potential using phase analysis light scattering in a simple dip cell arrangement". In: *Colloids and Surfaces A: Physicochemical and Engineering Aspects* 396 (2012), pp. 169–176. DOI: `10.1016/j.colsurfa.2011.12.065`.

[136] C. van der Wel et al. "Surfactant-free Colloidal Particles with Specific Binding Affinity". In: *Langmuir* 33.38 (2017), pp. 9803–9810. DOI: `10.1021/acs.langmuir.7b02065`.

[137] R. Raveendran and M. A. G. Namboothiry. "Surface-Treated Poly(dimethylsiloxane) as a Gate Dielectric in Solution-Processed Organic Field-Effect Transistors". In: *ACS Omega* 3 (2018), pp. 11278–11285. DOI: `10.1021/acsomega.8b01629`.

[138] Robert A. Erb. "The wettability of Gold". In: *J. Phys. Chem.* 72 (1968), pp. 2412–2417. DOI: `10.1021/j100853a023`.

[139] Mamdouh E. Abdelsalam et al. "Wetting of Regularly Structured Gold Surfaces". In: *Langmuir* 21 (2005), pp. 1753–1757. DOI: `10.1021/la047468q`.

[140] Kilian Dietrich et al. "Two-dimensional nature of the active Brownian motion of catalytic microswimmers at solid and liquid interfaces". In: *New J. Phys.* 19 (2017), p. 065008. DOI: `10.1088/1367-2630/aa7126`.

[141] Daniel B. Allan et al. *trackpy: Trackpy v0.4.1*. Apr. 2018. DOI: `10.5281/zenodo.1226458`. URL: `https://doi.org/10.5281/zenodo.1226458`.

[142] J. Palacci et al. "Sedimentation and Effective Temperature of Active Colloidal Suspensions". In: *Phys. Rev. Lett.* 105 (2010), p. 088304. DOI: `10.1103/PhysRevLett.105.088304`.

[143] Yongan Gu and Dongqing Li. "The ζ-Potential of Glass Surface in Contact with Aqueous Solutions". In: *Journal of Colloid and Interface Science* 226 (2000), pp. 328–339. DOI: 10.1006/jcis.2000.6827.

[144] A.J.T.M. Mathijssen et al. "Hydrodynamics of micro-swimmers in films". In: *J. Fluid. Mech.* 806 (2016), p. 35. DOI: 10.1017/jfm.2016.479.

[145] E. Lauga and T.M. Squires. "Brownian motion near a partial-slip boundary: A local probe of the no-slip condition". In: *Phys. Fluids* 17 (2005), p. 103102. DOI: 10.1063/1.2083748.

[146] H. Loussaief, L. Pasol, and F. Feuillebois. "Motion of a spherical particle in a viscous fluid along a slip wall". In: *Q. J. Mech. Appl. Math.* 68 (2015), p. 115. DOI: 10.1093/qjmam/hbv001.

[147] M.J. Lighthill. "On the squirming motion of nearly spherical deformable bodies through liquids at very small Reynolds numbers". In: *Commun. Pure Appl. Math.* 5 (1952), p. 109. DOI: 10.1002/cpa.3160050201.

[148] J.R. Blake. "A spherical envelope approach to ciliary propulsion". In: *J. Fluid Mech.* 46 (1971), p. 199. DOI: 10.1017/S002211207100048X.

[149] L. Rothschild. "Non-random Distribution of Bull Spermatozoa in a Drop of Sperm Suspension". In: *Nature* 198 (1963), pp. 1221–1222. DOI: 10.1038/1981221a0.

[150] Vasily Kantsler et al. "Ciliary contact interactions dominate surface scattering of swimming eukaryotes". In: *PNAS* 110 (2013), pp. 1187–1192. DOI: 10.1073/pnas.1210548110.

[151] Allison P. Berke et al. "Hydrodynamic Attraction of Swimming Microorganisms by Surfaces". In: *Phys. Rev. Lett.* 101 (2008), p. 038102. DOI: 10.1103/PhysRevLett.101.038102.

[152] Hans-Curt Flemming et al. "Biofilms: an emergent form of bacterial life". In: *Nat Rev Microbiol* 14 (2016), pp. 563–575. DOI: 10.1038/nrmicro.2016.94.

[153] C. Berne, C. K. Ellison, and A. Ducret. "Bacterial adhesion at the single-cell level". In: *Nat Rev Microbiol* 18 (2016), pp. 616–627. DOI: 10.1038/s41579-018-0057-5.

[154] H. Flemming and S. Wuertz. "Bacteria and archaea on Earth and their abundance in biofilms". In: *Nat Rev Microbiol* 17 (2019), pp. 247–260. DOI: 10.1038/s41579-019-0158-9.

[155] Stefania Ketzetzi et al. "Slip Length Dependent Propulsion Speed of Catalytic Colloidal Swimmers near Walls". In: *Phys. Rev. Lett.* 124 (2020), p. 048002. DOI: 10.1103/PhysRevLett.124.048002.

[156] Mojdeh Heidari et al. "Self-Propulsion of Janus Particles near a Brush-Functionalized Substrate". In: *Langmuir* 36.27 (2020), pp. 7775–7780. DOI: 10.1021/acs.langmuir.0c00461.

[157] Stefania Ketzetzi, Joost de Graaf, and Daniela J. Kraft. "Diffusion-Based Height Analysis Reveals Robust Microswimmer-Wall Separation". In: *Phys. Rev. Lett.* 125 (2020), p. 238001. DOI: 10.1103/PhysRevLett.125.238001.

[158] W. E. Uspal et al. "Rheotaxis of spherical active particles near a planar wall". In: *Soft Matter* 11 (2015), pp. 6613–6632. DOI: 10.1039/c5sm01088h.

[159] M. Kuron et al. "Hydrodynamic mobility reversal of squirmers near flat and curved surfaces". In: *Soft Matter* 15 (2019), p. 5908.

[160] Sang-Hyuk Lee et al. "Characterizing and tracking single colloidal particles with video holographic microscopy". In: *Opt. Express* 15 (2007), pp. 18275–18282. DOI: 10.1364/OE.15.018275.

[161] Anna Wang et al. "Using the discrete dipole approximation and holographic microscopy to measure rotational dynamics of non-spherical colloidal particles". In: *Journal of Quantitative Spectroscopy and Radiative Transfer* 146 (2014), pp. 499–509. DOI: 10.1016/j.jqsrt.2013.12.019.

[162] Murray A. Brown and E. J. Staples. "Measurement of absolute particle-surface separation using total internal reflection microscopy and radiation pressure forces". In: *Langmuir* 6 (1990), pp. 1260–1265. DOI: 10.1021/la00097a012.

[163] Hilding Faxén. *Einwirkung der Gefässwände auf den Widerstand gegen die Bewegung einer kleinen Kugel in einer zähen Flüssigkeit*. Uppsala Universitet, 1921.

[164] Carl Wilhelm Oseen. "Neuere methoden und ergebnisse in der hydrodynamik". In: *Leipzig: Akademische Verlagsgesellschaft mb H.* (1927).

[165] Michael E O'Neill. "A slow motion of viscous liquid caused by a slowly moving solid sphere". In: *Mathematika* 11.1 (1964), pp. 67–74.

[166] S.G. Flicker and S.G. Bike. "Measuring double layer repulsion using total internal reflection microscopy". In: *Langmuir* 9.1 (1993), pp. 257–262. DOI: 10.1021/la00025a049.

[167] Aidin Rashidi and Christopher L Wirth. "Motion of a Janus particle very near a wall". In: *Journal of chemical physics* 147 (2017), p. 224906. DOI: 10.1063/1.4994843.

[168] Ruben W. Verweij et al. "Height distribution and orientation of colloidal dumbbells near a wall". In: *Phys. Rev. E* 102 (2020), p. 062608. DOI: 10.1103/PhysRevE.102.062608.

[169] Lou Coury. "Conductance Measurements Part 1: Theory". In: *Current Separations and Drug Development, Bioanalytical Systems* 18.3 (1999), pp. 91–96.

[170] D.C. Henry. "The cataphoresis of suspended particles. Part I.-The equation of cataphoresis". In: *Proc. R. Soc. London Ser. A* 133 (1931), p. 106.

[171] Joost de Graaf et al. "The raspberry model for hydrodynamic interactions revisited. II. The effect of confinement". In: *The Journal of chemical physics* 143.8 (2015), p. 084108. DOI: 10.1063/1.4928503.

[172] Shaltiel Eloul et al. "Reactive Momentum Transfer Contributes to the Self-Propulsion of Janus Particles". In: *Phys. Rev. Lett.* 124 (2020), p. 188001. DOI: 10.1103/PhysRevLett.124.188001.

[173] C. Zhou et al. "Photochemically powered AgCl Janus micromotors as a model system to understand ionic self-diffusiophoresis". In: *Langmuir* 34 (2018), p. 3289.

[174] Harry Moore et al. "Exceptional sperm cooperation in the wood mouse". In: *Nature* 418 (2002), pp. 174–177. DOI: 10.1038/nature00832.

[175] Cristian A. Solari, John O. Kessler, and Raymond E. Goldstein. "Motility, mixing, and multicellularity". In: *Genet Program Evolvable Mach* 8 (2007), pp. 115–129. DOI: 10.1007/s10710-007-9029-7.

[176] Marco Archetti and Kenneth J. Pienta. "Cooperation among cancer cells: applying game theory to cancer". In: *Nat Rev Cancer* 19 (2019), pp. 110–117. DOI: 10.1038/s41568-018-0083-7.

[177] Calvin K. Lee et al. "Social Cooperativity of Bacteria during Reversible Surface Attachment in Young Biofilms: a Quantitative Comparison of Pseudomonas aeruginosa PA14 and PAO1". In: *mBio* 11 (2020). DOI: 10.1128/mBio.02644-19.

[178] André Luis Souza dos Santos et al. "What are the advantages of living in a community? A microbial biofilm perspective!" In: *Mem Inst Oswaldo Cruz* 113 (2018), e180212. DOI: 10.1590/0074-02760180212.

[179] Luanne Hall-Stoodley, J. William Costerton, and Paul Stoodley. "Bacterial biofilms: from the Natural environment to infectious diseases". In: *Nat Rev Microbiol* 2 (2004), pp. 95–108. DOI: 10.1038/nrmicro821.

[180] Avraham Be'er and Gil Ariel. "A statistical physics view of swarming bacteria". In: *Mov Ecol* 7 (2019), p. 9. DOI: 10.1186/s40462-019-0153-9.

[181] Avraham Be'er et al. "A phase diagram for bacterial swarming". In: *Commun Phys* 3 (2020), p. 66. DOI: 10.1038/s42005-020-0327-1.

[182] Knut Drescher et al. "Fluid dynamics and noise in bacterial cell–cell and cell–surface scattering". In: *PNAS* 108 (2011), pp. 10940–10945. DOI: 10.1073/pnas.1019079108.

[183] Melissa B. Miller and Bonnie L. Bassler. "Quorum Sensing in Bacteria". In: *Ann Rev Micro* 55 (2001), pp. 165–199. DOI: 10.1146/annurev.micro.55.1.165.

[184] Jaideep Katuri et al. "Designing Micro- and Nanoswimmers for Specific Applications". In: *Acc. Chem. Res.* 50.4 (2017), pp. 2–11. DOI: 10.1021/acs.accounts.6b00386.

[185] Hailing Yu et al. "Confined Catalytic Janus Swimmers in a Crowded Channel: Geometry-Driven Rectification Transients and Directional Locking". In: *Small* 12 (2016), pp. 5882–5890. DOI: 10.1002/smll.201602039.

[186] Chang Liu et al. "Bimetallic Microswimmers Speed Up in Confining Channels". In: *Phys. Rev. Lett.* 117 (2016), p. 198001. DOI: 10.1103/PhysRevLett.117.198001.

[187] Megan S. Davies Wykes et al. "Guiding microscale swimmers using teardrop-shaped posts". In: *Soft Matter* 13 (2017), pp. 4681–4688. DOI: 10.1039/C7SM00203C.

[188] J. Katuri et al. "Directed Flow of Micromotors through Alignment Interactions with Micropatterned Ratchets". In: *ACS nano* 12 (2018), pp. 7282–7291. DOI: 10.1021/acsnano.8b03494.

[189] Mite Mijalkov and Giovanni Volpe. "Sorting of chiral microswimmers". In: *Soft Matter* 9 (2013), pp. 6376–6381. DOI: 10.1039/C3SM27923E.

[190] C. Jin et al. "Fine balance of chemotactic and hydrodynamic torques: When microswimmers orbit a pillar just once". In: *Phys Rev E* 110 (2020), 040601(R). DOI: 10.1103/PhysRevE.100.040601.

[191] Debora Schamel et al. "Nanopropellers and Their Actuation in Complex Viscoelastic Media". In: *ACS Nano* 8 (2014), pp. 8794–8801. DOI: 10.1021/nn502360t.

[192] Debora Walker et al. "Enzymatically active biomimetic micropropellers for the penetration of mucin gels". In: *Sci. Adv.* 1 (2015), e1500501. DOI: 10.1126/sciadv.1500501.

[193] Debabrata Patra et al. "Intelligent, self-powered, drug delivery systems". In: *Nanoscale* 5 (2013), pp. 1273–1283. DOI: 10.1039/C2NR32600K.

[194] Wei Gao et al. "Artificial Micromotors in the Mouse's Stomach: A Step toward in Vivo Use of Synthetic Motors". In: *ACS Nano* 9 (2015), pp. 117–123. DOI: 10.1021/nn507097k.

[195] Miguel García et al. "Micromotor-based lab-on-chip immunoassays". In: *Current Opinion in Colloid and Interface Science* 5 (2013), pp. 1325–1331. DOI: 10.1039/C2NR32400H.

[196] Laura Restrepo-Pérez et al. "Biofunctionalized self-propelled micromotors as an alternative on-chip concentrating system". In: *Lab on a chip* 14 (2014), p. 2914. DOI: 10.1039/c4lc00439f.

[197] Matan Yah Ben Zion et al. "Multiple-robot drug delivery strategy through coordinated teams of microswimmers". In: *Appl. Phys. Lett.* 105 (2014), p. 083705. DOI: 10.1063/1.4893695.

[198] Ivo Buttinoni et al. "Dynamical Clustering and Phase Separation in Suspensions of Self-Propelled Colloidal Particles". In: *Phys. Rev. Lett.* 110 (2013), p. 238301. DOI: 10.1103/PhysRevLett.110.238301.

[199] Adam Wysocki, Roland G. Winkler, and Gerhard Gompper. "Cooperative motion of active Brownian spheres in three-dimensional dense suspensions". In: *EPL* 105 (2014), p. 48004. DOI: 10.1209/0295-5075/105/48004.

[200] Matan Yah Ben Zion et al. "Cooperation in a fluid swarm of fuel-free micro-swimmers". In: *arXiv:2012.15087* (2021).

[201] Antoine Aubret et al. "Targeted assembly and synchronization of self-spinning microgears". In: *Nature Phys* 14 (2018), pp. 1114–1118. DOI: 10.1038/s41567-018-0227-4.

[202] Zuochen Wang et al. "Active colloidal molecules assembled via selective and directional bonds". In: *Nat Comm* 11 (2020), p. 2670. DOI: 10.1038/s41467-020-16506-z.

[203] Francisca Guzmán-Lastra, Andreas Kaiser, and Hartmut Löwen. "Fission and fusion scenarios for magnetic microswimmer clusters". In: *Nat Commun* 7 (2016), p. 13519. DOI: 10.1038/ncomms13519.

[204] Saverio E. Spagnolie et al. "Geometric capture and escape of a microswimmer colliding with an obstacle". In: *Soft Matter* 11 (2015), p. 3396. DOI: 10.1039/c4sm02785j.

[205] Jennifer E. Curtis and David G. Grier. "Structure of Optical Vortices". In: *Phys. Rev. Lett.* 90 (2003), p. 133901. DOI: 10.1103/PhysRevLett.90.133901.

[206] Michael Reichert and Holger Stark. "Circling particles and drafting in optical vortices". In: *J. Phys.: Condens. Matter* 16 (2004), S4085. DOI: 10.1088/0953-8984/16/38/023.

[207] C. Lutz et al. "Surmounting barriers: The benefit of hydrodynamic interactions". In: *EPL* 74 (2006), p. 719. DOI: `10.1209/epl/i2006-10017-9`.

[208] W E Uspal et al. "Shape-dependent guidance of active Janus particles by chemically patterned surfaces". In: *New J. Phys.* 20 (2018), p. 015013. DOI: `10.1088/1367-2630/aa9f9f`.

[209] Nima Sharifi-Mood, Ali Mozaffari, and Ubaldo M. Córdova-Figueroa. "Pair interaction of catalytically active colloids: from assembly to escape". In: *J. Fluid Mech.* 798 (2016), p. 910. DOI: `10.1017/jfm.2016.317`.

[210] Akhil Varma and Sébastien Michelin. "Modeling chemo-hydrodynamic interactions of phoretic particles: A unified framework". In: *Phys. Rev. Fluids* 4 (2019), p. 124204. DOI: `10.1103/PhysRevFluids.4.1242047`.

[211] Hartmut Löwen. "Colloidal soft matter under external control". In: *J. Phys.: Condens. Matter* 13.24 (2001), R415–R432.

[212] Shin-Hyun Kim et al. "Biofunctional colloids and their assemblies". In: *Soft Matter* 6.4 (2010), pp. 1092–1110. DOI: `10.1039/b920611f`.

[213] Gaoxiang Wu et al. "Confined Assemblies of Colloidal Particles with Soft Repulsive Interactions". In: *J. Am. Chem. Soc.* 139.14 (2017), pp. 5095–5101. DOI: `10.1021/jacs.6b12975`.

[214] Ming Han, Jonathan K. Whitmer, and Erik Luijten. "Dynamics and structure of colloidal aggregates under microchannel flow". In: *Soft Matter* 15.4 (2019), pp. 744–751. DOI: `10.1039/c8sm01451e`.

[215] Ece Yildiz-Ozturk and Ozlem Yesil-Celiktas. "Diffusion phenomena of cells and biomolecules in microfluidic devices". In: *Biomicrofluidics* 9.5 (2015), p. 052606.

[216] Hernán Míguez, San Ming Yang, and Geoffrey A. Ozin. "Optical Properties of Colloidal Photonic Crystals Confined in Rectangular Microchannels". In: *Langmuir* 19.8 (2003), pp. 3479–3485.

[217] Horacio Serna, Eva G. Noya, and Wojciech T. Goźdź. "The influence of confinement on the structure of colloidal systems with competing interactions". In: *Soft Matter* 16 (2020), p. 718.

[218]   P. Yang et al. "Patterning Porous Oxides within Microchannel Networks". In: *Adv. Mat.* 13.6 (2001), pp. 427–431.

[219]   Ranajit Mondal and Madivala G. Basavaraj. "Patterning of colloids into spirals via confined drying". In: *Soft Matter* 15.16 (2020), pp. 3753–3761.

[220]   Hung-Jen Wu and Michael A. Bevan. "Direct Measurement of Single and Ensemble Average Particle-Surface Potential Energy Profiles". In: *Langmuir* 21.4 (2005), pp. 1244–1254.

[221]   H Lorentz. In: *Adv. Theor. Phys.* 1 (1907), pp. 23–33.

[222]   H Faxen. "The resistance against the movement of a rigour sphere in viscous fluids, which is embedded between two parallel layered barriers". In: *Ann. Phys.* 4 (1922), pp. 79–89.

[223]   H Faxen. "Fredholm integral equations of hydrodynamics of liquids I". In: *Ark. Mat., Astron. Fys.* 18 (1924), pp. 29–32.

[224]   H Brenner. "The slow motion of a sphere through a viscous fluid towards a plane surface". In: *Chem. Eng. Sci.* 16 (1961), pp. 242–251.

[225]   Nasser A. Frej and Dennis C. Prieve. "Hindered diffusion of a single sphere very near a wall in a nonuniform force field". In: *J. Chem. Phys.* 98 (1993), p. 7552. DOI: 10.1063/1.464695.

[226]   S. A. Rogers et al. "Rotational Diffusion of Spherical Colloids Close to a Wall". In: *Phys. Rev. Lett.* 109 (2012), p. 098305. DOI: 10.1103/PhysRevLett.109.098305.

[227]   Kai Huang and Izabela Szlufarska. "Effect of interfaces on the nearby Brownian motion". In: *Nat Commun* 6 (2015), p. 8558. DOI: 10.1038/ncomms9558.

[228]   Laurent Lobry and Nicole Ostrowsky. "Diffusion of Brownian particles trapped between two walls: Theory and dynamic-light-scattering measurements". In: *Phys. Rev. B* 53 (1996), p. 12050. DOI: 10.1103/PhysRevB.53.12050.

[229]   Binhua Lin, Jonathan Yu, and Stuart A. Rice. "Direct measurements of constrained Brownian motion of an isolated sphere between two walls". In: *Phys. Rev. E* 62 (2000), p. 3909. DOI: 10.1103/PhysRevE.62.3909.

[230] E. R. Dufresne, D. Altman, and D. G. Grier. "Brownian dynamics of a sphere between parallel walls". In: *Europhys. Lett.* 53 (2001), pp. 264–270. DOI: `10.1209/epl/i2001-00147-6`.

[231] Thorben Benesch, Sotira Yiacoumi, and Costas Tsouris. "Brownian motion in confinement". In: *Phys. Rev. E* 68 (2003), p. 021401. DOI: `10.1103/PhysRevE.68.021401`.

[232] K Zembrzycki, S Błoński, and T A Kowalewski. "Analysis of wall effect on the process of diffusion of nanoparticles in a microchannel". In: *J. Phys.: Conf. Ser.* 392 (2012), p. 012014. DOI: `10.1088/1742-6596/392/1/012014`.

[233] Simon L. Dettmer et al. "Anisotropic diffusion of spherical particles in closely confining microchannels". In: *Phys. Rev. E* 89 (2014), p. 062305. DOI: `10.1103/PhysRevE.89.062305`.

[234] Pushkar P. Lele et al. "Colloidal diffusion and hydrodynamic screening near boundaries". In: *Soft Matter* 7 (2011), pp. 6844–6852. DOI: `10.1039/C0SM01466D`.

[235] V. N. Michailidou et al. "Dynamics of Concentrated Hard-Sphere Colloids Near a Wall". In: *Phys. Rev. Lett.* 102 (2009), p. 068302. DOI: `10.1103/PhysRevLett.102.068302`.

[236] Raphaël Pesché and Gerhard Nägele. "Stokesian dynamics study of quasi-two-dimensional suspensions confined between two parallel walls". In: *Phys. Rev. E* 62 (2000), p. 5432. DOI: `10.1103/PhysRevE.62.5432`.

[237] Burak Eral et al. "Anisotropic and hindered diffusion of colloidal particles in a closed cylinder". In: *Langmuir* 22 (2010), pp. 16722–16729. DOI: `10.1021/la102273n`.

[238] Bianxiao Cui, Haim Diamant, and Binhua Lin. "Screened Hydrodynamic Interaction in a Narrow Channel". In: *Phys. Rev. Lett.* 89 (2002), p. 188302. DOI: `10.1103/PhysRevLett.89.188302`.

[239] Junwei Wang et al. "Free Energy Landscape of Colloidal Clusters in Spherical Confinement". In: *ACS Nano* 13 (2019), pp. 9005–9015. DOI: `10.1021/acsnano.9b03039`.

[240] John Happel and Howard Brenner. *Low Reynolds number hydrodynamics with special applications to particulate media*. Springer, 1983. DOI: `https://doi.org/10.1007/978-94-009-8352-6`.

[241] Y. Han et al. "Brownian Motion of an Ellipsoid". In: *Science* 314.5799 (2006), pp. 626–630. DOI: `10.1126/science.1130146`.

[242] J. T. Padding and W. J. Briels. "Translational and rotational friction on a colloidal rod near a wall". In: *J. Chem. Phys.* 132.5 (2010), p. 054511. DOI: `h10.1063/1.3308649`.

[243] Daniela J. Kraft et al. "Brownian motion and the hydrodynamic friction tensor for colloidal particles of complex shape". In: *Phys. Rev. E* 88 (2013), 050301(R). DOI: `10.1103/PhysRevE.88.050301`.

[244] Tunrayo Adeleke-Larodo, Pierre Illien, and Ramin Golestanian. "Fluctuation-induced hydrodynamic coupling in an asymmetric, anisotropic dumbbell". In: *The European Physical Journal E* 42.39 (2019), p. 054511. DOI: `10.1140/epje/i2019-11799-5`.

[245] Maryam Haghighi et al. "Translational and Rotational Diffusion of Gold Nanorods Near a Wall". In: *J. Chem. Phys.* 139 (2013), p. 064710. DOI: `10.1063/1.4817405`.

[246] Maciej Lisicki, Bogdan Cichocki, and Eligiusz Wajnryb. "Near-wall diffusion tensor of an axisymmetric colloidal particle". In: *J. Chem. Phys.* 145 (2016), p. 034904. DOI: `10.1063/1.4958727`.

[247] Steven Delong, Florencio Balboa Usabiaga, and Aleksandar Donev. "Brownian dynamics of confined rigid bodies". In: *J. Chem. Phys.* 143 (2015), p. 144107. DOI: `10.1063/1.4932062`.

[248] Miguel X. Fernandes and José Garciá de la Torre. "Brownian Dynamics Simulation of Rigid Particles of Arbitrary Shape in External Fields". In: *Biophys J* 83.6 (2002), pp. 3039–3048. DOI: `10.1016/S0006-3495(02)75309-5`.

[249] Mauricio D. Carbajal-Tinoco, Ricardo Lopez-Fernandez, and José Luis Arauz-Lara. "Asymmetry in Colloidal Diffusion near a Rigid Wall". In: *Phys. Rev. Lett.* 99 (2007), p. 138303. DOI: `10.1103/PhysRevLett.99.138303`.

[250] J. Leach et al. "Comparison of Faxén' s correction for a microsphere translating or rotating near a surface". In: *Phys. Rev. E* 79 (2009), p. 026301. DOI: `10.1103/PhysRevE.79.026301`.

[251] Sylvia Jeney et al. "Anisotropic Memory Effects in Confined Colloidal Diffusion". In: *Phys. Rev. Lett.* 100 (2008), p. 240604. DOI: 10.1103/PhysRevLett.100.240604.

[252] Erik Schäffer, Simon F Nørrelykke, and Jonathon Howard. "Surface Forces and Drag Coefficients of Microspheres Near a Plane Surface Measured With Optical Tweezers". In: *Langmuir* 23 (2007), p. 3654. DOI: 10.1021/la0622368.

[253] N. Garnier and N. Ostrowsky. "Brownian dynamics in a confined geometry. Experiments and numerical simulations". In: *J. Phys. II* 1 (1991), pp. 1221–1232. DOI: 10.1051/jp2:1991129.

[254] Peter Holmqvist, Jan K G Dhont, and Peter R Lang. "Colloidal Dynamics Near a Wall Studied by Evanescent Wave Light Scattering: Experimental and Theoretical Improvements and Methodological Limitations". In: *J. Chem. Phys.* 126 (2007), p. 044707. DOI: 10.1063/1.2431175.

[255] Toshiharu Watarai and Toshiaki Iwai. "Direct observation of submicron Brownian particles at a solid-liquid interface by extremely low coherence dynamic light scattering". In: *Appl. Phys. Express* 7 (2014), p. 032502. DOI: 10.7567/APEX.7.032502.

[256] M. I. M. Feitosa and O. N. Mesquita. "Wall-drag effect on diffusion of colloidal particles near surfaces: A photon correlation study". In: *Phys. Rev. A* 44 (1991), p. 6677. DOI: 10.1103/PhysRevA.44.6677.

[257] K. H. Lan, N. Ostrowsky, and D. Sornette. "Brownian dynamics close to a wall studied by photon correlation spectroscopy from an evanescent wave". In: *Phys. Rev. Lett.* 57 (1986), p. 17. DOI: 10.1103/PhysRevLett.57.17.

[258] Peter Holmqvist, Jan K. G. Dhont, and Peter R. Lang. "Anisotropy of Brownian motion caused only by hydrodynamic interaction with a wall". In: *Phys. Rev. E* 74 (2006), p. 021402. DOI: 10.1103/PhysRevE.74.021402.

[259] Maciej Lisicki et al. "Translational and rotational near-wall diffusion of spherical colloids studied by evanescent wave scattering". In: *Soft Matter* 10 (2014), pp. 4312–4323. DOI: 10.1039/C4SM00148F.

[260] Yutaka Kazoe and Minami Yoda. "Measurements of the near-wall hindered diffusion of colloidal particles in the presence of an electric field". In: *Appl. Phys. Lett.* 99 (2011), p. 124104. DOI: 10.1063/1.3643136.

[261] D.C. Prieve. "Measurement of colloidal forces with TIRM". In: *Adv. Colloid Interface Sci.* 82 (1999), pp. 93–125. DOI: 10.1016/S0001-8686(99)00012-3.

[262] Giovanni Volpe et al. "Novel perspectives for the application of total internal reflection microscopy". In: *Opt. Express* 17 (2009), pp. 23975–23985. DOI: 10.1364/OE.17.023975.

[263] Lulu Liu et al. "Absolute position total internal reflection microscopy with an optical tweezer". In: *PNAS* 111 (2014), E5609–E5615. DOI: 10.1073/pnas.1422178112.

[264] Lisa Dixon, Fook Chiong Cheong, and David G. Grier. "Holographic deconvolution microscopy for high-resolution particle tracking". In: *Opt. Express* 19 (2011), p. 16410. DOI: 10.1364/OE.19.016410.

[265] Dan S. Bolintineanu et al. "Particle dynamics modeling methods for colloid suspensions". In: *Computational Particle Mechanics* 1 (2014), pp. 321–356.

[266] Christine Middleton et al. "Optimizing the Synthesis of Monodisperse Colloidal Spheres Using Holographic Particle Characterization". In: *Langmuir* 35 (2019), pp. 6602–6609. DOI: 10.1021/acs.langmuir.9b00012.

[267] Jorge Garcia-Sucerquia et al. "Digital in-line holographic microscopy". In: *Appl. Opt.* 45 (2006), p. 836. DOI: 10.1364/AO.45.000836.

[268] Pierre Marquet et al. "Digital holographic microscopy: a noninvasive contrast imaging technique allowing quantitative visualization of living cells with subwavelength axial accuracy". In: *Opt. Lett.* 30 (2005), pp. 468–470. DOI: 10.1364/OL.30.000468.

[269] Camila B Giuliano, Rongjing Zhang, and Laurence G Wilson. "Digital Inline Holographic Microscopy (DIHM) of Weakly-Scattering Subjects". In: *J Vis Exp.* 84 (2014), e50488. DOI: 10.3791/50488.

[270]   Wenbo Xu et al. "Digital in-line holography for biological applications". In: *PNAS* 98 (2001), pp. 11301–11305. DOI: 10.1073/pnas.191361398.

[271]   Lauren E. Altman and David G. Grier. "CATCH: Characterizing and Tracking Colloids Holographically Using Deep Neural Networks". In: *J. Phys. Chem. B* 124 (2020), pp. 1602–1610. DOI: 10.1021/acs.jpcb.9b10463.

[272]   J.H. Zhang et al. "Preparation of monodisperse silica particles with controllable size and shape". In: *J. Mater. Res.* 18.3 (2003), pp. 649–653. DOI: 10.1557/JMR.2003.0085.

[273]   W. S. Rasband. "ImageJ". In: *U. S. National Institutes of Health* (1997-2018). URL: https://imagej.nih.gov/ij/.

[274]   Solomon Barkley et al. *Holographic Microscopy with Python and HoloPy*. 2018. arXiv: 1806.00058 [eess.IV].

[275]   Daniel W. Mackowski and Michael I. Mishchenko. "Calculation of the T matrix and the scattering matrix for ensembles of spheres". In: *J. Opt. Soc. Am. A* 13.11 (1996), pp. 2266–2278.

[276]   Dan Allan et al. *soft-matter/trackpy: Trackpy v0.4.2*. Version v0.4.2. 2019. DOI: 10.5281/zenodo.3492186. URL: https://doi.org/10.5281/zenodo.3492186.

[277]   John C. Crocker and David G. Grier. "Methods of Digital Video Microscopy for Colloidal Studies". In: *Journal of Colloid and Interface Science* 179.1 (1996), pp. 298–310. DOI: 10.1006/jcis.1996.0217.

[278]   Jacob N Israelachvili. *Intermolecular and surface forces*. Academic press, 2011.

[279]   Raphael Wittkowski and Hartmut Löwen. "Self-propelled Brownian spinning top: Dynamics of a biaxial swimmer at low Reynolds numbers". In: *Phys. Rev. E* 85 (2012), p. 021406. DOI: 10.1103/PhysRevE.85.021406.

[280]   Hartmut Löwen. "Chirality in microswimmer motion: From circle swimmers to active turbulence". In: *Eur. Phys. J. Special Topics* 225 (2016), pp. 2319–2331. DOI: 10.1140/epjst/e2016-60054-6.

[281] Benno Liebchen et al. "Viscotaxis: Microswimmer Navigation in Viscosity Gradients". In: *Phys. Rev. Lett.* 120 (2018), p. 208002. DOI: `10.1103/PhysRevLett.120.208002`.

[282] Andreas Zöttl and Holger Stark. "Emergent behavior in active colloids". In: *J. Phys.: Condens. Matter* 28 (2016), p. 253001. DOI: `10.1088/0953-8984/28/25/253001`.

[283] Leticia F. Cugliandolo, Pasquale Digregorio Giuseppe Gonnella, and Antonio Suma. "Phase Coexistence in Two-Dimensional Passive and Active Dumbbell Systems". In: *Phys. Rev. Lett.* 119 (2017), p. 268002. DOI: `10.1103/PhysRevLett.119.268002`.

[284] Robin van Damme et al. "Interparticle torques suppress motility-induced phase separation for rodlike particles". In: *J. Chem. Phys.* 150 (2019), p. 164501. DOI: `10.1063/1.5086733`.

[285] Leonardo F. Valadares et al. "Catalytic Nanomotors: Self-Propelled Sphere Dimers". In: *Small* 6 (2010), pp. 565–572. DOI: `10.1002/smll.200901976`.

[286] Jin-Woong Kim, Ryan J. Larsen, and David A. Weitz. "Synthesis of Nonspherical Colloidal Particles with Anisotropic Properties". In: *J. Am. Chem. Soc.* 128 (2006), pp. 14374–14377. DOI: `10.1021/ja065032m`.

[287] B. Carrasco and J. Garcia de la Torre. "Improved hydrodynamic interaction in macromolecular bead model". In: *J. Chem. Phys.* 111 (1999), p. 4817. DOI: `10.1063/1.479743`.

[288] Vera Meester and Daniela J. Kraft. "Spherical, Dimpled, and Crumpled Hybrid Colloids with Tunable Surface Morphology". In: *Langmuir* 32 (2016), pp. 10668–10677. DOI: `10.1021/acs.langmuir.6b02952`.

[289] Daniela J. Kraft et al. "Surface roughness directed self-assembly of patchy particles into colloidal micelles". In: *PNAS* 109 (2012), pp. 10787–10792. DOI: `10.1073/pnas.1116820109`.

[290] Babak Vajdi Hokmabad et al. "Topological Stabilization and Dynamics of Self-Propelling Nematic Shells". In: *Phys. Rev. Lett.* 123 (2019), p. 178003. DOI: `10.1103/PhysRevLett.123.178003`.

[291] Abraham Savitzky and M. J. E. Golay. "Smoothing and Differentiation of Data by Simplified Least Squares Procedures". In: *Anal. Chem.* 36 (1964), pp. 1627–1639. DOI: 10.1021/ac60214a047.

[292] C. Candan and H. Inan. "A unified framework for derivation and implementation of Savitzky-Golay filters". In: *Signal Processing* 104 (2014), pp. 203–211. DOI: 10.1016/j.sigpro.2014.04.016.

[293] Liqiang Ren, Wei Wang, and Thomas E. Mallouk. "Two Forces Are Better than One: Combining Chemical and Acoustic Propulsion for Enhanced Micromotor Functionality". In: *Acc. Chem. Res.* 51 (2018), pp. 1948–1956. DOI: 10.1021/acs.accounts.8b00248.

[294] Sho C. Takatori et al. "Acoustic trapping of active matter". In: *Nat. Commun.* 7 (2016), p. 10694. DOI: 10.1038/ncomms10694.

[295] Hanumantha Rao Vutukuri et al. "Rational design and dynamics of self-propelled colloidal bead chains: from rotators to flagella". In: *Sci. Rep.* 7 (2017), p. 16758. DOI: 10.1038/s41598-017-16731-5.

[296] Bipul Biswas et al. "Linking Catalyst-Coated Isotropic Colloids into "Active" Flexible Chains Enhances Their Diffusivity". In: *ACS Nano* 11 (2017), pp. 10025–10031. DOI: 10.1021/acsnano.7b04265.

[297] L. Alvarez et al. "Reconfigurable Artificial Microswimmers with Internal Feedback". In: *arXiv:2009.08382* (2020).

[298] Indrani Chakraborty et al. "Colloidal joints with designed motion range and tunable joint flexibility". In: *Nanoscale* 9 (2017), pp. 7814–7821. DOI: 10.1039/C6NR08069C.

[299] Ruben W. Verweij et al. "Flexibility-induced effects in the Brownian motion of colloidal trimers". In: *Phys. Rev. Research* 2 (2020), p. 033136. DOI: 10.1103/PhysRevResearch.2.033136.

[300] Ruben W Verweij et al. "Conformations and diffusion of flexibly linked colloidal chains". In: *JPhys Materials* (2021). DOI: 10.1088/2515-7639/abf571.

[301] Casper van der Wel et al. "Micrometer-sized TPM emulsion droplets with surface-mobile binding groups". In: *J. Phys.: Condens. Matter* 30 (2018), p. 094005. DOI: 10.1088/1361-648X/aaab22.

Summary

From flocks of birds in the sky and schools of fish in the water, to tiny colonies of bacteria in the soil and cells in the human body, living organisms have evolved to grow and to maintain themselves. A few examples of them are shown in Figure 1A-E. Scientists often think of these organisms as *living materials*. These materials have remarkable abilities: they can control their shape, assemble, organize, and even heal themselves, to name a few. Living materials use these abilities to respond to the stimuli they sense from their environment. Take bacteria for instance. Bacteria use a mechanism called chemotaxis[1]: To feed or to protect themselves, their bodies' tiny flagella sense if the amount of food molecules or of toxins increases in a certain direction. In the same way, sperm moves towards the egg, and neutrophils chase after bacteria.

Nowadays, scientists have found great inspiration in living materials. They use this inspiration to create microscopic *synthetic materials* that will likewise move autonomously inside complex environments. These materials, known as *synthetic microswimmers*, can be very useful for industrial applications. For example, they could be used in bio-medicine and micro-surgery to transport and deliver drugs at specific locations within the body, or they could be used in environmental remediation to locate and decompose the source of pollution inside contaminated waters.

In this work, we prepared in the laboratory synthetic particles with sizes of about three micrometers, as in Figures 1F-H. Particles of this size are called *colloids*: they are so small that they cannot be seen with the naked eye, but we can image them using a microscope. Normally, when we place the colloids inside a liquid they move randomly, an effect known as Brownian motion. Here, by tailoring the surfaces of the colloids, we suppressed their random motion and instead we made colloids that could direct their own motion: we covered half their surface with the metal platinum and then we placed them inside water that also contained a small amount of hydrogen peroxide. In this liquid, the platinum-coated colloids immediately propel themselves with the platinum side on the back because of a catalytic process that takes place on the platinum. For this reason they are named *catalytic microswimmers* and can be used in experimental studies as models for synthetic microswimmers.

---

[1]In ancient greek $\tau\acute{\alpha}\xi\iota\varsigma$, from the verb $\tau\acute{\alpha}\sigma\sigma\omega$ which translates as to arrange, order
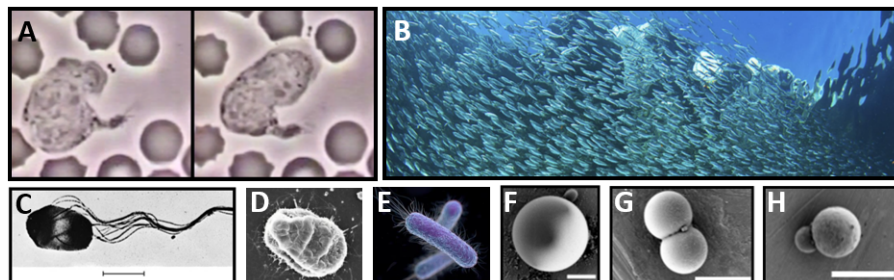
Figure 1: **Examples of biological (A-E) and synthetic (F-H) swimmers. A)** A white blood cell, called neutrophil, senses and chases after a bacterium. It moves between the red blood cells by constantly changing its shape. **B-E)** Examples of biological swimmers with different sizes and shapes. A school of fish (B), a *Salmonella* bacterium (C, the scale bar is 1 micrometer), a *Thiovulum majus* bacterium (D), and *Escherichia coli* bacteria (E). **F-H)** Examples of the synthetic microswimmers that we synthesized and studied in our laboratory. Our colloidal swimmers had sizes around 3 micrometers and were either spherical (F, scale bar is 1 micrometer) or shaped like dumbbells. The dumbbells were symmetric (G, scale bar is 3 micrometers) —the two lobes had the same size— or asymmetric (H, scale bar is 2 micrometers) — one lobe was smaller than the other.

Briefly, they achieve their motion as follows: the platinum acts as a catalyst that breaks down the hydrogen peroxide. This is a chemical reaction process, which creates reaction products around the platinum. These reaction products are colored green in Figure 2A. Simply put, hydrogen peroxide is the *fuel* that the colloid uses (consumes) to push itself forward. In essence, this happens because the reaction products interact with the colloid; this causes the liquid to move in one direction around the colloid and pushes (propels) the colloid forward. This mechanism of motion is similar to *self-phoresis* [2,3,4], but for these colloids the exact details of the mechanism are not known yet.

When we place the mixture of the synthetic swimmers and the liquid fuel inside a container, the swimmers tend to swim downwards towards the bottom. When they reach the bottom wall, they stay there and self-propel parallel to the wall, as sketched in Figure 2A. In **chapter 2**, we used a microscope to image the swimmers and to measure how fast they moved near the wall. We first used a wall

---

[2]In ancient greek $\phi \acute{o} \rho \eta \sigma \iota \varsigma$ from the verb $\phi \acute{\epsilon} \rho \omega$ which loosely translates as to bring, carry
[3]In general, phoresis describes the migration of colloids inside a liquid
[4]The prefix *self-* is used here because the colloid causes its propulsion by itself without external driving
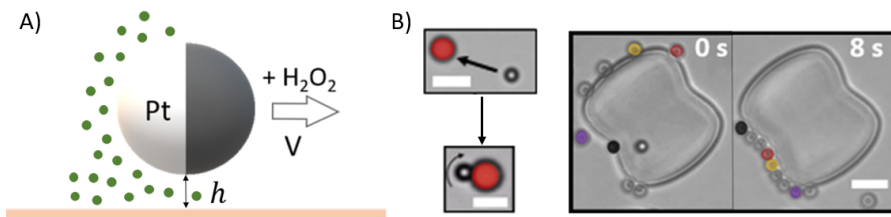
Figure 2: **A)** Our colloidal particles are half-coated with platinum (Pt) and self-propel with speed V parallel to a wall, and at a fixed height h from it, inside hydrogen peroxide (H_2O_2). The platinum breaks down the fuel (hydrogen peroxide) and creates reaction products (shown here as green dots). These drive fluid flows around the particle and the wall. **B)** We 3D-printed obstacles for the swimmers on the wall. The obstacles had circular (marked as red in the images on the left) or peanut shapes (images on the right). When the swimmers approached the obstacles they moved in orbits around them. The swimmers assembled themselves and formed long chains along the obstacles.

made of glass. Then, in some experiments we modified the surface of the glass wall, and in others we used walls made of other materials. We found that the swimmers moved with different speeds above the walls, sometimes faster and sometimes slower. We proposed that this happened because some walls were more slippery than others: slippery walls helped the liquid to flow along more easily. On the contrary, the liquid found a resistance along walls that were not slippery, which caused the swimmers above them to move slower. This work helped us to understand that nearby walls can affect the motion of synthetic microswimmers, as has already been known for biological microswimmers.

In **chapter 3**, we developed a simple method for measuring the distance (height) at which any swimmer (that is shaped like a sphere) moves above the wall. Our method uses quantitative mathematical relationships that connect the random motion (diffusion) of colloids to a height from the wall. Although for our swimmers random motion is suppressed, it is still present, and can be extracted from measurements taken by the microscope; afterwards, the height of the swimmer from the wall can be calculated from the diffusion. By using this method, we found that our swimmers move very close to the wall at heights of about 300 nanometers, a length that is much smaller than the size of the swimmers. To our surprise, we also found that the height remained almost constant when we changed various conditions in the experiments, for example the size of the swimmers or their electrical charge. We called the tendency of swimmers to move parallel to the wall and at fixed heights from the wall, "ypsotaxis" [5]. Our work

---

[5]From the greek word ύψος which means height

showed once again that walls influence the behavior of synthetic swimmers, and this helped us to put forward some new ideas about their motion mechanism.

In **chapter 4**, we used a 3D-printing technique to print and attach microstructures on top of the wall. These structures were larger than the swimmers and had either circular shapes or shapes that looked like peanuts, see for example Figure 2B. As the swimmers were moving parallel to the wall, they came across the structures and then started to orbit around them. We found that when more swimmers orbited the same structure, they were moving faster than when a swimmer was orbiting alone. It was very interesting to find a sense of cooperative motion between synthetic swimmers, because until now this was found only between biological swimmers like bacteria. In addition, the swimmers assembled themselves and formed long chains, which were orbiting around the structures. Finally, we found that the curvature of the structures affected the behavior of the long swimmer chains. This can be useful in the future for applications: we could think of strategies to use the curvature of the walls as a tool to control the motion of the swimmers.

In **chapter 5**, we developed a second method for measuring distances between colloids and walls. This technique was based on holographic microscopy. It can be used to measure the height from the wall for any colloid — not only the ones that look like spheres — as long as the surface of the colloid is the same everywhere. Because of this, we could not use it for the spherical swimmers with the platinum side, but instead we used it to study the random motion of colloids with more complex shapes. We studied colloids that looked like *dumbbells* after they settled above the wall. To make the dumbbells, we always attached together two spheres that had the same size. We found that the motion of the dumbbell above the wall depended on the size of the dumbbell. In water, the smaller dumbbells were positioned at preferred angles with respect to the wall. This did not happen when we used bigger dumbbells made of the same material: the bigger dumbbells oriented almost parallel to the wall instead. Our work showed that non-spherical colloids behave in complex ways near a wall. In the future, this can help us to develop models that will predict the movement of colloids with arbitrary shapes near walls.

In **chapter 6**, we were inspired by biological microswimmers which have non-trivial shapes. For biological microswimmers, shape is expected to be important: for example, different shapes may help the swimmers to navigate more easily inside complex environments. We were interested to see how shape affect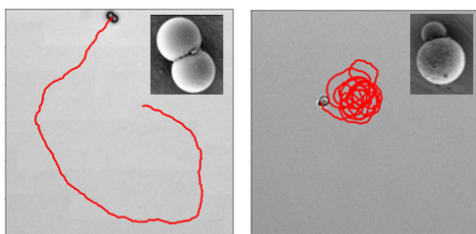s the motion of synthetic swimmers. We used dumbbells with different morphologies as shown in Figure 3. We added platinum on one side of the dumbbells and then placed them in the hydrogen peroxide fuel. Symmetric dumbbells self-propelled in the direction away from the platinum in a straight motion. In contrast, asymmetric dumbbells were moving in circles. Our finding agreed with previous research and confirmed that the shape and coating of the swimmer controls its trajectory.

Figure 3: Dumbbell-shaped swimmers with symmetric lobes moved almost in a straight-like fashion (left). Swimmers with asymmetric lobes moved in circles (right panel). The red lines show the trajectories of the swimmers.

Overall, the work presented in this thesis helped us understand how synthetic swimmers behave and which factors affect their speeds and trajectories. This understanding may be useful when using catalytic swimmers as models for microswimmers in science, but also in future applications: since synthetic swimmers will be needed to perform tasks in complex environments, this work may help in predicting and controlling their motion inside different environments.

Samenvatting

Van zwermen vogels in de lucht, scholen vissen in het water, kleine kolonies bacteriën in de bodem, tot cellen in het menselijk lichaam: levende organismen zijn door de eeuwen heen geëvolueerd om zichzelf op te bouwen en in stand te houden. Wetenschappers – en in het bijzonder, natuurkundigen – beschouwen deze organismen vaak als *levende materialen*. Deze materialen hebben opmerkelijke eigenschappen: ze kunnen van vorm veranderen, assembleren, organiseren en zelfs zichzelf genezen, om maar een paar voorbeelden te noemen. Levende materialen maken gebruik van deze speciale eigenschappen om te reageren op prikkels uit hun omgeving. Een goed voorbeeld hiervan zijn bacteriën. Bacteriën gebruiken een mechanisme dat chemotaxis[1] wordt genoemd: om zichzelf te voeden of te beschermen, voelen de bacteriën met kleine flagella (of zweepstaartjes) of de hoeveelheid voedselmoleculen of gifstoffen in een bepaalde richting toeneemt. Op dezelfde manier beweegt ook bijvoorbeeld sperma zich naar het ei en jagen witte bloedcellen achter bacteriën aan.

Wetenschappers putten inspiratie uit levende materialen om microscopisch kleine deeltjes te maken die zich autonoom kunnen verplaatsen in complexe omgevingen. Deze materialen, bekend als *synthetische microzwemmers*, kunnen zeer nuttig zijn voor industriële toepassingen. Ze zouden bijvoorbeeld kunnen worden gebruikt in de biogeneeskunde en microchirurgie, om medicijnen te transporteren en af te leveren op specifieke locaties in het lichaam. Verder kunnen ze worden toegepast bij milieusanering, om de bron van vervuiling in vervuild water te lokaliseren en af te breken.

Voor dit proefschrift hebben we in het laboratorium synthetische deeltjes gemaakt met afmetingen van ongeveer drie micrometer. Deeltjes van deze grootte worden *colloïden* genoemd: ze zijn zo klein dat ze niet met het blote oog kunnen worden waargenomen, maar met behulp van een microscoop kunnen we ze in beeld brengen. Normaal gesproken, wanneer de colloïden zich in een vloeistof bevinden, bewegen ze willekeurig. Deze willekeurige beweging staat bekend als de Brownse beweging of diffusie. Hier hebben we, door de oppervlakte-eigenschappen van de colloïden aan te passen, hun willekeurige beweging juist onderdrukt. In plaats daarvan hebben we colloïden gemaakt die zichzelf kunnen voortbewegen. We hebben hiervoor de helft van hun oppervlak met het metaal platina bedekt en hebben ook een kleine hoeveelheid waterstofperoxide toegevoegd aan de vloeistof waarin de colloïdale deeltjes zich bevonden. In deze

---

[1]Van het Oudgriekse woord $\tau\acute{\alpha}\xi\iota\varsigma$, wat rangschikking, ordening betekent

vloeistof stuwen de met platina bedekte colloïden zich voort met de platina-zijde op de rug, vanwege een katalytisch proces dat plaatsvindt op het platina. Om deze reden worden deze deeltjes *katalytische microzwemmers* genoemd en kunnen ze in experimentele studies worden gebruikt als modellen voor synthetische microzwemmers. In het kort werkt hun voorstuwingsmechanisme als volgt: het platina oppervlak werkt als een katalysator die het waterstofperoxide in de oplossing afbreekt. Dit is een chemisch reactieproces, waarbij de reactieproducten ontstaan aan het platina oppervlak. Simpel gezegd is waterstofperoxide een *brandstof* die door het colloïdale deeltje wordt verbruikt om zichzelf vooruit te duwen. Feitelijk gebeurt dit doordat de reactieproducten een interactie aangaan met het deeltje; dit zorgt ervoor dat de vloeistof in één richting rond het deeltje beweegt en deze dus naar voren wordt geduwd, wat resulteert in voorstuwing. Dit bewegingsmechanisme is vergelijkbaar met *zelf-forese*[2,3,4], maar voor deze colloïden zijn de exacte details van het mechanisme nog niet bekend.

Wanneer we onze synthetische zwemmers aan een oplossing van waterstofperoxide in water toevoegen, hebben ze de neiging om naar beneden te zwemmen, richting de bodem. Wanneer ze deze bereiken, verlaten ze de bodem niet meer en bewegen ze zichzelf evenwijdig aan het bodemoppervlak. In **hoofdstuk 2** hebben we met behulp van microscopie de zwemmers in beeld gebracht, om te meten hoe snel ze langs de bodem bewogen. We gebruikten eerst een bodem van glas, een oppervlak dat onderzoekers in de regel voor microscopie gebruiken. Vervolgens hebben we in een aantal experimenten het oppervlak van de glazen wand aangepast en ook hebben we wanden van andere materialen gebruikt. We ontdekten dat de zwemmers met verschillende snelheden boven de bodem bewogen afhankelijk van het gebruikte oppervlak: soms sneller en soms langzamer dan boven de glazen wand. Onze hypothese was dat dit gebeurde omdat sommige oppervlakken glibberiger waren dan andere: de glibberigere bodems lieten de vloeistof gemakkelijker langs het oppervlak stromen. Daarentegen ondervond de vloeistof meer weerstand langs oppervlakken die minder glibberig waren, waardoor de zwemmers erboven langzamer gingen bewegen. Dit zou kunnen verklaren waarom verschillende onderzoekers hebben opgemerkt dat vergelijkbare zwemmers zich met verschillende snelheden bewogen. Dit werk hielp ons te begrijpen dat nabijgelegen oppervlakken de beweging van synthetische microzwemmers kunnen beïnvloeden, iets wat al eerder bekend was voor biologische microzwemmers.

---

[2]Uit het Oudgrieks: $\phi\acute{o}\rho\eta\sigma\iota\varsigma$, afgeleid van het werkwoord $\phi\acute{e}\rho\omega$, wat zoals als dragen of brengen betekent

[3]In het algemeen beschrijft forese de migratie van colloïden in een vloeistof

[4]Het voorvoegsel *zelf-* wordt hier gebruikt omdat het deeltje de voortstuwing zelf veroorzaakt, zonder externe aandrijving

Voor **hoofdstuk 3**, waren we geïnteresseerd in het meten van de afstand tussen de zwemmers en de bodem. We ontdekten een eenvoudige methode om de hoogte van een zwemmer te meten, met behulp van een bolvormig deeltje wat zich boven het oppervlak beweegt. Zoals eerder besproken, diffunderen normale colloïden (niet zwemmers) willekeurig in een vloeistof. Kwantitatieve wiskundige relaties laten zien dat hun verspreiding langzamer is wanneer ze zich dichter bij het oppervlak bevinden. Hierdoor kan met behulp van de snelheid van de verspreiding rechtstreeks een hoogte vanaf de bodem worden uitgerekend. Deze willekeurige beweging is nog steeds, hoewel in mindere mate, aanwezig voor de zwemmers, en we kunnen de verspreiding als gevolg van deze bewegingen berekenen uit de microscopiemetingen. Door een kwantitatieve wiskundige formule te gebruiken, hebben we de hoogte berekend op basis van de diffusie van de zwemmers. We ontdekten dat de colloïden heel dicht op de bodem bewogen, op een hoogte van ongeveer 300 nanometer, een afstand die veel kleiner is dan de grootte van onze zwemmers. Tot onze verbazing ontdekten we ook dat de afstand bijna constant bleef als we verschillende parameters van de experimenten veranderden, zoals de grootte van de zwemmers of hun elektrische lading. We hebben deze neiging van de zwemmers om parallel aan, en op vaste hoogte van de bodem te bewegen "ypsotaxis"[5] genoemd. Ons werk toonde opnieuw aan dat nabije oppervlakken het gedrag van de synthetische zwemmers beïnvloeden. Dit heeft ons uiteindelijk geholpen om nieuwe verklaringen voor hun bewegingsmechanisme voor te stellen.

In **hoofdstuk 4**, hebben we een 3D-printtechniek gebruikt om obstakels voor de zwemmers op het oppervlak te printen en zo ook te bevestigen. Deze obstakels waren groter dan onze zwemmers en hadden ofwel ronde vormen, of vormen die op pinda's leken. Als de zwemmers parallel boven het oppervlak bewogen, kwamen ze soms de obstakels tegen en begonnen ze eromheen te cirkelen. We ontdekten dat wanneer meer zwemmers om hetzelfde obstakel cirkelden, ze sneller bewogen dan wanneer één zwemmer alleen in een baan om hetzelfde (soort) obstakel cirkelde. Het was erg interessant om zo een bepaalde manier van samenwerking tussen synthetische zwemmers te vinden, omdat dit tot nu toe alleen werd gevonden tussen biologische zwemmers, zoals bacteriën. Bovendien verzamelden de zwemmers zich bij elkaar en vormden ze op die manier lange ketens, welke zichzelf als geheel voortbewogen rond de obstakels. Ten slotte ontdekten we dat de kromming van de pinda-vormige obstakels het gedrag van de lange ketens beïnvloedde. Deze vondst kan leiden tot verscheidene mogelijke toepassingen: we zouden strategieën kunnen bedenken om de kromming van het oppervlak te gebruiken als een hulpmiddel om de beweging van de zwemmers te beheersen.

---

[5]Van het Griekse woord ὕψος voor hoogte

In **hoofdstuk 5**, hebben we een tweede methode ontwikkeld om afstanden tussen colloïdale deeltjes en oppervlakken te meten. Deze techniek is, in tegenstelling tot die van hoofdstuk 3, gebaseerd op holografische microscopie. Het kan worden gebruikt om de hoogte vanaf de wand te meten voor elk colloïdaal deeltje — niet alleen bolvormige deeltjes — zolang het oppervlak van het deeltje maar overal hetzelfde is. Hoewel we het niet konden gebruiken voor de bolvormige colloïden met een platina-zijde, hebben we het wel gebruikt om het gedrag van colloïden met complexere vormen te bestuderen. We richtten ons op colloïdale deeltjes die eruit zagen als halters, die in oplossing naar de bodem zakten. Voor het maken van de halterdeeltjes hebben we altijd twee even grote bollen aan elkaar vastgemaakt. We ontdekten dat de beweging van de halters in water boven het oppervlak afhankelijk was van de onder van de halter. De kleinere halterdeeltjes positioneerden zichzelf een specifieke hoek ten opzichte van de wand. Dit gebeurde niet voor grotere halters van hetzelfde materiaal: deze oriënteerden zich bijna parallel aan de bodem. Ons werk heeft aangetoond dat niet-bolvormige colloïden zich op complexe manieren gedragen in de buurt van een oppervlak. Deze vondst kan ons in de toekomst helpen modellen te maken, die de beweging in de buurt van een oppervlak van colloïden met willekeurige vormen beter kunnen voorspellen.

In **hoofdstuk 6**, werden we geïnspireerd door biologische microzwemmers met niet-triviale vormen. Onderzoekers verwachten dat vorm belangrijk is: verschillende vormen kunnen biologische zwemmers bijvoorbeeld helpen gemakkelijker te navigeren in complexe omgevingen. We waren benieuwd hoe vorm de beweging van synthetische zwemmers beïnvloedt. Om deze reden hebben we haltervormige colloïden gebruikt gemaakt van twee deeltjes met verschillende afmetingen. We voegden platina toe aan één kant van de halters en plaatsten ze vervolgens in de waterstofperoxide-brandstof. De symmetrische halterdeeltjes stuwden zichzelf voort in de richting van de zijde waar geen platinalaag was aangebracht en in een rechte beweging. In tegenstelling tot de symmetrische halters, bewogen de asymmetrische halterzwemmers zich in cirkels. Onze bevinding kwam overeen met eerder onderzoek en bevestigde dat de vorm van de zwemmer de bewegingsrichting bepaalt.

Samenvattend heeft het werk dat we in dit proefschrift beschreven ons geholpen te begrijpen hoe synthetische zwemmers zich gedragen en welke verschillende factoren hun snelheid en bewegingsrichting beïnvloeden. Dit nieuwe begrip kan nuttig zijn voor het gebruik van katalytische zwemmers als modellen voor microzwemmers voor onderzoeksdoeleinden, en in het algemeen voor het gebruik van synthetische zwemmers in toekomstige toepassingen. Aangezien van synthetische microzwemmers wordt verwacht dat ze taken zouden kunnen uitvoeren in complexe omgevingen, kan ons werk helpen bij het voorspellen en beheersen van de beweging van zwemmers in verschillende omgevingen.

Acknowledgements

appreciated our discussions, thank you for all your help and support, for being such a great house-mate and for agreeing to be my paranymph.

Finally, I wish to thank my parents for supporting my studies, and my brother for the support and encouragement we have always given each other. Dimitri, I cannot even begin to list the many reasons why I want to thank you; let me just say thank you for keeping me sane over the years.

<div align="right">

Stefania Ketzetzi
Leiden
May 31, 2021

</div>

List of Publications

Work presented in this thesis:

1. **S. Ketzetzi**, J. de Graaf, R. P. Doherty, and D. J. Kraft, Slip Length Dependent Propulsion Speed of Catalytic Colloidal Swimmers near Walls, **Phys. Rev. Lett.** 124, 048002 (**2020**) — **Chapter 2**
   Highlighted in Leiden University News and phys.org

2. **S. Ketzetzi**, J. de Graaf, and D. J. Kraft, Diffusion-Based Height Analysis Reveals Robust Microswimmer-Wall Separation, **Phys. Rev. Lett.** 125, 238001 (**2020**) — **Chapter 3**

3. **S. Ketzetzi**, M. Rinaldin, P. Dröge, J. de Graaf, and D. J. Kraft, Activity-induced microswimmer interactions and cooperation in one-dimensional environments, **Submitted** (**2021**) — **Chapter 4**

4. R. W. Verweij*, **S. Ketzetzi***, J. de Graaf, D. J. Kraft, Height Distribution and Orientation of Colloidal Dumbbells Near a Wall, **Phys. Rev. E** 102, 062608 (**2020**) — **Chapter 5**

5. **S. Ketzetzi**, I. Schrëtlen, R. P. Doherty, and D. J. Kraft, *In preparation* (**2021**) — **Chapter 6**

Other publications:

6. R. P. Doherty, T. Varkevisser, M. Teunisse, J. Hoecht, **S. Ketzetzi**, S. Ouhajji, and D. J. Kraft, Catalytically propelled 3D printed colloidal microswimmers, **Soft Matter** 16, 10463-10469 (**2020**).
   Highlighted in BBC, CNN, The London Times, Nature, NRC, and more

7. B. Weber*, Y. Nagata*, **S. Ketzetzi**, F. Tang, W. J. Smit, H. J. Bakker, E. H. G. Backus, M. Bonn, D. Bonn, Molecular Insight into the Slipperiness of Ice, **J. Phys. Chem. Lett.** 9, 2838 (**2018**).
   Highlighted in UvA News, ScienceDaily, phys.org and more

8. **S. Ketzetzi,** J. Russo, D. Bonn, Crystal Nucleation in Sedimenting Colloidal Suspensions, **J. Chem. Phys.** 148, 064901 (**2018**)

   * These authors contributed equally

About the author

I obtained my BSc degree in physics with specialization in *Atmospheric physics* from the Aristotle University of Thessaloniki (2014). My thesis, *Sensitivity of Direct Normal Solar Irradiance at Variations of Aerosol Optical Depth and Column Water Vapor*, was supervised by Prof. Dr. Alkiviadis Bais. I obtained my MSc degree in physics with specialization in *Experimental physics* from the University of Amsterdam (2016). My thesis, *Effect of Sedimentation on Crystal Nucleation in Colloidal Systems*, was supervised by Prof. Dr. Daniel Bonn. In 2017, I started as a PhD candidate in *Active soft matter physics* at Leiden University under the supervision of Dr. Daniela Kraft. I studied the self-propulsion of catalytic microswimmers near walls, the results of which are presented in this thesis. Parts of this work were performed in collaboration with Dr. Joost de Graaf (Utrecht University), Dr. Ruben Verweij, Dr. Rachel Doherty and Dr. Melissa Rinaldin (Kraft Lab).

During my PhD studies, I assisted in the BSc courses *Moleculaire Physica* and *Physics Experiments 2* as well as (co)supervised the theses of four BSc and MSc students with projects ranging from the self-propulsion of spherical and non-spherical catalytic model swimmers near curved and planar walls respectively, to colloidal diffusion, sedimentation and wall distance measurements with holographic microscopy. Since 2016, I have given multiple poster presentations and talks at conferences, PhD schools, and seminars. Most notably, I contributed talks at the APS (Boston, USA 2019 and Denver, USA 2020) and at CHAINS (Veldhoven, Netherlands 2020) and I gave the Nanoseminar of the Debye Institute for Nanomaterials (Utrecht, Netherlands 2020, invited). In 2020, I was nominated for the ''Discoverer of the Year'' Public Award representing the Leiden Institute of Physics; I finished third by public vote.